Structural evolution of isotactic-polypropylene under mechanical load: a study by synchrotron *X*-ray scattering

Der Fakultät Maschinenwesen der Technischen Universität Dresden zur Erlangung des Grades Doktor-Ingenieur (Dr.-Ing.) vorgelegete

Dissertation

Von

Baobao Chang, M.Sc

Geboren am 26.07.1989

in Henan, China

Defense date: 11th September, 2018

Gutachter: Prof. Dr. Gert Heinrich

Prof. Dr. Rene Androsch

Abstract

The relationship between microstructure and mechanical properties of semicrystalline polymer materials has been a hot topic since many years in materials science and engineering. Isotactic polypropylene (iPP) is frequently used as a model material, due to its good mechanical properties and wide applications. In the past few years, numerous studies have been performed in the field of structural evolution during deformation. Previous results revealed that phase transition from crystal to mesophase happens in the crystal scale, lamellae orientation and fragmentation occurs in the lamellae scale, and even cavitation behavior exists in the larger scale. Although abundant work has been done, some problems remain under debate, for instance the relationship between lamellae deformation and cavitation behavior, the role of phase transition on the void formation, et al. In this study, well defined microstructure of iPP is obtained by annealing or adding nucleating agent. Afterward, the structural evolution under three types of mechanical load modes (including uniaxial stretching, creep, and stress relaxation) is in-situ monitored by synchrotron X-ray scattering.

During uniaxial stretching, we revealed, for the first time, how lamellae deformation occurs in the time scales of elastic deformation, intra-lamellar slip, and melting-recrystallization, separated by three critical strains which were only rarely found to be influenced by annealing. Strain I (a Hencky strain value of 0.1) marks the end of elastic deformation and the onset of intra-lamellar slip. Strain II (a Hencky strain value of 0.45) signifies the start of the recrystallization process, from where the long period in the stretching direction begins to decrease from its maximum and the polymer chains in the crystal start to orient along the stretching direction. The energy required by melting arises from the friction between the fragmented lamellae. Strain III (a Hencky strain value of 0.95) denotes the end of the recrystallization process. Beyond the strain of 0.95, the long period and the crystal size remain nearly unchanged. During further stretching, the extension of the polymer chains anchored by lamellae triggers the strain hardening behavior. On the other hand, annealing significantly decreases the critical strain for voids formation and increases the voids number, but restricts the void size. For those samples annealed at a temperature lower than 90 $^{\circ}$C, voids are formed between strain II and strain III. The voids are oriented in the stretching direction once they are formed. For those samples annealed at a temperature higher than 105 $^{\circ}$C, voids are formed between strain I and strain II. The voids are initially oriented with their longitudinal axis perpendicular to the stretching direction and then transferred along stretching direction via voids coalescence. Additionally, the formation of voids influences neither the critical strains

for lamellae deformation, nor the final long period, the orientation of polymer chains or the crystal size.

β-iPP is a kind of metastable phase which can be induced only under special condition. By adjusting the morphology of N,N'-dicyclohexyl-2,6-naphthalene dicarboxamide (NJS) through self-assembly, the relative content of β-iPP (K_β) is successfully controlled, under the condition that the weight content of NJS in the composite keeps at 0.3 wt. %. The microstructural evolution of the iPP/NJS composites with different K_β during uniaxial stretching is studied. The results show that a higher K_β could increase the number of the voids. However, the size of the voids is similar regardless of the NJS morphology. The β-α phase transition takes place after voids formation. During intralamellar and inter-lamellar slip, no obvious polymer chains orientation can be found for α-iPP. In the strain range of 0.1~0.6, the *c*-axis of the β-iPP crystal tends to orient perpendicular to the stretching direction due to lamellae twisting, which is a unique deformation mode of β-iPP lamellae. And the lamellae twisting are proposed to be responsible for the intense voids formation of the composite with higher K_β.

During creep, the evolution of the long period can be divided into four stages (primary creep, transition stage, secondary creep, and tertiary creep). This fits quite well with the macroscopic displacement and strain evolution. In primary creep, the long period along loading direction ($L_p^\parallel$) increases with time due to the stretching of amorphous phase, whereas the long period perpendicular to loading direction ($L_p^\perp$) decreases slightly. In secondary creep, strain increases linearly with time. Both $L_p^\parallel$ and $L_p^\perp$ exhibit the same tendency with strain. The increase of the long period is caused by lamellae thickening, which is a kind of cooperative motion of molecular chains with their neighbors onto the lamellae surface. The increasing rate of $L_p^\parallel$ is larger than that of $L_p^\perp$, indicating that the orientation of molecular chains along loading direction decreases the energy barrier for the cooperative motion. In tertiary creep, strain grows dramatically within a limited time. The lamellae are tilted and rotated, and then disaggregated. In addition, fibrillary structure is formed during lamellae breaking. The length of the fibrillary structure increases from 364 nm to 497 nm but its width stays at 102 nm as creep time increases.

During stress relaxation, the local deformation behavior of the long period is affine with the macroscopic stress relaxation. However, the evolution of the crystal orientation and the void size lag behind the macroscopic stress relaxation. The decrease of the long period is mainly

caused by the relaxation of the strained polymer chains in the amorphous phase. The retardation of the evolution of the crystal orientation is probably caused by the phase transition from stable α-iPP to metastable mesomorphic-iPP. By phase transition, the highly oriented α-iPP is transferred to weakly oriented mesomorphic-iPP. Due to the fact that the void is confined by the network of the strained polymer chains where lamellae blocks serve as the physical anchoring points, the phase transition contributes greatly to the viscoplastic deformation of the network. Consequently, the evolution of the voids size shows a similar trend with that of the phase transition.

With this thesis, we gained a deeper insight into the relationship between structure and properties of semicrystalline polymers. The current study will not only benefit the understanding of polymer materials science but also serve as guidance for the processing of semicrystalline polymers for engineering applications.

Abstrakt

Die Korrelation von Mikrostruktur und mechanischen Eigenschaften teilkristalliner Polymermaterialien ist seit vielen Jahren ein wichtiges Thema von Materialforschung und Anwendungstechnik. Isotaktisches Polypropylen (iPP) wird wegen seiner guten mechanischen Eigenschaften und der breiten Verwendung häufig als Modellmaterial verwendet. In den letzten Jahren wurden zahlreiche Studien auf dem Gebiet der Strukturentwicklung während der Deformation durchgeführt. Frühere Resultate zeigten, dass der Phasenübergang vom Kristall zur Mesophase in der Dimension der Kristallite erfolgt und die Orientierung sowie die Fragmentierung der Lamellen in lamellaren Dimensionen auftritt; während Kavitationseffekte in größeren Dimensionen stattfinden. Obwohl umfangreiche Arbeiten durchgeführt wurden, sind einige Probleme weiterhin in der Diskussion wie zum Beispiel der Zusammenhang von Lamellendeformation und Kavitationsverhalten, die Rolle des Phasenüberganges bei der Entstehung von Voids und andere Fragestellungen. In dieser Arbeit wurden definierte Mikrostrukturen durch Temperung und Verwendung von Nukleierungsmitteln hergestellt. Anschließend wurde die Strukturentwicklung bei drei unterschiedlichen mechanischen Belastungen (uniaxiale Dehnung, Kriechen, Spannungsrelaxation) mittels in-situ Röntgenstreuung am Synchrotron beobachtet.

Es konnte erstmalig gezeigt werden, wie die Lamellendeformation in der uniaxialen Dehnung in den Zeitskalen des intralamellaren Gleitens und der Rekristallisation stattfindet; gekennzeichnet durch drei kritische Deformationen, bei denen nur selten ein Einfluss des Temperns beobachtet wurde. Deformation I (eine Hencky-Deformation von 0,1) kennzeichnet das Ende der elastischen Deformation und das Einsetzen des intralamellaren Gleitens. Deformation II (eine Hencky-Deformation von 0,45) markiert den Beginn des Rekristallisationsprozesses, bei dem die Langperiode in Dehnungsrichtung beginnend vom Maximum abnimmt und die Polymerketten in den Kristalliten beginnen sich in Dehnungsrichtung zu orientieren. Die zum Schmelzen benötigte Energie resultiert aus der Reibung zwischen den Lamellenfragmenten. Deformation III (eine Hencky-Deformation von 0,95) definiert das Ende des Rekristallisationsprozesses. Bei der Deformation oberhalb von 0,95 bleiben die Langperiode und die Kristallitgröße nahezu unverändert. Bei weiter zunehmender Dehnung bewirken die durch die Lamellen verankerten Ketten die Dehnverfestigung. Andererseits senkt das Tempern signifikant die kritische Deformation für die Bildung von Voids und erhöht die Anzahl der Voids, wobei aber die Größe der Voids begrenzt wird. Bei den Proben die bei Temperaturen unter 90 °C getempert wurden, werden

die Voids zwischen kritischer Deformation II und III gebildet. Diese Voids werden während ihrer Entstehung in Dehnungsrichtung orientiert. Die Proben, welche bei Temperaturen größer als 105 °C getempert wurden, zeigen die Entstehung der Voids zwischen kritischer Deformation I und II. Diese Voids sind anfänglich mit ihrer Längsachse senkrecht zur Dehnungsrichtung orientiert und werden dann durch Koaleszenz der Voids in Dehnungsrichtung orientiert. Außerdem beeinflusst die Bildung der Voids nicht die kritischen Deformationen für die Lamellendeformation, die endgültige Langperiode, die Orientierung der Polymerketten oder die Kristallitgröße.

β-iPP ist eine spezielle metastabile Phase, die unter definierten Bedingungen erzeugt werden kann. Bei der Einstellung der Morphologie von N,N'-Dicyclohexyl-2,6-Naphthalendicarboxamid (NJS) durch Selbstorganisation kann der relative Anteil von β-iPP (K_β) erfolgreich gesteuert werden, unter der Bedingung dass der Gewichtsanteil von 0,3 % NJS eingehalten wird. Die Entwicklung der Mikrostruktur der iPP/NJS Proben mit unterschiedlichem K_β wurde während der uniaxialen Dehnung untersucht. Die Ergebnisse zeigen, dass ein höherer K_β –Anteil die Anzahl der Voids erhöhen kann. Hingegen ist die Größe der Voids unabhängig von der Morphologie des NJS. Der β-α Phasenübergang findet nach der Entstehung der Voids statt. Während der intralamellaren und interlamellaren Gleitvorgänge kann keine bemerkenswerte Orientierung der Polymerketten beim α-iPP nachgewiesen werden. Im Dehnungsbereich von 0,1 ~ 0,6 tendiert die *c*-Achse der β-iPP Kristallite zu einer Orienterung senkrecht zur Dehnungsrichtung. Dies wird durch eine Verdrehung der Lamellen verursacht, welche ein typischer Deformatiosmodus von β-iPP Lamellen ist. Es wird angenommen, dass die Verdrehung der Lamellen verantwortlich für die intensive Bildung von Voids bei Proben mit höherem K_β ist.

Beim Kriechen kann die Veränderung der Langperiode in vier Stufen unterteilt werden (primäres Kriechen, Übergangsstufe, sekundäres Kriechen und tertiäres Kriechen). Diese Stufen stimmen sehr gut mit den makroskopischen Verschiebungen und der Veränderung der Dehnung überein. Beim primären Kriechen vergrößert sich die Langperiode entlang der Belastungsrichtung ($L_p^\parallel$) mit der Zeit infolge der Dehnung der amorphen Phase, wobei die Langperiode senkrecht zur Belastungsrichtung ($L_p^\perp$) schwach abnimmt. Während des sekundären Kriechens steigt die Deformation linear mit der Zeit. $L_p^\parallel$ und $L_p^\perp$ weisen die gleiche Tendenz in Abhängigkeit von der Deformation auf. Die Zunahme der Langperiode wird durch eine Verdickung der Lamellen hervorgerufen, welches eine Form der kooperativen Bewegung der Molekülketten mit ihren Nachbarn auf der Lamellenoberfläche ist. Da die Wachstumsrate

von $L_p^{\parallel}$ ist größer als die von $L_p^{\perp}$ ist, ist dies ein Hinweis darauf, dass die Orientierung der Molekülketten in Beanspruchungsrichtung die Energiebarriere für die kooperative Bewegung erniedrigt. Beim tertiären Kriechen steigt die Deformation sehr stark für eine begrenzte Zeit. Die Lamellen werden gebogen und gedreht und letztendlich zerbrochen. Zusätzlich entsteht eine fibrilläre Struktur während des Zerbrechens der Lamellen. Die Länge der fibrillären Struktur erhöht sich von 364 nm auf 497 nm wobei die Dicke von 102 nm während der Kriechzeit konstant bleibt.

Während der Spannungsrelaxation verhält sich die lokale Deformation der Langperiode affin zur makroskopischen Spannungsrelaxation. Hingegen bleibt die Veränderung der kristallinen Orientierung und der Größe der Voids hinter der makroskopischen Spannungsrelaxation zurück. Die Abnahme der Langperiode wird hauptsächlich durch die Relaxation der gedehnten Polymerketten in der amorphen Phase verursacht. Die verzögerte Veränderung der kristallinen Orientierung ist wahrscheinlich durch den Phasenübergang vom stabilen α-iPP zum metastabilen mesomorphen iPP bedingt. Während des Phasenüberganges wird das hoch orientierte α-iPP zum gering orientierten mesomorphen iPP umgewandelt. Infolge der Tatsache, dass die Voids durch das Netzwerk der gedehnten Polymerketten begrenzt werden, wobei die lamellaren Blöcke als Verankerungspunkte dienen, trägt der Phasenübergang erheblich zur viskoplastischen Deformation des Netzwerkes bei. Infolgedessen zeigt die Veränderung der Größe der Voids den gleichen Trend wie der Phasenübergang.

Mit dieser Arbeit wurde eine vertiefende Einsicht in die Struktur-Eigenschafts-Beziehungen von teilkristallinen Polymeren erreicht. Diese Arbeit will nicht nur das materialwissenschaftliche Verständnis von Polymeren bereichern, sondern auch als Anleitung für Verarbeitung von teilkristallinen Polymeren für technische Anwendungen dienen.

Table of content

1 Introduction

1.1 Isotactic polypropylene (iPP)

Polypropylene (PP) is a thermoplastic polymer (see **Figure 1-1**). Due to its outstanding properties, such as low dielectric loss, good heat resistance, non-toxicity and good mechanical properties, PP has been used in a wide variety of applications including cables, packaging, and automotive components.[1-3] PP was polymerized by G. Natta in 1954.[4] And according to a survey by PlasticsEurope, the total European plastic demand for PP was about 9.5 million tons in 2016.[5]
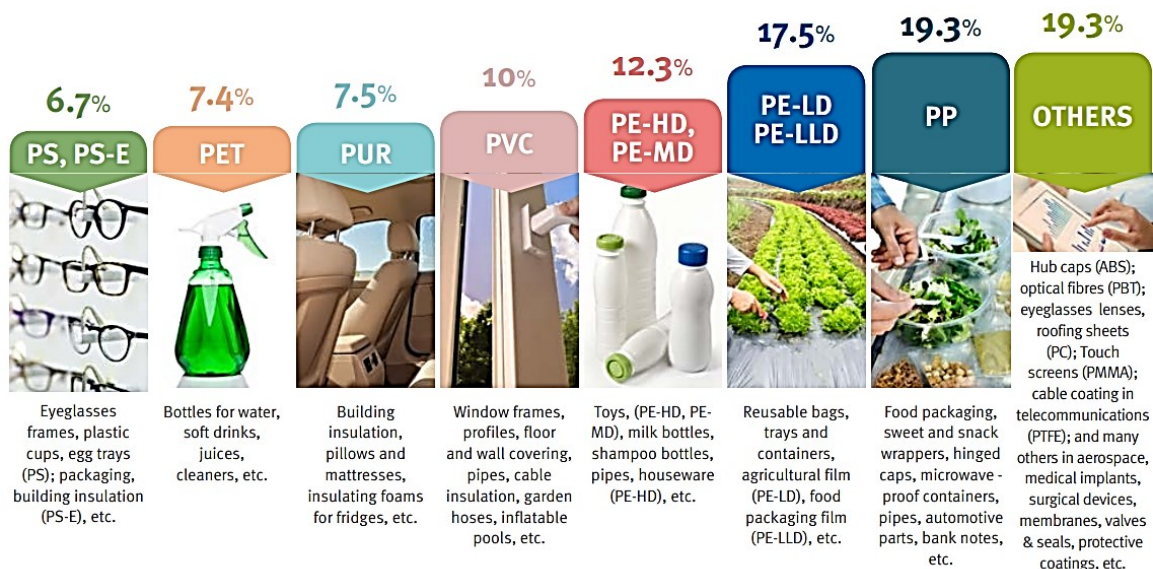
Figure 1-1 European plastics demand by polymer type 2016.[5]

1.1.1 Chain structure of PP

The structural unit of PP is shown in **Figure 1-2**. Depending on the position of the methyl group with respect to the chain backbone, PP can be divided into three types including syndiotactic-PP (sPP), atactic-PP (aPP), and isotactic-PP (iPP). sPP: the position of methyl groups is alternated regularly; aPP: the position of methyl groups is randomly distributed; iPP: all methyl groups are located on the same side. Due to its high regularity, iPP crystallizes easily under common processing condition compared with the other two types.
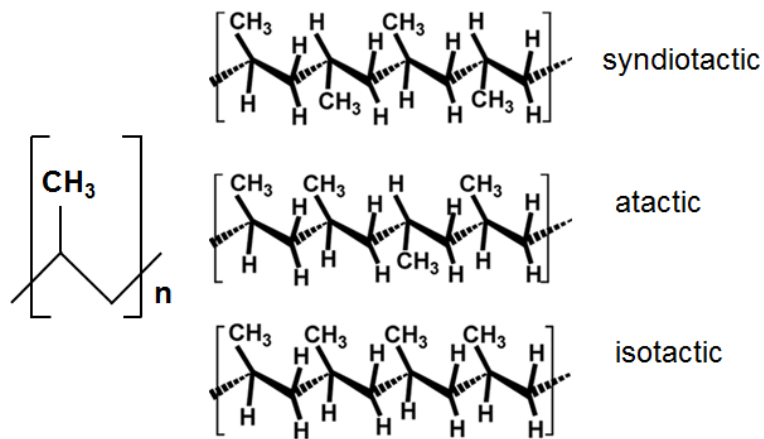
Figure 1-2 The structural unit of PP, and schematic illustration of three type configurations of PP: syndiotactic-PP (sPP), atactic-PP (aPP), and isotactic-PP (iPP).

1.1.2   Crystal forms of iPP

As a kind of polymorphic semicrystalline polymer, iPP has several crystal forms: monoclinic α-iPP, trigonal β-iPP, orthorhombic γ-iPP, and mesomorphic-iPP [6, 7]. The chain conformation for each crystal form is the 3_1 helix [8]. The difference lies in how the chains are packed in the unit cell. The methyl groups are positioned "up" and "down" if the chain is packed as a "left" or "right" handed helix conformation. As an example, **Figure 1-3** presents a helix with "down" position of the methyl group.
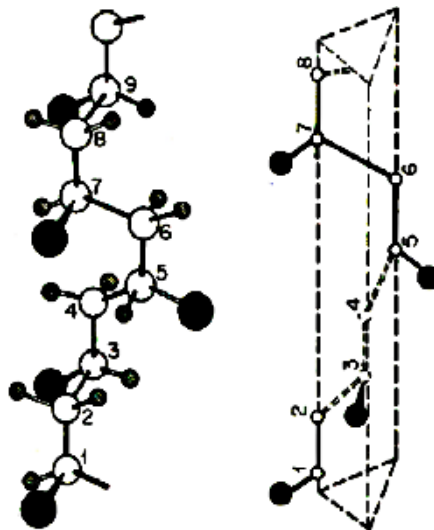
Figure 1-3 Left shows the helical structure of iPP chain with 'down' positions of the methyl group (black spheres). Right is the same helix in a triangular bar. See Ref. [9].

2

α-iPP is thermodynamically stable and is the most encountered form during polymer processing. β-iPP is metastable and can be induced only under special conditions: crystallize under pressure [10], the temperature gradient [11], the flow field [12, 13], or by adding a nucleating agent during crystallization [14]. The γ-iPP is relatively rare, however, it is favored when iPP crystallizes under elevated pressure or the isotactic sequence length is interrupted.[15] The mesophase can be formed by quenching from the melt fast enough. For instance, such a condition can be reached by quenching the melt below 0 ^{o}C with a cooling rate larger than 80 K/s.[16]

The crystalline structures of α-iPP, β-iPP, and γ-iPP are illustrated in **Figure 1-4**. The monoclinic α-iPP has a unit cell with a=0.665 nm, b=2.096 nm, c=0.65 nm and β=99.2^{o}. Each unit cell contains 4 polymer chains with chain axes aligned parallel to the c-axis. The α-iPP can be described by an alternation of layers parallel to the ac-plane and composed of only left handed (L) or right handed (R) helix. The methyl group in both helices can be positioned up (up) or down (dw).[17] The trigonal β-iPP owns a unit cell with a=b=1.103 nm, c=0.65 nm, and γ=120°.[8, 18] Three isochiral helices coexist in the unit cell. The orthorhombic γ-iPP exhibits a unit cell with a=0.854 nm, b=0.993 nm, and c=4.241 nm.[19] γ-iPP is the first identified crystal form where chains in the unit cell are non-parallel packed.
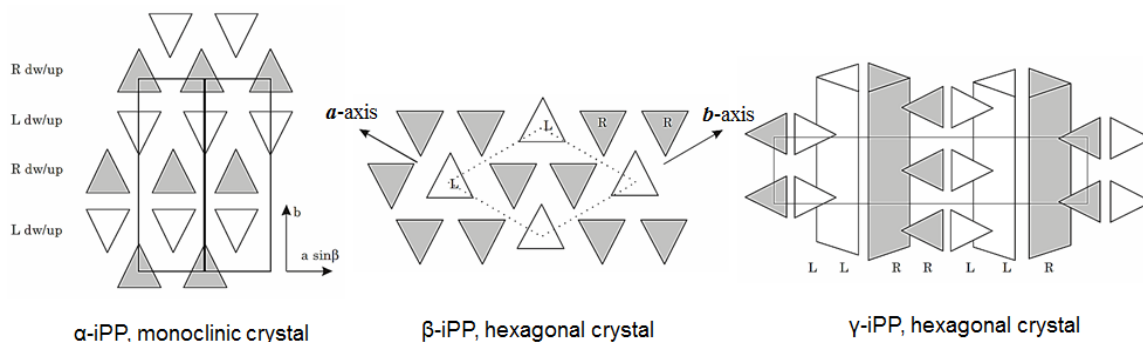
Figure 1-4 Illustration of different unit cells of iPP. L is short for left handed and R is short for right handed helix. Up or dw means that the methyl group in the helix is positioned up or down. See Ref. [20]

The mesophase of iPP contains parallel helices with the same 2*3$_1$ helix in the crystalline phase.[7] Two characteristic halos existed on the WAXS pattern of the mesophase: one locates at a spacing of about 0.59 nm, corresponding to the distance between parallel aligned chains, and the other one is at a distance of 0.41 nm, originated from the repeating period within the helices.[21] The interpretation about the WAXS pattern of the mesophase is still

under debate. One assumes the presence of small crystallites of hexagonal structure[22, 23], but the other one prefers that the lateral local correlation of chain segments in the mesophase is closer to monoclinic.[24]

1.1.3 Lamellae of iPP

The most common morphology of iPP under melt processing condition is the lamellar like crystallite. The chains are arranged in the lamella and the unit cell as described above. In α-iPP and β-iPP, polymer chains (*c*-axis direction) are aligned perpendicular to the ***ab***-plane of the crystal. In γ-iPP, polymer chains are inclined with an angle of $\pm 40^o$ with respect to the normal direction of the lamellae.[19]

The crystalline morphology of iPP is schemed in **Figure 1-5**. The lamella is surrounded by two adjacent amorphous phases. The amorphous phase and the lamella are connected by chain loops, tie chains as well as chain cilia.[25] Polymer chains between the lamella and amorphous phase are highly coupled with the crystals in the lamella, giving rise to the existence of an intermediate phase. To be clarification, the intermediate phase and amorphous phase is also named as rigid amorphous fraction (RAF) and mobile amorphous fraction (MAF).[26] RAF and MAF were first termed by Wunderlich while investigating the glass transition of poly(oxymethylene).[27] Polymer chains in MAF mobilize at the glass transition temperature (T_g), while polymer chains in RAF mobilize at temperature higher than T_g.
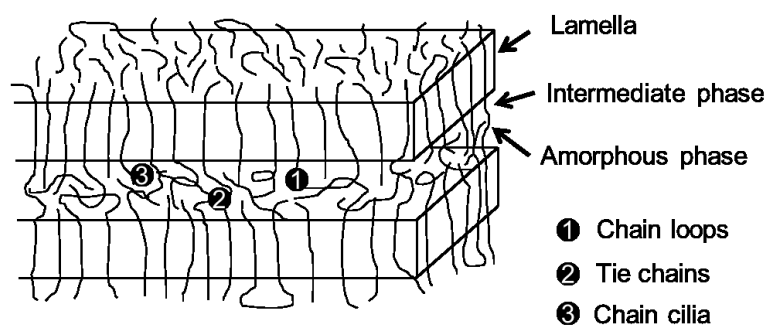
Figure 1-5 Schematic drawing of the morphology of lamellae, amorphous phase and the interface between them.

1.1.4 The morphology of the supra-structure of iPP

Depending on the flow conditions (quiescent or flow induced crystallization), the presence of the filler (nucleating agent, inorganic additives, fibers etc.), iPP may exhibit spherulite,[28, 29]

cylindrites,[30] transcrystalline structure,[31] shish-kebab,[32] and extended-chain structure.[33]

1.2   Structural evolution during deformation

1.2.1   Deformation process of semicrystalline polymers

Under mechanical load, the morphology of semicrystalline polymers is transformed from either homogeneous (the core region of injection molded sample, the compression molded sample) or heterogeneous (the skin region of injection molded sample, melt blowing films, fibers) to highly oriented structure at large strains, if the stretching temperature is above the glass transition temperature.[34, 35] In the early stage of deformation, the stress increases almost linearly with the strain, see **Figure 1-6**. The macroscopic deformation consists both amorphous phase and lamellae microscopic deformation.[36] The deformation in the amorphous phase is easily activated but it is rapidly exhausted due to the different alignment of crystalline lamellae with respect to the deformation direction. The deformation in this stage is mainly interlamellae separation and slip. At the end of the linear regime, the sample is subjected to a non-linear deformation which is caused mainly by interlamellar slip.[37, 38] Upon further stretching, the stress reaches a maximum value which is normally labeled as the yielding point. The yielding point marks the beginning of plastic (irreversible) deformation. After yielding, the stress suffers a slight decrease, generally due to the localization of strain and necking. The plastic deformation will be the dominant process until breaking.
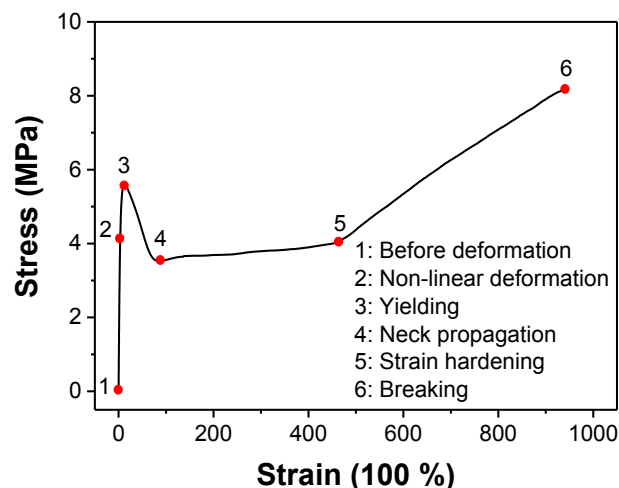
Figure 1-6 Engineering stress-strain curve of iPP stretched at 135 $^{\circ}$C. The crosshead speed is 50 mm min^{-1}.

Up to now, two distinctly different mechanisms have been suggested for the yielding of semicrystalline polymers.

The first concept was initially proposed by Peterson:[39] the emission of dislocations from the edges of the lamellae across the narrow faces and their travel across crystals via crystallographic slips. This idea was further explored by Guiu [40] and Young.[41] The crystallographic slips mechanism was evidenced by different researchers in the past.[42-50] The basic mechanism of crystallographic slips essentially involves the glide of dislocations, which are already present in the lamellar crystals or are nucleated at the boundary of a crystal upon application of a stress level above a threshold value reached at the yielding point. For polymers, the intrinsic nature of chain-molecules necessarily entails slip systems with slip planes parallel to the chain axes and slip directions either parallel (chain slips) or perpendicular (transverse slips) to chain axes.[51] In addition, because of the presence of chain folds, slip planes parallel to the basal planes of the lamellar crystals containing the chain folds are generally preferred, because a slip in these planes does not disrupt the folding scheme at the crystal surfaces. Dislocation theory predicts the correct order of magnitude of the yield stress that agrees best for the Burgers vector of dislocations equal to the crystallographic unit cell dimension along macromolecular chains.[50] However, there are experimental evidences that the yield stress of semicrystalline polymers depends not only on crystal thickness but also on the degree of crystallinity.[50, 52, 53] The increase of the yield stress has been observed together with the increase in thickness of the crystals in the sample. However, there are difficulties to maintain the same degree of crystallinity in samples together with varying crystal thickness. In the case of polyethylene such relationship is observed for a certain range of the crystals' thickness, up to 40 nm, while above this level, the increase of crystal thickness is not accompanied by a further increase in yield stress.[54, 55] The authors of the above-mentioned articles explained the observed relationship by the presence of a new, effective source of dislocation, active in thick crystals and at low temperature but inactive in thinner crystals.

The second mechanism for yielding connected with non-crystallographic changes, related to destroying crystals and resulting in a new crystalline ordering of the material, irrespective of the original structure but characteristic for the temperature of deformation was proposed later.[56-60] It was suggested that during deformation an adiabatic heating occurs when accompanied by the applied stress, partial melting and recrystallization takes place.[61] It was also suggested that raising the temperature is not a necessary condition for partial melting and

6

recrystallization.[62-64] Those experiments and considerations did not, however, established at which elongation a partial melting and recrystallization are initiated nor did not predict the correct order of magnitude of the yield stress. Despite numerous studies being carried out, the mechanisms of plastic deformation of semicrystalline polymers due to complex, hierarchical architecture of such materials still require more detailed research. The deformation of a semicrystalline polymer is a process which we should take into account the presence of crystalline lamellae as well as amorphous layers lacking order. At temperatures at which amorphous phase exhibits rubber-like properties (above the glass transition temperature), it is in the interlamellar regions that the initial stage of deformation takes place.

1.2.2   Cavitation behavior of semicrystalline polymers

Cavitation behavior is found in many semicrystalline polymers, including iPP,[65, 66] PE,[67, 68] poly(1-butene) (P1B)[69], etc., when these polymers are stretched above their glass transition temperature. Stress whitening can be regarded as the scattering of visible light by voids detected by naked eye. As the size of the voids exceeds 0.5 μm, most of the visible light shed on the sample will be scattered, transforming the sample from transparent one to opaque one. In the pioneering work by Peterlin,[70] randomly distributed cracks were found in the neck region of PP specimen. In addition, the formation of small cracks was reported to arise earlier than macroscopic stress whitening.[71] Recent works about the cavitation behavior of semicrystalline have been reviewed excellently by Pawlak, Galeski, and Rozanski.[72] Generally, cavitation behavior of semicrystalline polymers can be influenced by many factors which can be divided into two groups. One of them is attributed to experimental factors such as stretching temperature and stretching speed. Generally, a lower stretching temperature or a larger stretching speed favors voids formation. Another group is attributed to the microstructure of polymers, for instance the crystal form, the thickness of lamellae, as well as the state of the amorphous phase.

1.2.2.1   Role of crystal form

Aboulfafaj et. al.[73] found that under tensile deformation α-iPP spherulites exhibited a brittle failure. The cavitation appeared at boundaries of spherulites or at the region perpendicular to the tensile direction. However, no cavitation could be observed in the sample comprising β-iPP spherulites. The β-iPP spherulites were deformed plastically up to large deformation. Chu [74] prepared iPP films containing more than 90 % β-iPP. These samples crystallized under either isothermal or non-isothermal conditions. The porosity of the stretched films, which is

caused by the existence of voids, was determined. The results showed that the porosity of a film increased with the drawing ratio. The voids observed by scanning electron microscopy (SEM) were elongated along stretching direction and confined by the fibrillary structures. The formation of numerous voids was proposed to be caused by the volume contraction of the film. β-iPP belongs to a metastable phase, so a β-α phase transformation was induced during deformation. The density of α-iPP is higher than that of β-iPP. Therefore, a volume contraction occurred and led to the formation of voids in the sample. The more pronounced stress whitening behavior in β-iPP rich iPP samples was also confirmed by Pawlak.[66]

1.2.2.2 Role of lamellae arrangement

In α-iPP, the lamellae are arranged in a unique "cross-hatched" structure, where daughter lamellae grow 80° inclined to the mother lamellae.[8] Nitta et. al observed that cavitation appears earlier if there were more tangential lamellae in a single spherulite. Otherwise, Pawlak found that the reduction of tangential daughter lamellae would advance the formation of voids.[72]

1.2.2.3 Role of crystallinity

By annealing, Na et. al prepared PP samples with crystallinity ranging from 48 to 56 %. The cavitation behavior of the sample was investigated by measuring the volume increase. The results showed that in annealed samples the cavitation behavior was significantly intensified due to the increased stress concentration sites.[75] Boger examined the cavitation behavior of metallocene PP with crystallinity ranging from 0 to 62 %. For the sample with crystallinity higher than 36 %, the signal originated from a fibrillary structure showed up on the synchrotron SAXS as the elongation ration is larger than 3. In case of β-iPP, annealing could advance the appearance of cavitation.[76]

1.2.2.4 Role of the thickness of lamellae

Generally thinner lamellae would prevent the formation of voids. The reason responsible for that was proposed by Seguela: a thinner lamella bears a larger tie chain density, which transfers the load to lamellae in a better way and leads to the plastic deformation of lamellae instead of the cavitation in the amorphous phase.[77]

1.2.2.5   Role of lamellae orientation

The cavitation behavior of oriented β-iPP was investigated by Bao et al.[78] The samples were cut from extruded sheets and the deformation direction is parallel to the orientation of β-iPP lamellae. Their results proved that at temperatures lower than 110 ^{o}C, the orientation of β-iPP is almost unchanged during deformation, and void forms before fragmentation and reorientation of β-iPP. As the deformation temperature risen to 130 and 140 °C, β-iPP reorient gradually upon stretching, and the size of voids decreases because that less β crystal fragmentation takes place at high stretching temperature.

1.2.2.6   Role of the state of amorphous phase

Pawlak and Galeski compared the cavitation behavior of PP characterized with similar crystallinity and crystal thickness but different molecular masses of 400 and 250 kg/mol. It was found that the sample having lower molecular weight showed more intensive cavitation, as a result of reduced number of entanglements in the amorphous phase.[79] Rozanski and Galeski extracted the additives in the amorphous phase by critical CO_2 and also by a mixture of nonsolvent. Their results showed that purified PP exhibited more intense cavitation than pristine PP.[80] The intensified cavitation process in the purified samples was caused by the changes in free volume by eliminating low fractions and soluble additives in the amorphous phase, indicating that the nucleation of voids existed in the material itself in contrast to heterogeneous nucleation on foreign substances. In their later work, it was proved that only partial filling of the free volume pores of the amorphous phase with low molecular weight modifier leads to a decrease of intensity or complete elimination of the cavitation phenomenon.[81]

1.3   Synchrotron X-ray scattering

1.3.1   X-ray and its sources

X-rays, a kind of electromagnetic radiation (see **Figure 1-7**), is also named as Röntgen radiation after Wilhelm Röntgen who discovered X-rays in 1895.[82] Since that time, X-rays has been employed in the field of materials science as a non-destructive analytical technique. Traditionally, X-rays are produced by X-ray tubes where the electrons, emitted from cathode wire, are accelerated by an electric voltage before hitting the target. The wavelength of X-rays produced by X-ray tubes depends on the target material. For instance, the characteristic wavelength of the X-ray produced is 1.54 Å by Cu target, and 1.79 Å by Co target.
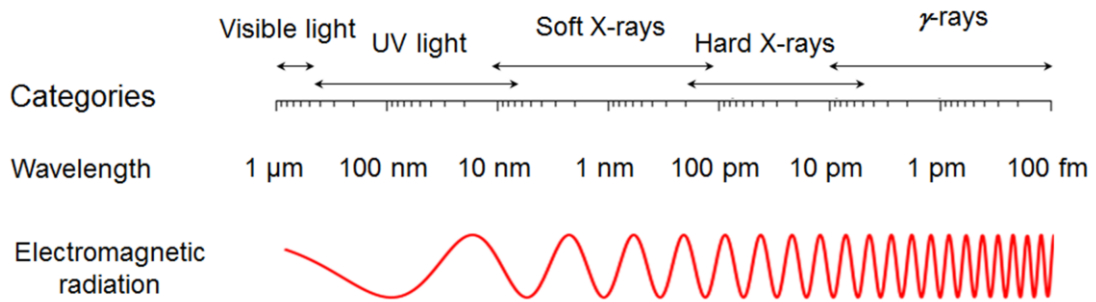
Figure 1-7 Categories of electromagnetic radiation.

The main disadvantages of X-ray tubes are their low intensity, low brilliance, and broad focus (around 2×12 mm).[83] In the mid of 1970s, the limitation of X-ray tube was overcome due to the availability of the synchrotron radiation from ring accelerators, where electrons orbiting in a magnetic field lose energy continually in the form of electromagnetic radiation. The first synchrotron light source was the Standford Synchrotron Radiation Laboratory (SSRL) build in 1977.[84] Nowadays, a few synchrotron radiations have been set up all over the world and the synchrotron radiation has been developed into the 3rd generation, to name a few, European Synchrotron Radiation Facility (ESRF) in France,[67] Deutsches Elektronen-Synchrotron (DESY) in Germany (see **Figure 1-8**), [85] and Shanghai Synchrotron Radiation Facility (SSRF) [86] in China etc. At PETRA III of DESY the size of the X-ray beam can reach a few micrometers and the exposure time is in the range of milliseconds. The high spatial and time resolution of synchrotron X-ray source enables the scientists to perform in-situ X-ray scattering measurements combining complicate thermal/mechanical environment.

Figure 1-8 PETRA III, the 3rd generation of synchrotron light source at DESY Germany.

1.3.2 The interaction between X-rays and objects

As X-rays interact with an object, they can be absorbed or scattered. For the scattering of X-rays by a single free electron, assuming elastic scattering the wavelength of the scattered wave is the same with that of the incident one. The relation between the scattered wave E_2 and incident wave E_1 follows,

$$E_2 = E_1 \frac{e_0{}^2}{m_0 c^2 r} \exp(-iqr) \qquad \textbf{Equation (1-1)}$$

where $\frac{e_0{}^2}{m_0 c^2} = r_0$, r_0 is the electron radius, which equals 3.54×10^{-4} Å.[87] r is the position of the electron and q is the scattering vector. The magnitude of the scattering vector is

$$q = \frac{4\pi}{\lambda} sin\theta \qquad \textbf{Equation (1-2)}$$

θ is the scattering angle. In addition to q, another scattering vector s is also widely used in the field of scattering,

$$q = 2\pi s \qquad \textbf{Equation (1-3)}$$

The efficiency of the scattering process could be described by the differential scattering cross-section $(d\sigma/d\Omega)$,[87] which is given by

$$\left(\frac{d\sigma}{d\Omega}\right) = \frac{I_m}{\Phi_0 \Delta\Omega} = \frac{|E_2|^2}{|E_1|^2} R^2 \qquad \textbf{Equation (1-4)}$$

σ is total scattering intensity, Ω is the solid angle, I_m is measured scattering intensity, i.e. the number of scattered photons recorded per second by the detector, Φ_0 defines the number of photons passing through unit area per second, and R is the distance between the object and the detector.

Depending on the distance between the object and the detector, the scattering experiments can be divided into four subareas, which are wide-angle X-ray scattering (WAXS) containing the classical X-ray diffraction, middle angle X-ray scattering (MAXS) covering the characteristic scattering of liquid-crystalline structure and rigid-rod polymers, small angle X-ray scattering (SAXS) comprising the typical nanostructure in semicrystalline polymers and thermoplastic elastomers, and ultra-small angle X-ray scattering (USAXS) extending the detection range to micrometer scale.[83] Considering the scope of this chapter, SAXS will be emphasized especially. SAXS comprises the scattering angle range $2\theta < 2^o$. In this range, structures with the size of 1~500 nm can be detected, covering the size of lamellae and small voids.

1.3.3 Wide angle X-ray scattering

A crystalline material is built by regularly repeating the unit cell. The points at which the origins of the unit cell are located form a lattice which exists in three dimensions. **Figure 1-9** presents a 2D rectangular lattice (for simplification), which can be described by a set of vectors R_n with

$$R_n = n_1 a_1 + n_2 a_2 \qquad\qquad \text{Equation (1-5)}$$

where a_1 and a_2 are the lattice vectors, and n_1 and n_2 are integers.

Miller indices are usually used to specify families of planes in a crystal. For a given family of planes, the Miller indices (*hkl*) refers to the plane which is closest to the origin and has intercepts $(a_1/h, a_2/k, a_3/l)$ on the axes (a_1, a_2, a_3). As an example, (1,2) planes on the 2D lattice is pointed in **Figure 1-9**. Since that the crystal planes are equally spaced, so the lattice spacing d_{hkl} can be calculated. For instance, the d spacing of a cubic lattice is given by

$$d_{hkl} = \frac{a}{\sqrt{h^2 + k^2 + l^2}} \qquad\qquad \text{Equation (1-6)}$$

where *a* is the lattice parameter.

When X-rays interact with lattice planes with a spacing of *d*, the requirement that the path length of the interfered scattered waves is an integer multiple of the wavelength leads to the well-known statement of Bragg's law:

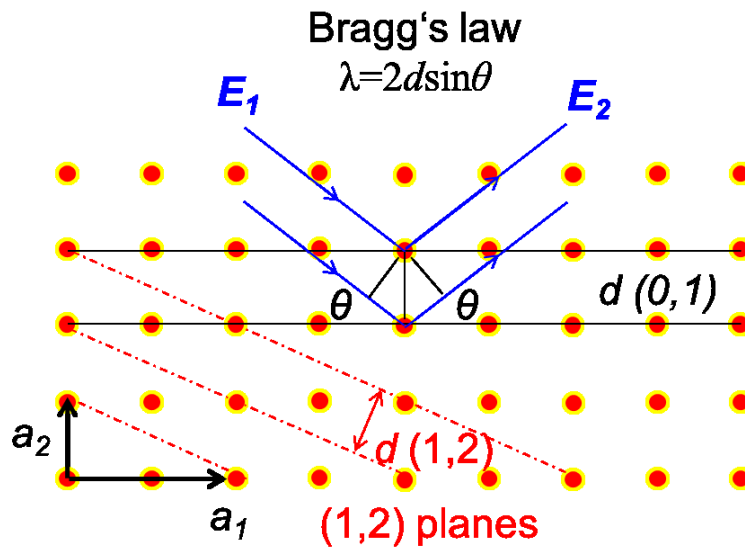$$\lambda = 2d\sin\theta \qquad\qquad \text{Equation (1-7)}$$

Figure 1-9 2D-crystal lattice in real space as well as the scheme of Bragg's law. E_1 refers to the incident X-ray and E_2 refers to the scattered X-ray.

Following Bragg's equation, the diffraction peaks caused by the interference should come out as infinitely sharp point-like peaks. However, in reality the peaks are observed to have a certain width. Besides instrumental broadening, the reasons for this can be imperfections in the crystalline stacking (e.g. due to strains) or a finite size of the crystallites.[88] The Scherrer equation relates the width of the crystalline peak $\Delta\theta$ to the size of the crystallite τ_{hkl} normal to the scattering plane (*hkl*):

$$\tau_{hkl} = \frac{K\lambda}{\cos(\theta/2)} \qquad\qquad \textbf{Equation (1-8)}$$

K is a constant of the order of 0.89.

1.3.4 Small angle X-ray scattering

In SAXS measurement, X-rays detect the electron density difference $\Delta\rho$, and the measured scattering intensity (I_m) is

$$I_m(\boldsymbol{s}) = \Delta\rho^2 V_p^2 |\mathcal{F}(\boldsymbol{s})|^2 \qquad\qquad \textbf{Equation (1-9)}$$

$\mathcal{F}(\boldsymbol{s})$ is the form factor and V_p is the volume fraction of the region with different electron density (for instance the lamella in semicrystalline polymers, the voids during deformation, and "shish" structure during shear induced crystallization). R_g is the radius of gyration of the polymer chain. In the extremely small scattering angle range, $sR_g \to 0$,

$$\mathcal{F}(s) \approx 1 - \frac{s^2 R_g^2}{10} \qquad\qquad \textbf{Equation (1-10)}$$

and the initial intensity decay is approximated by Guinier's approximation

$$I_m(s) \approx \Delta\rho^2 V_p^2 \left[1 - \frac{s^2 R_g^2}{10}\right]^2 \approx \Delta\rho^2 V_p^2 \left[1 - \frac{s^2 R_g^2}{5}\right]$$

$$\approx I_m(0)\exp(-4\pi^2 R_g^2 s^2) \qquad\qquad \textbf{Equation (1-11)}$$

The scattering invariant Q which is independent of the shape of the scatters,

$$Q = \iiint_{s\to 0}^{s\to\infty} I(\boldsymbol{s})d\boldsymbol{s} \propto \Delta\rho^2 V_p(1 - V_p) \qquad\qquad \textbf{Equation (1-12)}$$

The pattern of SAXS measurement depends on the structural units of the material. For the material with the periodically stacked structure (lamellae in semicrystalline polymers) inside, the pattern exhibits a homogeneous ring or "two-spots" depending on the orientation of lamellae. For the material with the oriented elongated structure for instance extended chain structure (shish induced by flow) as well as voids, a streak scattering will show up in the pattern.

1.3.4.1 Ruland streak method

Considering a perfect orientation of the cylindrical structures, Ruland [89] proposed the integral breadth $B_{obs}(s_{12})$ of the elongated structure measured as a function of s_{12} follows

$$B_{obs}(s_{12}) = \int_{-\infty}^{\infty} I(s_{12}, s_3) ds_3 / I(s_{12}, 0) \qquad \textbf{Equation (1-13)}$$

s_{12} is the scattering vector perpendicular to the reference direction (stretching or shearing direction), s_3 is the scattering vector along the reference direction. The average length $\langle L \rangle$ of the elongated structure is

$$\langle L \rangle = \frac{1}{B_{obs}(s_{12})} \qquad \textbf{Equation (1-14)}$$

If misorientation has to be taken into account, the orientation distribution of the streak must be considered, then the apparent azimuthal integral breadth

$$B_{obs}(s) = \frac{1}{I(s, \pi/2)} \int_{-\pi/2}^{\pi/2} I(s, \varphi) d\varphi \qquad \textbf{Equation (1-15)}$$

depends on the width of the peak on the azimuthal intensity distribution curve. The evolution of $B_{obs}(s)$ as a function of s follows

$$B_{obs}^2(s) = \frac{B_p^2}{s^2} + \frac{1}{s^2 \langle L \rangle^2} + B_g^2 \qquad \textbf{Equation (1-16)}$$

if a Gaussian can describe the orientation distribution. B_p describes the inevitable instrumental broadening and B_g is the true integral breadth of the orientation distribution. Or

$$B_{obs} = \frac{B_p}{s} + \frac{1}{\langle L \rangle} + s B_g \qquad \textbf{Equation (1-17)}$$

if a Lorentzian fits the orientation distribution.

2 Motivation and objectives

Semicrystalline polymers comprise a large part of polymer materials, including mainly polyethylene (PE), polypropylene (PP), polyamide (PA), polyimide (PI), et al. They are used in the field of packaging, textiles, automotive components, engineering plastic parts, and medical devices. The mechanical properties of semicrystalline polymers are a particularly interesting topic, which is of great scientific and industrial importance. And the relationship between structure-properties of semicrystalline polymers is a key issue in polymer physics and polymer engineering. Since 1960s, numerous studies have been performed attempting to shed light on the relationship between structure-property of semicrystalline polymers, but the mechanism behind that remains an open topic due to the following three aspects: 1). The multiscale structure and morphology of semicrystalline polymers themselves (chain structure, crystal structure, lamellae morphology, etc.); 2). The multiscale structural evolution happened during deformation (for instance the lamellae fragmentation, melting-recrystallization, orientation, cavitation); 3. Distinct different mechanical load modes (uniaxial stretching, creep test, stress relaxation test, etc.) used in the test. The main obstacle for the study is the lacking of in-situ characterization technique which can capture the structural evolution under mechanical load in different scale simultaneously with sufficiently temporal resolution.

Synchrotron radiation sources are employed in polymer science increasingly in the past 20 years. Due to the high brilliance, high flux, high stability, polarization and coherence behavior, synchrotron X-ray scattering can capture the structural change in a temporal resolution of millisecond. In addition, by employing micro-focus synchrotron X-ray scattering, a spatial resolution of micrometer can be realized. What's more, by adjusting the distance between the sample and the detector, the structural evolution ranging from a few angstroms to a few micrometers can be detected.

Isotactic-PP (iPP), one of the frequently used polymers in industrial processing and scientific research, is used as a model material in this work. The iPP samples with well-defined microstructure are obtained by annealing or adding nucleating agent. The structural evolution under uniaxial stretching, creep, and stress relaxation tests are monitored by in-situ synchrotron *X*-ray scattering measurements. The interests in this work are focused on the following topics:

- ❖ The microstructure arrangement (lamellae branching and polymer chains orientation) in a single iPP spherulite.

- ❖ The crystalline structure of iPP after annealing, including the lamellae thickness, the long period, the crystallinity, as well as the mechanical relaxation behavior of polymer chains in the amorphous phase.

- ❖ The lamellae deformation and cavitation behavior of the annealed iPP during uniaxial stretching. The critical strains for lamellae fragmentation, melting-recrystallization, polymer chains orientation, and the critical strain for void formation. And lastly, the relationship between lamellae deformation and cavitation behavior.

- ❖ The self-assembly behavior of the nucleating agent (N,N'-dicyclohexyl-2,6-naphthalene dicarboxamide), and its influence on the rheology and crystallization behavior of iPP.

- ❖ The cavitation behavior, lamellae deformation, as well as the β-α phase transition during uniaxial stretching of iPP containing different content of β-iPP.

- ❖ The microstructural evolution including lamellar thickening and shish formation during creep.

- ❖ The phase transition, evolution of long period, and cavitation behavior during stress relaxation.

At all, the focus of this work is to gain new insight into the structure-property relationship of semicrystalline polymer and provide guidance for the processing of semicrystalline polymers.

3 Samples preparation and basic characterization

3.1 Materials and samples preparation

iPP (M_w=365 kg/mol, M_n=67.6 kg/mol) used in this study is a polypropylene homopolymer (commercial product name: HD120MO) obtained from Borealis GmbH, Linz, Austria. The melt flow index is 8 g/10 min (230 ^{o}C, 2.16 kg).

Carbon fiber (CF) with a trademark of T300-3K was purchased from Toray Inc., Japan.

N,N'-dicyclohexyl-2,6-naphthalene dicarboxamide (NJS), kindly provided by Rika International Limited (Oldham, U.K.), was used as the nucleating agent (NA) in this study. The weight content of NJS in iPP/NJS composites is 0.3 %, and the composite was mixed by a single screw extruder.

3.1.1 Preparation of iPP films with single layer of spherulites and transcrystalline regions

A piece of iPP film and two perpendicular CFs were placed between two coverslips in a "sandwich-like" arrangement followed by heating up to 210 ^{o}C with a heating rate of 10 K min^{-1}. As the film was melt totally, it was squeezed slowly to 40 μm at 210 ^{o}C and kept for 5 min to fully erase any thermal history. Subsequently, the film was cooled to 138 ^{o}C with a cooling rate of 10 K min^{-1}. Upon reaching 138 ^{o}C, both CFs were pulled a few millimeters manually to induce transcrystalline around the CFs. After that, the film was crystallized at 138 ^{o}C for 20 min, and then at 130 ^{o}C for 30 min.

3.1.2 Preparation of iPP plates crystallized with different thermal histories

iPP plates with a thickness of 1 mm were prepared by compression molding in the following procedure: firstly, the plates from injection molding were kept at 210 ^{o}C for 10 min to fully erase any thermo-mechanical history. Afterward, the plates were cooled by water (10 ^{o}C) and kept at room temperature for 48 h. Then the water-cooled plates were annealed in a vacuum oven (Thermo Scientific, USA) under 75 ^{o}C, 90 ^{o}C, 105 ^{o}C, 120 ^{o}C, and 135 ^{o}C for 6h. For clarification, the plate without annealing was named PPna and the plates with annealing were named PPT$_a$-t with T_a refers to the annealing temperature and t refers to the annealing time. For instance, PP75-6 means that the plate was annealed at 75 ^{o}C for 6 h. The plates with an annealing time of 6 h were also named as PPT$_a$ for short, for instance PP75. For comparison,

iPP plates crystallized directly from the melt were also prepared. The samples prepared by melt crystallization were named as PPMT$_c$.

3.1.3 Preparation of iPP/NJS plates with different morphologies of NJS

Two compression molding machines were employed at the same time to realize the heating protocol as follows: firstly, the extruded iPP/NJS composite granules were heated from room temperature to a final heating temperature (T_f) with the heating rate of 30 K/min, then kept at T_f for 15 min. T_f used in this study was 260 ^{o}C, 270 ^{o}C, 280 ^{o}C, 290 ^{o}C, 300 ^{o}C, and 310 ^{o}C. Secondly, the iPP/NJS composite was transferred to another compression molding machine which was pre-set at 160 ^{o}C, then kept for 60 minutes. For clarification, the iPP/NJS composite with different T_f was named iPP/NJS03-T_f. For example, iPP/NJS03-260 means that the sample was treated with T_f of 260 ^{o}C. The thickness of the plate was 1 mm.

3.1.4 Preparation of microinjection molded iPP/NJS sample

To get the microinjection molded specimens, the composites were microinjection molded with the following parameters: the barrel temperature is 280 °C, the mold temperature is 25 °C, and the injection molding speed is 25 cm^3/s. The thickness of the sample is 0.3 mm.

3.2 Characterization

3.2.1 Differential scanning calorimetry (DSC)

The melting behavior of the sample was characterized by DSC measurements on Q2000 (TA Instruments, USA). The instrument was temperature and melting enthalpy calibrated by using indium as a standard before the test. Dry nitrogen was used as a purge gas at a rate of 50 mL min^{-1} during the test. A 5 mg sample sealed in an aluminum pan was heated from -80 ^{o}C to 200 ^{o}C with a heating rate of 10 K min^{-1}. The crystallinity ($X_{c\text{-DSC}}$) could be calculated by

$$X_{c-\text{DSC}} = \frac{\Delta H_m}{\Delta H_m^*} \times 100\ \%$$ **Equation (3-1)**

where ΔH_m and ΔH_m^* are the fusion enthalpy and the equilibrium melting enthalpy of samples, for iPP ΔH_m^* is 207 J g^{-1}.[90]

To get the recrystallization behavior of the sample, the temperature-modulated DSC (TMDSC) measurements were performed on the same instrument. The parameters for TMDSC measurements were as follows: the temperature amplitude is 0.318 K, the oscillation period is 40 s, and the heating rate is 2 K min^{-1}.
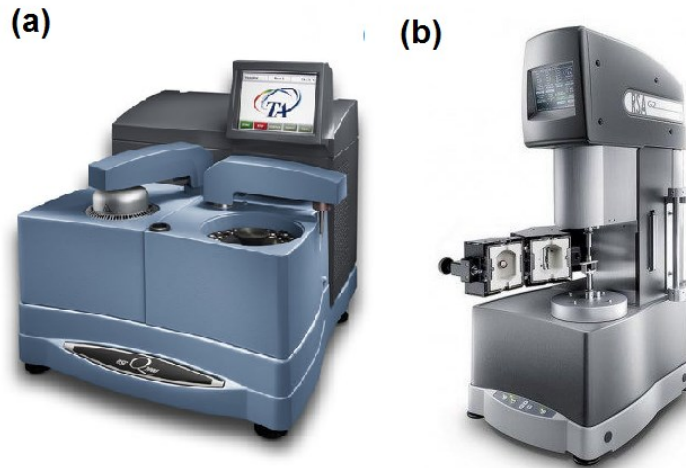
Figure 3-1 (a) Q2000 (TA Instrument) to detect the melting or recrystallization behavior of the sample; **(b)** ARES G2 (TA Instrument) for dynamic mechanical analysis and rheology test.

3.2.2 Dynamic mechanical analysis (DMA)

The mechanical relaxation behavior of the sample was tested with an ARES G2 rheometer (TA Instruments, USA). The sample with a width of 11 mm and a free length of 10 mm was cut from the 1 mm thick plate. Nitrogen was used as the heating gas during the measurement. Each test was started 4 min after the sample was inserted into the rheometer to ensure the attainment of thermal equilibrium. During the temperature sweep tests, the angular frequency used was 1 rad s^{-1}, the strain amplitude was 0.05 %, the temperature range was from -70 $^{\circ}$C to 160 $^{\circ}$C, and the heating rate was 5 K min^{-1}. During the temperature-frequency sweep tests, the specimens were scanned from 0.05 rad s^{-1} to 100 rad s^{-1} at different temperatures (-70 $^{\circ}$C to 160 $^{\circ}$C in steps of 5 $^{\circ}$C).

3.2.3 Scanning electron microscopy (SEM)

The SEM measurement was done on Zeiss Ultra Plus (Germany) with an accelerating voltage of 3 kV. Before the SEM observation, a permanent etching method [91] was used to get the lamellae morphology of the sample. The etching was performed in a mixture of KMnO$_4$-H$_2$SO$_4$-HNO$_3$ for 2-3 h, afterward the etched sample was spur coated with 6 nm layer of platinum.
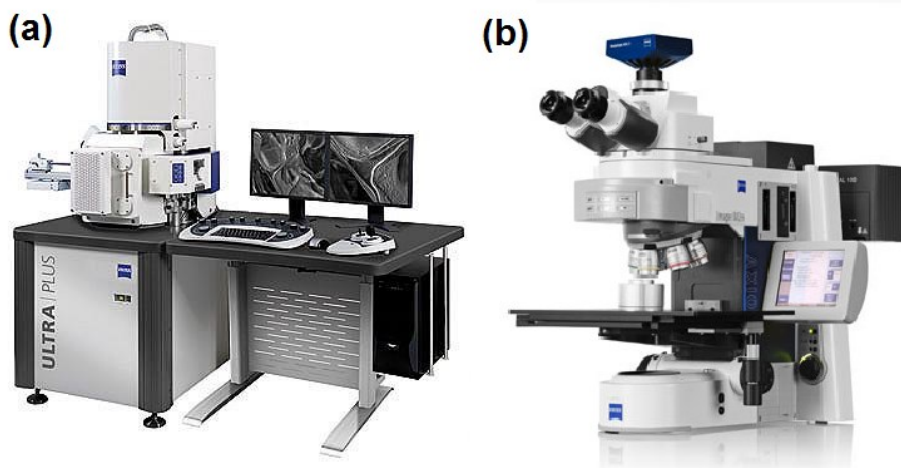
Figure 3-2 (a) The field emission scanning electron microscope (Ultra plus, Carl Zeiss, Germany); (b) The polarized optical microscope (Axio Imager, Carl Zeiss, Germany).

3.2.4   Polarized optical microscopy (POM)

A polarized optical microscope (Axio Imager, Carl Zeiss, Germany) equipped with a hot stage (Linkam TS1500, United Kingdom) was used to observe the morphological changes of iPP spherulite or NA self-assembly.

3.2.5   Rheology test

Rheological measurements were performed on a rheometer (ARES2, TA Instruments, USA) equipped with $\varnothing$ 25 mm parallel plate geometry. The sample chamber was purged by a continuous flow of nitrogen gas in order to avoid degradation of the composites. The linear viscoelastic region of the sample was determined by a strain sweep from strain amplitude (γ) of 0.05 to 1000 % at an angular frequency (ω) of 1 rad s^{-1}. Then small amplitude oscillatory shear (SAOS) tests were conducted from 0.05 to 100 rad s^{-1} with γ of 0.5 %. Additionally, the steady-state shear flow properties were also determined. For each sample, a continuous shear flow with a constant shear rate ($\dot{\gamma}$) was applied until reaching a steady state.

The investigation about the kinetic of shear-induced crystallization was also performed on the rheometer according to the following procedure. The time-sweeping test with ω of 10 rad s^{-1} and γ of 0.25 % was performed to trace the evolution of the storage modulus (G') until the end of the crystallization process. The gap between the parallel plates was set at 0.5 mm initially and adjusted automatically throughout the crystallization process to ensure the normal stress change within ± 0.05 N for the accuracy of the test.

3.2.6 Gel Permeation Chromatography (GPC)

The molecular weight of un-stretched iPP and stretched iPP was determined by DAWN Heleos-II (Wyatt technology). The solvent used was 1,2,4-trichlorobenzene (stabilized with 0.1% BHT) and the flow rate was 1.0 ml min^{-1}.

3.2.7 In situ synchrotron *X*-ray scattering measurements

In situ synchrotron *X*-ray scattering measurements were performed at the MiNaXS Beamline at Deutsches Elektronen Synchrotron (DESY), in Hamburg, Germany. The wavelength of the *X*-ray was 0.106917 nm. An exposure time of 0.1 s and a time interval of 0.15 s were used to realize a high time resolution without burning the sample by *X*-ray during stretching. For SAXS measurements, the patterns were recorded by a Pilatus 1M detector (981×1043 pixels, pixel size 172×172 μm^2) and the distance between the sample and the detector was 4961 mm. For WAXS measurements, the patterns were recorded using a Pilatus 300K detector (487×619 pixels, pixel size 172×172 μm^2) and the distance between the sample and the detector was around 200 mm. Pattern preprocessing including masking and reconstruction of blind areas was performed by a self-written subroutine on PV-Wave from Visual Numerics.

3.2.7.1 Uniaxial stretching

The uniaxial stretching was performed on a custom-made miniature tensile machine designed by Leibniz Institute of Polymer Research Dresden (IPF) for online studies at the synchrotron. Waist-shape specimens were produced by CNC milling from the plates. During the measurement, both grips moved simultaneously in opposite directions to keep the *X*-ray beam at a fixed position on the sample. The temperature was controlled by a heating gun. In every test, the specimen was stretched with a cross-head speed of 0.02 mm s^{-1}. The local strain at the *X*-ray beam position during the stretching was determined optically by monitoring a grid pattern (0.35 mm × 0.35 mm) painted on the surface of the sample. The optical images were taken every 1s during stretching.
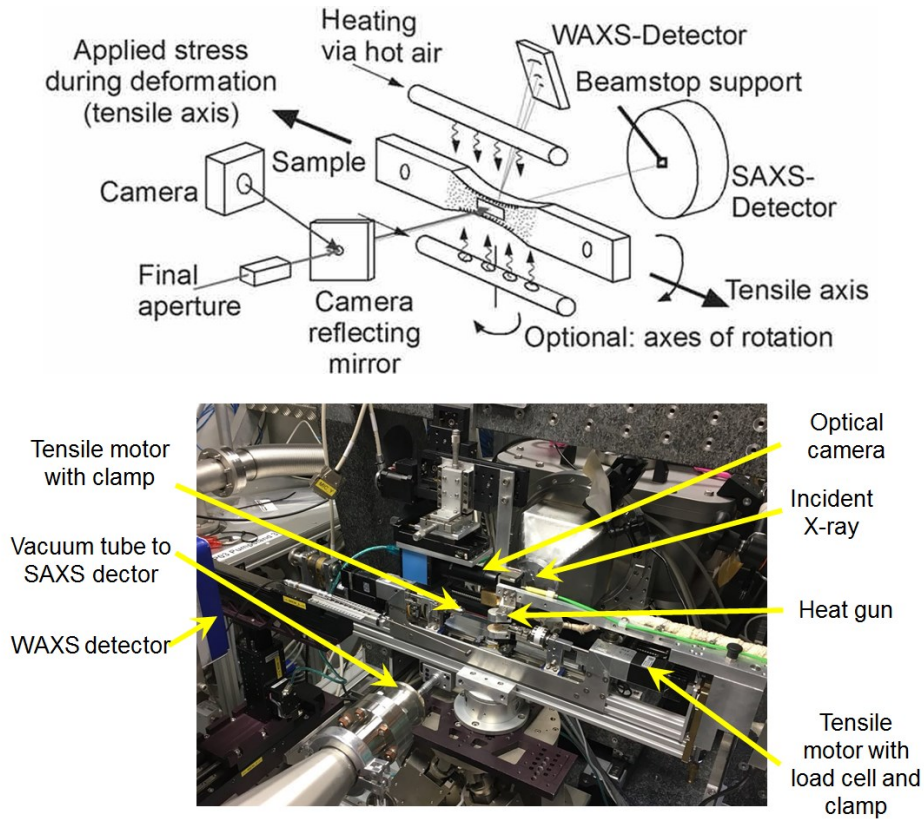
Figure 3-3 A schematic and a photograph of the experiment. The schematic can be also found in Ref.[92].

The Hencky strain ε_H is used as a basic quantity of the local strain, which is defined as

$$\varepsilon_H = ln\frac{\Delta L + L_0}{L_0} \qquad \qquad \textbf{Equation (3-2)}$$

where L_0 and ΔL are the initial length and displacement of the painted grid pattern during stretching, respectively. The stress σ is given as

$$\sigma = \frac{F}{A_0}\left(1 + \frac{\Delta L}{L_0}\right) \qquad \qquad \textbf{Equation (3-3)}$$

where F and A_0 are the instantaneous force and the initial cross section area. **Figure 3-3** presents a schematic and a photograph of the in-situ synchrotron SAXS and WAXS experiment. The schematic can be also found in Ref.[92].

Additionally, the stress-strain curve was also determined by a digital image correlation (DIC) system (ARAMIS; GOM GmbH, Germany), especially in the small strain region. To allow for sufficient optical signal detection and to avoid heating the specimen during testing, the light directed onto the specimen was provided by a cold light system Dedocool (Dedo

Weigert Film GmbH, Munich, Germany). One example of the stress-strain curve and the DIC system is provided in **Figure 3-4**.
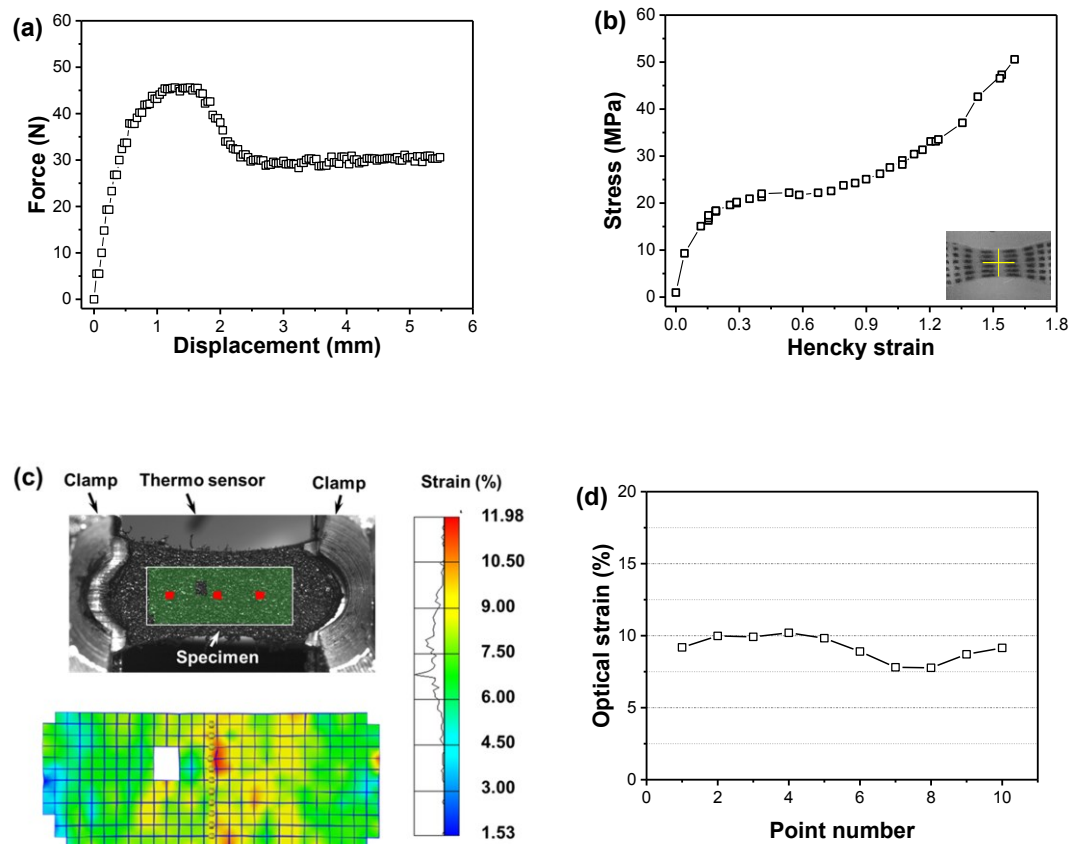

Figure 3-4 (a) Force-displacement curve and **(b)** stress-strain curve of PPna during uniaxial stretching. The stretching temperature is 75 $^{\circ}$C. The optical image was taken every 1 second to record the local strain at the beam position (indicated by the yellow cross). The beam position was corrected by a laser before the measurement. **(c)** Photograph of the specimen monitored by the digital image correlation (DIC) system. A sketch of the optical strain in the region of interest is provided. **(d)** The contour of the optical strain in the center region of the specimen.

3.2.7.2 Creep test

Creep tests were performed in force-controlled mode on the same custom-made miniature tensile machine used in **section 3.2.7.1**. The creep temperature is 120 $^{\circ}$C. During creep, both grips move simultaneously in opposite directions to keep the beam position on the sample at a fixed point. In any test, the specimen was loaded with a cross-head speed of 0.1 mm s^{-1} up to the chosen stress, which was then preserved constantly during the test. An exposure time of 0.5 s and a time interval of 7.5 s were chosen.

3.2.7.3   Stress relaxation test

Stress relaxation tests were performed at 60 $^{\circ}$C and 90 $^{\circ}$C. The specimens were pre-stretched to induce highly oriented microstructure inside. During the stress relaxation, the strain was kept unchanged. The stress-time curve was recorded and the WAXS/SAXS measurements were performed with an exposure time of 0.15 s during the relaxation process.

3.2.8   X-ray scattering pattern processing and calculation

Figure 3-5 presents a raw 2-dimensional (2D) WAXS pattern. Due to the existence of non-physical pixel values (e.g. caused by the beamstop and beamstop holder, blind areas of the diode array, the cosmic scattering), the pattern needs to be masked. The masked pattern can be reconstructed based on the fiber symmetry. Afterwards, the reconstructed pattern should be background corrected to remove the scattering from the air.
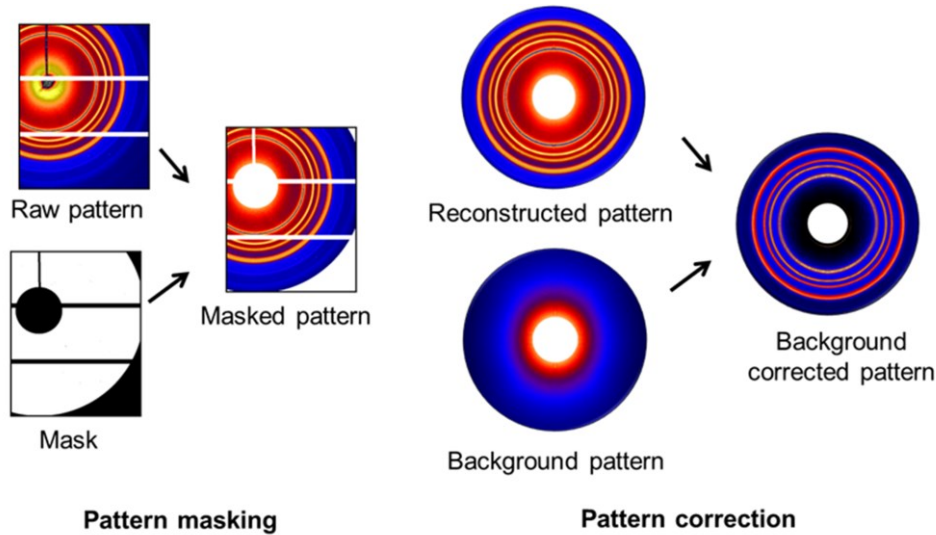

Figure 3-5 A schematic drawing of the pattern masking, reconstruction, and background correction process.

The background correction is performed in the following way. Firstly, the sample transmission coefficient (τ_s) is given as

$$\tau_s = \frac{I_{s,out}}{I_{s,in}} \frac{I_{bg,in}}{I_{bg,out}} \qquad \textbf{Equation 3-4}$$

I is the intensity, the subscript "s" means the sample and "bg" means the background, the subscript "in" means the incident X-ray beam and "out" means the scattered X-ray beam. Then the background corrected intensity I_c is

$$I_c = I_{s,out} - \tau_s \times I_{bg,out} \qquad\qquad \textbf{Equation 3-5}$$

If we take the thickness of the sample in consideration, the normalized intensity I_n is

$$I_n = I_c \frac{-1}{\tau_s \ln(\tau_s)} \qquad\qquad \textbf{Equation 3-6}$$

The raw 2D-SAXS patterns were masked, reconstructed, and background corrected in the similar way.

3.2.8.1 Evaluation of the WAXS pattern

By circular integration of the 2D-WAXS pattern, the 2D-WAXS pattern can be transferred to 1-dimensional (1D) WAXS curve. On the 1D-WAXS curve, the scattering intensity is plotted as a function of the scattering vector.
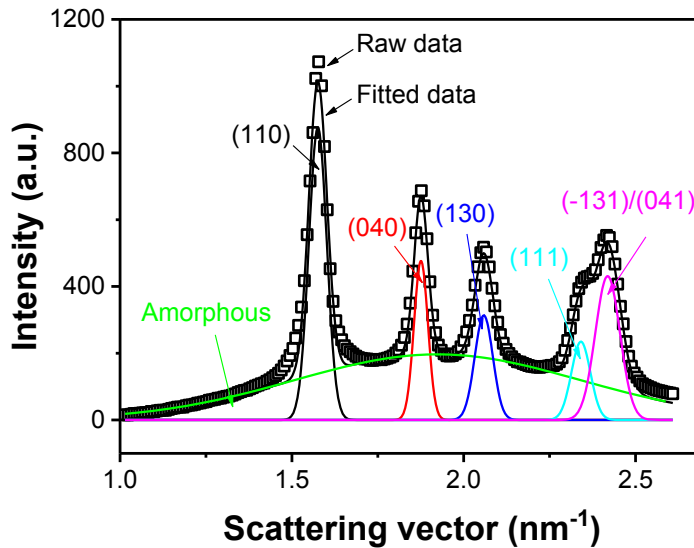
Figure 3-6 A standard peak fitting procedure to get the area of crystalline peak and amorphous peak.

The crystallinity (X_c) can be obtained by

$$X_c = \frac{\sum A_{crystalline}}{\sum A_{crystalline} + \sum A_{amorphous}} \times 100\% \qquad\qquad \textbf{Equation (3-7)}$$

where $A_{crystalline}$ and $A_{amorphous}$ are the areas of the crystalline and the amorphous part in the azimuthally integrated 1D-WAXS intensity profile.

The relative content of β-iPP (K_β) can be calculated using the methodology developed by Obadal,[93] when the system consists of α-, β-, and γ-iPP:

$$K_\beta = \frac{A_{\beta(300)}}{A_{\alpha(110)} + A_{\alpha(040)} + A_{\alpha(130)} + A_{\beta(300)} + A_{\gamma(117)}} \qquad \textbf{Equation (3-8)}$$

where $A_\beta(300)$ is the area of the $(300)_\beta$ peak on the 1D-WAXS curve; $A_\gamma(117)$ is the area of the (117) peak; and $A_\alpha(110)$, $A_\alpha(040)$, and $A_\alpha(130)$ are the areas of the $(110)_\alpha$, $(040)_\alpha$, and $(130)_\alpha$ peaks. In case that no γ-iPP exists in the sample, $A_{\gamma(117)}$ equals 0.

The orientation of the crystal with respect to the reference direction (normally the deformation direction) can be estimated according to Herman's orientation method,[83]

$$f_H = \frac{3\langle cos^2\varphi \rangle - 1}{2} \qquad \textbf{Equation (3-9)}$$

here f_H is Herman's orientation factor. The value of f_H varies between -0.5 and 1 for perpendicular and parallel crystal orientation with respect to the reference direction.

$$\langle cos^2\varphi \rangle = \frac{\int_0^{\pi/2} I(\varphi,\psi) cos^2(\psi,\varphi) sin(\psi,\varphi) d\psi}{\int_0^{\pi/2} I(\varphi,\psi) sin(\psi,\varphi) d\psi} \qquad \textbf{Equation (3-10)}$$

φ is the angle between the crystal and stretching direction, ψ is the azimuthal angle, $I(\varphi,\psi)$ is the azimuthal intensity distribution at a constant value of θ. For α-iPP which belongs to the monoclinic system, then

$$\langle cos^2\varphi_a \rangle + \langle cos^2\varphi_b \rangle + \langle cos^2\varphi_c \rangle = 1 \qquad \textbf{Equation (3-11)}$$

$$\langle cos^2\varphi_b \rangle = \langle cos^2\varphi_{040} \rangle \qquad \textbf{Equation (3-12)}$$

$$\langle cos^2\varphi_c \rangle = 1 - 0.90054\langle cos^2\varphi_{040} \rangle - 1.09945\langle cos^2\varphi_{110} \rangle \qquad \textbf{Equation (3-13)}$$

according to Wilchinsky.[94] Combining **Equation (3-9)** and **Equation (3-13)**, the orientation of c-axis (namely the direction of polymer chains) in the crystal can be estimated.

3.2.8.2   Evaluation of the SAXS pattern

By circular integration (the homogenous pattern) or cutting a slice of the 2D-SAXS pattern, the 1D-SAXS curve can be obtained. The long period (L_p) can be estimated by

$$L_p = \frac{2\pi}{q_{max}} \qquad \textbf{Equation (3-14)}$$

q_{max} is the peak position on the 1D-SAXS curve (see **Figure 3-7a**).

The domain thickness, including the thickness of crystalline phase (L_c), the intermediate phase (L_{im}), and amorphous phase (L_a) could be readily described by a 1D correlation function ($K(z)$) without resorting to any models.[83, 95-101] The prerequisite for $K(z)$ is that the density of each phase is different. In iPP, the density of the intermediate phase has been proved to be 10-

15% lower than that of the crystalline phase, but higher than that of the amorphous phase.[102] Therefore, $K(z)$ can be employed and it is given as:

$$K(z) = \frac{\int_0^\infty q^2 I(q)\cos(qz)dq}{\int_0^\infty q^2 I(q)dq}$$ **Equation (3-15)**

where z represents the length in real space with a unit of nm. **Figure 3-7b** gives a representative $K(z)$ curve of iPP. L_{im} and L_a can be determined by the upper and lower limits of the straight line section. Then, L_c can be acquired by subtracting $2L_{im}$ and L_a from L_p.
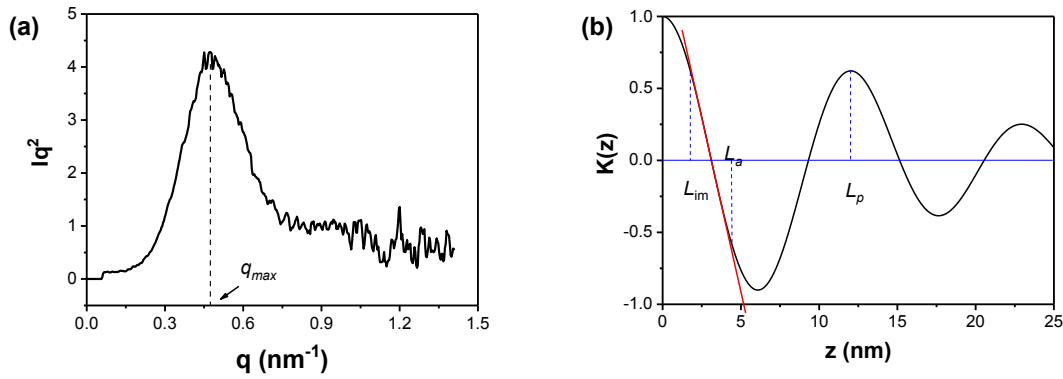
Figure 3-7 A representative 1D correlation function $K(z)$ of iPP as a function of z.

During deformation, the voids can be induced in the sample. The existence of the voids gives rise to a streak on the 2D-SAXS pattern. Based on the Ruland streak method introduced in **Section 1.3.4**, the size of the voids could be estimated. Due to beam stop, the scattering in the center region of the pattern is covered. To calculate the size of the voids, the scattering in the blanked region in **Figure 3-8** is extrapolated and fitted by a sum of two 2D-Gaussian functions

$$I(s) = p_{v0}\exp(-p_{v1}s^2 - p_{v2}\cos(2\phi)\,s^2)$$
$$+p_{m0}\exp(-p_{m1}s^2 - p_{m2}\cos(2\phi)\,s^2)$$ **Equation (3-16)**

$$\phi = arctan\frac{i}{j}$$ **Equation (3-17)**

i and j define the pixel position in 2D-SAXS patterns with respect to the beam center. The first Gaussian curve describes the void with three parameters. p_{v0} is the scattering intensity at the beam position, and $p_{v1} + p_{v2}$ and $p_{v1} - p_{v2}$ are the axes of the elliptical structure respectively. The second Gaussian curve describes the scattering of the matrix with slight anisotropy in a similar way. The extrapolation and fitting process are realized by a self-written subroutine on PV wave.[103] The fitting procedure is illustrated in **Figure 3-8**.
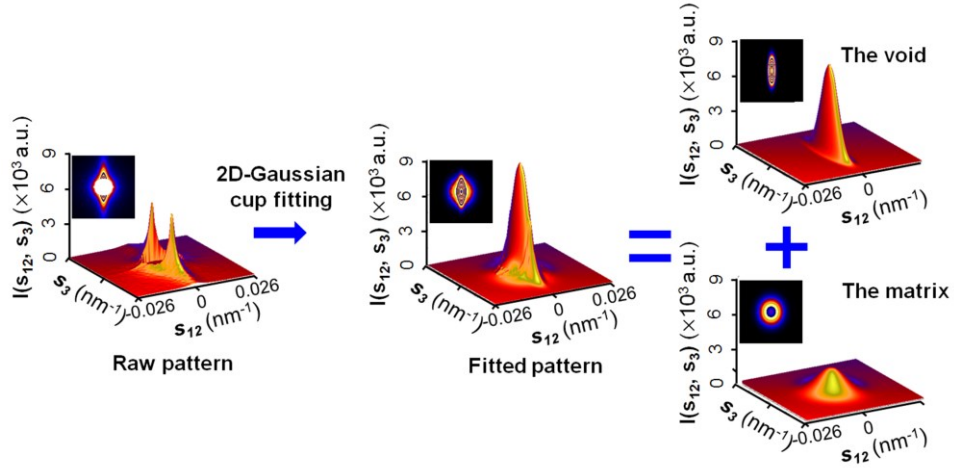
Figure 3-8 Center fitting and modeling of a scattering pattern by the sum of the voids signal and the matrix signal according to Guinier's approximation. s_{12} is the loading direction.

Assuming that the shape of the voids is cylindrical,[104] combining **Equation (3-16)**, **Equation (2-14)** and **Equation (2-15)**, the void size along the stretching direction ($S^{\parallel}$) and the void size perpendicular to the stretching direction ($S^{\perp}$) should be

$$S^{\parallel} = \sqrt{\frac{p_{v1}+p_{v2}}{\pi}}$$
Equation (3-18)

$$S^{\perp} = \sqrt{\frac{p_{v1}-p_{v2}}{\pi}}$$
Equation (3-19)

The integrated scattering intensity, as a measure of the scattering invariant (Q) of the system, is related to the volume fraction of the dispersed phase (namely the void in this work) and the electron density contrast between the heterogeneities and the surrounding matrix. In this work, the void can be regarded as the dispersed phase. Q is given as

$$Q = \frac{1}{2}\int_{-\infty}^{\infty}\int_{0}^{\infty} I(s_{12},s_3)s_3 ds_{12}ds_3 = 2\pi^2 V_m V_v (\rho_m - \rho_v)^2$$
Equation (3-20)

where V_m and V_v are the volume ratio of the matrix and the void, ρ_m and ρ_v are the electron density of the matrix and the void. Since $\rho_v = 0$, **Equation (3-21)** is rewritten into

$$Q = 2\pi^2(1 - V_v)V_v\rho_m^2$$
Equation (3-21)

4 Microstructure characterization in a single iPP spherulite by synchrotron microfocus wide angle *X*-ray scattering[1]

Position-resolved microstructures in a single spherulite of iPP are quantitatively studied by synchrotron microfocus WAXS. The precise location of the X-ray beam on the sample is realized with the help of a carbon fiber (CF). The results in this chapter show that the normal of mother lamellae in a spherulite is aligned mainly perpendicular to the radius, and the subsidiary daughter lamellae are inclined 80.75^{o} with respect to that of the dominant mother lamellae. The crystallinity in the spherulite is in the range of 46 % to 56 %, which is rarely influenced by the crystallization temperature. The ratio between the daughter lamellae and the mother lamellae is 0.18 when iPP crystallizes at 138 ^{o}C and it decreases to 0.11 as the crystallization temperature is decreased to 130 ^{o}C. The *b*-axis and *c*-axis in the mother lamellae tend to orient perpendicular to the radius direction, and the *a*-axis prefers to align in the radius direction.

---

[1] The main part in this chapter has been published as "B. Chang, K. Schneider, N. Patil, S. Roth, G. Heinrich. Microstructure characterization in a single isotactic polypropylene spherulite by synchrotron microfocus wide angle X-ray scattering, Polymer 142 (2018) 387-393."

4.1   Introduction

Polymer crystallization is a key process associated with the arrangement of molecular chains. Typically, semicrystalline polymers crystallize into spherulites during cooling from viscous melts or solutions under static conditions. The growth mechanism of spherulite has been investigated extensively over the past few years.[105-108] Binsbergen and Lange [109] assumed that spherulite growth occurs through a sequential development of dominant and subsidiary lamellae. During the early stages of crystallization, bundles of dominant lamellae are formed. Gradually, spherulites grow in their radial direction generating space for the formation of subsidiary lamellae in the later stages. The formation and growth of subsidiary lamellae are attributed to the noncrystallographic branching,[110] secondary nucleation on existing fibrils,[111] and growth around a giant screw dislocation.[112, 113]

In iPP, the subsidiary lamellae are induced by the loose folds and/or cilia having orientation order on the basal surface of dominant lamellae. The formation of the subsidiary lamellae leads to the unique "cross-hatched" structure.[28, 91, 109] In the work by White and Bassett, [114] the cross-hatching frequency in iPP spherulites was studied quantitatively with the help of electron microscope. The results revealed that the cross-hatches per μm decreases from 57 to 40 as the crystallization increases from 115 to 140 ^{o}C, regardless of the nucleation type. The ratio between the subsidiary and dominant lamellae influences the thermal stability, the optical properties, and also the mechanical properties of iPP.[107, 115] Therefore, understanding of the ratio between the subsidiary and dominant lamellae will be of great importance. However, quantitative information relevant to lamellae branching in a single iPP spherulite is rare reported, let alone the position-resolved lamellae branching as a function of the radius of the spherulite. The main obstacle lies in the precise location of the detecting probe in the single spherulite. For instance, a conventional *X*-ray beam size for scattering experiments is around several hundred micrometers, which is nearly the same as the size of a spherulite. The size of the traditional *X*-ray beam is too large to obtain the micrometer-scale inhomogeneity in a single spherulite.

Synchrotron microfocus *X*-ray scattering is a powerful tool to obtain the structural information on local spatial inhomogeneity of nanostructure in a micrometer scale with sufficient spatial resolution.[85, 116-118] Recently, synchrotron microfocus *X*-ray scattering has been fruitfully utilized to study the secondary crystallization kinetic [117] and the crystal fractions in iPP spherulites.[119] In this chapter, synchrotron microfocus *X*-ray scattering is used for the investigation of lamellae branching in a single spherulite. The spherulite was

prepared on a hot stage equipped with an optical microscope. In particular, the precise position of the synchrotron X-ray beam on the spherulite is realized using carbon fibers (CF).

4.2 The nucleation efficiency of the carbon fiber on iPP

Figure 4-1 shows the nucleation effect of the pulled and un-pulled CF on iPP. For comparison, two CFs were embedded in the iPP matrix. The horizontal CF was pulled, whereas the vertical CF was not pulled. It can be found that after pulling, a layer of nuclei was formed on the surface of the pulled CF. After crystallization for 5 min, β-iPP can be found around the horizontal CF. However, on the surface of the un-pulled CF, only a few nucleation points can be found, suggesting the weak nucleation effect of CF on iPP. After crystallization for 5 min, it is obvious that α-iPP is induced on the surface of un-pulled CF, proving the α-nucleation effect of CF on iPP. Since that under static condition, the CFs used in this study has an only α-nucleation effect on iPP, the formation of β-iPP transcrystals is attributed to shear-induced crystallization.[120-122] As discovered by Varga,[122] during fiber pulling row-nuclei were formed on the surface of the CF due to the melt-shearing. These row-nuclei belong to α-iPP. Therefore, they were named as α-row-nuclei. In the following crystallization process, α-row nuclei allow the formation of β-iPP transcrystals in the temperature range of 100 °C~140 °C.
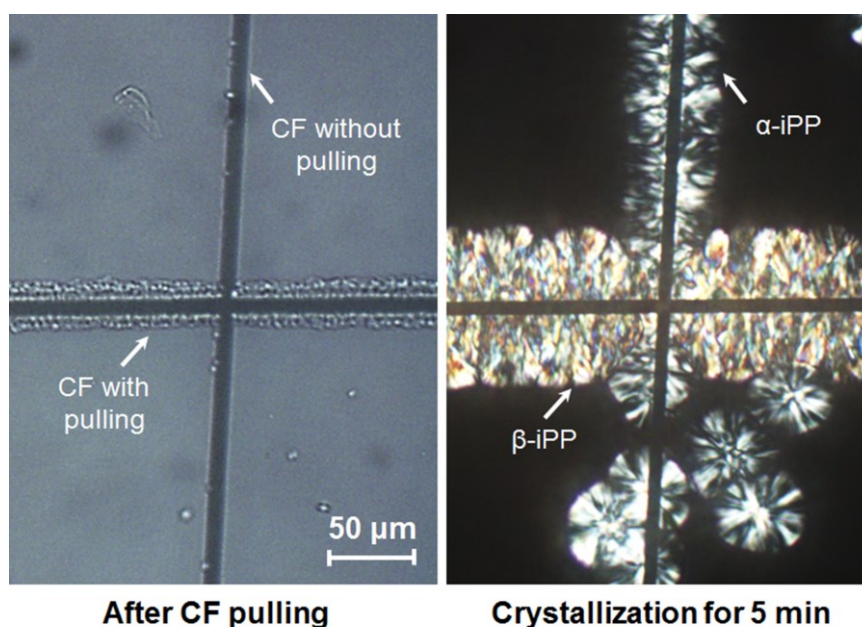
Figure 4-1 The optical microscopy images of the crystallization process of iPP around the CFs. The horizontal CF was pulled, but the vertical CF was not pulled for comparison.

4.3   Morphology of iPP spherulites and transcrystalline region

The morphology of the film with single layer of spherulites and transcrystalline region is shown in **Figure 4-2**. Dark lines along the vertical and horizontal directions in **Figure 4-2a** display the CFs. Transcrystalline regions in the immediate vicinity of CFs comprises mainly β-iPP crystals**.** The edge-on and flat-on lamellae morphology of β-iPP crystals in the transcrystalline region, and the spherulite structure with the dominant "mother" lamellae and subsidiary "daughter" lamellae, are presented in **Figure 4-2b** and **Figure 4-2c**. Since the direction of the CF is horizontal in **Figure 4-2b**, it can be concluded that in the β-iPP crystal lamellae grow perpendicular to the CF and twist during the growth process.
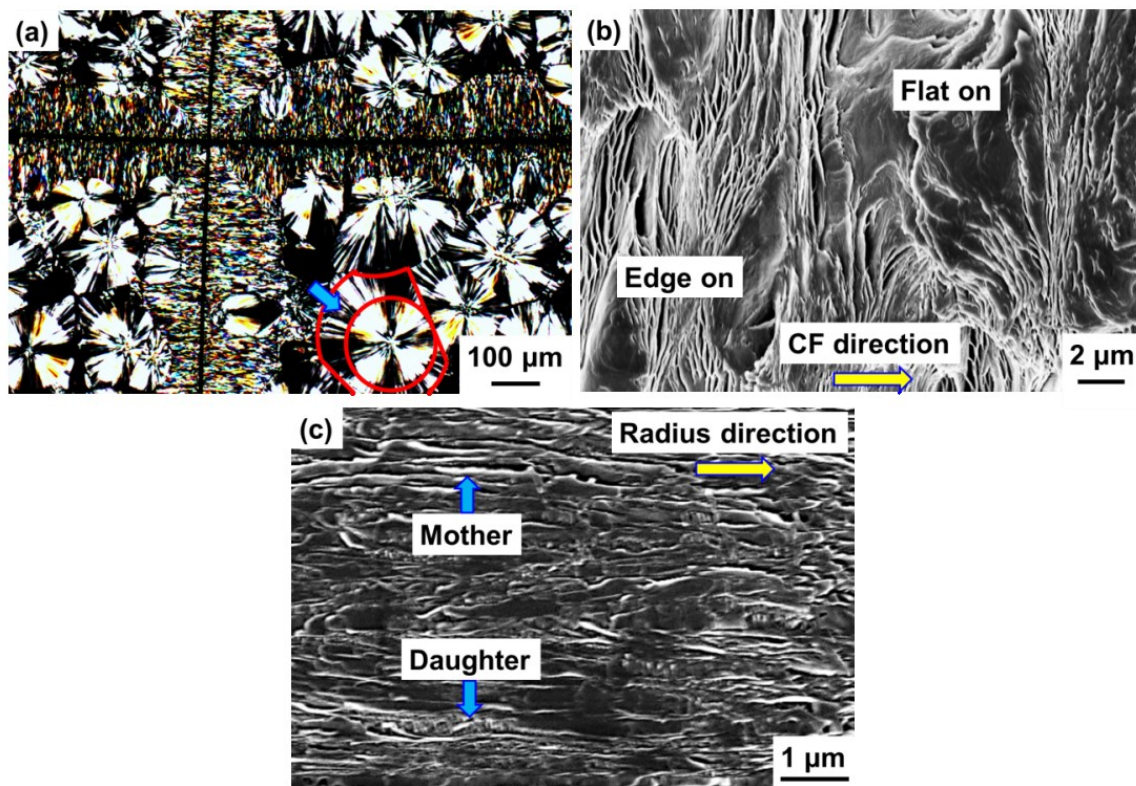
Figure 4-2 (a) Polarized optical micrograph collected at the end of crystallization. Prior to that, iPP was crystallized at 138 °C for 20 min and then at 130 °C for 30 min. The dark lines along the vertical and horizontal directions are carbon fibers (CFs). The thickness of the sample is 39 μm; **(b)** The SEM image of the edge-on and flat-on lamellae in the transcrystalline region; and **(c)** The SEM image of the spherulite depicting the mother and the daughter lamellae.

The region adjacent to the transcrystalline region shows the developed α-iPP spherulites with a dark Maltese cross. The Maltese cross will not be changed by rotating the spherulite in the viewing direction.[28] The mother lamellae are found to grow mainly along the radius

direction and the daughter lamellae grow inclined to the radius direction. (cf. **Figure 4-2c**) The averaged angle of 80.75° between "mother" and "daughter" lamellae according to epitaxial growth is in agreement with the studies by Khoury.[123] The birefringence appearance of the spherulite and the surrounding ring is closely related to the "cross-hatched" structure.[8, 28, 115, 123] In an earlier work by Norton and Keller, α-iPP was classified into three distinct types based on the feature of birefringence.[115] Spherulites grown below 134 °C have a slight positive birefringence (type I), spherulites grown above 138 °C have a negative birefringence (Type II), and spherulites grown between 134 °C and 138 °C often display a mixed birefringence ("mixed" type). The presence or absence of the daughter lamellae directly specifies the differences existing between the three types of the spherulites.[115] Therefore, the less bright ring (indicated by the arrow in **Figure 4-2a**) surrounding the spherulite indicates entering the zone in which the spherulite continued to grow at a crystallization temperature decreased from 138 °C to 130 °C, which inhibits the formation of daughter lamellae.

4.4   Defining of the position of the carbon fiber

The horizontal and the vertical scans are performed to precisely locate the *X*-ray beam with respect to spherulites. The 1D-WAXS intensity profiles for the horizontal and the vertical scan are presented in **Figure 4-3a** and **Figure 4-3b.** Several peaks at different scattering vectors *s*, corresponding to the (110), (300), (040), (130), (111)/(-131) lattice planes, are noticed. Detailed assignments of the peak to the iPP crystal form are summarized in **Table 4-1**. Among the peaks, (300) lattice plane is the characteristic lattice plane of β-iPP. In both horizontal and vertical scans, the intensity of the peaks and the presence/absence of β-iPP vary with the change of the position. Accordingly, the position of the CF is determined by the following rules: 1) the diameter of the CF used in this study is 19 μm and the sample thickness is 39 μm. Hence, if the X-ray beam is on the CF, the intensity of the peak should decrease drastically; 2) β-iPP transcrystallization is induced by the *α*-row nuclei formed during CF pulling.[120, 121] Therefore, the presence of both α-iPP and β-iPP crystals are anticipated when the X-ray beam is on the CF. Considering the two rules listed above, the intersection of the CFs in **Figure 4-2a** can be identified as $x = 59.908mm, y = -3.1458mm$.
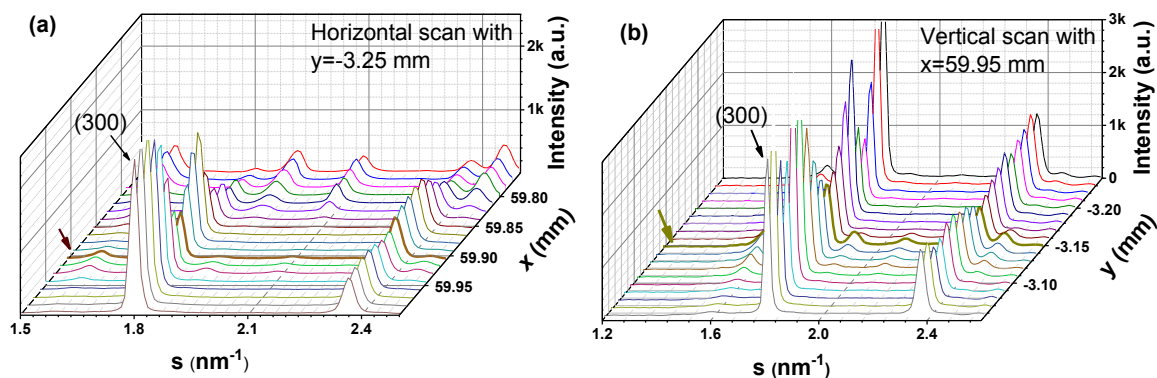
Figure 4-3 1D-WAXS intensity profiles as a function of scattering vector (*s*) for **(a)** the horizontal and **(b)** the vertical scan, obtained by azimuthal integration of 2D-WAXS patterns. Horizontal scan ($y = -3.25\ mm$) is performed with a step of 12.5 μm and vertical scan ($x = 59.95\ mm$) was performed with a step of 10 μm.

Table 4-1 A summary of peak position and its corresponding lattice plane.

	Scattering vector (nm^{-1})						
	1.60	1.81	1.92	2.10	2.37	2.37	2.46
Lattice plane	(110)	(300)	(040)	(130)	(311)	(-131)	(041)
Crystal form	α	β	α	α	β	α	α

4.5 Microstructure studies of the spherulite

Once the position of the CF is defined, the microstructure in spherulites can be studied in detail. The optical micrograph of α-iPP spherulite with a Cartesian coordinate system and some representative 2D-WAXS patterns is provided in **Figure 4-4a**. Vertical scans are performed on the spherulite with a step width of 10 μm. On the 2D-WAXS patterns, a few arcs can be found from the inner to the outer region. The azimuthal angle of the arc varies as the scanning position is changed. In addition, the (110) lattice plane is split into four arcs on the 2D-WAXS patterns, implying the existence of "mother" and "daughter" lamellae.[123]
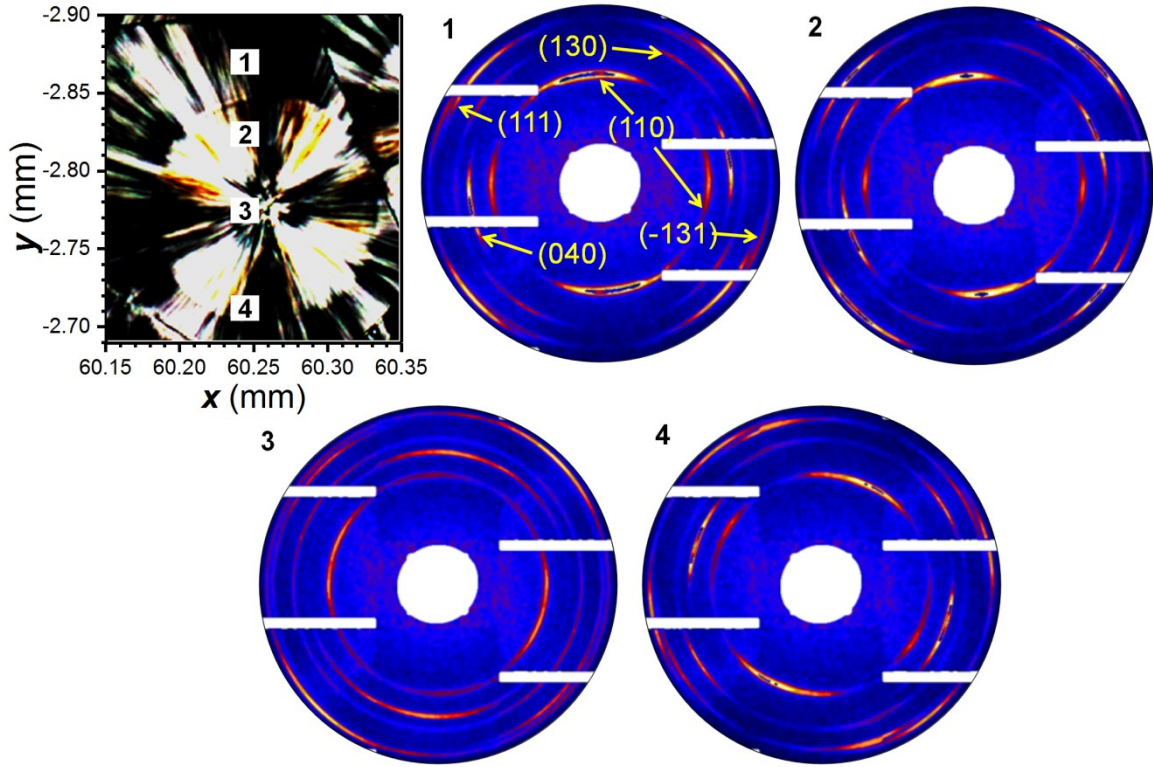
Figure 4-4 The optical micrograph of α-iPP spherulite with a Cartesian coordinate system and some representative 2D-WAXS patterns acquired at different positions as indicated in the micrograph. The WAXS patterns are completed using rotational symmetry by 180°, the white regions stem from blind regions of the PILATUS-detector.

4.5.1 Crystallinity in the spherulite

To investigate the microstructure as a function of radius quantitatively, the Cartesian coordinate system is transferred to the Angular coordinate system in the following way

$$r^2 = \sqrt{(x - O_x)^2 + (y - O_y)^2}$$
Equation (4-1)

(O_x, O_y) is the center of the spherulite, which is (60.263 mm, -2.769 mm), x and y refer to the positon of the beam on the spherulite. **Figure 4-5** shows that X_c in the spherulite is in the range of 46 % to 56 %. It is higher than the value reported by Cong et al,[124] which is about 18 % in the spherulite center, and decreased gradually towards the edge of the spherulite and finally reached 10 %. The substantially larger difference is probably caused by the different crystallization conditions. In the work by Cong et al, the crystallization temperature was 145 ^{o}C, and the 2D-WAXS measurements were performed during the crystallization process where the sample was not fully crystallized. As demonstrated by Riekel et al.,[125] the crystallization process of the spherulite consists of primary and secondary crystallization. At

the end of the secondary crystallization, X_c could reach a value of 61 % which coincides well with the result in this study.
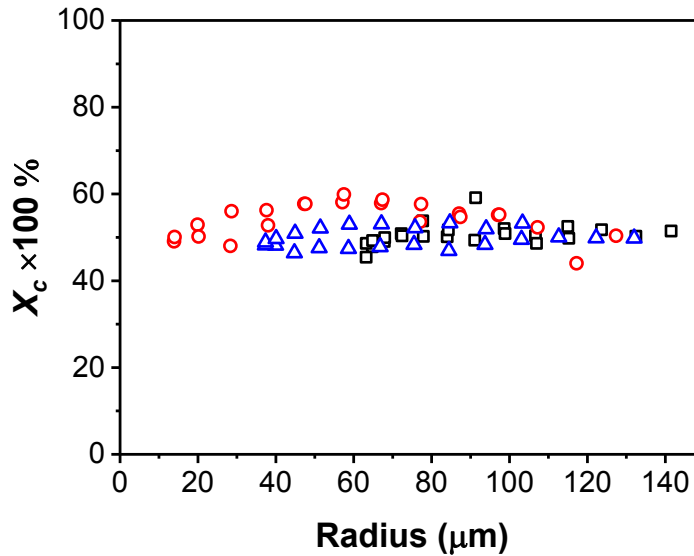
Figure 4-5 X_c in the spherulite as a function of the radius of three vertical scans $x = 60.20$ mm (square), $x = 60.25$ mm (circle), and $x = 60.30$ mm (triangle).

4.5.2 The ratio between "daughter" lamellae and "mother" lamellae in the spherulite

The azimuthal intensity distribution of (110) lattice plane is plotted in **Figure 4-6a-c**. One can see that on the azimuthal intensity distribution curve the peak area varies as the scan position is changed, indicating the change of the lamellae branching. The ratio of peak areas between "daughter" lamellae and "mother" lamellae ($R_{D/M}$) could be obtained by [126]

$$R_{D/M} = \frac{A_d}{A_m} \qquad \textbf{Equation (4-2)}$$

A_d and A_m are the peak area of "daughter lamellae" and "mother lamellae" on the azimuthal intensity distribution curve. The results are presented in **Figure 4-6d**. It can be found that as the radius is smaller than 90 μm, $R_{D/M}$ keeps at around 0.18. A decrease of $R_{D/M}$ shows up as the radius exceeds 90 μm, where the crystallization temperature was decreased from 138 °C to 130 °C. At 140 μm $R_{D/M}$ is 0.11. The change of $R_{D/M}$ with the radius coincides well with the results in **Section 4.3**: decreasing the crystallization temperature will inhibit the formation of subsidiary daughter lamellae.
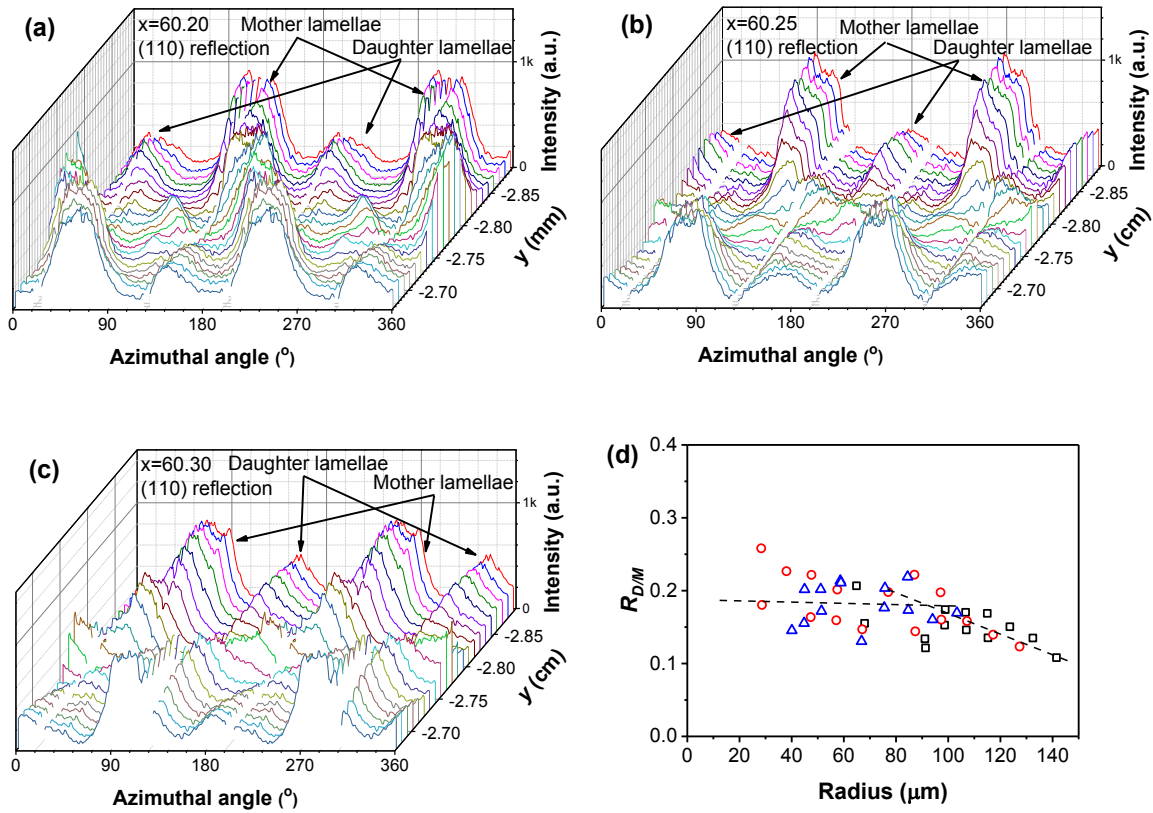
Figure 4-6 Azimuthal intensity distribution of (110) reflection at the scan of x=60.20 mm, 60.25 mm, and 60.30 mm; (d) The ratio between the "daughter" lamellae and the "mother" lamellae ($R_{D/M}$) as a function of the radius of three vertical scans x = 60.20 mm (square), x = 60.25 mm (circle), and x = 60.30 mm (triangle).

4.5.3 The orientation of the crystal axis in the spherulite

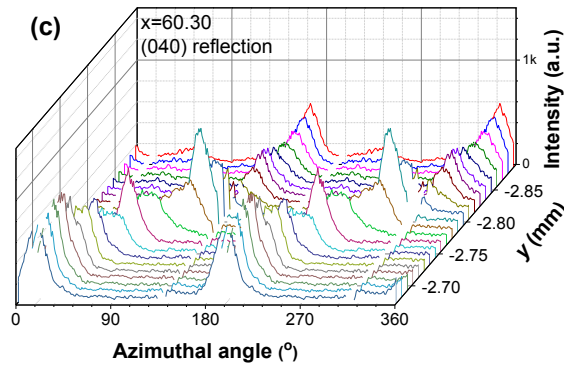The azimuthal intensity distribution of the (040) lattice plane is given in **Figure 4-7**.
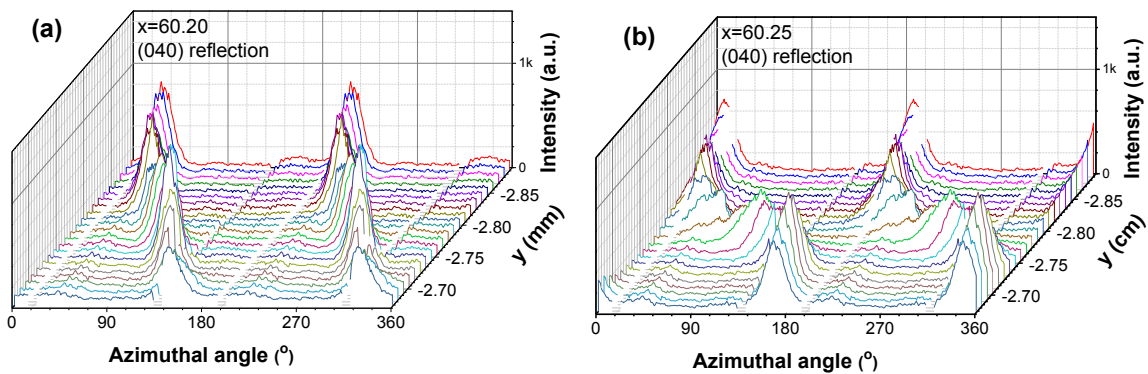
Figure 4-7 The azimuthal intensity distribution of (040) reflection at different positions of the spherulite of three vertical scans $x = 60.20$ mm (square), $x = 60.25$ mm (circle), and $x = 60.30$ mm (triangle).

Different to the results given in **Figure 4-6a-c**, only two peaks could be found on the curves in **Figure 4-7**. This is because the "mother" and "daughter" lamellae share the same a-c layers as proposed by Lotz.[8] In **Figure 4-6** and **Figure 4-7**, one can also notice that the peak position shifts as the scanning position is changed, which is a result of the changed crystal orientation. The Herman's orientation factor of a-axis(f_{Ha}), b-axis(f_{Hb}), and c-axis(f_{Hc}) in the spherulite are shown in **Figure 4-8**. It can be found that with the increase of the radius, f_{Ha} increases gradually from 0.25 to 0.62. As the radius is larger than 90 μm, f_{Ha} remains constant at the value ~ 0.62, which means that the a-axis in the crystal prefers to orient along the radius direction. As the radius is smaller than 90 μm, f_{Hb} decreases slightly from -0.27 to -0.35 with increasing radius. When the radius exceeds 90 μm, it keeps at -0.35, suggesting that the b-axis is perpendicular to the radius direction. In addition, f_{Hc} decreases from 0 to -0.3 with the increase of the radius. And as the radius is larger than 90 μm f_{Hc} is around -0.3, indicating c-axis tends to be perpendicular to the radius direction. We note that as the radius is smaller than 90 μm, the gradual increase of f_{Ha} or decrease of f_{Hc} does not imply that the orientation of the polymer chains in the crystal is enhanced. The reason responsible for that finding is given as follows: the size of the beam used in this study is 23 μm×13 μm, which is much larger than the thickness of the lamellae (ranging within a few dozen nanometers, see **Figure 4-2c**). All crystals in the region where the X-ray passes contribute to the azimuthal intensity distribution curve. In the region close to the center of the spherulite, the angle deviation of the lamellae is quite large, which results in a lower polymer chains orientation degree. In the region far away from the center of the spherulite, the angle deviation of the lamellae decreases significantly, so a relative higher polymer chains orientation degree could be detected. Although Herman's

orientation factor is greatly influenced by the size of the X-ray beam, the plateau value at a radius larger than 90 μm suggests that the influence of the beam size is negligible therein. So, the results in **Figure 4-8** suggest that **b**-axis and **c**-axis in the crystal are aligned mainly perpendicular to the radius, and **a**-axis is along the radius.
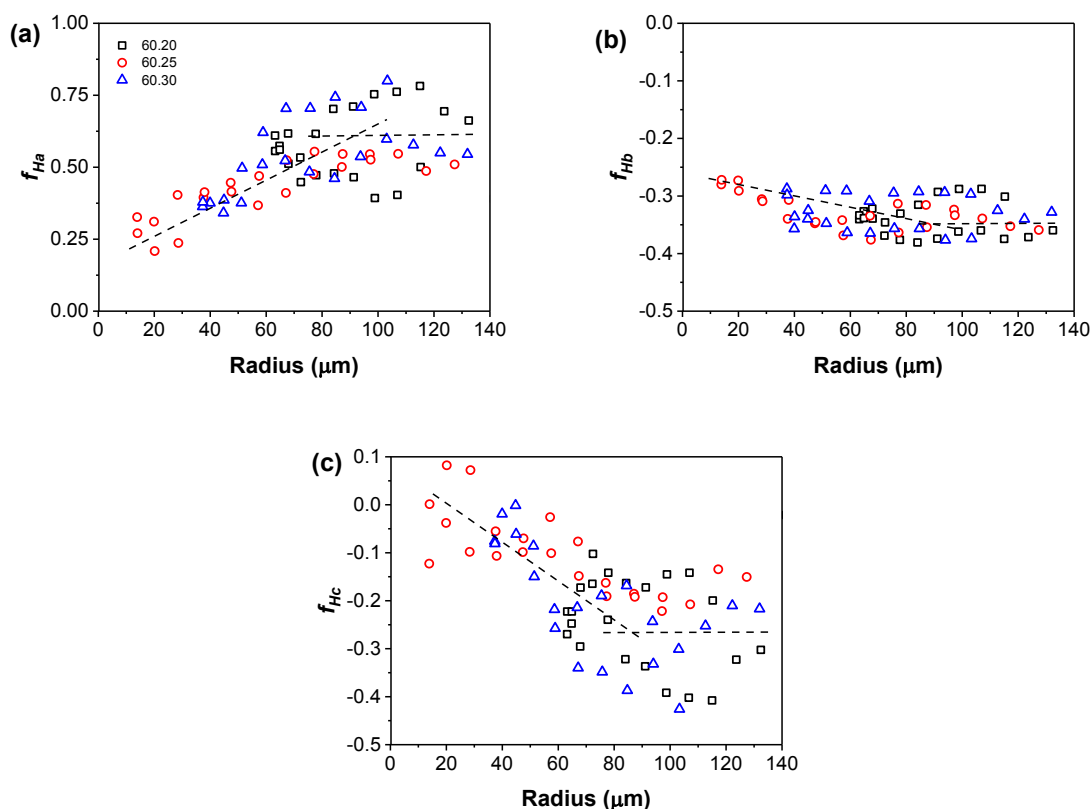

Figure 4-8 The Herman's orientation factor of **a**-axis(f_{Ha}), **b**-axis(f_{Hb}), and **c**-axis(f_{Hc}) in the crystal of "mother" lamellae as a function of the radius of three vertical scans x = 60.20 mm (square), x = 60.25 mm (circle), and x = 60.30 mm (triangle).

4.6 Conclusion

With the help of carbon fibers, the precise location of the X-ray beam in the spherulite is realized in this chapter. The results show that the mother lamellae in the spherulite are aligned mainly along the radius, and the daughter lamellae are inclined 80.75° with respect to the radius. The lamellae and polymer chains arrangement in a single spherulite are quantitatively investigated by synchrotron microfocus wide angle X-ray scattering. The crystallinity in the spherulite is in the range of 46 % to 56 %, which is rarely influenced by the crystallization. The ratio between the subsidiary daughter lamellae and the dominant mother lamellae is 0.18 when iPP crystallizes at 138 $^{\circ}$C and it decreases to 0.11 as the crystallization temperature is

decreased to 130 $^{\circ}$C. The **b**-axis and **c**-axis in the crystal are oriented perpendicular to the radius direction, and the **a**-axis is aligned in the radius direction. In addition, the results in this study prove the possibility of detecting the microstructure in a single isotactic polypropylene spherilute by synchrotron microfocus *X*-ray scattering. This methodology can be used also on other semicrystalline polymers, including polyethylene, polylactide, polyamide, et al.

5 Influence of annealing on the mechanical α_c-relaxation of iPP: a study from the intermediate phase perspective[2]

The mechanical α_c-relaxation of iPP samples crystallized with different thermal histories is investigated in this chapter. In the sample without annealing, polymer chains in the intermediate phase are constrained by crystallites with a broad size distribution, leading to one α_c-relaxation peak with an activation energy (E_a) of 53.39 kJ/mol. With an annealing temperature between 60 ^{o}C-105 ^{o}C imperfect lamellae melting releases a part of the constraining force. Consequently, two α_c-relaxation peaks could be observed (α_{c1}- and α_{c2}-relaxation in the order of increasing temperature). Both relaxation peaks shift to higher temperatures as annealing temperature increases. E_a of α_{c1}-relaxation decreases from 38.43 kJ/mol to 35.55 kJ/mol as the intermediate phase thickness increases from 2.1 nm to 2.15 nm. With an annealing temperature higher than 105 ^{o}C, a new crystalline phase is formed, which enhances the constraining force on the polymer chains. So the α_{c1}-relaxation peak is broadened and its position shifts to a higher temperature. Moreover, the polymer chains between the initial and the newly formed crystalline phase are strongly confined. Therefore, the α_{c2}-relaxation is undetectable. E_a of α_{c1}-relaxation decreases from 23.58 kJ/mol to 13.68 kJ/mol as the intermediate phase thickness increases from 2.26 nm to 2.99 nm.

5.1 Introduction

The relationship between mechanical properties and microstructure of iPP has been a hot topic since it was polymerized by G. Natta in 1954.[4] In the past few years, the mechanical relaxation behavior of iPP has been investigated by plentiful studies. Generally, iPP has four relaxation peaks in the plot of loss angle (tanδ) as a function of temperature. The peaks are designated as δ, γ, β, and α_c-relaxation, in the order of increasing temperature.[127-137] The δ-relaxation, located mainly below 100 K, is related to the hindered rotation of CH_3 groups.[138] The γ-relaxation appeared between 150 K and 230 K, is attributed to local motions of chain ends or branches in the amorphous phase.[134] The β-relaxation (the glass-rubber transition) between 250 K and 300 K is attributed to cooperative motions of chain segments in the amorphous phase.[133, 139-142] Finally, the α_c-relaxation is localized below the melting temperature.
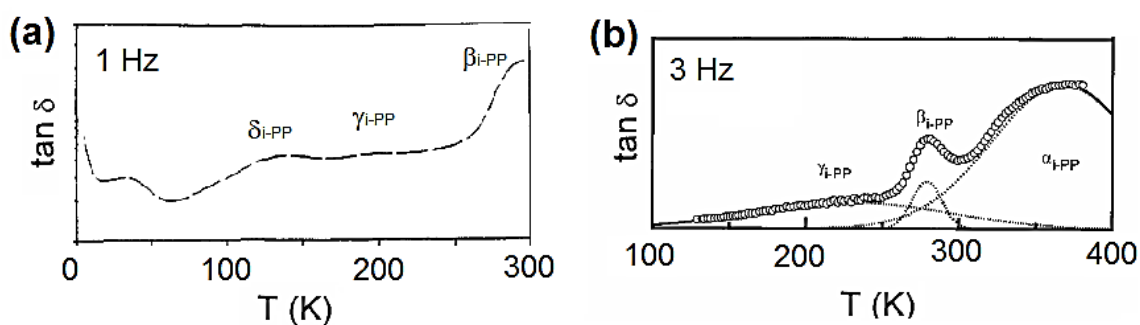
Figure 5-1 (a) Dependence of tanδ on temperature at 1 Hz of iPP; [138] **(b)** Deconvolution of the dynamic mechanical relaxation curve (tanδ) at 3 Hz of iPP. [134]

Although abundant studies have been performed, the genesis of α_c-relaxation is still uncertain and sometimes even controversial in the literature[128, 129, 131, 133, 137, 143] In some cases, the multiple nature of α_c-relaxation even complicates the situation.[131, 143] Normally, the α_c-relaxation exists only in the presence of the crystalline phase. Hence, the simplest hypothesis is to assign it to some phenomenon occurring in the crystalline phase. McCrum[137] pointed out that its origin is most likely an additional relaxation of the amorphous fraction triggered by the onset of molecular rotation within the crystal. Jourdan[133] suggested that α_c-relaxation originating within the crystalline phase could be attributed to the long-distance stress-assisted diffusion of defects inside the crystalline phase. But the amorphous phase also plays an important role, because defects have to adapt themselves to the deformation compatibility of crystalline and amorphous phases by cooperative movements. Pluta[131] proposed that in the case of samples containing large

spherulites, α_c-relaxation could be attributed to the friction phenomena between boundaries of the crystalline lamellae and to a certain extent arise from the intralamellar regions accompanied by a restricted reorientation of crystalline elements within oriented lamellae. For nonspherulitic samples, two components of α_c-relaxation process were found. The low-temperature component was attributed to the stress relaxation of the fraction of the noncrystalline phase containing strained molecules and segments of molecules belonging to the specific (irregular) arrangement of the surface layer of the crystallites. The high-temperature component was connected with the viscous slip process of the crystalline elements within the noncrystalline phase. Moreover, the high-temperature component of α_c-relaxation process could be strongly affected by orientation[143] or the length of chain folding at the interphase between a crystalline phase and an amorphous phase.[137] In the reviews by Boyd,[128, 129] a viewpoint was proposed that the two-phase model of well-developed crystals plus the amorphous phase may be inadequate to illustrate the origin of α_c-relaxation, and, as consequence, an additional intermediate phase should be taken into consideration. This proposal was further demonstrated in the work by Hu with the help of nuclear magnetic resonance spectroscopy: the chain diffusion occurring at the intermediate phase is responsible for α_c-relaxation.[144, 145]

The position and intensity of α_c-relaxation vary with many factors (thermal history, crystalline structure, density, etc.). To name a few, Tiemblo[132] studied the relationship between α_c-relaxation and thermo-oxidation kinetics of PP. The results revealed that samples bearing α_c-relaxation show a strong decrease in the parameter p_0 at temperatures below 115 $^\circ$C, where p_0 is related to the initial concentration of oxidizable sites. However, the decrease in p_0 is not observed in samples where the α_c-relaxation is not resolved. In their late work,[135, 146] the relative influence of microstructure, molar mass and morphology of PP on α_c-relaxation was assessed. Among the factors considered, microstructure and isotactic average length (n_1) have been found to drive mainly the quality of α_c-relaxation. The intensity of α_c-relaxation depends on the final crystalline distribution, provided the requirements that some microstructural features related to n_1 are fulfilled. On the other hand, a critical average isotactic length around 30 propylene units has been found, below which the β-relaxation is promoted with respect to α_c-relaxation. The fraction of the low melting point crystals, which determines the degree of constraint within the interlamellar region, drives the relative intensities of α_c- and β-relaxation processes. In a recent work, Suljovrujic[136] proved that the position, intensity and activation energy of α_c-relaxation were strongly affected by gamma radiation exposure. The intensity of

α_c-relaxation increases nonlinearly with absorbed dose and the shift in the position of α_c-relaxation is most intensive for iPP exposed to lower doses ($\leq$100 kGy). In addition, the evolution of the activation energy with absorbed dose is relatively similar to that observed for the position of α_c-relaxation.

The scope of this chapter focuses on the relationship between mechanical α_c-relaxation and the intermediate phase of iPP. As in the case of most of the semi-crystalline polymers,[102, 147-149] the formation of the intermediate phase in iPP could be greatly influenced by annealing.[150-155] Therefore, samples with different thermal histories were prepared. With the analysis of the results of this study, we attempt to gain a further insight into the mechanical α_c-relaxation in semi-crystalline polymers.

5.2   Crystal form of water cooled and annealed iPP

It is well known that iPP has three kinds of polymorphism for crystalline structure (α-, β-, and γ-iPP) [156] and one "mesophase" which is an intermediate state between amorphous and crystal.[157, 158] In the study by Androsch,[157] it is proved that α-iPP will be the dominant phase when the cooling rate is smaller than 20 K s^{-1}. The "mesophase" starts to show up when the cooling rate is higher than 20 K s^{-1} and totally replaces α-iPP when the cooling rate is higher than 80 K s^{-1}. The "mesophase" is stable at room temperature but it will transform into α-iPP when the temperature is higher than 40 ^{o}C.[159] As the dynamic mechanical analysis was performed with a temperature range from -70 ^{o}C to 160 ^{o}C, the existence of a "mesophase" will lead to a misinterpretation of mechanical relaxation behavior. Therefore, it is of primary importance to check the crystal form of the sample (especially the water cooled one) used in this study. In order to clarify the crystal form of the sample used in this study, 1D-WAXS curves are provided in **Figure 5-2a**. In **Figure 5-2a** one can see the certain peaks for water cooled and annealed samples: (110), (040), (130), (111), and (-131) in the order of increasing scattering vector (q). All peaks mentioned above are characteristic reflexes of α-iPP[18] and no "mesophase" halo could be found, indicating that the samples are composed mainly by α-iPP. X_c of the sample with different annealing temperature is summarized in **Figure 5-2b**. X_c of PPna is 0.48. It stays the same when the annealing temperature is lower than 90 ^{o}C and increases from 0.53 to 0.59 when the annealing temperature is increasing from 105 ^{o}C to 150 ^{o}C.
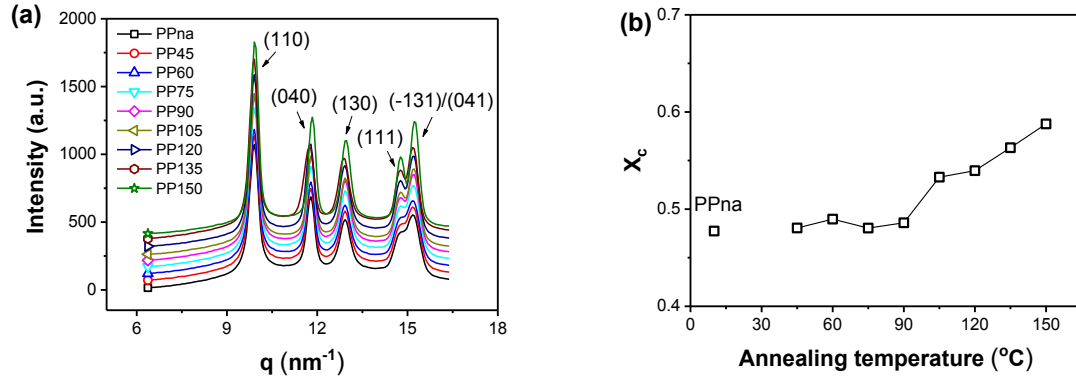
Figure 5-2 (a) 1D-WAXS curves of water cooled and annealed iPP, for clarification the curves are shifted vertically; **(b)** X_c of iPP as a function of annealing temperature.

5.3   Microstructure of iPP with different thermal history

Figure 5-3 shows the 1D-SAXS curve for iPP with various thermal histories. Lorentz correction ($I(q) \rightarrow q^2 I(q)$) is employed because there no lamellae orientation exists in the compression molded samples.[83] The long period (L_p), containing one crystalline phase, one amorphous phase, and one intermediate phase, could be estimated from the peak position (q_{max}) in 1D-SAXS curve. In addition, the width of the scattering peak (full width at half maximum, *FWHM*) providing the information about the statistic of L_p could be obtained by peak fitting. In **Figure 5-3a'**, one can see that with the increase of crystallization temperature, L_p of the melt crystallized iPP increases linearly from 15.2 nm to 20.0 nm and *FWHM* decreases slightly from 0.19 nm^{-1} to 0.15 nm^{-1}. For PPna, L_p is 11.0 nm and *FWHM* is 0.30 nm^{-1}. Annealing at 45 °C for 6 h has a negligible effect on both L_p and *FWHM*. As the annealing temperature increases, L_p increases continually from 11.6 nm to 18.25 nm and *FWHM* decreases from 0.28 nm^{-1} to 0.13 nm^{-1}. **Figure 5-3c** provides the 1D-SAXS curve for the samples annealed at 75 °C for different times. A slight increase of L_p and decrease of *FWHM* could be found after annealling for 1 h, and then both of them stay nearly constant until 6 h. For the samples annealed at 135 °C (**Figure 5-3d'**), the scenario is quite different. An obvious increase of L_p from 11.0 nm to 16.4 nm and decrease of *FWHM* from 0.30 nm^{-1} to 0.15 nm^{-1} could be found in 2 h. After that, L_p and *FWHM* remain nearly unchanged.
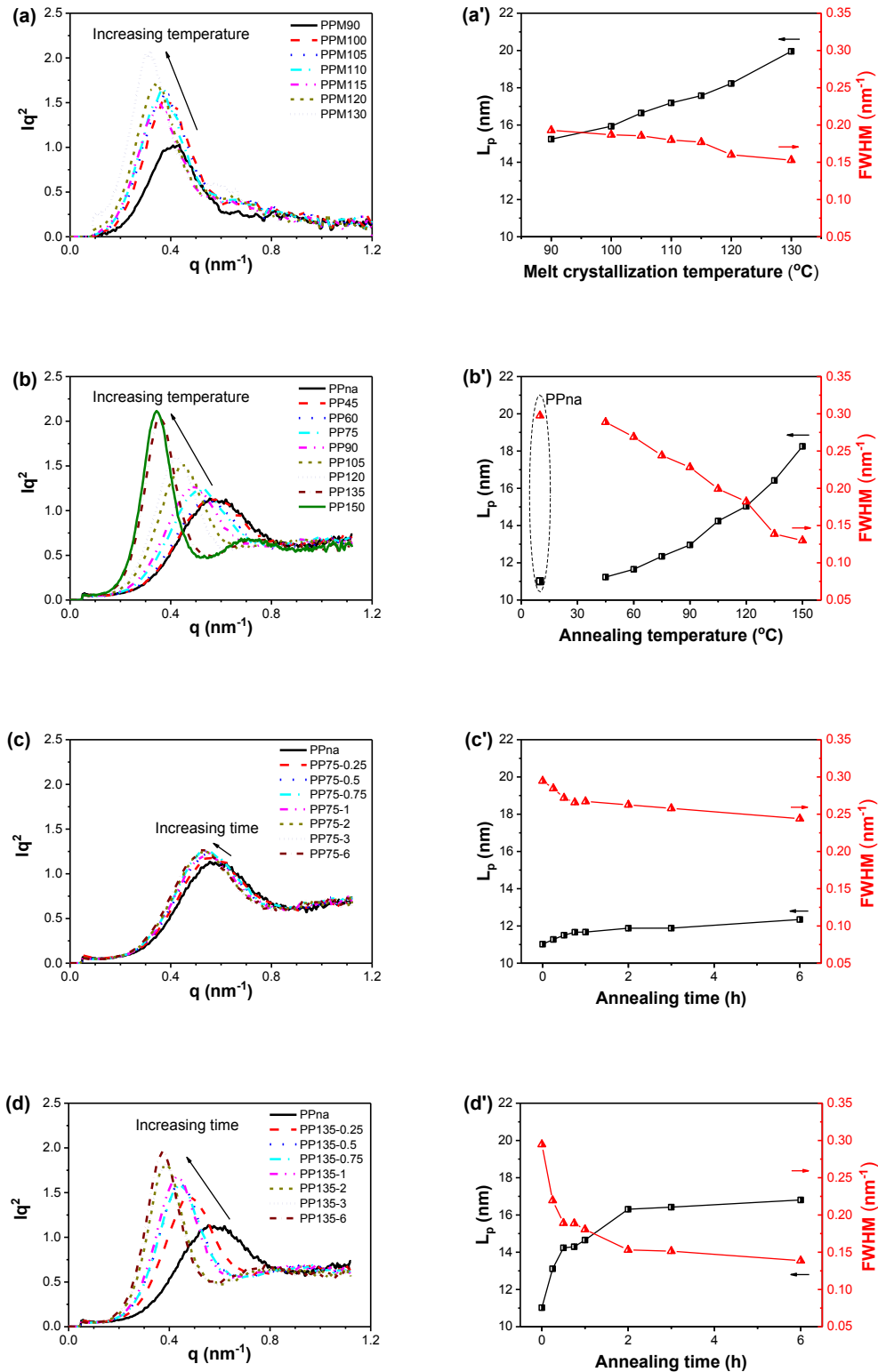
Figure 5-3 Lorentz-corrected 1D-SAXS curves on the left side, L_p and full width at half maximum of the scattering peak (*FWHM*) on the right side. Samples prepared by melt crystallization **(a)** and **(a')**; by annealing at different temperatures for 6 h **(b)** and **(b')**; by annealing at 75 °C for different times **(c)** and **(c')**; and by annealing at 135 °C for different times **(d)** and **(d')**.

In **Figure 5-3b** a shoulder peak at a higher q value shows up for the sample annealed at a temperature higher than 105 °C. Generally, there are two possible origins for the appearance of the shoulder peak: secondary crystallization during annealing, resulting in the formation of new lamellae with larger L_p; or the perfection of original lamellae, leading to a higher order scattering peak. In our case, the former one is preferred, which will also be verified in the following part by DSC and TMDSC. The shoulder peak in **Figure 5-3d** can be ascribed to the same origin above mentioned.

The domain thickness, including the thickness of crystalline phase (L_c), the intermediate phase (L_{im}), and amorphous phase (L_a) of iPP with various thermal histories are summarized in **Figure 5-4a**. It shows that for the melt crystallized iPP, only a slight increase of L_a and L_{im} could be found as the crystallization temperature increases. However, an evident increase can be found for L_c. This confirms Strobl' theory[160] that the reciprocal of L_c should be linear related to the crystallization temperature. In the meantime, the ratio of L_{im}/L_c decreases as crystallization temperature increases, coinciding with the results from other literature.[152, 161] During melt crystallization, the mobility of the polymer chains is quite high. The formation of crystalline phase with perfect regular fold-surfaces is preferred and the coupling between the crystalline phase and the amorphous phase is weak.[161, 162] Consequently, the formation of the intermediate phase is restricted.

For PPna, the values of L_c, L_a, and L_{im} are 3.83 nm, 3.75 nm, and 2.02 nm. The influence of annealing temperature on the domain thickness evolution after annealing could be divided into three regions (see **Figure 5-4b**). Region I: with an annealing temperature lower than 45 °C, in this range only a weak influence can be found on the domain thickness; Region II: from 60 °C to 90 °C, in this range L_{im} and L_c keeps nearly constant, but L_a increases slightly; Region III: from 105 °C to 150 °C, all the domain thickness L_c, L_a, and L_{im} increase obviously with the increase of annealing temperature. L_c increases from 4.15 to 6.08 nm, L_a from 3.93 to 5.33 nm and L_{im} from 2.4 to 3.2 nm. The influence of the annealing time on the domain thickness evolution is given in **Figure 5-4c** and **Figure 5-4d**. It is obvious that L_c, L_a, and L_{im} of iPP annealed at 75 °C for different times hardly change. Whereas, a drastic increase of L_c and L_a can be found for iPP annealed at 135 °C for 2 h. L_c increases from 4.12 to 4.86 nm and L_a increases from 3.89 to 5.24 nm. After that, a slight increase can be found for L_c and L_a until 6 h. As to L_{im}, the evident increase from 2.02 to 2.33 nm could be found in 0.5 h, and then it grows gradually until 6 h.
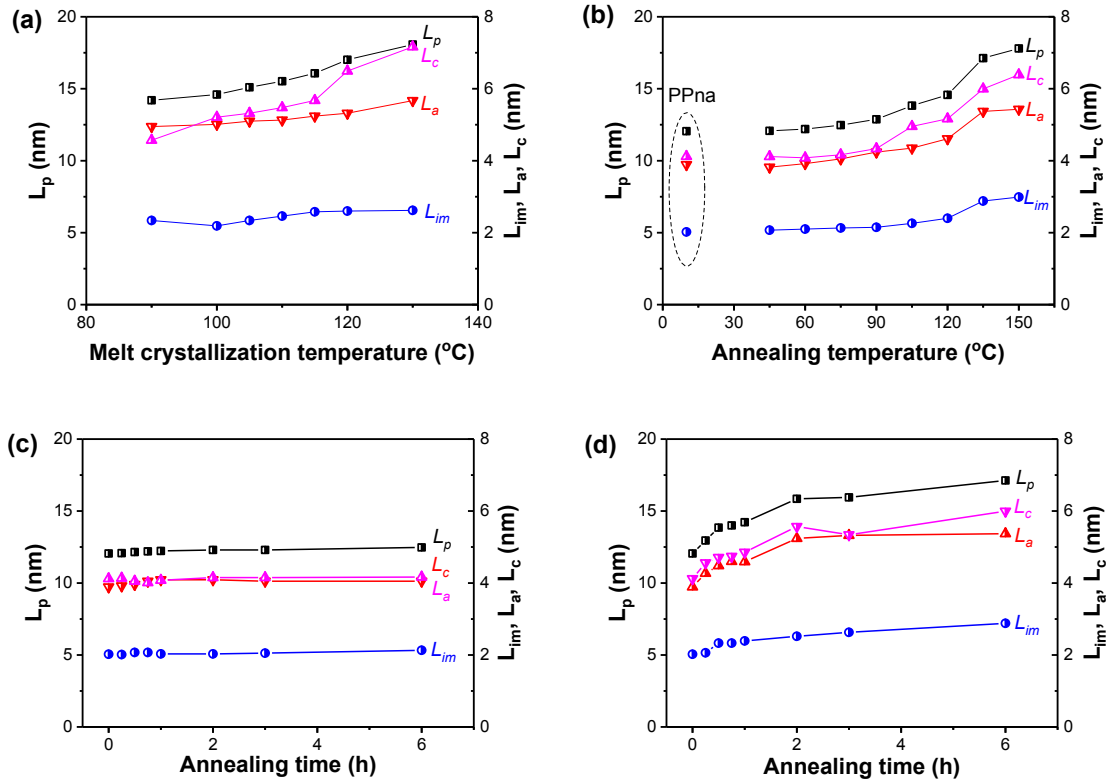
Figure 5-4 The crystalline phase thickness (L_c), the intermediate phase thickness (L_{im}) and the amorphous phase thickness (L_a) of iPP prepared by melt crystallization **(a)**, annealing at different temperatures for 6 h **(b)**, annealing at 75 $^{\circ}$C for different times **(c)**, and annealing at 135 $^{\circ}$C for different times **(d)**.

The evolution of the domain thickness during isothermal annealing is an irreversible process. Sanchez[163] found that the rate of lamellae thickening is proportional to the derivative of the surface free energy with respect to lamellae thickness, which could be described by the following equation:[163]

$$x^2 \frac{dl}{dt} = -k_0 exp[-v\Delta H(T_m^0 - T_a)/RT_a T_m^0]\frac{dG_s}{dl} \qquad \textbf{Equation (5-1)}$$

where x and l are the lateral dimension and thickness of crystalline phase, G_s is the surface free energy, t is the annealing time, ΔH is the heat of fusion per mole of molecular chains, T_m^0 is the equilibrium melting point, T_a is the annealing temperature, v is the number of molecular chains which diffuse simultaneously from amorphous phase to crystalline phase and k_0 is a proportionality constant. The surface free energy G_s of a lamellar crystal with square cross section is given by

$$G_s = 4xl\sigma + 2x^2\sigma_e = 4(lV)^{1/2}\sigma_l + 2V\sigma_b/l \qquad \textbf{Equation (5-2)}$$

where σ_b is the surface free energy of the basal plane, σ_l is the surface free energy of the lateral surface, and $V=x^2l$ is the volume of the crystalline phase. At a certain thickness l^*, $dG_s/dl=0$ and the crystal will reach its equilibrium dimensions of l^* and a corresponding x^*. It is obvious that, if the volume V of crystal remains constant, then

$$l^* = (\sigma_b^2 V/\sigma_l^2)^{1/3} \qquad\qquad \textbf{Equation (5-3)}$$

$$x^* = (\sigma_l V/\sigma_b)^{1/3} \qquad\qquad \textbf{Equation (5-4)}$$

$$l^*/x^* = \sigma_b/\sigma_l \qquad\qquad \textbf{Equation (5-5)}$$

Therefore, for a single lamella, if l/x is smaller than l^*/x^*, the lamella can reduce its surface free energy by an increase in l and a decrease in x. But if the initial ratio of l/x exceeds l^*/x^*, the direction would be the melting of the lamella. Therefore, depending on the size of the initial crystalline phase two competitive processes could happen: one is the melting process if l/x exceeds l^*/x^*, the other one is the lamellae thickening process if l/x is smaller than l^*/x^*.

In region I, no structural change could be detected by SAXS. In region II, L_{im} and L_c keep constant, $FWHM$ decreases drastically and L_a increases slightly. The results suggest that the melting of imperfect lamellae is the dominant process in this region. Lamellae thickening hardly happen because the mobility of polymer chains is too weak. In region II, the decrease of $FWHM$ continues and an evident increase of the L_c, L_a and L_{im} shows that in this region lamellae thickening and imperfect lamellae melting coexist. At higher annealing temperatures, more lamellae melt providing more space and polymer chains for the lamellae thickening process. In addition, the mobility of polymer chains enhances with the increase of annealing temperature. Annealing at 135 ^{o}C for different time provides more details about the process. The increase of the intermediate phase thickening stops after 0.5 h, but the thickening of the crystalline phase and the melting of the imperfect lamellae continues until 2 h. Generally, the lamellae thickening proceeds by transforming the intermediate phase into the lamellae which was verified by Lei and his coworkers.[99] In their work, in-situ SAXS is employed to detect the domain thickness evolution during annealing, and a slight decrease of the intermediate phase thickness at the beginning of annealing and the afterward increase has been observed. The reason responsible for that can be given as follows: in semi-crystalline polymers, the polymer chains directly neighboring the crystalline phase have a higher conformational ordering compared to those away from the surface of the crystalline phase. Thus, a lower energy barrier is needed for the transformation from the intermediate phase to the crystalline phase.[155, 164]

5.4   Melting behavior of iPP with different thermal history

The melting behavior of iPP with different thermal history is shown in **Figure 5-5**. Two melting peaks could be found for PPM90 in **Figure 5-5a**. With the increase of crystallization temperature, the peak on left side shifts to a higher temperature gradually, suggesting the thickness of crystalline phase increases with the melt crystallization temperature. The peak on the right side is due to the melting and recrystallization of the previous crystal. For PPna, only one melting peak at 166 ^{o}C corresponding to the melting of α-iPP can be found in **Figure 5-5b**. As annealing temperature increases, the peak position keeps constantly. For the samples annealed at a temperature higher than 105 ^{o}C, a shoulder peak (indicated by the arrows in **Figure 5-5b** can be found at the low-temperature side of the main peak. The shoulder peak becomes better distinguished and its position shifts gradually from 113 ^{o}C to 151 ^{o}C with increasing annealing temperature. The appearance of the shoulder peak is assigned to the melting of newly formed crystallites formed by annealing,[98, 165] which confirms the result in 1D-SAXS that at high annealing temperature a new crystalline phase is formed. **Figure 5-5c** suggests that annealing at 75 ^{o}C has a negligible effect on the crystalline phase, as has been found in **Figure 5-4c**. In **Figure 5-5d**, the shoulder peak appears after annealing for 0.5 h at 135 ^{o}C, which is consistent with the observation from 1D-SAXS. This shoulder peak shifts to the higher temperature side but main melting peak hardly moves as annealing time increases.
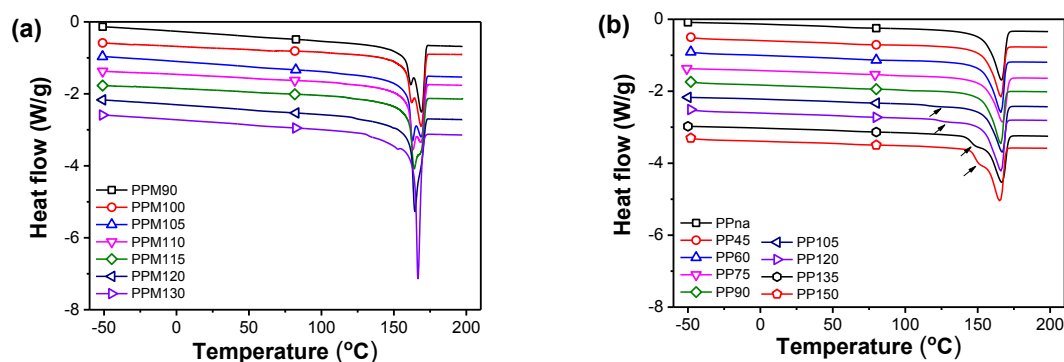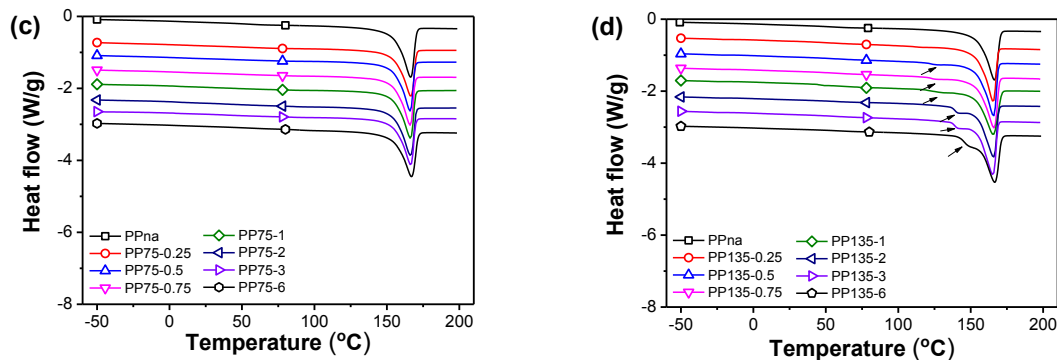
Figure 5-5 Melting behavior of *i*PP prepared by melt crystallization **(a)**, annealing at different temperatures for 6 h **(b)**, annealing at 75 ^{o}C for different times **(c)**, and annealing at 135 ^{o}C for different times **(d)**. For clarification, the curves were vertically shifted.

In TMDSC measurements, with a small sinusoidal modulation superimposed on the conventional linear heating program, the obtained total heat flow could be divided into a (heat capacity-related) reversible heat flow and a (kinetic-related) nonreversible heat flow. Generally, melting appears in not only reversible heat flow but also nonreversible heat flow, but crystallization or enthalpy relaxation can be found only in nonreversible heat flow.[166-168] **Figure 5-6** provides the TMDSC results of iPP. In the reversible heat flow (**Figure 5-6a** and **Figure 5-6b**), for both melt crystallized iPP and annealed iPP only endotherm peak could be found for all samples, which originates from the melting of the crystalline phase. For the nonreversible heat flow (**Figure 5-6c** and **d**), the situation is quite different. For PPna, an exothermal peak can be observed which results from the recrystallization process during the heating.[99, 102, 169] It is well established that the recrystallization process occurs at the surface of the crystalline phase, where the conformational ordering of the polymer chains is higher than those in the amorphous phase. The area for the exothermal peak decreases drastically, accompanied by the appearance of an endothermic peak when the annealing temperature was higher than 105 ^{o}C, Thus, it is reasonable to infer that the melting of the newly formed crystalline phase greatly reduces the conformational order in the intermediate phase, which restricts the recrystallization process. This suggests that the newly formed crystalline phase should be located nearby the initial crystalline phase. Otherwise, the melting of the newly formed lamellae should have no influence on the recrystallization process during heating. No exothermal peak could be found for the melt crystallized *i*PP, due to the melting of the original crystal which covers the signal of recrystallization.
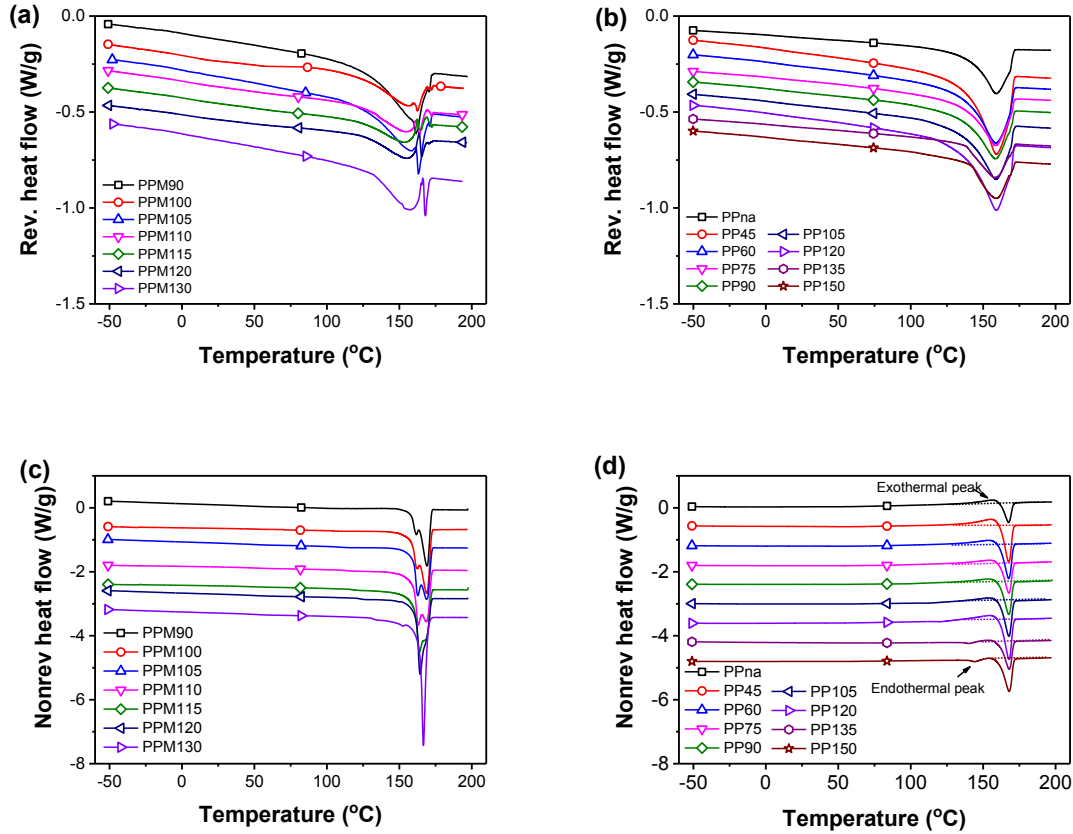
Figure 5-6 Reversible heat flow of melt crystallized iPP **(a)** and annealed iPP **(b)**, and nonreversible heat flow of melt crystallized iPP **(c)** and annealed iPP **(d)**.

5.5 Mechanical relaxation behavior of iPP with different thermal history

The mechanical relaxation of iPP subjected to different thermal histories is shown in **Figure 5-7**. As can be seen, all the curves are characterized by multiple peaks. The peak located at about. 0 ^{o}C is labeled as β-relaxation and the others are labeled as α_c-relaxation. It is obvious that the β-relaxation is very sharp while the α_c-relaxation is broad. For the melt crystallized samples (**Figure 5-7a**), the peak temperature of α_c-relaxation ($T_{\alpha c}$) keeps at about. 84 ^{o}C when crystallization is lower than 110 ^{o}C and it increases gradually from 85 ^{o}C to 93 ^{o}C as crystallization temperatures further increase. For the annealed iPP (**Figure 5-7b**), the case of α_c-relaxation is especially remarkable. One broad α_c-relaxation peak could be found at 83 ^{o}C for NA. Annealing at 45 ^{o}C shifts the α_c-relaxation peak slightly to 84 ^{o}C. With an annealing temperature between 60 ^{o}C-90 ^{o}C, two well-separated α_c-relaxation peaks can be found. The left one is labeled as α_{c1}-relaxation and the right one is labeled as α_{c2}-relaxation. As annealing temperature increases, $T_{\alpha c2}$ and $T_{\alpha c1}$ move from 87 ^{o}C and 56 ^{o}C to 124 ^{o}C and 66 ^{o}C, respectively. When the annealing temperature is higher than 105 ^{o}C, $T_{\alpha c1}$ moves from 72 ^{o}C to

123 ^{o}C and the width of α_{c1}-relaxation is broadened obviously. In the meantime, $T_{\alpha c2}$ could not be detected. The mechanical relaxation behavior of iPP annealed at 75 ^{o}C and 135 ^{o}C for different times is provided in **Figure 5-6c** and **d**. It is worth noting that for the samples annealed at 75 ^{o}C, double relaxation peaks show up after 0.25 h. With the increase of annealing time, $T_{\alpha c1}$ decreases from 69 ^{o}C to 65 ^{o}C and then keeps constantly. $T_{\alpha c2}$ moves from 95 ^{o}C to 103 ^{o}C after annealing for 1 h and then increases slightly to 112 ^{o}C. For the samples annealed at 135 ^{o}C, only the α_{c1}-relaxation peak can be found, which shifts from 89 ^{o}C to 94 ^{o}C.
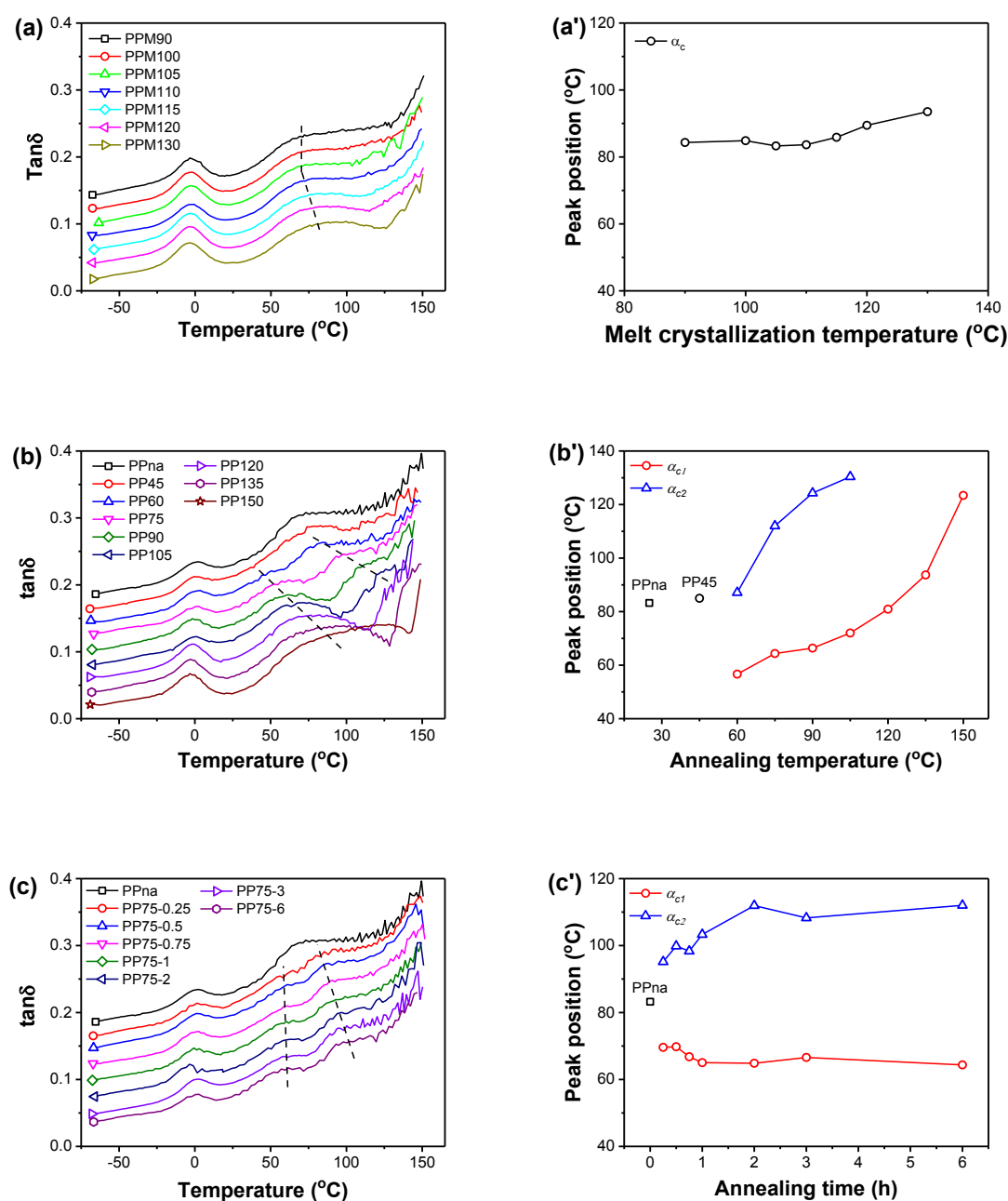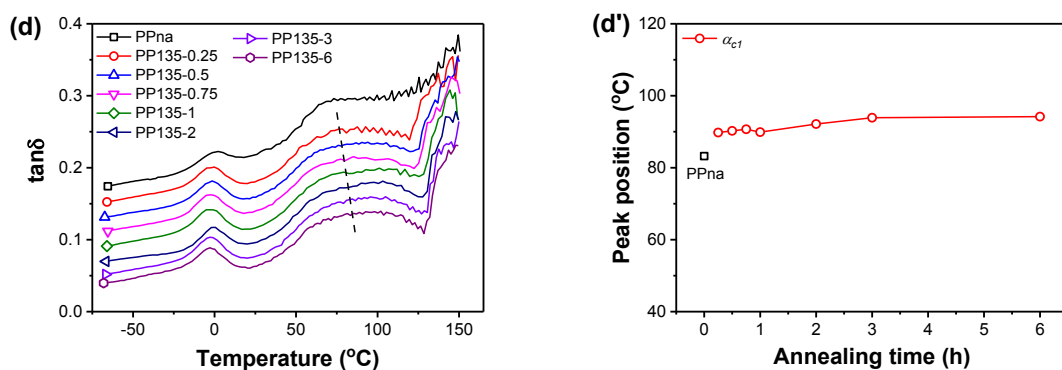
Figure 5-7 Temperature dependence of loss factor (tanδ) tested with a testing frequency of 1 rad s^{-1} for samples after isothermal crystallization at different temperatures **(a)**; samples after quenching and subsequent annealing at different temperatures for 6 h **(b)**; and by quenched and annealing at 75 ^{o}C **(c)** and 135 ^{o}C **(d)** for different time. For clarification, the curves are vertically shifted. **(a')**, **(b')**, **(c')** and **(d')** show the peak position of mechanical α_c-relaxation for the iPP with different thermal history.

The observation of the two well-separated α_c-relaxation peaks is also reported in other studies.[131, 132, 137, 143, 170] Traditionally, α_c-relaxation has an origin in inter- or intracrystalline motion.[143] Pulta [131] ascribed α_{c1}-relaxation to the stress relaxation of the fraction of the noncrystalline phase containing strained molecules, and connected α_{c2}-relaxation with the viscous slip process of the crystalline elements within the noncrystalline phase. The explanation works but it is not satisfying. In our case, it has been proved by SAXS and DSC that annealing at 75 ^{o}C has a tiny influence on the crystalline phase. What really happens is the melting of imperfect lamellae, as has been evidenced by the decrease of *FWHM*. The melting of imperfect lamellae will release the constraint force not only on the polymer chains in the amorphous phase but also on the polymer chains in the intermediate phase neighboring the amorphous phase. The release of the constraint force results in a non-homogenous intermediate phase. Recently, a concept of "continuum of mobility" was proposed by Esposito and his coworkers.[171] The concept can be extended to a wide range of semi-crystalline polymers when the crystalline phase and the amorphous phase are strongly coupled. "Continuum of mobility" means that polymer chains in that phase have a broad distribution of relaxation times. And those polymer chains close to the crystalline phase are strongly tied and the relaxation will happen at a higher temperature. The larger the distance of the polymer chains from the crystalline phase surfaces, the less they are influenced by the interfacial geometrical constraints and relax at a lower temperature. Therefore, the concept of

"continuum of mobility" is borrowed here to describe the relaxation behavior of the polymer chains in the intermediate phase. α_{c1}-relaxation at lower temperature side could be ascribed to the relaxation of polymer chains neighboring the amorphous phase, and α_{c2}-relaxation at higher temperature side originates from the relaxation of the polymer chains close to the crystalline phase. The shift of α_{c2}-relaxation towards higher temperature for those samples annealed at 75 °C indicates that the conformational ordering of the polymer chain close to the crystalline phase is enhanced, which facilitates the formation of the new crystalline phase.

Combining the results from the SAXS, DSC and TMDSC measurements, the structural dependence of mechanical α_c-relaxation of annealed iPP could be explained as follows, a schematic drawing of the relationship between the intermediate phase and mechanical α_c-relaxation is given in **Figure 5-8**.
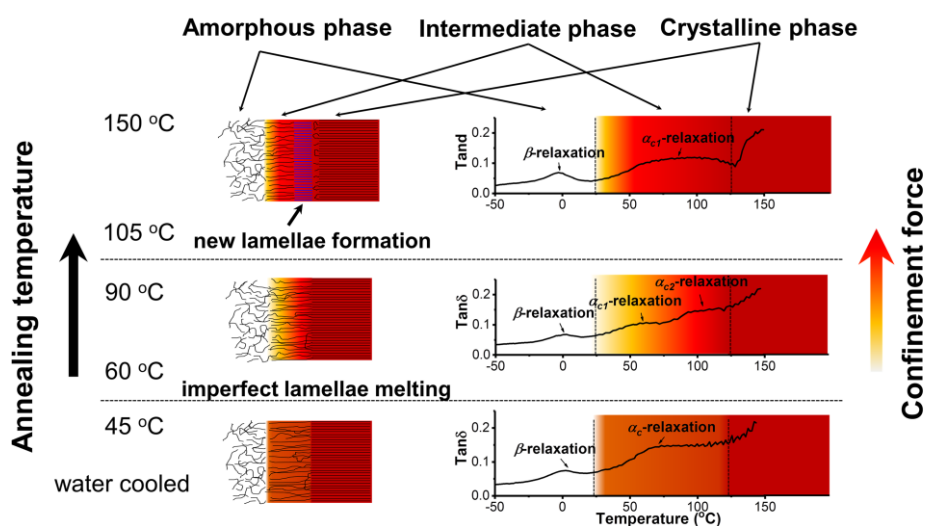
Figure 5-8 A schematic drawing of the relationship between the intermediate phase and mechanical α_c-relaxation.

In the water-cooled iPP lots of imperfect crystallites exist which could be inferred from the large *FWHM*. The polymer chains are constrained by those small crystallites. Annealing at 45 °C has negligible influence on the domain thickness. Therefore the relaxation behavior is nearly the same compared with NA. With an annealing temperature between 60 °C to 90 °C, the melting of imperfect lamellae releases a part of the constraint force on the polymer chains in the intermediate phase. As a consequence, heterogeneous polymer chains mobility should be expected in the intermediate phase, which gives rise to two α_c-relaxation peaks. When the annealing temperature is higher than 105 °C, initial lamellae are thickened and a new crystalline phase is formed in the intermediate phase. As a result, α_{c1}-relaxation peak is

broadened obviously. The peak temperature for α_{c1}-relaxation is further increased because of the enhanced conformational order of polymer chains. Moreover, the confinement in the region between the initial crystalline phase and the new crystalline phase is strongly enhanced. Therefore, α_{c2}-relaxation could not be detected unless the newly formed crystalline phase melts.

The activation energy of the mechanical α_c-relaxation could be obtained from the relaxation map in **Figure 5-9**. For the melt crystallized iPP (**Figure 5-9a**), the plot of ln$f$ as a function of 1000/T could be well fitted by the Arrhenius equation:

$$lnf_{max} = A - \frac{E_\alpha}{k_B} \times \frac{1}{T}$$
Equation (5-6)

where A is a pre-factor, E_α is the activation energy and k_B is the Boltzmann's constant.

Whereas, for the annealed samples (**Figure 5-9b**), a distinct transition of the slope could be found. The departure of the slope is caused by the melting of the imperfect lamellae or the newly formed lamellae during the test. So only the lower part of the plot is employed to calculate the activation energy of annealed iPP.
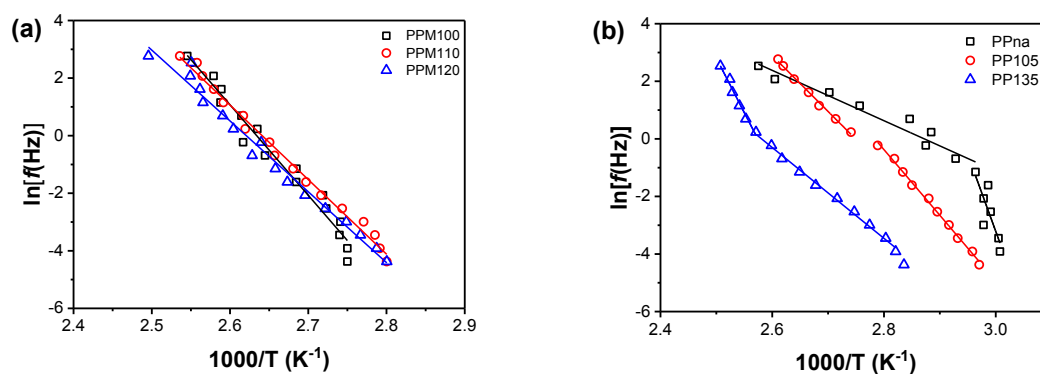
Figure 5-9 Mechanical relaxation map of melt crystallized iPP **(a)** and annealed iPP **(b)**.

Figure 5-10 demonstrates the dependence of the activation energy of α_c-relaxation on the intermediate phase thickness. For the melt crystallized iPP, the activation energy decreases linearly with the increase of the intermediate phase thickness, which is a result of decreased confinement force on the polymer chains. For water-cooled iPP, the activation energy is 53.39 kJ/mol. With an annealing temperature lower 90 °C, the activation energy decreases to 35.55 kJ mol^{-1} while the thickness of the intermediate phase increases from 2.02 nm to 2.15 nm. Obviously, the drastic decrease of the activation energy with a small increase of the intermediate phase is caused by imperfect lamellae melting. With an annealing temperature

higher than 105 °C, the activation energy decreases from 23.59 kJ mol^{-1} to 13.68 kJ mol^{-1} while the thickness of the intermediate phase increases from 2.26 nm to 2.99 nm.
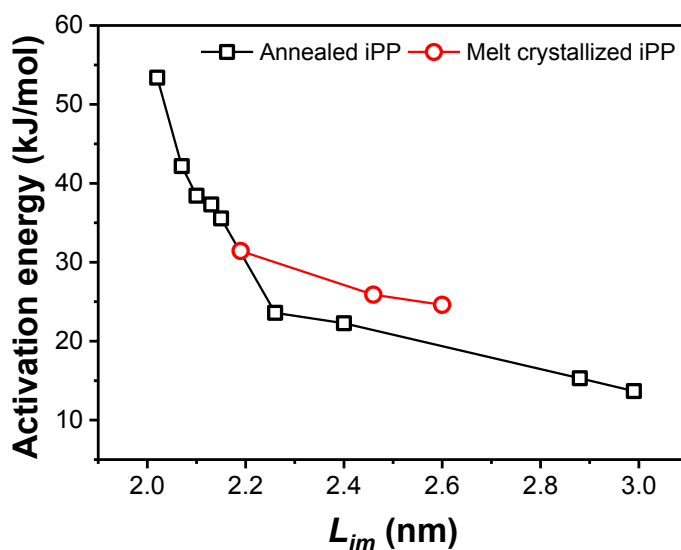
Figure 5-10 Activation energy of α_c-relaxation as a function of the intermediate phase thickness.

5.6 Conclusion

The influence of annealing on the mechanical α_c-relaxation behavior of iPP is investigated in this chapter. The results reveal that the mechanical α_c-relaxation behavior depends strongly on the confinement force on the polymer chains in the intermediate phase. For the water-cooled sample, abundant crystallites with a broad size distribution are formed. The polymer chains in the intermediate phase are constrained by the crystallites, giving rise to one broad α_c-relaxation peak with an activation energy of 53.39 kJ mol^{-1}. With an annealing temperature between 60 °C-105 °C, imperfect lamellae melting releases a part of the constraining forces, which reduces the conformational ordering of the polymer chains neighboring the amorphous phase. Consequently, two separate α_c-relaxation peaks could be observed which are labeled as α_{c1}-relaxation and α_{c2}-relaxation. α_{c1}-relaxation and α_{c2}-relaxation describe the relaxation behavior of polymer chains in the region close to the amorphous phase and the crystalline phase, respectively. Both relaxation peaks shift to higher temperatures as annealing temperature increases. In this range, the activation energy of α_{c1}-relaxation decreases drastically to 35.55 kJ mol^{-1} as the thickness of the intermediate phase increases from 2.02 nm to 2.15 nm. With an annealing temperature higher than 105 °C, a new crystalline phase is

formed in the intermediate phase, which enhances the constraining force on the polymer chains. Therefore, the α_{c1}-relaxation peak is broadened and its position shifts to a higher temperature as the annealing temperature increases. Moreover, the α_{c2}-relaxation is undetectable because the polymer chains in the region between the initial crystalline phase and the newly formed crystalline phase are strongly confined. The activation energy of α_{c1}-relaxation decreases to 13.68 kJ mol^{-1} as the thickness of the intermediate phase increases to 2.99 nm.

6 Critical strains for lamellae deformation and cavitation during uniaxial stretching of annealed iPP[3]

In the former chapter, iPP samples with different thermal history (annealing and melt crystallization) were well controlled and characterized. In this chapter, the lamellae deformation and cavitation behavior of annealed iPP during uniaxial stretching were comprehensively investigated by in situ synchrotron SAXS and WAXS measurements. We reveal how lamellae deformation occurs in the time scales of elastic deformation, intra-lamellar slip, and melting-recrystallization, separated by three critical strains which are only rarely influenced by annealing. Strain I (0.1) marks the end of elastic deformation and the onset of intra-lamellar slip, beyond which the crystallinity decreases gradually. Strain II (0.45) signifies the start of the recrystallization process, from where the long period in the stretching direction begins to decrease from its maximum and the polymer chains in the crystal start to orient along the stretching direction. The energy required for melting arises from the friction between the fragmented lamellae produced by intra-lamellar slip. Strain III (0.95) denotes the end of the recrystallization process. Beyond the strain of 0.95, the long period and the crystal size remain nearly unchanged. During further stretching, the newly formed lamellae serve as the anchoring points for polymer chains in the amorphous phase. The extension of the polymer chains in between lamellae triggers the strain hardening behavior. On the other hand, annealing significantly decreases the critical strain for voids formation and increases the voids number, but restricts the void size. For those samples annealed at a temperature lower than 90 °C, voids are formed between strain II and strain III. And voids are oriented in the stretching direction once they are formed. However, for those samples annealed at a temperature higher than 105 °C, voids are formed between strain I and strain II. In this case, voids are initially oriented with their longitudinal axis perpendicular to the stretching direction and then transferred along stretching direction via void coalescence. Additionally, the formation of voids influences neither the critical strains for lamellae deformation nor the final long period, the orientation of polymer chains or the crystal size. The final long period, the orientation of polymer chains in the crystal, and the crystal size are determined only by the stretching temperature through melting-recrystallization.

---

[3] The main part in this chapter has been published as "B. Chang, K. Schneider, F. Xiang, S. Roth, G. Heinrich. Critical strains for lamellae deformation and cavitation during uniaxial stretching of annealed isotactic-polypropylene", Macromolecules, 51 (2018) 6276-6290

6.1   Introduction

Uniaxial stretching is one of the most frequently encountered loading modes which arises in the tensile test, or fiber spinning.[172] During uniaxial stretching, a macroscopic necking phenomenon of the specimen combined with a yield point on the engineering stress-strain curve is readily observed.[34, 173, 174] After necking, the original lamellae will be transformed into highly oriented structure along the loading direction.[175] In the past decades, abundant works have been carried out via experimental method [36] and simulation procedure [176] on the plastic deformation of lamellae in various semicrystalline polymers, for instance polyamide 6 (PA6),[36, 177] poly(ε-caprolactone) (PCL),[178] PE,[179, 180] PB-1,[181] and iPP.[182-185] Based on the results, two distinct mechanisms have been proposed to account for the plastic deformation of lamellae.[38] The first one was proposed by Peterson[39] and further explored by Shadrake and Guiu,[40] and Yong,[51] which supposed that crystallographic slips are triggered by the emission of screw dislocation from the edges of lamellae. The advantage of the crystallographic slip theory is that it could describe quite well the yield stress dependency of the lamellae thickness.[45] The second one is the partial melting-recrystallization theory[56, 178] which was supported by the evidence that the newly formed crystalline lamellae after the yield point depended only on the stretching temperature irrespective of the original structure.[186, 187]

Except for the lamellae plastic deformation, a stress whitening phenomenon could be observed during uniaxial stretching in most cases, indicating the formation of numerous voids inside the bulk material.[66, 72, 75, 177, 188-190] Recent investigations about voids formation in semicrystalline polymers were elaborately reviewed by Pawlak, Galeski and Rozanski.[191] Generally, the voids can be induced before the yield,[192] during the yield or after the yield,[74, 193] depending on the crystal form,[194] crystallinity,[195, 196] lamellae branching,[197] lamellae thickness,[72] and the state of the amorphous phase.[65]

The relationship between lamellae deformation and cavitation behavior has caught a lot of attentions in the past few years. In the work of Pawlak and Galeski,[188] a set of semicrystalline polymers with different lamellae thicknesses and crystallinity were used. An assumption was proposed that the cavitation or crystal plastic deformation could be activated only when the local stress σ is higher than that required for cavitation (σ_{cav}) or crystallographic slip (σ_{sh}). For a thick lamella with high plastic resistance σ_{cav} is lower than σ_{sh}, as a consequence the initiation of cavitation occurs first and cavitation can be readily observed. Whereas for a thinner lamella σ_{sh} is lower than σ_{cav}, then the crystal slip occurs first. The

assumption was further checked by Humbert,[198] in his work quite simple equations were proposed to describe the relationship between the lamellae thickness and σ_{cav} or σ_{sh}. The important point about the equations is that σ_{cav} decreases with the thickness of lamellae, while σ_{sh} increases. In addition to the study above mentioned, Hughes related the onset of both intense micro-voiding and stress-induced martensitic phase transitions of PE to the yield point.[199] However, Schneider found that martensitic transformation arose earlier than cavitation.[67] Auriemma found that in iPP initially crystallized α and/or γ-iPP will be transformed into the mesomorphic-iPP with a small fraction of nanovoids formed by the effect of stretching.[200] Despite the fact that numerous studies have been performed on the relationship between lamellae deformation and the void formation, it is still an ongoing topic.

The main objective of this chapter is to comprehensively investigate the lamellae plastic deformation and the cavitation behavior in the semicrystalline polymer during uniaxial stretching, especially the critical strains for each structural evolution process. For this purpose, iPP was used as a model polymer because of its wide applications in both industrial fields and scientific studies. The microstructure including the thickness of lamellae, the crystallinity, and the mobility of the polymer chains in the amorphous phase was controlled by an annealing process. In particular, in-situ SAXS and WAXS measurements were performed with the synchrotron X-ray beam to monitor the complex hierarchical structural evolution including void formation, lamellae fragmentation, melting-recrystallization, polymer chains orientation, and more.

6.2   The true stress-strain curves of iPP uniaxial stretched at 75 ^{o}C

The true stress-strain curves of iPP stretched at 75 ^{o}C are recorded in **Figure 6-1a**. **Figure 6-1b** is the enlargement of the square region in **Figure 6-1a**. The increase of the true stress with strain shows a similar trend for all curves. A linear increase of the true stress can be found in small strain region. Then the slope of the curve decreases gradually and afterwards reaches a constant value which continues in a quite large strain region. The onset of this region represents the maximum force on the force-displacement curve,[201] which can be labeled as the yield strain (ε_y). Finally, a sharp increase of the true stress appears implying the appearance of the strain hardening. ε_y and the onset strain of the strain hardening (ε_h) are summarized in **Figure 6-1c**. It can be found that regardless of the annealing temperature (T_a), ε_y and ε_h are around 0.1 and 0.95, respectively.

61
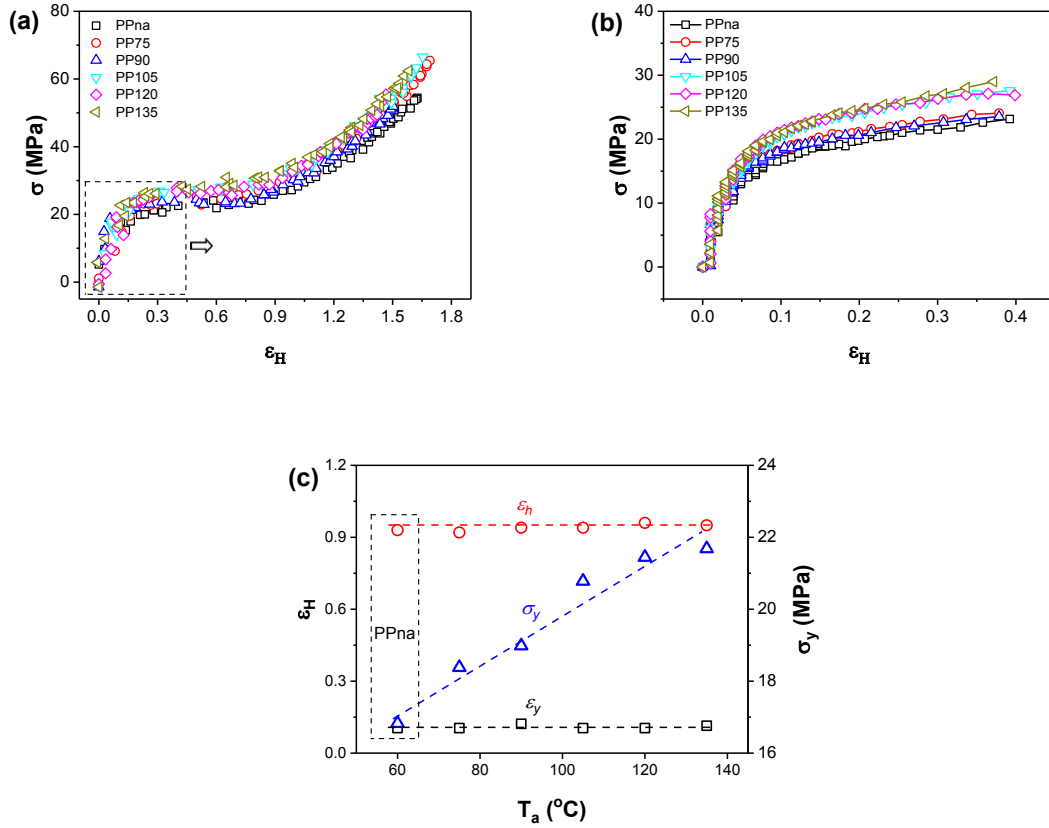
Figure 6-1 (a) The stress-strain curves of iPP with and without annealing uniaxial stretched at 75 °C; **(b)** The enlargement part of the square region in (a) obtained by DIC system; **(c)** The plots of the critical strain at the end of elastic deformation (ε_y) and the onset of strain hardening (ε_h), and the yield stress (σ_y) as a function of annealing temperatures.

Figure 6-1c also shows that the yield stress (σ_y) increases with T_a, which could be understood by employing the screw dislocation theory[202]

$$\sigma_y = \frac{K(T,\dot{\varepsilon})}{2\pi} exp\left[-\left(\frac{2\pi\Delta G_a(T)}{L_c K(T,\dot{\varepsilon})b_v^2} + 1\right)\right] \qquad \textbf{Equation (6-1)}$$

where $K(T,\dot{\varepsilon})$ is the crystalline shear modulus of the slip planes (which depends on the stretching temperature and strain rate), ΔG_a is the Gibbs free energy for dislocation nucleation (assumed to be proportional to the absolute temperature), b_v is the magnitude of the Burgers vector, and L_c can be regarded as the lamellae thickness. For the sample stretched at a constant temperature (namely 75 °C in this case), σ_y is controlled only by L_c. As has been demonstrated in the former chapter, annealing will perfect the lamella and increase the thickness of lamellae, which results in a larger L_c in **Equation (6-1)**, consequently leads to a larger σ_y.

6.3 In Situ SAXS and WAXS Results

In **Figure 6-2**, some representative 2D-SAXS patterns during stretching are provided. The specified strain for each pattern is provided. The stretching temperature is 75 $^{\circ}$C and the stretching direction is horizontal.
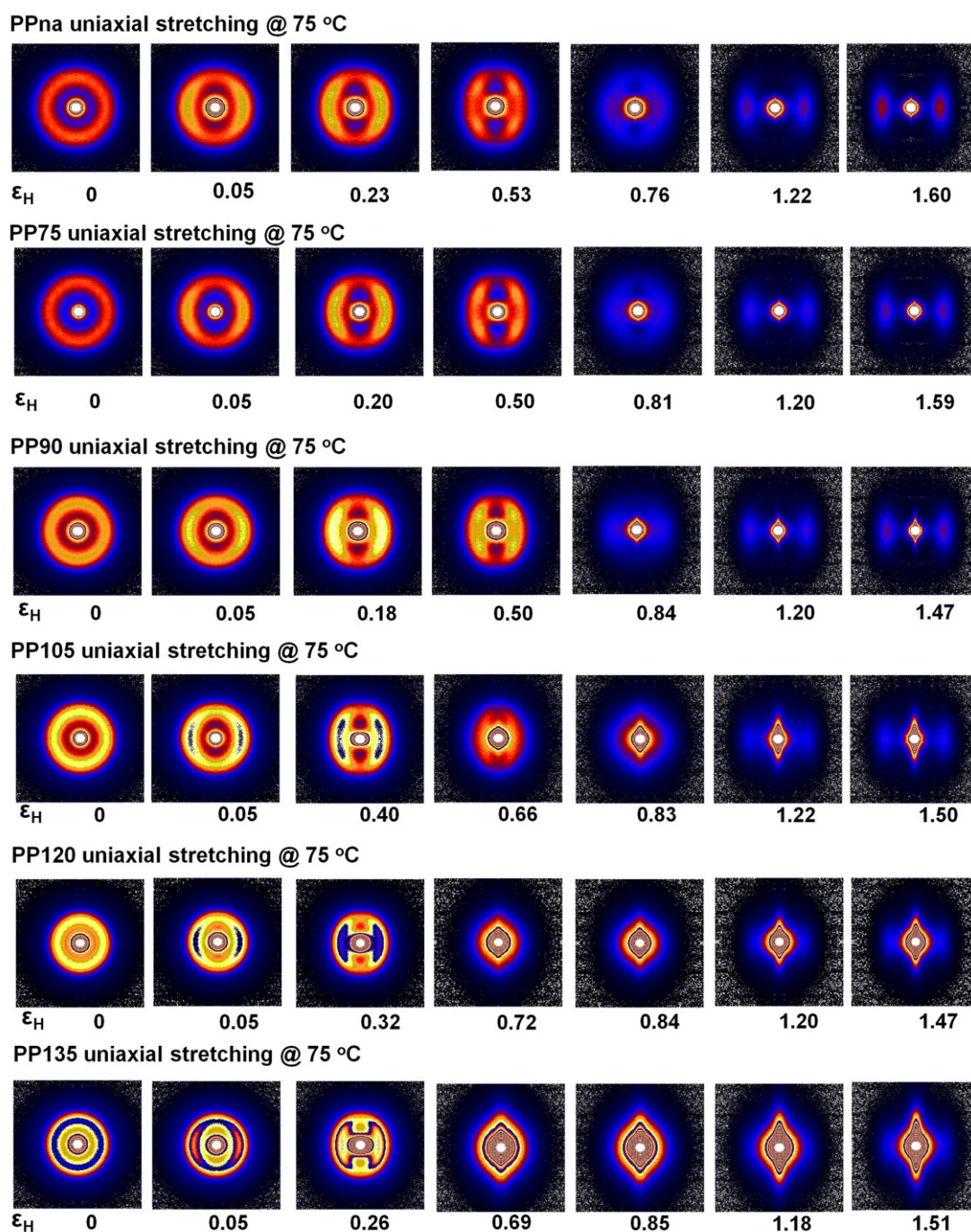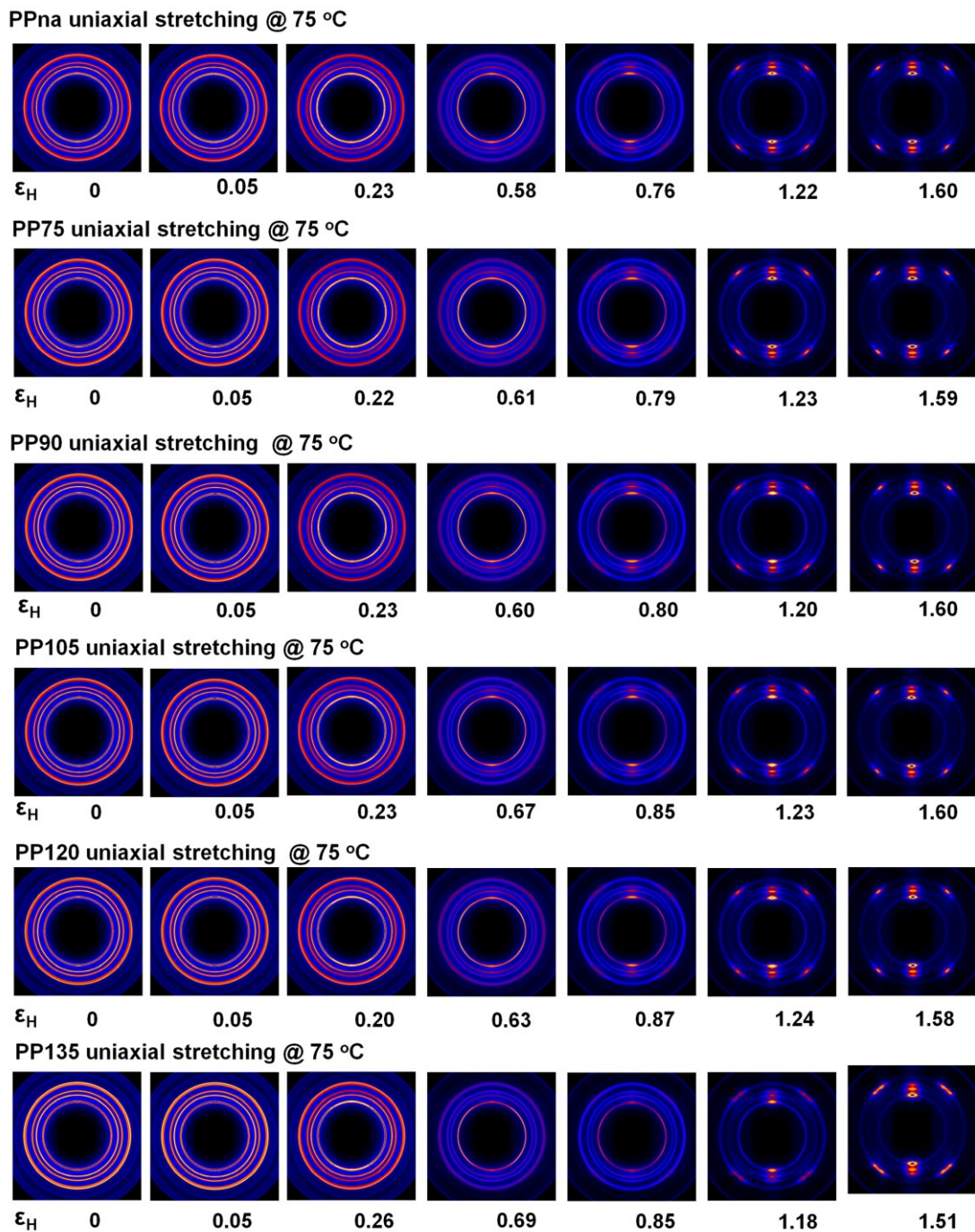

Figure 6-2 Representative 2D-SAXS patterns of iPP with different annealing histories during uniaxial stretching at 75 $^{\circ}$C. The color scale is linear and identical for all patterns. The size of the pattern is 600×600 pixels. The loading direction is horizontal.

Without stretching, all patterns exhibit a homogenous ring, suggesting a random lamellae distribution with respect to the stretching direction. With the increase of T_a, the radius of the ring decreases and the intensity of the ring is enhanced, which results from a larger L_p and a narrow distribution of L_p. Upon stretching, the evolution of the pattern is quite different with varying annealing temperatures. For PPna, at the ε_H of 0.05 the homogenous ring changes into "two arcs" shape concentrated on the equator, indicating the slight lamellae orientation along the loading direction.[203] As ε_H increases to 0.53, the "two arcs" pattern is replaced by a "four arcs" elliptical pattern with the intensity focused at oblique angles. The "four arcs" elliptical pattern originates from the tilting of lamellae.[203] With a strain of 0.76 the lamellar scattering becomes very blurry, indicating the melting of the lamellae. And the diffusing scattering focuses mostly on the equator. As ε_H increases further to 1.22, the "two lobes" shape scattering can be found at the equator, suggesting the formation of new lamellae with their normal direction aligned along the loading direction. And in the center region of the pattern, a diamond shape scattering could be found in the vertical direction. Generally, the appearance of the diamond shape signal means the formation of elongated structure, such as fibrillary structure or voids. Since no obvious stress whitening is observed at this strain value, thus no certain cause can be ascribed to the streak signal immediately. In order to figure out the origin of the weak diamond scattering, the morphology of PPna after stretching is investigated by SEM measurement. The result is provided in **Figure 6-3.**
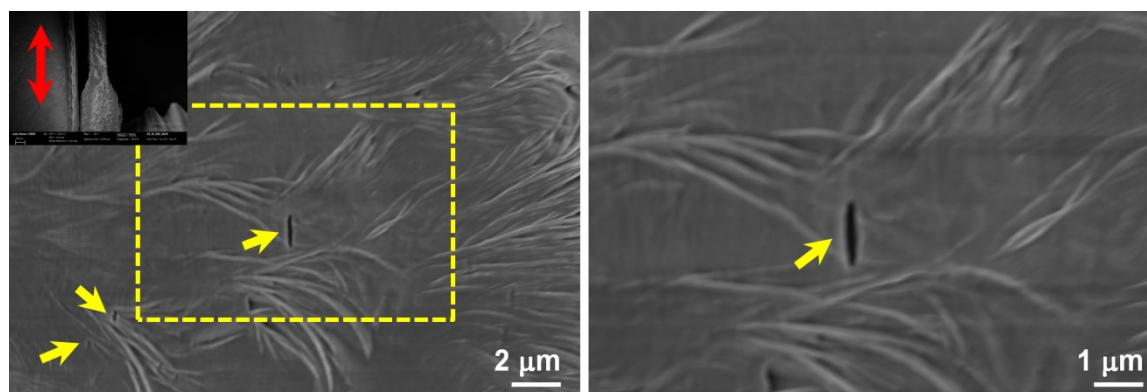
Figure 6-3 The morphology of PPna after stretching at 75 °C. The yellow arrows are referred to the voids. The Figure inserted in the left image provides geometry of the whole sample (the red arrow indicates the stretching direction). The Figure on the right side is the enlargement of the square region in the left image.

On the SEM image, the lamellae are roughly oriented with their normal along the stretching direction. And a few voids, rather than fibrillary structure, indicated by the arrow can be

found, verifying that the diamond scattering in the center region of the 2D-SAXS pattern originates from voids. For PP105, the "two arcs" pattern shows up at the strain of 0.05. And the "four arcs" elliptical pattern can be found at the strain of 0.40, which is similar to that of PPna. Furthermore, the scattering in the center region starts to grow along the horizontal direction, which is greatly different from that of PPna. The scattering on the equator provides evidence for the formation of the elongated structure, and the elongated structure is arranged with its longitude axis perpendicular to the stretching direction. With the increase of ε_H, the "four arcs" scattering diminishes gradually, suggesting the disappearance of the lamellae. Additionally, the scattering in the center region grows in the vertical direction, implying the direction transition of the elongated structure. At the ε_H of 1.22, the lamellae scattering shows up again in the form of "two lobes" at the equator and the diamond scattering is fully oriented in the meridian. For PP135, the typical "two-arc" pattern existed in PPna and PP105 can be found again at the ε_H of 0.05. With the increase of ε_H, the intensity in the center region of the pattern starts to grow noticeably at the equator without the formation of the "four arcs" pattern. The disappearance of the "four arcs" pattern indicates that no lamellar tilting occurs here. The evolution of the scattering at the equator changes in a similar way as that of PP105. When ε_H is further increased, the direction of the scattering transforms from the equator to the meridian and the scattering undergoes a significant thinning process. In addition, lamellae scattering can also be found at the equator.

The 2D-WAXS patterns during stretching are presented in **Figure 6-4**. With the increasing of ε_H, the scattering of crystal planes changes in a similar trend for all samples regardless of the annealing histories. As the strain is increased, the scattering of crystal planes containing the axis of polymer chains ((110), (040), and (130) crystal planes) tend to focus their intensity on the meridian. Meanwhile, the scattering of the external two crystal planes with the index of (hk1) transforms into a four-point pattern, indicating the presence of two populations of lamellae in the material.[184] As ε_H is further increased, the scattering width of the crystal planes is broadened noticeably due to the formation of defective crystals. [184, 204]

Figure 6-4 Selected 2D-WAXS patterns of iPP with different annealing histories during uniaxial stretching at 75 °C. The color scale is linear and identical for all patterns. The size of the pattern is 600×600 pixels. The stretching direction is horizontal.

6.3.1 Synchronize mechanical test and in-situ SAXS/WAXS measurement

To get the critical strain for lamellae deformation and void evolution during stretching, the in-situ SAXS/WAXS measurements and the uniaxial stretching test should be synchronized. As

has been proved by Millot,[36] in the elastic strain range the scattering intensity from the lamellae and crystal over the whole azimuthal distribution always exhibited a heterogeneous feature once the load is applied. The heterogeneous feature at a small strain (0.05) can be also found in **Figure 6-2**, which is caused by the positive tensile stress in stretching direction and the internal compressive stress perpendicular to stretching because of the Poisson effect. The heterogeneous intensity distribution could be well described by Herman's orientation factor (f_H). **Figure 6-5** gives an example of the synchronization process. Before deformation, f_H is -0.016 and -0.006 for lamellae and (040) crystal plane. The small negative deviation is due to the slight compression force caused by the thermal expansion of the sample under 75 ^{o}C. Upon stretching, both f_H values increase linearly in the elastic deformation region. Via this process, the onset of the mechanical test and the onset of SAXS/WAXS measurements could be well synchronized. In **Figure 6-5**, one can also see that at the same displacement, the growth of f_H from the lamellae side is 4 times larger than that from the (040) reflections. This is because the constraint force from the lattice is much higher compared to the rigidity of the amorphous phase, which benefits a larger rotation angle of the lamella.
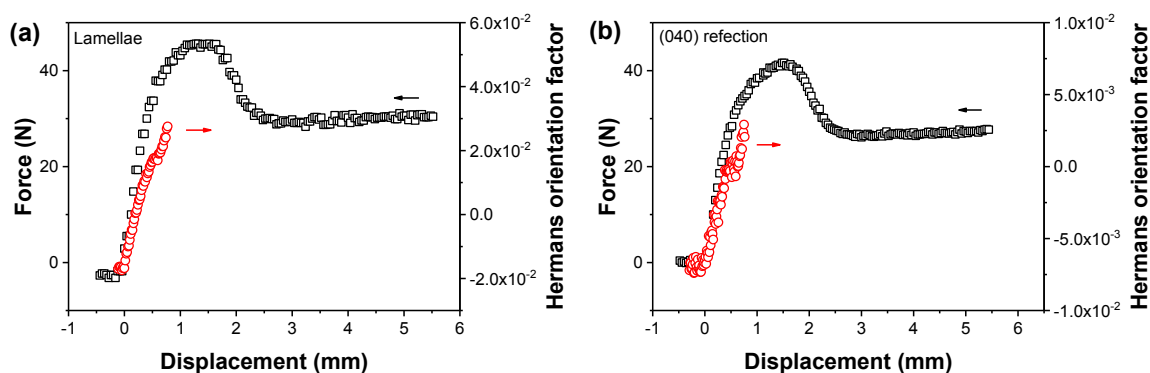
Figure 6-5 (a) Engineering force-displacement curve (square) and the Hermann's orientation factor of lamellae (circle) of PPna uniaxial stretched at 75 ^{o}C; **(b)** Engineering force-displacement curve (square) and the Hermann's orientation factor of (040) crystal plane (circle) of PPna uniaxial stretched at 75 ^{o}C.

6.4 Lamellae deformation

6.4.1 The evolution of the long period

In this section, the evolution of L_p along the stretching direction is studied, reflecting the deformation of the lamellae aligned with their normal direction along the stretching direction and therefore suffer a tensile stress during stretching. It should be pointed out that some 2D-

SAXS patterns exhibit elliptical "four arcs" scattering due to lamellae tilting.[103] The scattering maximum is located off to the equator. By plotting the 1D-SAXS curve at different azimuthal angle, it is found that the intensity difference between the scattering on the equator and on the arc is only 2 a.u., suggesting that a large group of lamellae are still oriented with their normal direction along the stretching direction. So the definition of L_p along the stretching direction is valid during the whole stretching process. The evolution of L_p as a function of ε_H is summarized in **Figure 6-6a.** Without stretching, L_p increases with the increase of T_a as a result of imperfect lamellae melting and lamellar thickening.[205] Upon stretching, the evolution of L_p shows a similar trend for all samples. Firstly, L_p increases gradually due to the separation of lamellae since that amorphous phase in between has a lower modulus.[36] Then L_p reaches a maximum at the ε_H of 0.45. As expected, the maximum L_p increases with T_a. With the further increase of ε_H, L_p starts to decrease which was also found by other researchers in the system of iPP,[183, 206, 207] PCL,[178] and PE.[208, 209] At an even larger ε_H, L_p reaches a plateau value and all samples show a same L_p as ε_H is larger than 0.95. The decrease of L_p at moderate ε_H is caused by the melting-recrystallization process, which inserts newly formed lamellae into the old one. The DSC results in **Figure 6-6b** verify that L_c of the stretched samples is also the same, which confirms the occurrence of the melting-recrystallization process during stretching. After yielding, the massive fragmentation of lamellae via inter-lamellar slip happens and continues during the following stretching. The friction between the fragmented lamellae leads to an increase of the temperature of the sample,[206] providing the energy for the melting.
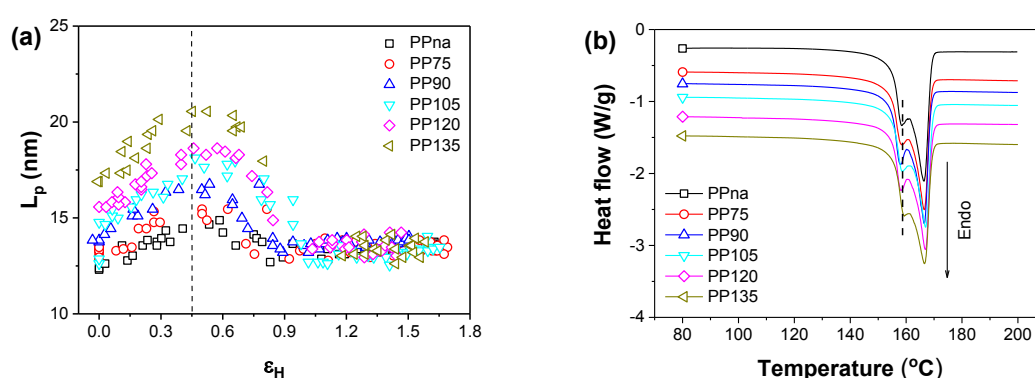
Figure 6-6 (a) Evolution of L_p along the stretching direction as a function of ε_H; **(b)** The melting behavior of the uniaxial stretched sample.

In **Figure 6-7** the dependence of the reciprocal of the lamellae thickness ($1/L_c$) on the stretching temperature is plotted. The lamellae thickness increases as the stretching temperature is increased. Recently, the stretching induced crystallization was investigated by Men.[210] In his work, the stretching induced crystallization was proposed to be mediated by a mesomorphic phase, which was based on the crystallization proposed by Strobl.[211] For the crystallization via a mesomorphic phase, the crystallization line could be defined as[211]

$$T_{mc}^{\infty} - T \approx \frac{2(\sigma_{acn}-\sigma_{am})}{\Delta H_{cm}} \frac{\Delta z}{L_c}$$ **Equation (6-2)**

where T_{mc}^{∞} is the transition temperature between the mesomorphic phase and crystalline phase, ΔH_{cm} is the heat of transition from mesomorphic phase to crystalline phase, Δz is the stem length increment per structural unit, and σ_{ac_n} and σ_{cm} denote the surface free energy of the native crystal layer and the mesomorphic layer, respectively. The slope in this study is larger than the one obtained by Men.[210] The difference of the slope may be caused by the higher molecular weight iPP used in this study, which increases the surface-free energy of the native crystal formed from the mesomorphic phase.[186]
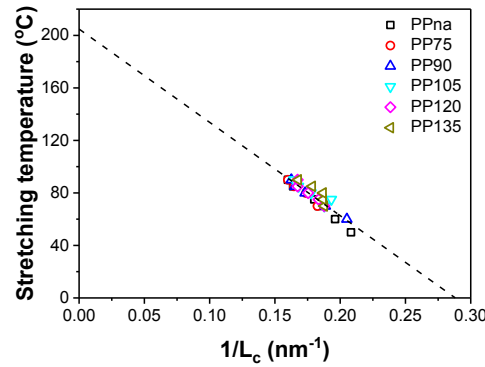
Figure 6-7 Dependence of the reciprocal of the lamellae thickness ($1/L_c$) on the stretching temperatures.

6.4.2 The evolution of the crystal size

In addition to L_p, the evolution of the crystal size from (110) and (040) crystal reflections are calculated based on the Scherrer equation[185]. The change of the crystal size as a function of strain is given in **Figure 6-8**. Interestingly, annealing has only a small influence on the crystal size. The initial $\tau_{(110)}$ is around 19.5 nm for all samples. Obviously, the evolution of the $\tau_{(110)}$ with ε_H can be divided into three regions. Region I covers a strain range from 0~0.1. In this region the $\tau_{(110)}$ decreases drastically from 19.5 nm to 16.2 nm; region II starts at a strain

of 0.1 and ends at 0.95, and the $\tau_{(110)}$ decreases further to 9.0 nm; region III covers the last part of the plot, and the $\tau_{(110)}$ levels off to a plateau with only small variation. The $\tau_{(040)}$ is larger than the $\tau_{(110)}$. But its evolution trend takes place in a similar way as the latter one. Two distinct transition strains (0.1 and 0.95) can be also found. Before stretching, the $\tau_{(040)}$ is 40 nm and it decreases to 32 nm at a strain of 0.1. Further increase of the strain results in a further decrease of the $\tau_{(040)}$ to 21 nm. In the last region, the $\tau_{(040)}$ is changed only slightly. It should be pointed out that the critical strains existing in **Figure 6-8a** coincide with the ε_y and ε_h in **Figure 6-1**. The crystal size is determined by the peak position and the peak width of the reflection. To get deep insight into the structural cause of the decrease of the crystal size, the peak position and peak width of (040) crystal plane are provided in **Figure 6-8b** and **c.** In the strain range of 0~0.1, an instance increase in the instance of peak position and peak width could be found. Since the peak position and peak width are obtained by the vertical cut from the 2D-WAXS patterns, the increase of the peak position of (040) crystal plane indicates that the lamellae with their *c*-axis aligned along the loading direction are subjected to a compression force in the *b*-axis direction. In the same range, the peak position changes less than 1 % (see **Figure 6-8b**), suggesting a very small deformation of the crystallites. Consequently, the crystallite size is mainly reflected by the width of the peaks. In the strain range of 0.1~0.95, the peak width increases continually with strain (see **Figure 6-8c**), which is the result of lamellae tilting and intra-lamellae slip. By lamellae tilting and intra-lamellae slip, the initial lamellae are fragmented into lamellae blocks.

(c)
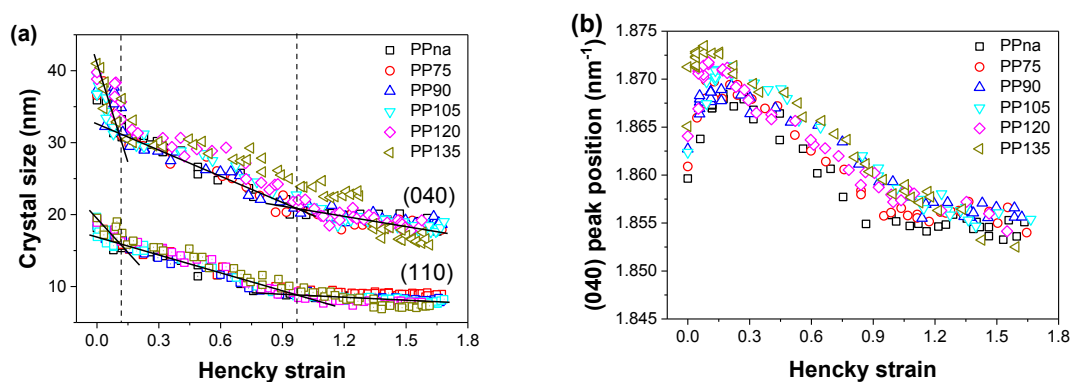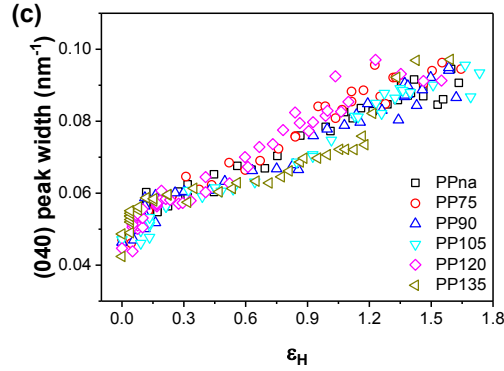
Figure 6-8 (a) The plots of the crystal size calculated from (110) and (040) crystal planes as a function of strain; **(b)** The plots of the peak position of (040) crystal plane as a function of strain; **(c)** The plots of (040) reflection peak width as a function of strain.

6.4.3   The orientation of the *c*-axis of the crystal

The orientation of the *c*-axis of the crystal is given in **Figure 6-9**. In the meantime, *b*-axis orientation obtained from $\langle \cos^2 \varphi_{040} \rangle$ is also provided. As it appears, annealing has a very weak influence on the orientation of the *b*-axis and the *c*-axis. Before stretching, the orientation factor is nearly 0, which suggests the random orientation of the crystal. As the strain is increased, a transition strain of 0.45 can be found for both *b*-axis and *c*-axis orientation. Beyond the strain of 0.45, the orientation of the *b*-axis starts to decrease and the orientation of *c*-axis increases gradually, meaning that the *c*-axis of the iPP crystal starts to orient along stretching direction while the *b*-axis orients perpendicular to the stretching direction. The critical strain for *b*-axis and *c*-axis orientation here coincides with the one observed in **Figure 6-6a**, where the long period starts to decrease from its maximum. The results here further prove the recrystallization process proposed in **section 6.4.1**. Otherwise the *c*-axis orientation will start to increase at a strain of 0.1 if the lamellae deformation proceeds only by intralamellar slip.
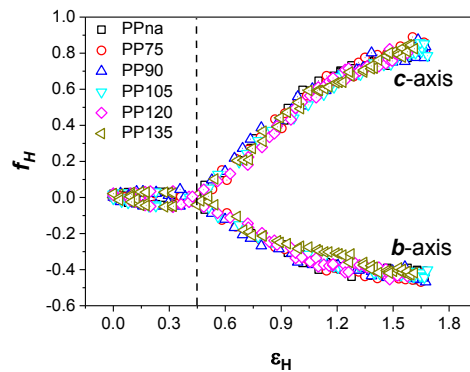
Figure 6-9 The Herman's orientation factor (f_H) of ***b***-axis and ***c***-axis of the crystal during uniaxial stretching.

It should be noted that the polymer chains orientation discussed above is valid only for the crystalline phase because (110) and (040) reflections are related to the crystal. The polymer chains orientation in the amorphous phase is not investigated in this work. Recently, by using Raman measurement and small-angle neutron scattering (SANS) the molecular conformation and single chain orientation in the amorphous phase of PE during cold drawing were studied by López-Barrón,[179] which would be helpful to have an overview about the polymer chains orientation in the crystalline and the amorphous phase. López-Barrón's results showed that the molecular alignment in the amorphous phase grew steadily throughout the initial elastic deformation and the subsequent plastic deformation, and reached a plateau at the onset of mechanical strain hardening because further stretching would need more energy to pull the chains out from the lamellae or rupture the tie chains.

6.4.4   The evolution of the crystallinity

The crystallinity of iPP during stretching is provided in **Figure 6-10.** It is obvious that after annealing, a higher crystallinity can be found. The evolution trend is similar for all samples with different annealing histories. Before the strain of 0.1, the crystallinity stays nearly the same, suggesting that mainly elastic deformation happens. Beyond the yield strain, a continuous decrease of the crystallinity sustains until the end of stretching. The crystallinity is higher for the sample with a higher annealing temperature at any strain during stretching. The slope of the decreasing trend of the crystallinity for the samples does not change much during the whole stretching process, which is similar with the result by Lin[212] when a stretching temperature between 40~90 °C is chosen. The critical strains for the melting-recrystallization and the strain hardening do not show up on the plot, due to that the crystallinity of semi-crystalline polymers is influenced by many factors including intra-lamellae slip, melting-recrystallization, phase transition, and pulling out of polymer chains from crystals.[183, 185, 212, 213]
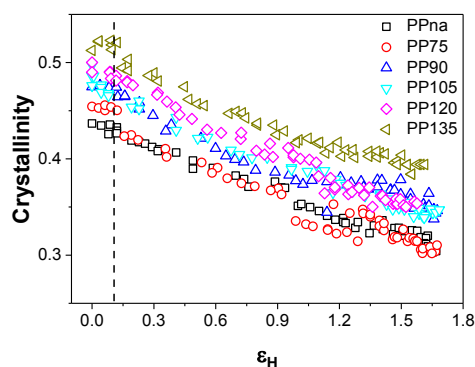
Figure 6-10 The evolution of the crystallinity as a function of Hencky strain.

Combining the results from macroscopic true stress strain curve with microscopic long period, crystal size, polymer chains orientation, and crystallinity development during stretching, a few critical strains rarely influenced by annealing are found. According to the critical strains, the lamellae deformation during stretching could be divided into four regions. Region I covers a strain range from 0 to 0.1. In this region, elastic deformation is the dominant process resulting in a steep increase of true stress. In the meantime, the long period along the stretching direction is slightly increased, which is mainly caused by the elastic elongation of the amorphous phase.[36] In addition, the crystal size suffers a steep decrease, but the crystallinity stays with negligible variation. Region II starts at 0.1 and ends at 0.45. In this region, the deformation of lamellae occurs mainly by intra-lamellar slip. The lamellae are fragmented into blocks without orientation. The friction between the fragmented lamellae during intra-lamellar slip provides the energy of lamellae melting. Region III has a strain range from 0.45 to 0.95. In this region, recrystallization happens and the distinct polymer chains orientation appears because the newly formed lamellae are aligned with their *c*-axis along the stretching direction. The recrystallization process is mediated by the formation of a mesomorphic phase.[186] The long period of newly formed lamellae depends only on the stretching temperature. Region IV covers all the strain above 0.95. The long period and the crystal size stay nearly unchanged, suggesting that the recrystallization process is terminated. The newly formed lamellae serve as the anchoring point for the polymer chains in the amorphous phase. The tightening of the polymer chains in the amorphous phase in between the lamellae blocks gives rise to the strain hardening behavior.

6.5 Cavitation behavior

6.5.1 The onset strain of the voids formation and the voids direction transition

The evidence of the void formation, as shown in **Figure 6-2** is the appearance of a streak or elongated elliptical signal depending on the annealing temperature. In both cases, the scattering of voids is quite weak at the very beginning. In fact, the scattering in the center region of the 2D-SAXS patterns is made up by two parts: the heterogonous elongated one from the voids and the homogenous one from the matrix. Therefore, to extract the void scattering out from the pattern, the intensity correction of $I_{hv}(s) = I_h(s) - I_v(s)$ or $I_{vh}(s) = I_v(s) - I_h(s)$ is employed, depending on the direction of the void. $I_h(s)$ and $I_v(s)$ represent the plot of the scattering intensity as a function of the scattering vector in horizontal and vertical cut, respectively. Meanwhile, at the small angle region of the 2D-SAXS pattern, the scattering intensity as a function of scattering vector should obey Guinier's law, which is given by

$$I(s) = I_0\rho^2 V^2 \exp(-4\pi^2 s^2 R^2/3) \qquad \textbf{Equation (6-3)}$$

where $I(s)$ is the corrected intensity of scattering, I_0 is the scattering intensity at the scattering vector of 0, ρ is the electron density difference, V is the volume of scattering, and R is the gyration radius.[214] **Figure 6-11a** and **b** show the evolution of the corrected intensity of PP120 as a function of ε_H. Once the void is formed, R should be larger than 0 if the intensity correction is performed in the streak direction, and R will be increased during the growth of voids, see **Figure 6-11c**. Therefore, the ε_H where $R > 0$ is used as the critical strain for void formation. As the direction of voids is changed, R should be larger than 0 in the direction transversal to the initial direction, see the plot of the red circles in **Figure 6-11c**. The critical strain for voids formation and voids direction transition are summarized in **Figure 6-11d**. In **Figure 6-11d**, two types of void formation can be confirmed.
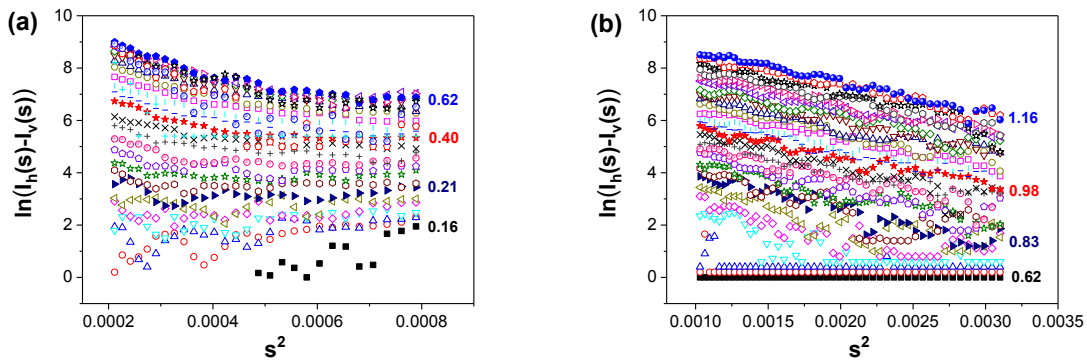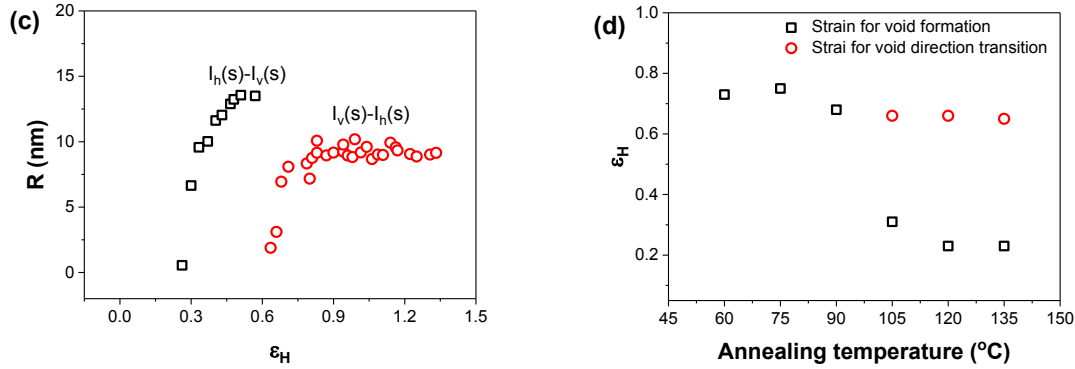
Figure 6-11 The logarithm of the corrected scattering intensity as a function of s^2 at different strains of PP120: **(a)** covers Hencky strains from 0.16 to 0.62 (formation of Type II voids) and **(b)** covers Hencky strains from 0.62 to 1.16 (direction transition for Type II voids). For clarification, the plots are vertically shifted; **(c)** The radius of gyration (R) as a function of the Hencky strain via the slope of **Figure (a)** and **(b)**; (d) The critical Hencky strain for the void formation and void direction transition of iPP with different annealing history during uniaxial stretching at 75 °C.

Type I exists in the sample with T_a lower than 90 °C, of which the critical strain for void formation is 0.73, 0.75, and 0.68 for PPna, PP75, and PP90. The longitudinal size of the voids is along the stretching direction once the voids is formed. Type II can be found in the sample with T_a higher than 105 °C, of which the longitudinal direction of the voids is perpendicular to the stretching direction once voids are formed, and transfers toward the stretching direction at a larger strain. The critical strain of type II void formation decreases slightly from 0.31 to 0.23 as T_a is increased from 105 °C to 135 °C. Meanwhile, the critical strain of the voids direction transition is around 0.66.

6.5.2 The evolution of the voids size

The evolution of the void size is shown in **Figure 6-12**. For PPna, $S_\parallel$ increases from 190 nm to 339 nm as the strain increases from 0.8 to 1.6. PP75 and PP 90 show a similar trend, but the slope decreases from 187 nm/1 (PPna) to 121 nm/1 (PP90). For PP105, PP120, and PP135, $S_\parallel$ increases from 35 nm to 82 nm and $S_\perp$ is around 198 nm in the small strain range. During the void direction transition, the extrapolation and fitting process does not work because no obvious streak signal could be recognized in the 2D-SAXS pattern. So no information about the void size is provided in the strain region of 0.4~0.8. As the void direction is totally transferred, $S_\parallel$ grows from 116 nm to 216 nm for PP105, from 111 nm to 195 nm for PP120,

and from 99 nm to 157 nm for PP135. The slope of the plot decreases from 111 nm/1 to 105 nm/1 and then further to 98. In addition, in the large strain range, $S_\perp$ is nearly the same for all samples and it decreases slightly from 68 nm to 55 nm. From **Figure 6-12** it can be found that $S_\parallel$ decreases with the increasing of annealing temperature, which is also found by Men.[215] In addition, the slope of $S_\parallel$ as a function of the strain decreases continually from 187 to 98, suggesting that a larger energy barrier needs to be overcome as the annealing temperature is increased. The possible reason for this lies in the difference of the number of voids per volume, which will be explored in the following part.
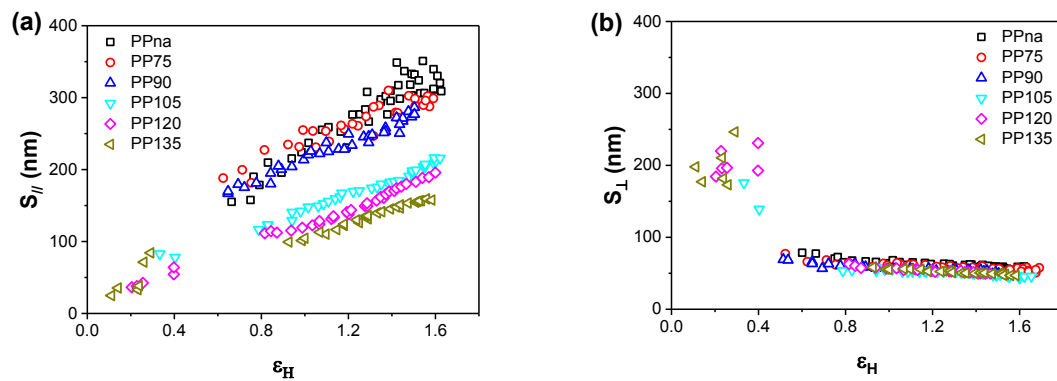
Figure 6-12 Evolution of **(a)** the void size along the stretching direction ($S_\parallel$) and **(b)** the void size perpendicular to the stretching direction ($S_\perp$) of iPP with different annealing histories uniaxial stretched at 75 °C.

6.5.3 The scattering invariant (*Q*) of the voids

Figure 6-13 plots the change of Q as a function of ε_H. Apparently, with the increase of T_a Q is enhanced greatly especially for PP105, PP120, and PP135, which meaning that the volume fraction of voids is greatly increasing. Due to that the size of the voids is decreased as shown in **Figure 6-12**, it can be inferred that the number of voids per volume is increased with annealing. As ε_H is larger than 1.35, a slight decrease shows up for PP105 which is caused by the thinning of voids. For PP135, the decrease of Q as ε_H exceeds 1.25 is probably caused partly by the void coalescence[216] and partly by the fact that the size of the void exceeds the detection resolution of SAXS.
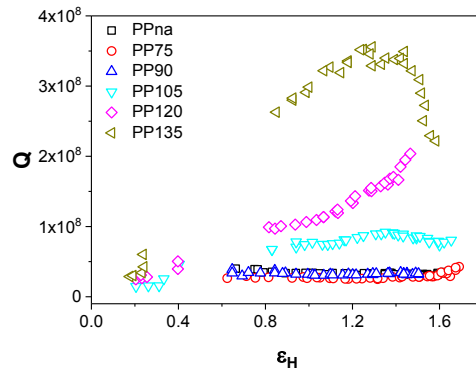
Figure 6-13 Evolution of scattering invariant (Q) of iPP with different annealing histories uniaxial stretched at 75 $^{\circ}$C.

6.5.4 The morphology of voids

The morphology of PPna with ε_H of 1.5, and PP135 with ε_H of 0.25 and 1.5 are provided in **Figure 6-14**. Two types of void can be clearly seen. For PPna with ε_H of 1.5, a few voids with their longitude direction along the stretching direction can be found. For PP135 with ε_H of 0.25, the number of voids is much larger than that in PPna with ε_H of 1.5. In addition, the longitude direction of the void is mainly perpendicular to the stretching direction. The average size in the long axis and short axis direction are 280 nm and 80 nm, which fits the result in **Figure 6-12**. For PP135 with ε_H of 1.5, abundant crazes consisting of voids and fibrillary links separating voids can be found. The direction of the longitude of the voids is transferred to the stretching direction. The SEM images in **Figure 6-14** coincide well with the results obtained from SAXS measurement where a smaller voids size and larger voids number exist in PP135 compared with PPna.
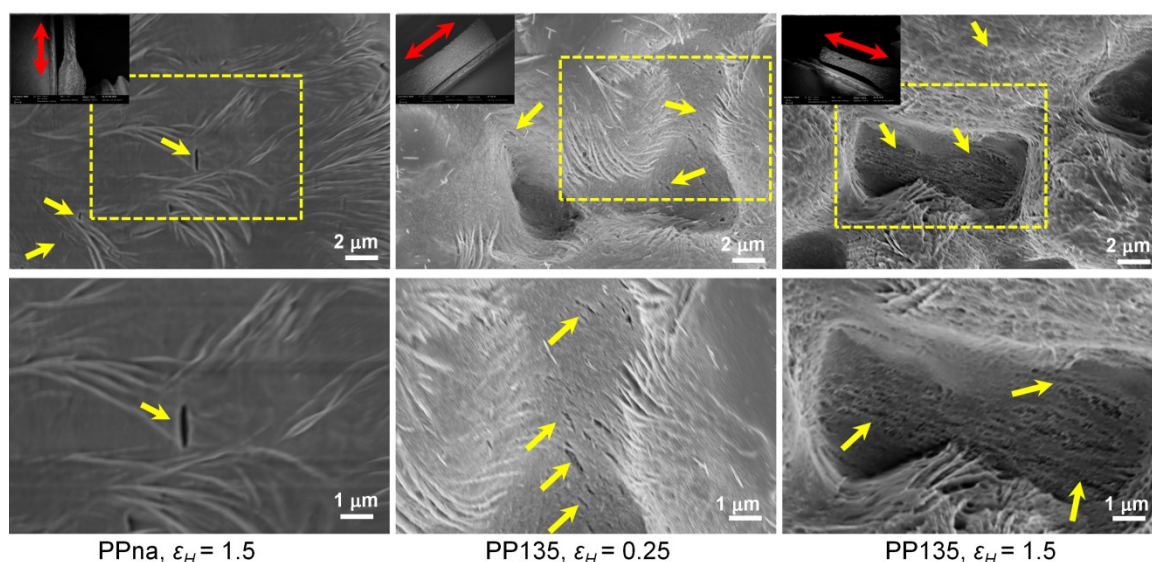
Figure 6-14 The morphology of PPna with ε_H of 1.5, and PP135 with ε_H of 0.25 and 1.5. The yellow arrows are referred to the void. Figures inserted in the left corner showing the sample geometry could provide the information about the stretching direction (indicated by the red arrow). The images on the second row are the enlargement of the square region in the images on the first row.

In the past few years the molecular origin of void formation was studied by different groups. Since the voids are formed mainly in the amorphous phase, the molecular origin of void formation was related to the molecular motion in the amorphous phase. In the work by Lu,[182] the void formation at large strain deformation was proposed to be a consequence of the disentanglement of the highly oriented amorphous network initiated by the breaking of interfibrillar tie chains. Whereas, Ge[217] proposed that disentanglement is not geometrically necessary to accommodate void propagation because the chains in deformed glassy polymers are constrained by their rheological tubes rather than by entanglements that act like discrete cross-links. And Ge proposed that clustering of the polymer chains into fibrils may be the mechanism of void formation without entanglement loss.[217] The molecular weight of PP135 with and without abundant cavitation is given in **Figure 6-15**. It is obvious that the molecular weight of the two samples overlaps quite well, suggesting that the breaking of polymer chains is not the compulsive condition for void formation. However, the conclusion by Ge was deduced from crazing behavior of the glassy polymer. In this study, the sample was stretched at 75 $^{\circ}$C which is much higher than the glass transition (around 0 $^{\circ}$C for crystallized iPP). At this temperature, the chains in the amorphous phase of the polymer will have a higher mobility. Therefore, no stringent conclusion concerning whether the polymer

chains are disentangled or not can be inferred from **Figure 6-15**. More work dealing with the molecular origin of void formation in semicrystalline polymers should be performed in the future.
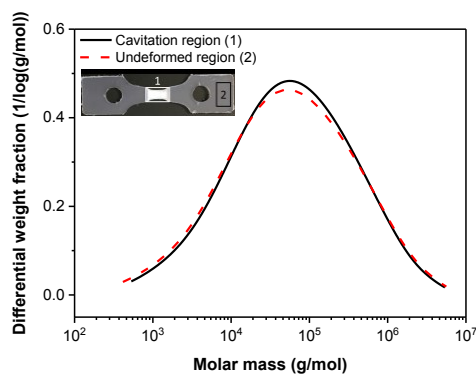
Figure 6-15 The molecular weight of iPP from the un-deformed region and stress-whitening region.

The existence of two types of voids might be related to very different local stresses in the amorphous phase. For the sample with an annealing temperature lower than 90 ^{o}C, Type I voids in the stretching direction are formed. The voids are induced in an oriented network in which the crystals serve as the skeleton and the polymer chains connect the crystals together. The amorphous phase is subjected to a strong constraint force in the direction perpendicular to the stretching direction, that's why the voids are oriented along the stretching direction. For the samples with an annealing temperature higher than 105 ^{o}C, the connection between the amorphous phase and the lamellae is stronger. The extension force is transmitted to the amorphous phase in a better way. Meanwhile, the lamellae are thicker and stiffer. Due to the restriction of the lamellae, type II voids are formed initially transversal to the stretching direction. As the strain increases, the voids come in contact with other ones nearby during the growth process and then coalesce with each other into larger voids, which were verified by Selles with the help of the magnified holotomography technique.[177] With the further increase of the strain, the lamellae are fragmented into blocks and oriented fibrillar structures are formed, hence the constraint force in the direction perpendicular to the stretching direction is enlarged. Therefore, the void direction transfers finally to the stretching direction.

6.6   Final discussion

On the basis of SAXS and WAXS results, the critical strains for lamellae deformation as well as void formation and growth of iPP with various annealing histories are summarized in

Figure 6-16. And the relationship between lamellae deformation and voids formation is also discussed here.
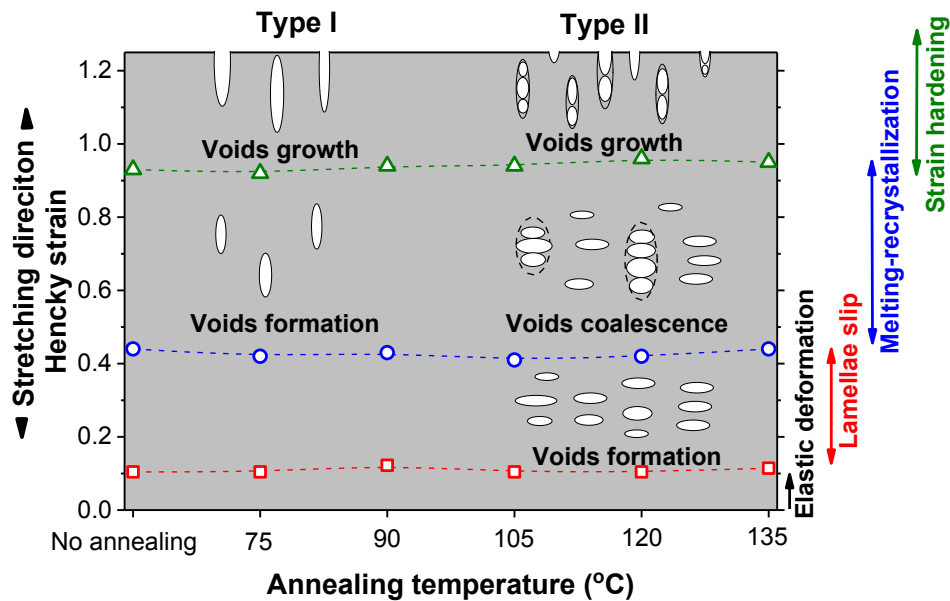
Figure 6-16 Critical strains for lamellae deformation as well as voids formation and growth for iPP with various annealing histories during uniaxial stretching at 75 °C.

Firstly, the lamellae deformation is revealed to proceed in the time scales of inter- and intra-lamellar slip, fragmentation, and melting-recrystallization separated by three critical strains which were rarely influenced by annealing. Strain I (0.1) marks the end of elastic deformation and the onset of intra-lamellar slip. Strain II (0.45) signifies the start of the recrystallization process, where the long period in the stretching direction begins to decrease from its maximum and the polymer chains in the crystal start to orient along stretching direction. The energy for the melting arises from the friction between the fragmented lamellae produced by inter-lamellar slip. Strain III (0.95) denotes the end of the recrystallization process. Beyond the strain of 0.95, the long period of the lamellae and the crystal size remain nearly unchanged. The newly formed lamellae serve as anchoring points for polymer chains in the amorphous phase during further stretching. The extension of the polymer chains between the lamellae triggers the strain hardening behavior.

Secondly, annealing significantly intensifies the formation of cavities by advancing the critical strain of voids formation and increasing the number of voids. For those samples annealed at a temperature lower than 90 °C, voids are formed between strain II and strain III. The voids are oriented in the stretching direction once they are formed. For samples annealed

at a temperature higher than 105 ^{o}C, voids are formed between strain I and strain II. In this case the voids are initially oriented with their longitude axis perpendicular to stretching direction and then transferred along the stretching direction via small void coalescence.

The existence of two types of voids might be related to very different local stresses in the amorphous phase. For the sample with an annealing temperature lower than 90 ^{o}C, voids are formed between strain II and strain III. During void formation the dominant lamellae deformation process is lamellae melting-recrystallization. Therefore the critical strain for void formation shows no obvious dependence on lamellae thickness, because most of the lamellae have been fragmented via intra-lamellar slip. In addition, as evidenced in **Figure 6-9Figure 6-9** The Herman's orientation factor (f_H) of **b**-axis and **c**-axis of the crystal during uniaxial stretching. the polymer chains in the crystal are oriented along the stretching direction. So the voids are induced in an oriented network in which the crystals serve as the skeleton and the polymer chains in amorphous phase connect the crystals together. The amorphous phase is subjected to a strong constraint force in the direction perpendicular to the stretching direction, that's why the voids are oriented along the stretching direction once the voids are formed. For the samples with an annealing temperature higher than 105 ^{o}C, the critical strain for type II void formation is located between 0.1 and 0.45. By annealing the lamellae are thicker and have a higher inter-lamellar slip resistance. Therefore, the connection between the amorphous phase and the lamellae is stronger. The extension stress is better transmitted to the amorphous phase. Due to the restriction of the lamellae, type II voids are formed initially transversal to the stretching direction. As the strain increases, the voids come in contact with other ones nearby during the growth and then coalesce with each other into larger voids, which were verified by Selles with the help of the magnified holotomography technique.[177] With the further increase of the strain, the lamellae are fragmented into blocks and oriented fibrillary structures are formed, hence the constraint force in the direction perpendicular to the stretching direction is enlarged. Therefore, the voids direction transfers finally to the stretching direction. During the further stretching process, the voids grow in the stretching direction and become thinner in the transverse direction.

Thirdly, the advancing of the voids formation by annealing influences neither the critical strains for lamellae deformation nor the final long period, the orientation of polymer chains or the crystal size. This is different from the results of the group of Rozanski.[65, 184, 218, 219] By controlling the state of the amorphous phase, a cavitation/non-cavitation iPP model system with an identical lamellae structure was obtained by Rozanski. They demonstrated that the

81

reduction of the crystallites of cavitating iPP was approximately 5 %-10% greater than in the case of the non-cavitating system, suggesting that the presence of cavities clearly facilitates generating instability and increases the intensity of the lamellae fragmentation process. The orientation degree of polymer chains (at the identical value of the local strain) is significantly higher in the case of cavitating iPP, because smaller crystallites present in the cavitating material will easily undergo tensile-induced rotation around the deformation direction, in contrast to the case of a non-cavitating material. Therefore, the key point is the question about factors contributing to the increase of the orientation of polymer chains in the crystal: rotation of fragmented crystallites or newly formed crystals by recrystallization with the polymer chains aligned along stretching direction. In our case, the recrystallization process is verified to take place in the strain range of 0.45~0.95. Consequently, the final long period, the orientation of polymer chains in the crystal, and the crystal size were controlled by the recrystallization process, which is scarcely influenced by void formation.

6.7   Conclusion

The lamellae deformation and cavitation behavior of annealed isotactic-polypropylene during uniaxial stretching were comprehensively investigated by in situ synchrotron small-angle *X*-ray and wide-angle *X*-ray scattering. On one hand, lamellae deformation was revealed to occur in the time scale of elastic deformation, intra-lamellar slip, and melting-recrystallization separated by three critical strains which were rarely influenced by annealing. On the other hand, annealing significantly intensified the cavitation behavior by decreasing the critical strain for the void formation and increasing the number of voids. Additionally, voids formation influences neither the critical strain values for lamellae deformation nor the final long period, polymer chains orientation or the crystal size. The final long period, polymer chains orientation in the crystal and the crystal size were determined only by the stretching temperature through the melting-recrystallization process. Since the recrystallization process is controlled mainly by stretching temperature, further work on the influence of stretching temperature on lamellae deformation and cavitation behavior is in progress. The work will be helpful to understand the relationship between the microstructure evolution and the mechanical properties of semicrystalline polymers during stretching.

7   Accelerating shear-induced crystallization and enhancing crystal orientation of iPP by controlling the morphology of N,N'-dicyclohexyl-2,6-naphthalene dicarboxamide[4]

Accelerating shear-induced crystallization and enhancing crystal orientation of isotactic-polypropylene (iPP) via controlling the morphology of N,N'-dicyclohexyl-2,6-naphthalene dicarboxamide (NJS) is reported in this chapter. By adjusting the final heating temperature, dotlike, needlelike, and treelike NJS are formed in the composite. Polymer chains with higher molecular weight are anchored on the surface of NJS due to selective absorption. During shear-induced crystallization, the anchoring points will inhibits the relaxation of oriented polymer chains once shear ceases. The reserved oriented polymer chains forms into shish to induce the formation of highly oriented "shish-kebab" structure. Since that the composite with treelike NJS provides the largest number of anchoring points, so it has the shortest crystallization induction time. In addition, the NJS branches detached from the tree orient themselves in the shear direction, facilitating greatly the crystal orientation in the composite. The results provide a possibility to use the nucleating agent more efficiently during shear-induced crystallization, which sheds light in the field of scientific research and industrial processing.

7.1   Introduction

Shear flow, which exists broadly in injection molding, extrusion, and fiber spinning, influences greatly the crystallization kinetic [220-222] and the crystalline morphologies [223-225] of semicrystalline polymers. The first evidence of shear-induced crystallization (SIC) was obtained by Pennings.[226] By means of stirring, Pennings proved that a highly oriented crystal morphology different from spherulites was formed, consisting of a long extended-chain crystal (shish) surrounded by chain-folded lamellae (kebab).[226] Normally, the shish serves as the nuclei and the kebab grows epitaxial on shish. So, the formation of shish is the key for the existence of shish-kebab structure. The thermodynamic mechanism responsible for the formation of shish is that via applying the flow field the entropy of polymer chains is reduced,[227, 228] which facilitates the nucleation process. From the molecular aspect, a few models have been proposed. The first model is that polymer chains with a molecular weight higher than the critical molecular weight (M^*) will undergo a coil-to-stretch transition.[229] The fully stretched chains are assigned to form shish. However, with the help of deuterium labeling and small-angle neutron-scattering, Kimata et al.[221] found that long chains are not overrepresented in the shish relative to their concentration in the material as a whole. In the meantime, Li et al.[230] found that the critical strain for shish formation in the polyethylene (PE) melt is 1.57. The value is much smaller than the critical strain needed to fully stretch the polymer chains, but enough to ensure full extension of chain segments locked between two adjacent entanglement points. Therefore, it is proposed that the formation of shish stems from stretched polymer chains network rather than coil-stretch transition.[231, 232]

The shish formation is sensitive to the addition of fillers, due to the interaction between polymer chains and fillers.[233-236] And the interaction is influenced greatly by the morphology of fillers.[237-242] To name a few, Byelov et al.[243] observed that compared to isotopic cis-endo-bicyclo[2.2.1]heptane 2,3-carboxylate disodium salt, platelet-like talcum powder or elongated 2,20-methylene bis(4,6-di-tert-butylphenol) phosphate sodium salt lead to greater numbers of shear-induced nuclei. Xu et al.[240] found that both one-dimensional carbon nanotubes (CNTs) and two-dimensional graphene nanosheets (GNSs) could serve as nucleating agents in accelerating the crystallization kinetics of poly(l-lactide) (PLLA); but the ability of CNTs to induce crystallization was stronger than that of GNSs.

Although fruitful results have been obtained in this field, some of the results are controversial with each other. For example, Feng et al.[244] demonstrated that sorbitol-based nucleating agents could stabilize the shear-induced shish nuclei. Patil et al.[242] observed that single

wall carbon nanotubes (SWCNT) led to increased shish formation, while zirconia nanoparticles destabilized shish formation. Phillips et al.[235] found that the shish relaxes faster in the presence of fillers because that the fillers induce lower molecular weight chains to participate in shish formation. The apparent controversial results may be caused by the fact that not only the morphology of the filler is changed, but also the substance of the fillers is different in previous reports.

Recently, the self-assembly process of N,N'-dicyclohexyl-2,6-naphthalene dicarboxamide (NJS) has caught a lot of attentions.[245-248] The self-assembly of NJS is proposed to proceed by dissociation/association of hydrogen bonds connecting the small molecules in solid NJS.[247, 248] During heating, the dissociation of hydrogen bonds results in the diffusion of small NJS molecules into iPP matrix. By controlling the final heating temperature (T_f), different amount of NJS is reserved in iPP melt. Upon cooling, the diffused small molecules tend to grow on the residuary NJS particles by hydrogen bonds association.[248-250] Via self-assembly, NJS can form into dotlike, needlelike, and treelike morphologies. The various morphologies exhibited by NJS endow a possibility to investigate the role of filler morphology in shear-induced crystallization of semi-crystalline polymer.

In this chapter, the interaction between polymer chains and NJS is studied based on its rheological behavior. Then the shear-induced crystallization behavior of iPP/NJS composite with dotlike, needlelike, and treelike NJS is investigated. The microstructure and morphology of the composite after crystallization are also checked. The results prove that by controlling the morphology of NJS, distinctly different crystallization kinetics and lamellae orientation degree are obtained, which is of great scientific and industrial importance. In addition, the possible mechanism responsible for the crystallization is given.

7.2   The self-assembly process of N,N'-dicyclohexyl-2,6-naphthalene dicarboxamide

Figure 7-1a shows the morphology of NJS during the heating process. At 260 ^{o}C, NJS forms dotlike particles. The particles are randomly distributed in the iPP matrix. As the final heating temperature (T_f) increases, the density of the particles decreases gradually. At 280 ^{o}C, the majority of NJS disappears. And when T_f is higher than 290 ^{o}C, NJS vanishes totally in the iPP matrix. As the matrix is cooled from different T_f, three distinct types of NJS morphology can be found (see **Figure 7-1b**), which are dotlike (260 ^{o}C and 270 ^{o}C), needlelike (280 ^{o}C), and treelike (290 ^{o}C, 300 ^{o}C, and 310 ^{o}C). It is obvious that the morphology of NJS after cooling heavily depends on the residual part before the cooling process. In the work by Feng

[248], the self-assembly process of N,N′-dicyclohexylterephthalamide (DCTH) in iPP matrix was investigated by Fourier transform infrared spectroscopy (FTIR). It was revealed that the self-assembly of DCTH was related to the dissociation/association of hydrogen bonds and the conformational change of DCTH molecules.
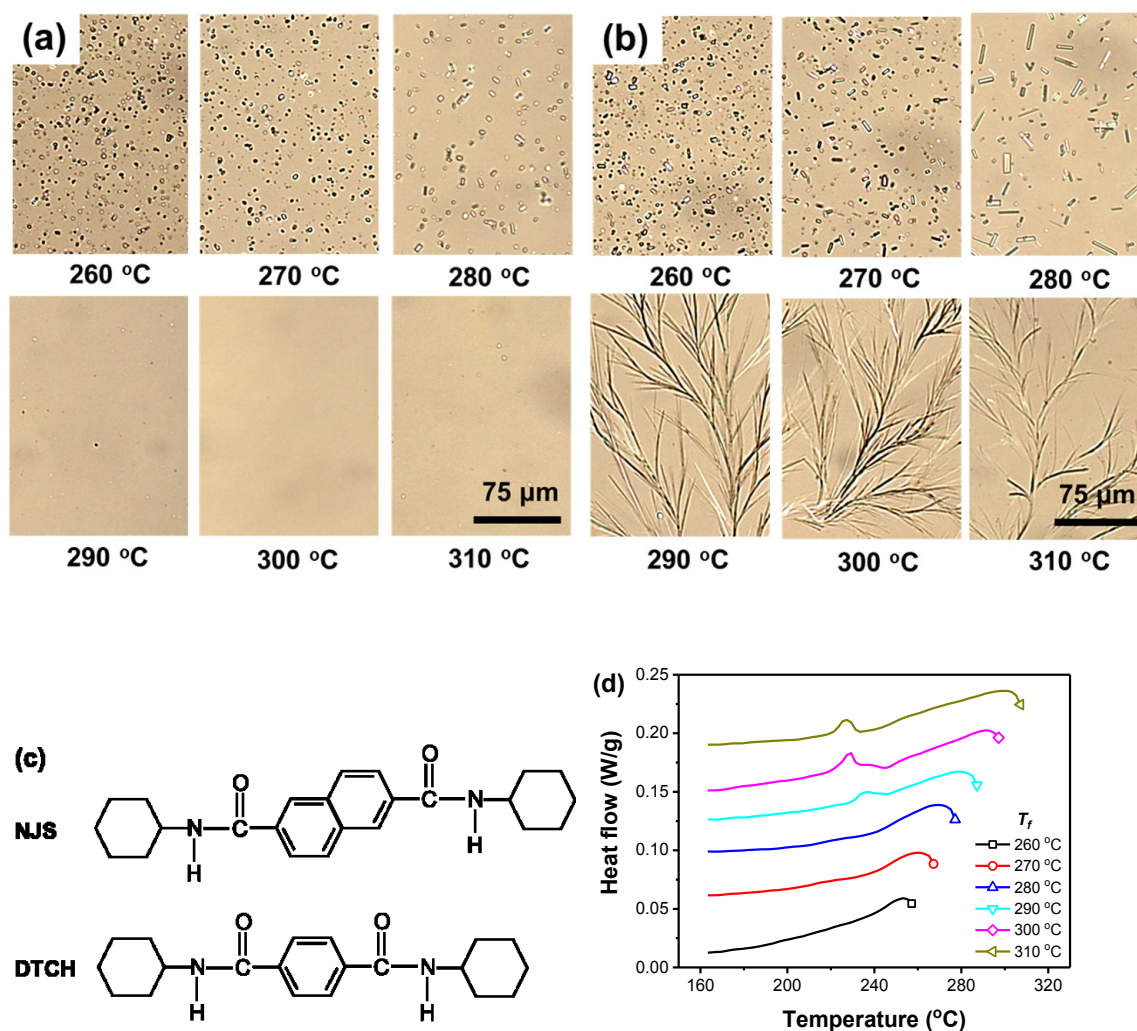
Figure 7-1 (a) Optical micrographs of the NJS morphology at different temperatures during the heating process; **(b)** the morphology of NJS at 160 ^{o}C cooled from different final heating temperatures (T_f); **(c)** the molecular formula of NJS and DCTH; **(d)** the heat release of NJS during the cooling process of iPP/NJS composites after annealing at different T_f. For clarification, the curves are vertically shifted.

The molecular formulas of NJS and DCTH are quite similar (see **Figure 7-1c**). Both of them comprise amido bond and the molecules are connected by hydrogen-bonds. Therefore, it is reasonable to infer that the dissolution of NJS in **Figure 7-1a** could be regarded as the dissociation of hydrogen-bonds upon heating. The dissociation releases the small NJS

molecules into the matrix. The higher the temperature, the more NJS dissolves. Because of the hydrogen-bonds, the small dissolved NJS molecules tend to crystalize on the remaining NJS particles during the cooling process. As a consequence, the length of NJS particles grows gradually while the number of NJS particles remains nearly unchanged, resulting in the formation of needlelike NJS. The crystallization process of NJS during cooling is also confirmed by DSC, see **Figure 7-1d**. When T_f is lower than 280 ^{o}C, a broad diffuse crystallization peak shows up on the curve, indicating the gradual growth of NJS. However, when T_f is higher than 290 ^{o}C the crystallization peak is quite sharp, suggesting the crystallization process. The crystallization peak shifts towards lower temperatures with increasing T_f, which is probably caused by the more intense dissolution of mobile NJS small molecules in the iPP.

The length of NJS particles as a function of temperature during cooling is provided in **Figure 7-2**. When T_f is lower than 270 ^{o}C, a slight increase of the NJS length can be found. This means that the morphology of NJS remains dotlike during cooling. When T_f reaches 280 ^{o}C, the length of NJS increases noticeably from 4 μm to 11 μm. In addition, it can be found that the growth of NJS completes before the temperature reaches 205 ^{o}C during cooling. As T_f is higher than 290 ^{o}C, no residual NJS exists in iPP matrix. Once the nucleating point in the matrix is formed, the small NJS molecules crystalize on the nucleating point rapidly, leading to the formation of treelike NJS. Therefore, the length of the treelike NJS is not displayed in **Figure 7-2**. The growth of the treelike NJS during cooling is presented in a more vivid way in Video S1 of the Supporting Information of Ref. [245].
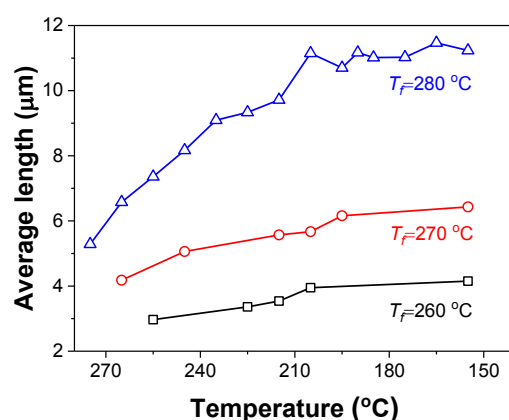
Figure 7-2 The length of the dotlike and needlelike NJS as a function of temperature during the cooling process.

7.3 Rheological behavior

7.3.1 Frequency sweep test

Figure 7-3 provides the plot of G' as a function of ω. At small frequency ($\omega < 0.3$ rad/s), composites with dotlike or needlelike NJS have a smaller G' than pure iPP. The slope in the low frequency regime is larger than that of pure iPP. As the morphology of NJS changes from dotlike to needlelike, the slope decreases from 1.67 to 1.56. The composites containing treelike NJS have a larger G' and smaller slope (about 0.8) in the low frequency regime than that of pure iPP, indicating the enhancing effect of treelike NJS on G'. The enhancement is typical for polymer based composites comprising a filler network.[251]
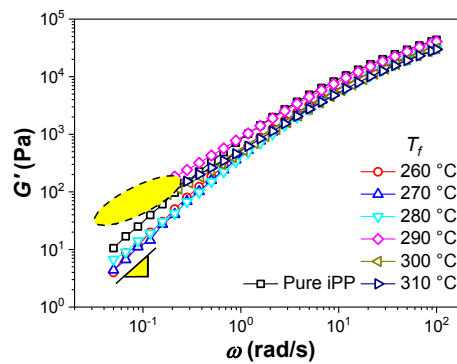
Figure 7-3 G' as a function of ω of pure iPP and iPP/NJS composites cooled from different T_f.

7.3.2 Strain sweep test

Figure 7-4 presents the plot of G' as a function of γ during strain sweep. Due to the strain induced disentanglement of polymer chains, a drastic drop of G' shows up as strain amplitude exceeds a critical strain (γ_c). The γ_c is about 166 % for pure iPP. For the composites with dotlike or needlelike NJS, the γ_c is nearly the same with that of pure iPP, indicating that the addition of dotlike or needlelike NJS has a negligible influence on the disentanglement of polymer chains, although the accelerated disentanglement of polymer chains by slip at the polymer/filler interfaces[252] or strain amplification effect[253] was previously reported. The composites with treelike NJS exhibit two γ_c. The first γ_c is at only 6 %, and the second γ_c is 277 %. The appearance of the first γ_c can be ascribed to the breakdown of NJS network, which is frequently observed in the composite with a high volume ratio of fillers.[254] The breakdown of NJS network is caused by the de-bonding of NJS branches from the tree upon dynamic shear flow. The second γ_c should be ascribed to the disentanglement of polymer

88

chains in the matrix. In addition, it is interesting to note that all iPP/NJS composites have lower G' than pure iPP. For instance, at the γ of 0.1 %, the G' of pure iPP and iPP/NJS composites are 671 Pa and 434, 419, 378, 614, 495, 425 Pa as T_f increases from 260 °C to 310 °C. This weakening effect is controversial with the common case where the adding of fillers leads to a higher G' than pure polymer.[255] The abnormal decrease of G' should be caused by the special interaction between polymer chains and NJS. The reason responsible for that will be further discussed below.
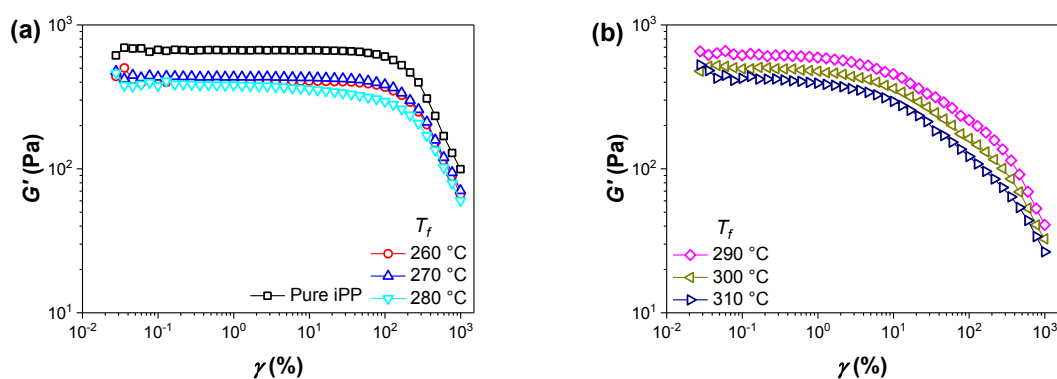
Figure 7-4 G' as a function of strain amplitude (γ) of pure iPP and iPP/NJS composites cooled from T_f.

7.3.3 Steady-state shear test

In **Figure 7-5** a comparative study of the steady-state shear viscosity ($\eta(\dot{\gamma})$) and dynamic complex viscosity $\eta^*(\omega)$ is provided. The Cox-Merz rule holds for pure iPP and the composite with dotlike NJS. For the composite with needlelike NJS, a decrease of η shows up as $\dot{\gamma}$ overpasses 10^{-2} as a result of the preferential orientation of NJS in the shear direction. For the composite with treelike NJS, η is decreased drastically during the steady-state shear test. And obviously, Cox-Merz rule fails for the iPP/NJS composites with treelike NJS. As shown in **Figure 7-4**, the treelike NJS is stable unless γ is smaller than 6 %. So, herein it is reasonable to relate the failure of the Cox-Merz rule with the disruption of the network of treelike NJS.[256] During disruption the NJS branches are detached from the tree, leading to the formation of tremendous needlelike NJS in the melt. And the orientation of needlelike NJS gives rise to the obvious decrease of η with a function of $\dot{\gamma}$.
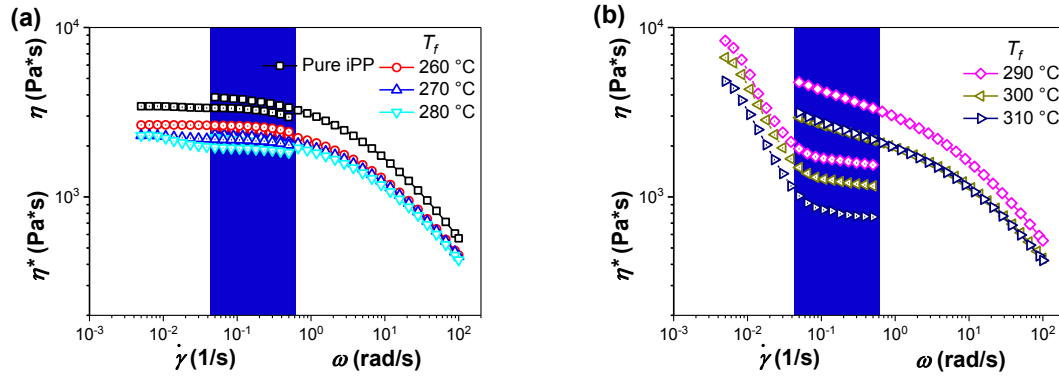
Figure 7-5 Steady-shear viscosity (η) and complex viscosity (η^*) of pure iPP and iPP/NJS composites cooled from different T_f.

In **Figure 7-5**, it can be also found that compared with pure iPP, the viscosity of the composite is decreased, which coincides with the decrease of G' in **Figure 7-4**. The reduction of viscosity may facilitate polymer processing procedures. But it is quite abnormal since that according to Einstein,[257] the addition of rigid particles to a liquid will lead to an increase in viscosity. The decreased viscosity in iPP/NJS composites can be understood by the selective adsorption mechanism proposed by Jain.[258] Based on the selective adsorption mechanism, the anchoring of polymer chains on the surface of fillers happens in the following way: at the beginning, a layer of polymer chains is formed surrounding fillers rapidly. The molecular weight distribution in the layer is the same as the matrix. However, polymer chains in the layer are in a non-equilibrium state and they are attached to the surface of fillers by anchoring point. A higher molecular weight gives rise to more anchoring points; subsequently, polymer chains with low molar mass move away from the layer into the matrix because they have less anchoring points on the surface of fillers. In the meantime, the higher molar mass chains are attached to the surfaces due to the increased anchoring points; finally, the matrix of the composite is composed of polymer chains with lower molecular weight. According to the power law, the zero-shear viscosity decreases with molecular weight with a power of 3.4. Consequently, the viscosity of the composite is lower than that of pure iPP.

As the morphology of NJS changes from dotlike to needlelike, the viscosity of the composite is further decreased as shown in **Figure 7-5**. This is because that a larger length will provide more anchoring points for polymer chains. In the composite with treelike NJS, the network of treelike NJS is disrupted upon the shear flow. The broken of NJS network leads to the detachment of branches from the tree. Therefore, abundant needlelike NJS are formed in the sheared melt. The drastic increase of the number of needlelike NJS further enlarges the

anchoring possibility of polymer chains on the surface of NJS. Consequently, the composite with treelike NJS owns the lowest viscosity.

7.4 Shear-induced crystallization

7.4.1 Crystallization kinetics studied by rheological method

Figure 7-6 shows the changes of G' with the crystallization time at 142 $^{\circ}$C. The increase of G' can be correlated to the growth of crystals.[255, 259] Generally, the curves show an evolution from the initial low plateau value at the beginning of crystallization to a rapid increase, and then approaching a plateau value at the ending of the crystallization range, which is similar with the evolution trend reported by other researchers.[237, 260] The onset time for the rapid increase is defined as the nucleation induction time (t_0).[261] For pure iPP, no crystallization happens during the test. The composite with dotlike or needlelike NJS owns a t_0 of 620 s, suggesting the accelerating effect of NJS on the shear-induced crystallization behavior of iPP. As the morphology of NJS changes into treelike, t_0 is decreased drastically to 250 s, indicating a stronger accelerating effect of treelike NJS on the shear-induced crystallization kinetics of iPP.
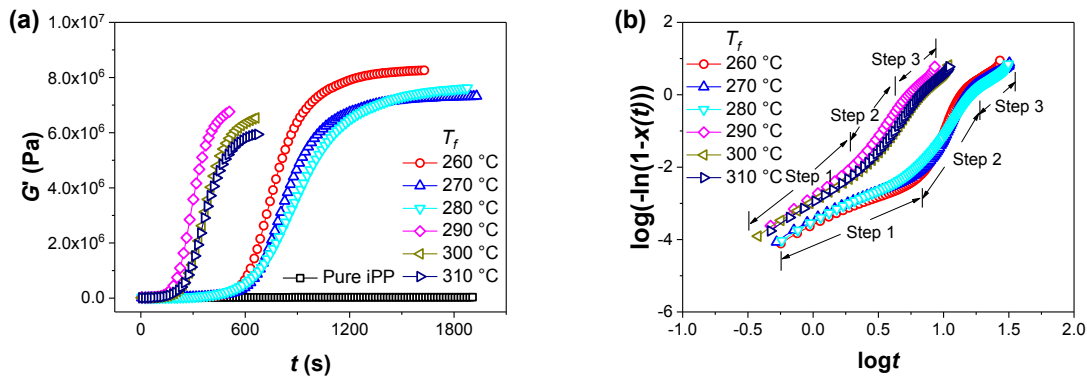
Figure 7-6 (a) G' as a function of crystallization time (t) during isothermal crystallization after shear of pure iPP and iPP/NJS composites with different T_f; **(b)** Avrami plots during isothermal crystallization after shear of pure iPP and iPP/NJS composites with different T_f. The shear rate is 1 s^{-1}, the shear duration is 10 s and the crystallization temperature is 142 $^{\circ}$C.

The crystallization kinetics of the composite can be quantitatively described by the Avrami equation,[262]

$$\ln(-\ln(1-x(t))) = n\ln t + \ln K \qquad \textbf{Equation (7-1)}$$

where K is the growth function, n is the Avrami exponent, and $x(t)$ is the relative crystallinity. $x(t)$ is normally estimated by logarithmically normalizing G':[263, 264]

$$x(t) = \frac{\log G'(t) - \log G'_{min}}{\log G'_{max} - \log G'_{min}}$$
Equation (7-2)

where G'_{min} and G'_{max} are the initial and ending plateau of the storage modulus, $G'(t)$ is the instant storage modulus. The Avrami plots of the composite are given in **Figure 7-6b**. It is obvious that the whole crystallization process could be divided into three steps: step 1 can be regarded as the primary crystallization stage, i.e., the formation of nuclei and their subsequent growth induced by the systematic effect of shear flow and NJS; step 2 can be ascribed as the crystallization process of the iPP matrix located between NJS, and step 3 is the occurrence of secondary crystallization (i.e., impingement of the spherulites and/or insertion of new crystals in between the already existing ones) is characterized by a deviation from linearity in the Avrami plots.

Table 7-1 The Avrami exponent n obtained from the Avrami plot of the composite with various T_f during the isothermal crystallization after shear.

	T_f (°C)					
	260	270	280	290	300	310
n (step 1)	1.54	1.52	1.67	2.51	2.19	2.39
n (step 2)	9.06	7.69	5.36	5.06	5.10	5.16

The Avrami exponents (n) during step 1 and step 2 are summarized in **Table 7-1**. In step 1, n is between 1 and 2 as the morphology of NJS changes from dotlike to needlelike. The composites with treelike NJS own an n value between 2 and 3. In step 2, n decreases from 9 to 5.4 as NJS changes from dotlike to needlelike. And n is *ca*. 5.1 if NJS is in the form of treelike. Generally, Avrami exponent was extensively adopted to describe the dimensionality of crystal growth under static condition. And the value of n implies the growth geometry of the crystal. For instance, *n=2* means a two-dimensional lamellar growth and *n=3* means a three-dimensional in case that there are heterogeneous nucleation points under static condition. However, this classic explanation may not fit in our case since that n in step 2 is far beyond 4. An n value larger than 4 has been also reported elsewhere.[265] Therefore, the physical background of n during shear-induced crystallization of polymer composites remains an open

topic. Instead of the crystal growth geometry, another possible physical meaning of *n* proposed recently is the number of growth points in the crystals.[265-268] The larger the *n* values, the bigger the numbers of growth points. In fact, the second explanation is not contrary to the classic one. For instance, *n*=3 means that the crystal grows in the spherulite geometry; and it can be also understood in the following way: there are more branches of lamellae in the spherulite, which gives rise to a larger number of growth points. Therefore the *n* value of the spherulite should be larger.[267] Based on the second explanation, it can be inferred from **Table 7-1** that in the primary crystallization stage the number of growth points is the largest in the composite with treelike NJS, and smallest in the composite with dotlike NJS. In step 2, the *n* value is much larger than that in the primary crystallization, due to the growth of spherulite induced by thermal nucleation. During the growth of the spherulite, the existed lamellae can serve as the nucleation points to trigger the formation of new lamella. Therefore, the number of nucleating points is increased greatly and the Avrami exponents are higher. In addition, compared with the composite with treelike NJS, less iPP matrix is consumed in the primary crystallization of the composite with dotlike NJS, so more nucleation points are formed due to the growth of spherulites. Therefore, the n value for the composite with dotlike NJS is even higher.

7.4.2   In-situ SAXS measurement

The microstructure evolution during crystallization was monitored by in-situ 2D-SAXS measurements. For clarification, the schematic drawing of the sample arrangement is provided in **Figure 7-7a. Figure 7-7b** presents some selected 2D-SAXS patterns of pure iPP, and the composites with T_f of 260 $^{\circ}$C as well as 300 $^{\circ}$C during crystallization. The 2D-SAXS pattern at 0 s corresponds to an amorphous melt. The opaque scattering ring comes from the Kapton window. No lamellae scattering can be found through the whole process of pure iPP, indicating that no crystallization happens. For the composite with T_f of 260 $^{\circ}$C, the lamellae scattering shows up at 880 s after shear ceases. The scattering is mainly focused on the meridian, indicating that the normal of lamellae is aligned in the shear direction. With increasing crystallization time, the elliptic 2D-SAXS pattern transforms gradually into a spindle shape. in addition, the scattering intensity is enhanced. For the composite with T_f of 300 $^{\circ}$C, the lamellae scattering shows up in a shorter time (440 s). The scattering intensity is focused on the meridian. And the 2D-SAXS pattern develops finally into "two-lobes" shape, indicating that the lamellae have a wide distribution of periodicity and lateral size.[269] In all

SAXS patterns, no equatorial streak can be found, suggesting that no row-nuclei (shish) can be detected. The absence of shish is probably because that the size of the shish is too small and beyond the detection limit of 2D-SAXS.[270]
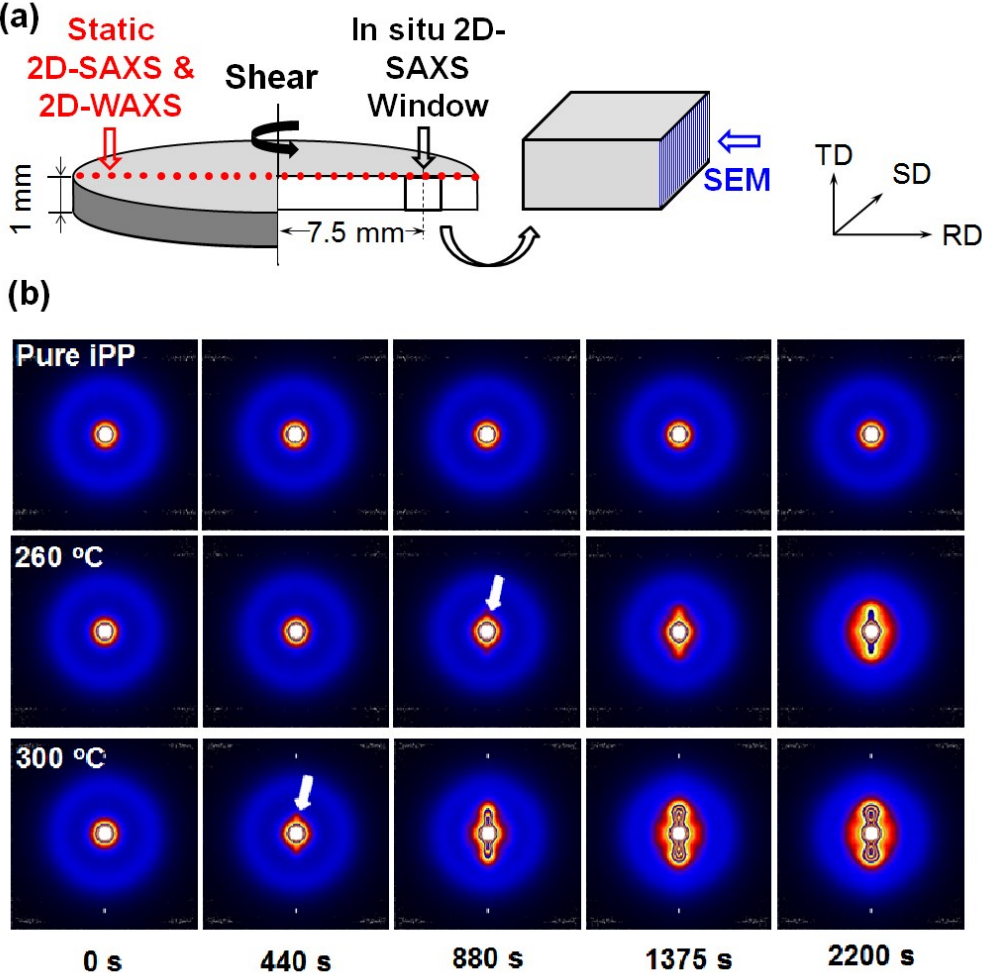
Figure 7-7 (a) The schematic drawing of the sample arrangement during in-situ 2D-SAXS measurements; **(b)** representative 2D-SAXS patterns during isothermal crystallization of pure iPP, iPP/NJS composites with T_f of 260 °C and 300 °C. The scale is linear 150, the size of the pattern is $0.32 \ nm^{-1} \times 0.32 \ nm^{-1}$, and the shear direction is vertical.

The evolution of the scattering invariant (*Q*) with crystallization time is given in **Figure 7-8a**. As expected, the *Q* of pure iPP stays constant in the whole process indicating that no crystallization happens, which coincides well with the rheological results in. The crystallization induction time in **Figure 7-8a** is 930 s for the composite with dotlike NJS, and 430 s for the composite with treelike NJS. The results here verify that the composite with treelike NJS owns the shortest crystallization time. However, the crystallization induction

times here are larger than those obtained in the rheological test, which are 620 s and 250 s, respectively. The discrepancy lies in the different settings and sensitivity of the experimental devices during rheological test and in-situ SAXS measurements. To be more specified, during rheological test the sample is placed between two parallel plates, the shear rate in the plate increases gradually in the radius direction. So the crystallization process is faster in the region where the shear rate is larger. In addition, the G' detected is an averaged value of the whole plate. However, during in-situ SAXS measurements, the X-ray beam is located in the region where the shear rate is 7.5 s^{-1}. And the size of the X-ray beam is only 23×13 μm^2. So, the crystallization kinetics obtained by in-situ SAXS measurement only represents the crystallization behavior in a limited defined region, but not the whole sample.
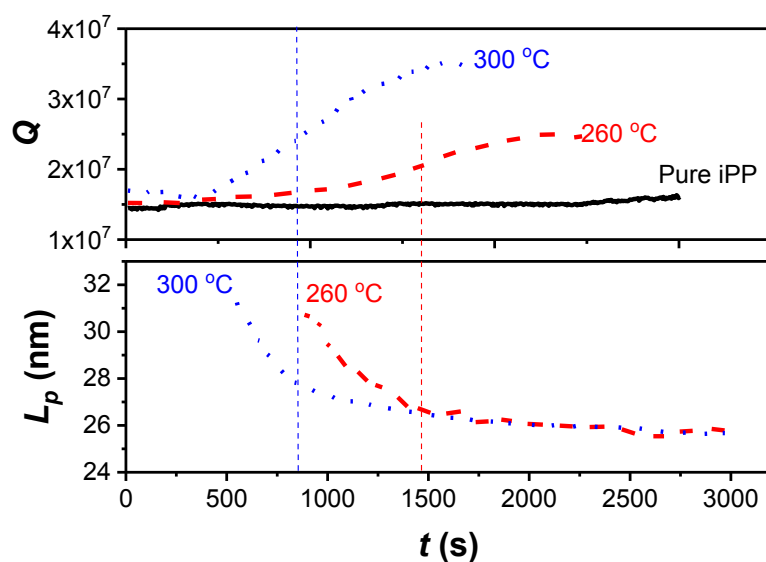
Figure 7-8 (a) The evolution of scattering invariant (Q) and **(b)** the long period (L_p) of iPP/NJS composite with T_f of 260 °C and 300 °C during isothermal crystallization after shear.

The evolution of the long period (L_p), comprising one crystalline phase and one amorphous phase, during crystallization are provided in **Figure 7-8b**. The multi-step crystallization process showed in **Figure 7-6** is also found in **Figure 7-8b**. In the primary crystallization stage, Q is increased gradually, but L_p is decreased drastically to a plateau. This suggests that in the primary crystallization stage nucleation is the dominant process. The decrease of L_p is caused by the inserting of newly formed lamellae into the existed lamellae. In step 2, L_p is changed slightly, but Q is increased continually, suggesting that in this crystallization stage the increase of Q is mainly caused by lamellae thickening.

7.4.3 Microstructure of iPP after shear-induced crystallization

The crystal form, crystal orientation, and lamellae arrangement of pure iPP and the composites with dotlike or treelike NJS after shear-induced crystallization are studied in this section. On the 2D-WAXS pattern of iPP/NJS with treelike NJS, a few crystal planes can be found, which are $(110)_\alpha$, $(300)_\beta$, $(040)_\alpha$, $(130)_\alpha$, $(117)_\gamma$, $(111)_\alpha/(311)_\beta$ and $(\bar{1}31)_\alpha$ from inner to outer region of the pattern (see **Figure 7-9**). Among the crystal planes, $(300)_\beta$ and $(041)_\beta$ belong to β-iPP, $(117)_\gamma$ belongs to γ-iPP, the others are ascribed to α-iPP. The scattering of the crystal planes is focused at specified angles due to the crystal orientation. For instance, the scattering of $(300)_\beta$ crystal plane is focused on the equator. But the scattering of $(110)_\alpha$ crystal plane can be found not only in the equator direction but also in the direction 12.5° off to the meridian, because of the unique "cross-hatched" structure of α-iPP. In the "cross-hatched" structure, the "daughter" lamellae grow epitaxial on the "mother" lamellae. The angle between the normal of "daughter" and "mother" lamellae is about 80°.[8] On the 2D-WAXS pattern of the composite with dotlike NJS, the orientation of the crystal is greatly weakened. On the 2D-WAXS pattern of pure iPP, no crystal orientation could be found. In addition, $(300)_\beta$ reflex is absent in pure iPP, implying that no β-iPP are formed.
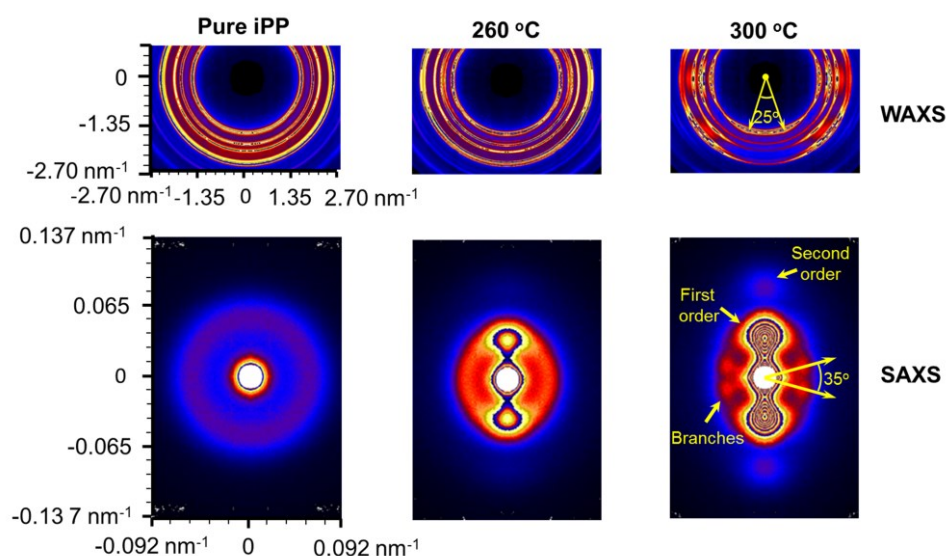
Figure 7-9 Selected 2D-WAXS and 2D-SAXS patterns of pure iPP, iPP/NJS composites with T_f of 260 °C and 300 °C after shear-induced crystallization.

On the 2D-SAXS patterns, the information about the lamellar arrangement can be obtained. Starting from the iPP/NJS composite with treelike NJS, it can be found that the scattering is focused on the meridian. In addition, a second order scattering appears in the meridian,

implying that lamellae are arranged in a highly ordered way. What's more interesting, the scattering from the "daughter" lamellae can be found in the direction 17.5° off to the equator, which is different with 12.5° in the 2D-WAXS pattern. The deviation is probably caused by the different resolution and detecting scales of 2D-WAXS and 2D-SAXS.[270] It is well known that WAXS provides the information of the crystal, which is normally in the scale of an angstrom. But 2D-SAXS shows the information of the lamellae in the scale of a nanometer. As the morphology of NJS in the composite changes from treelike to dotlike, the second order scattering and the scattering from the "daughter" lamellae disappear, indicating a less ordered arrangement of lamellae. In pure iPP, the scattering is a homogeneous ring, which means that the lamellae inside are randomly distributed.

The relative content of β-iPP (K_β) distribution on the sheared sample is provided in **Figure 7-10a**. In pure iPP, no β-iPP can be found. In the composite with dotlike NJS, K_β is 0.45 as shear rate is lower than 0.5 s^{-1}. With the increasing of shear rate, K_β decreases obviously and reaches 0.03 as shear rate is 5.5 s^{-1}. Finally K_β keeps constant as shear rate exceeds 5.5 s^{-1}. In the composite with treelike NJS, only trace amount of β-iPP could be found. The drastic decrease of K_β with increasing shear rate in the composite with dotlike NJS and suppressing of β-iPP formation in the composite with treelike NJS can be understood by the following explanation: during shear-induced crystallization, shear-induced nuclei are formed in the melt.[271, 272] The shear-induced nuclei will trigger the formation of α-iPP, therefore the growth of β-iPP will be depressed. With the increase of shear rate, the number of shear induced nuclei will be increased, leading to the decreasing of K_β.
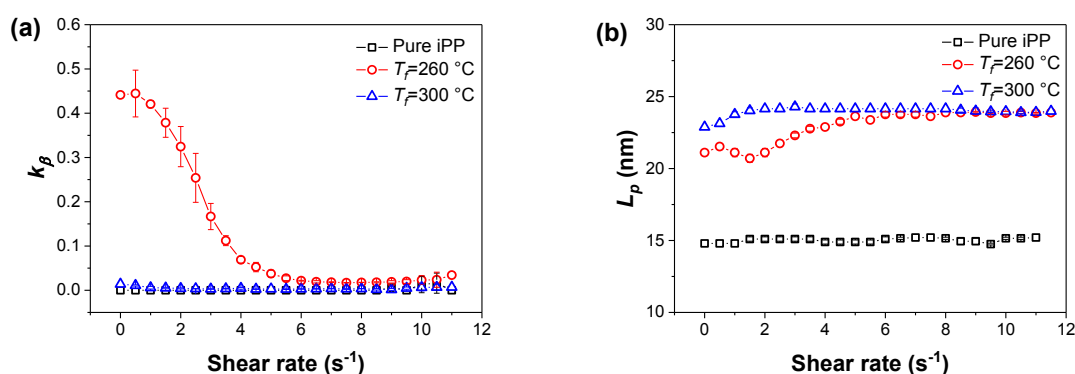
Figure 7-10 (a) The relative content of β-iPP (K_β) and **(b)** the long period (L_p) of pure iPP, iPP/NJS composites with T_f of 260 °C and 300 °C after shear induced crystallization.

In **Figure 7-10b**, L_p as a function of shear rate is provided. In pure iPP, L_p is 14.8 nm in the whole range. The composites own a much larger L_p compared to pure iPP. In the composite with dotlike NJS, L_p is 21.1 nm as the shear rate is 0. L_p increases gradually and reaches a plateau of 23.6 nm at the shear rate of 6 s^{-1}. In the composite with treelike NJS, L_p increases from 22.9 nm to 24.2 nm and stays unchanged as shear rate is higher than 2 s^{-1}.

The Hermanns' orientation factor of the crystal is given in **Figure 7-11.** It shows that in pure iPP, the orientation of polymer chains in the crystal is very weak. In the composite with dotlike NJS, f_{Hc} increases slightly from 0.23 to 0.39 as the radius is increased from 0 to 6 mm. In the composite with treelike NJS, f_{Hc} increases drastically from 0.24 to 0.66 as the radius is increased from 0 to 3 mm. The results in **Figure 10** prove that during shear induced crystallization, the addition of NJS can enhance the crystal orientation. And the composite with treelike NJS shows the highest crystal orientation.
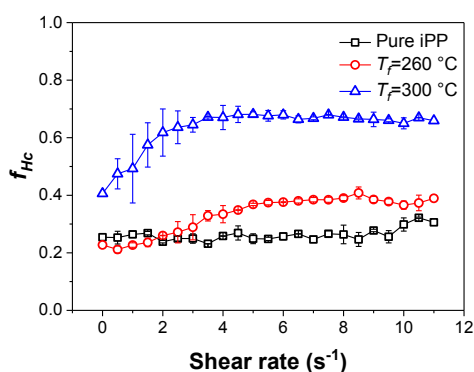
Figure 7-11 Hermans orientation factor of the crystal and the lamellae in pure iPP and iPP/NJS composites with T_f of 260 ^{o}C and 300 ^{o}C.

7.4.4 The morphology of the sample

The morphology of the composite with dotlike and treelike NJS is shown in **Figure 7-12**. In "TD-SD" plane, lamellae are distributed randomly in the composite with dotlike NJS. And dotlike NJS can be found without preferential orientation. Whereas, in the composite with treelike NJS, highly oriented needlelike NJS (indicated by the yellow arrow) oriented along the shear direction can be found, verifying that NJS branches are detached from the tree upon shear flow evidenced in the steady-state shear test. In addition, the density of the lamellae is higher than that in the composite with dotlike NJS, indicating that more nucleating points are formed.
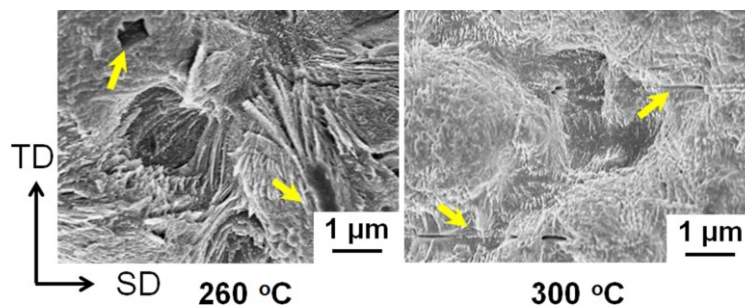
Figure 7-12 The morphology of iPP/NJS composites with T_f of 260 $^{\circ}$C and 300 $^{\circ}$C after shear-induced crystallization. The shear rate is 1 s^{-1}. TD is short for "thickness direction", RD is short for "radius direction", and SD is short for "shear direction".

7.4.5 The crystallization mechanism

The results prove that the addition of NJS could accelerate the shear-induced crystallization of iPP and enhance the crystal orientation. What's more, the crystallization kinetics and the crystal orientation are greatly influenced by the morphology of NJS: the composite with treelike NJS has the shortest crystallization induction time and largest crystal orientation. The mechanism responsible for that is given below, and a schematic illustration of the mechanism is shown in **Figure 7-13**.
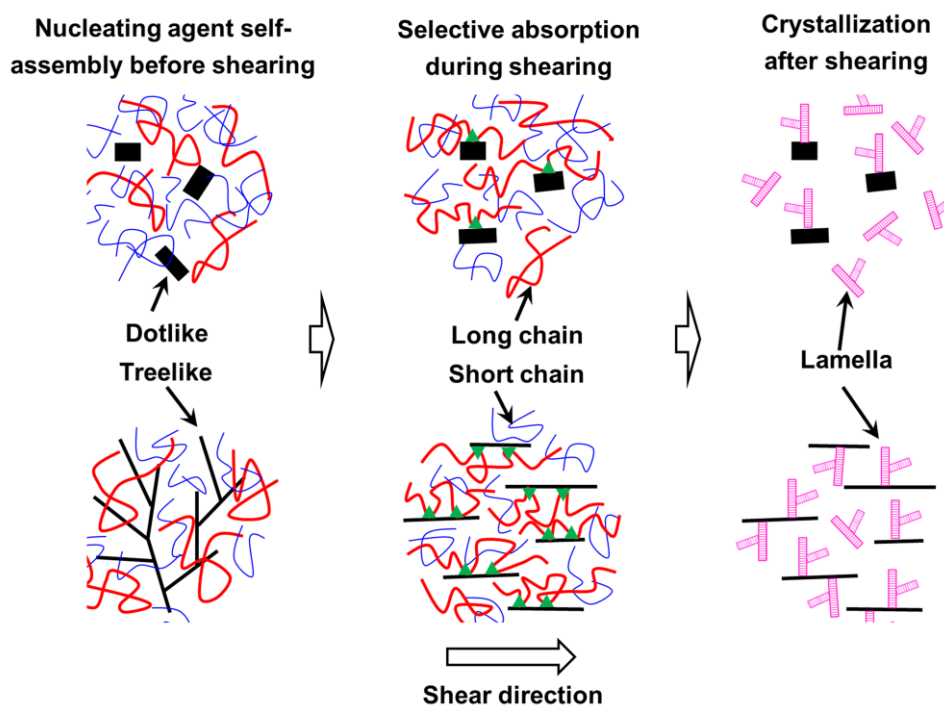
Figure 7-13 Schematic illustration of the crystallization process of the iPP/NJS composite upon after shear.

99

Through dissociation/association of hydrogen bonds connecting small NJS molecules, NJS forms into dotlike, needlelike, and treelike morphologies in the composite. However, the network of treelike NJS is unstable. Under shear flow, the NJS branches are detached from the treelike, leading to the formation of tremendous needlelike NJS in the melt. Due to selective absorption mechanism, a large fraction of long polymer chains is anchored on the surface of NJS, leading to the decrease of viscosity of the matrix. The composite with treelike NJS owns the lower viscosity suggesting that more polymer chains are anchored on the surface of NJS. In addition, because of the applied shear flow, polymer chains tend to orient along the flow direction. Once the shear ceases, the oriented polymer chains will relax. But the relaxation process can be inhibited by the anchoring effect. Therefore, a larger degree of polymer chains orientation will be reserved in the composite containing more anchoring points. The reserved oriented polymer chains play a catalytic role recruiting other chains adjacent to them into the formation of shish. During the following crystallization process, in addition to the self-nucleation points in the melt, the shish formed on the surface of NJS induces the growth of "mother" lamellae and "daughter" lamellae grow epitaxial on "mother" lamellae. Since that the composite with treelike NJS provide the largest number of anchoring points, therefore the composite with treelike NJS owns the shortest crystallization induction time. The highest crystal orientation in the composite with treelike NJS benefits from the orientation of the detached NJS branches from the tree themselves.

7.5   Conclusion

The influence of NJS morphology on shear-induced crystallization of iPP is investigated in this chapter. The results prove that by adding NJS, the crystallization kinetics can be accelerated and the orientation of crystals can be enhanced. Furthermore, the accelerating effect is greatly influenced by the morphology of NJS. The composite with treelike NJS owns the shortest crystallization induction time and highest crystal orientation since that treelike NJS provides the largest number of anchoring point for polymer chains. In addition, the NJS branches detached from the tree orient themselves in the shear direction, which facilitates the crystal orientation in the composite. It is interesting to point out that the morphology of NJS is adjusted in the case that the concentration of NJS is the same (0.3 *wt*. %). The results in this work provide a possibility to use the nucleating agent more efficiently during shear-induced crystallization, which is of great importance in both scientific research and industrial processing.

8 Influence of nucleating agent self-assembly on structural evolution of iPP during uniaxial stretching[5]

The iPP/NJS composites with different K_β are prepared by controlling the self-assembly of NJS. And then the deformation behavior of the composites was characterized by in-situ synchrotron WAXS and SAXS. The results show that during uniaxial stretching, a higher K_β could increase the number of voids. However, the size of voids is similar regardless of the NJS morphology. The β-α phase transition takes place after void formation. During intralamellar and interlamellar slip, no obvious polymer chains orientation can be found for α-iPP. In the strain range of 0.1~0.6, the *c*-axis of the β-iPP crystal tends to orient perpendicular to the stretching direction. This is caused by lamellae twisting, a unique deformation mode of β-iPP lamellae. The lamellae twisting are proposed to be responsible for the intense voids formation of the composite with higher K_β. At a strain larger than 0.6, the drastic increase of orientation is mainly caused by the rotation of the residual fragmented lamellae and the orientation of the newly formed crystals.

---

[5] The main part in this chapter has been published as "B. Chang, K. Schneider, R. Vogel, G. Heinrich. Influence of nucleating agent self-assembly on structural evolution of isotactic polypropylene during uniaxial stretching, Polymer 138 (2018) 329-342."

8.1   Introduction

Under mechanical load, the hierarchical structural evolution covering the scale from angstrom to micrometer has been found, which depends strongly on the morphology and microstructure of iPP before deformation. Understanding the structural evolution of iPP is of great importance to optimize its mechanical properties. In the past, many studies have been performed with attention focused on the cavitation [66, 74], lamellae deformation [69, 175, 201], and β-α phase transition [60, 273, 274] of iPP during stretching or compressing. For instance, by X-ray microdiffraction with synchrotron radiation, Riekel et al. [273] investigated the strain-induced β-α phase transition in the plastic zone of β-iPP. Their results showed that the bulk β-iPP was gradually transformed into highly oriented, conformationally disordered α-iPP as the strain increased. Zhang found that cavitation took place at a stretching temperature lower than 120 ^{o}C. β-α phase transition happens when the drawing temperature is higher than 30 ^{o}C, below which the β-iPP will be transformed into mesophase [275]. Bao found that β-iPP lamellae were locally destroyed and fragmented into smaller crystals or crystal blocks, and cracks formed running approximately perpendicular to the stretching direction due to the disintegration of the oriented β-iPP lamellae [276]. Despite the fact that numerous studies have been performed, the mechanism responsible for the structural evolution and the relationship between the hierarchical deformations themselves remains under debate. The general structural evolution process of semicrystalline polymer was proposed by Men et al.[277] to be from intralamellar slipping of crystalline blocks occurs at small deformation to a stress-induced crystalline block disaggregation-recrystallization process occurs at a strain larger than the yield strain. In their later work, the second process was further proved to be a stress-induced melting-recrystallization.[181] As to β-α phase transition during uniaxial of iPP, two distinctly different mechanisms have been put forward. Lezak proposed that the (110)[001] β-iPP chain slip and (110)[1$\bar{1}$0] β-iPP transverse slip were responsible for the β-α solid state phase transition [278]. However, the solid-state phase transformation seemed to be problematic because it required reversal of helical handedness. Considering that, the melting-recrystallization appeared to be an easier path for β-α phase transition [60, 279], which coincides with the stress-induced melting-recrystallization mechanism proposed by Men.[181] By transmission electron microscopy (TEM), the melting spot was found by Li among the lamella parallel with the loading direction [60], which provided strong evidence for melting-recrystallization. In addition to the continuing discussions about the mechanism for the β-α phase transition, the β-α transformation was

claimed to be associated with void formation [78, 280], which further complicated the understanding of structural evolution during deformation.

Taking the above ongoing arguments into account, a systematic study concerning the structural evolution of iPP during deformation is of great importance. NJS was chosen as the nucleating agent in this work. The self-assembly process of NJS was used to control the microstructure of iPP, which was characterized elaborately. Lastly, the cavitation behavior, β-α-iPP phase transition, and polymer chains orientation of iPP during uniaxial stretching were investigated by in-situ synchrotron SAXS and WAXS measurements. Through this study, we received a deeper insight into the relationship between the NJS self-assembly and the structural evolution of iPP during deformation.

8.2   The morphology of the NJS in the compression molded iPP

The results in the former chapter prove that by controlling T_f, different NJS morphologies can be obtained. However, whether the morphology of NJS can be successfully controlled under compression molding conditions remains unclear, because the thermal-mechanical conditions are more complicated in comparison to the well-controlled hot stage. Therefore, the morphology of NJS in the compression molded plate was checked by SEM. As shown in **Figure 8-1a** and **b**, the dotlike NJS can be readily seen for iPP/NJS-260, and treelike NJS can be found for iPP/NJS-290. The morphology of the interface between NJS and iPP matrix is provided in **Figure 8-1c**. Two representative NJS particles are shown by the arrows, one is aligned in the observed plane and the other one is perpendicular to the observed plane. In both cases iPP lamellae grow perpendicular to the surface of NJS. The morphology of the interface is in accordance with the previous reports, suggesting the nucleating effect of the NJS on iPP [281, 282].
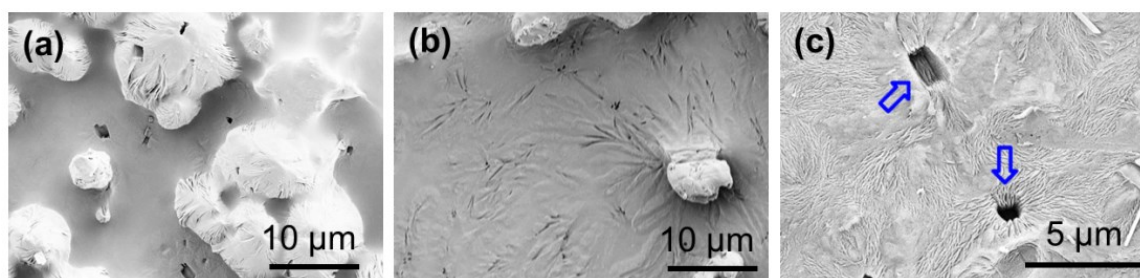
Figure 8-1 The morphology of NJS in iPP/NJS composite with different T_f, (a): iPP/NJS-260, (b): iPP/NJS-290; (c) the morphology of the interface between NJS and iPP matrix.

8.3 Microstructure of iPP with different NJS morphologies

The long period of the compression molded iPP/NJS composites, which comprises one layer of the crystalline phase and one layer of the amorphous phase in the "two-phases" model of semicrystalline polymers, is given in **Figure 8-2a**. It can be seen that the dependence of long period follows two regimes on T_f. As the morphology of NJS transforms from the dotlike to the needlelike form, the long period decreases from 13.9 nm to 13.0 nm and finally to 12.4 nm. For the treelike NJS, the long period increases considerably to 14.8 nm. With the further increase of T_f, the long period decreases gradually to 14.1 nm and then to 13.7 nm. X_c and K_β of the compression molded sample are given in **Figure 8-2b**. X_c keeps at around 48 % when T_f is lower than 280 °C. And it increases to 53 % when T_f becomes 290 °C. The further increase of T_f reduces X_c gradually to 48 %. The results in **Figure 8-2b** show that the morphology of NJS has a weak influence on X_c. However, it is interesting that K_β varies greatly as the morphology of NJS is changed. The evolution trend of K_β is similar to that of the long period: K_β decreases from 18 % to 15 % and then to 5 % as NJS changes from dotlike to needlelike. The formation of treelike NJS enlarges K_β greatly to 47 %. The further increase of T_f leads to a slight decrease of K_β, which finally reaches 43 %. The melting behavior of the composite provided in **Figure 8-2c** further confirms the change of K_β in iPP/NJS composites. On the melting curves, except for the main peak at 165 °C, one or two shoulder peaks at lower temperature side of this peak could be found. The main peak originates from the melting of α-iPP and the shoulder peak can be ascribed to the melting of β-iPP [282-284]. As T_f is increased, the area of the β-iPP melting peak decreases gradually, suggesting a decrease of K_β. The β-iPP peak disappears nearly totally for the sample with T_f of 280 °C. When treelike NJS is formed, the area of the β-iPP melting peak is greatly enlarged.
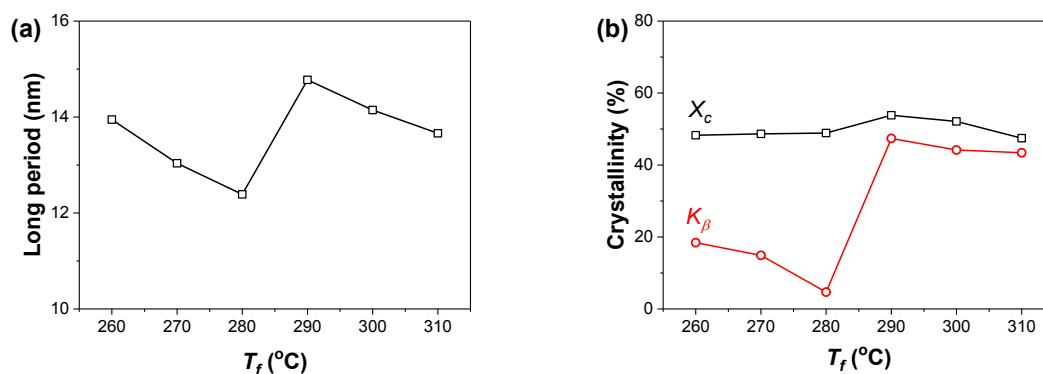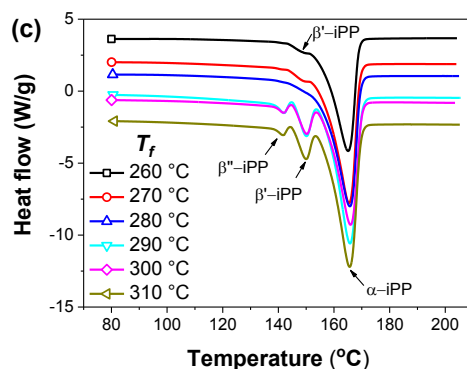
Figure 8-2 (a) The long period, **(b)** the total crystallinity (X_c) and the β-iPP relative crystallinity (K_β), **(c)** the melting behavior of iPP/NJS composites with different T_f.

The influence of NJS morphology on the microstructure of iPP can be summarized shortly as such: as the morphology of NJS transforms from dotlike to needlelike, the long period of the sample decreases from 13.9 nm to 12.4 nm and K_β decreases from 18 % to 5 %. The formation of treelike NJS enlarges the long period to 14.8 nm and K_β to 47 %. The further increase of T_f leads to a slight decrease of the long period and K_β. The reason for this is that during the cooling process, there is a competition between thermal nucleation and the nucleation by NJS. The former one gives rise to α-iPP and the latter one leads to β-iPP. Therefore, the β-iPP nucleation efficiency of NJS is determined by two factors: one is the contacting surface area between NJS and the iPP matrix, and the other one is the spatial distribution of NJS. The dotlike NJS and the treelike NJS have much better spatial distribution than the needlelike NJS, and the treelike NJS has a larger lateral surface than the dotlike NJS. Consequently, treelike NJS shows the highest β-iPP nucleation effect and the needlelike NJS exhibits the lowest β-iPP nucleation effect.

8.4   In-situ SAXS results

The cavitation and lamellae deformation behavior during deformation could be well captured by 2D-SAXS measurements. Depending on the shape of the scattering entity, a qualitative evaluation of the structural evolution can be obtained. **Figure 8-3** shows some representative 2D-SAXS patterns of iPP/NJS composites during uniaxial stretching.
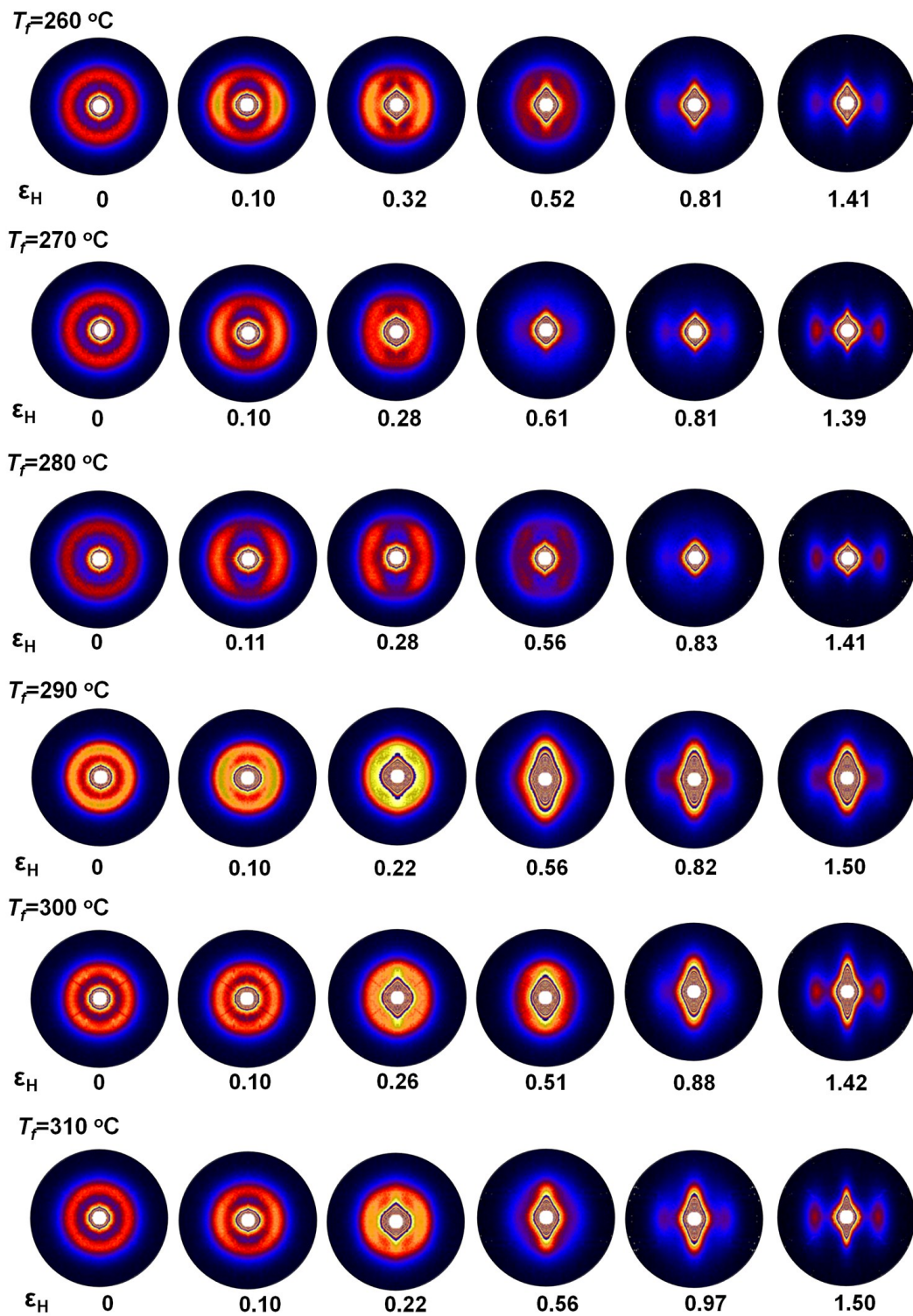
Figure 8-3 Representative 2D-SAXS patterns of iPP/NJS composites with different T_f during uniaxial stretching. The number located at the bottom of the pattern is the Hencky strain. The color scale is linear and identical for all patterns. The stretching direction is horizontal.

Before deformation, the 2D-SAXS patterns show a broad isotropic ring, indicating a random orientation of lamellae. For iPP/NJS03-260, at a strain of 0.1 the scattering starts to focus in the equator leading to the appearance of the "two-arcs" pattern. The "two-arcs" pattern is the sign for lamellae orientation. Due to the fact that the strain is quite small, the deformation is still in the elastic range, the orientation of lamellae should be realized by the rotation of lamellae towards the loading direction. At a strain of 0.32, the scattering of the lamellae grows into an ellipse. The ellipse scattering suggests that the lamellae are tilted [103, 203], which means that the molecular axis in the lamellae is not perpendicular to the lamellar surface. The tilting of lamellae is caused by intra- and inter-lamellae slip [78, 278]. In addition, the scattering in the center region of the pattern turns into a diamond shape, indicating the formation of a void. The direction of the diamond shape scattering is vertical. Therefore the void inside the sample is aligned with its longitude along the stretching direction [78]. As the strain is further increased to 0.52, the scattering intensity of the lamellae is reduced noticeably, suggesting the disappearance of the initial lamellae. At an even larger strain (0.81), the scattering of the lamellae arises again in the form of "two-drops" in the equatorial direction, implying the formation of new lamellae. The newly formed lamellae are aligned with their normal direction along the stretching direction. Meanwhile, the diamond shape scattering in the center becomes thinner as a result of void growth and orientation. The described evolution trend of the scattering patterns in iPP/NJS03-260 is generally the same for all samples. The difference lies mainly in the scattering of the voids. For example, as T_f increases from 260 ^{o}C to 270 ^{o}C, the void scattering at the end of stretching is decreased. For iPP/NJS03-280, the void scattering becomes even weaker. However, as T_f is further increased, it is obvious that void scattering is significantly enhanced. The void scattering decreases again gradually as T_f is increased from 290 ^{o}C to 310 ^{o}C. The variation of the void scattering indicates that the self-assembly of NJS has a great influence on the cavitation behavior of iPP during stretching.

8.4.1　Cavitation behavior

Due to the fact that the longitude of the void is along the stretching direction, so $S_\parallel$ and $S_\perp$ can be referred to as the length and width of the void. The evolution of the void size is presented in **Figure 8-4**. It can be found that the length of the voids increases gradually as the strain is increased, while the width of the voids stays nearly the same. Surprisingly, at the same strain, the void length of the iPP/NJS composite is nearly the same, independent of the thermal

history. This suggests that the self-assembly of NJS has quite a weak influence on void size during deformation.
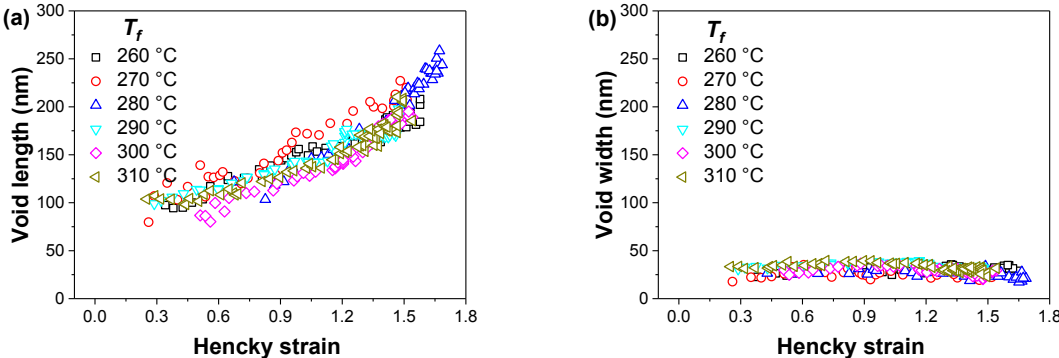
Figure 8-4 Evolution of the void length and the void width of iPP/NJS composites with different T_f during stretching.

The evolution of Q as a function of strain is provided in **Figure 8-5**. If V_v is in the range of 0~0.5, Q depends positively on V_v. For the sample with T_f lower than 280 °C, Q increases slightly as the strain is increased. For the sample with T_f equal to or higher than 290 °C, a drastic increase of Q could be found as the strain is larger than 0.1. The drastic increase of Q indicates the formation of abundant voids. It demonstrates that the void formation of the sample with T_f equal to or higher than 290 °C happens before the yield point. Then Q reaches a maximum at a strain of 0.3 (the yield strain). Beyond that, a decrease of Q can be found as a result of void coalescence. As the strain is further increased, Q increases only slightly.
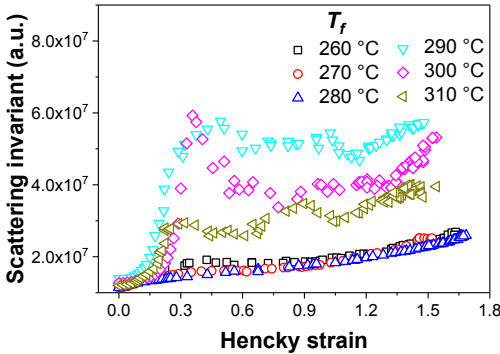
Figure 8-5 Evolution of the scattering invariant (Q) of iPP/NJS composites with different T_f during uniaxial stretching.

108

Combining the result in **Figure 8-4**, it can be found that at the same strain, the length of the void is quite the same for all samples. However, Q is greatly enhanced as K_β is increased, suggesting that the number of voids is greatly increased for the iPP/NJS03 composite with higher K_β. In addition, as the strain is increased, the length of voids is increased gradually, but Q is constant (iPP/NJS03-300 and iPP/NJS03-310) or even decreases gradually (iPP/NJS03-290). Therefore it can be inferred that the growth of voids in iPP/NJS03-290, iPP/NJS03-300, and iPP/NJS03-310 occurs mainly by the coalescence of voids [177].

In fact, the cavitation behavior of iPP was investigated extensively in the past few years. Galeski [66, 188, 191] proposed that during deformation there is a competition between two processes: cavitation of the amorphous phase and plastic deformation of the lamellae. If lamellae are compliant or defected, then their plastic deformation is easy while the strength of the amorphous phase prevents the formation of voids. If lamellae are thick and have a reduced number of dislocations, the breaking of the amorphous phase is easier, which promotes the formation of voids. The proposal by Galeski was further developed by Humbert [198] and also widely accepted by other researchers [185, 189, 190]. Different from the proposal by Galeski that cavitation happens in the amorphous phase, another view, that cavitation starts from the crystalline phase, is proposed by Men at al.[69, 190, 285] Men et al. considered that the cavitation was initiated by opening of the block boundaries within crystalline lamellae, which resulted in the plate-like cavities passing through several connected lamellae and interlamellar amorphous phase. As to α-iPP and β-iPP, it is well known that the lamellae strength of α-iPP is stronger than that of β-iPP [286]. Therefore, the cavitation behavior should be less intense with the increase of K_β considering the proposal by Galeski, which is totally contradictory to the results in this study. As a matter of fact, the easier cavitation behavior of β-iPP is in line with previous reports. Pawlak found that stress whitening was more pronounced in the sample with higher β-iPP content [66]. Henning found that microvoids were visible only in the polar region of α-iPP spherulites, but in the whole area of β-iPP spherulites [287]. Therefore, additional explanations need to be put forward, except for the competition between the cavitation of the amorphous phase and plastic deformation of the lamellae. Chu et. al. proposed that β-α phase transition during deformation will result in volume contraction of the matrix, which would greatly enhance the void formation [74, 288]. Bao suggested that void formation was related to the fragmentation of β-iPP lamellae [78]. Considering this, no certain conclusion related to the intense void formation in the sample with higher K_β can be made here. The possible reason for the increasing number of voids in

the β-iPP rich sample will be discussed in the following section in relation to the β-α phase transition and the polymer chains orientation.

8.4.2 Evolution of the long period

In addition to the void formation, the initial lamellae are deformed by intralamellar and interlamellar slip, lamellar tilting and recrystallization, as shown in **Figure 8-3**. In order to describe quantitatively the deformation of lamellae, the evolution of the long period in the stretching direction is presented in **Figure 8-6**. It should be noted that the long period in the stretching direction represents those lamellae whose normal directions are aligned along the stretching direction. During the stretching process, they will suffer a tensile stress. It can be found in **Figure 8-6** that for all samples the long period first increases with increasing strain and then drops after reaching a peak value. The transition strain corresponds to the yield strain. The maximum long period depends on the initial long period before deformation. The larger the initial long period, the larger the maximum long period. In addition, it is interesting that the long period at the plateau is nearly the same (about 13.3 nm) regardless of the initial long period. The increase of the long period is mainly caused by the stretching of the interlamellar amorphous phase [209]. The decrease of the long period is caused by the fragmentation of lamellae which leads to the relaxation of the strained amorphous phase [79], and also the recrystallization process which inserts a newly formed lamella into the old one [25, 210]. The same long period at the plateau suggests that the long period after deformation is determined only by the stretching temperature.
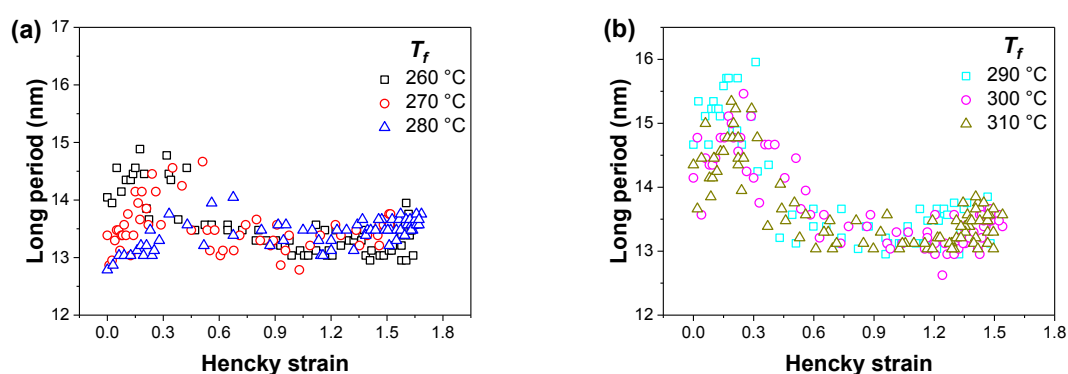
Figure 8-6 Evolution of the long period in the stretching direction for iPP/NJS composites with different T_f during uniaxial stretching.

8.5 In-situ WAXS results

Figure 8-7 shows some representative 2D-WAXS patterns during stretching. The diffraction rings in the patterns originate from the lattice planes of iPP crystal.
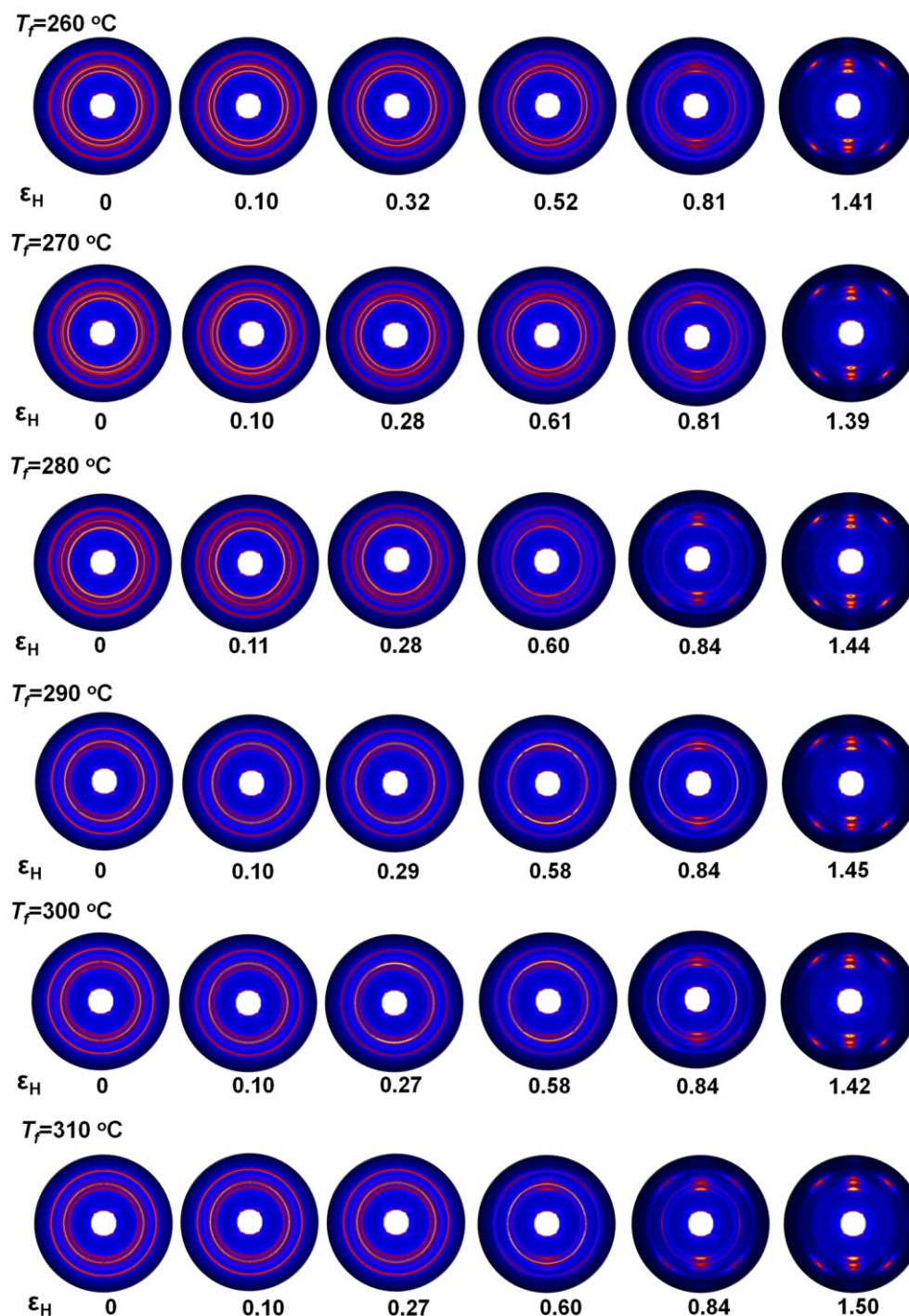
Figure 8-7 Representative 2D-WAXS patterns of iPP/NJS composites with different T_f during uniaxial stretching. The color scale is linear and identical for all patterns. The stretching direction is horizontal.

The radius of the rings is determined by Bragg's law. From inner to outer, the rings can be assigned to (110), (300), (040), (130), (111)/($\bar{1}$31)/(311) lattice planes. Among them (300) and (311) belong to β-iPP and the others are from α-iPP. Before deformation, the rings are homogeneous in all directions, suggesting a random orientation of the crystals. With the increase of strain, the intensity of (hk0) lattice plane starts to focus on the meridian and the intensity of (hk1) lattice plane concentrates off-axis of the meridian [289], implying the orientation of the crystal. As the strain is further increased, the orientation is enhanced.

8.5.1 The β-α phase transition behavior

As mentioned in above, X_c and K_β could be obtained from the 1D-WAXS curves by a standard peak fitting procedure. It should be pointed out that two methods have been employed to get 1D-WAXS curves from 2D-WAXS patterns during stretching. One is circular integration from the inner to the outer region of the 2D-WAXS pattern [78]. The intensity at a specified scattering vector is averaged azimuthally. The other one is the vertical or horizontal cutting of the 2D-WAXS patterns [290]. The methods are outlined in **Figure 8-8a**. **Figure 8-8b** and **Figure 8-8c** show the differences between the two methods. Before deformation (see **Figure 8-8b**), 1D-WAXS curves are quite the same. But for the sample with a strain of 1.4 (see **Figure 8-8c**), the intensity at the same scattering vector varies greatly due to the crystal orientation. Furthermore, the (300) reflection (indicated by the arrow in **Figure 8-8c**) is invisible in the vertical cut 1D-WAXS curve, because vertical or horizontal cutting captures only the scattering from those lamellae with preferential orientation. Therefore, the circular integration is employed in this study.
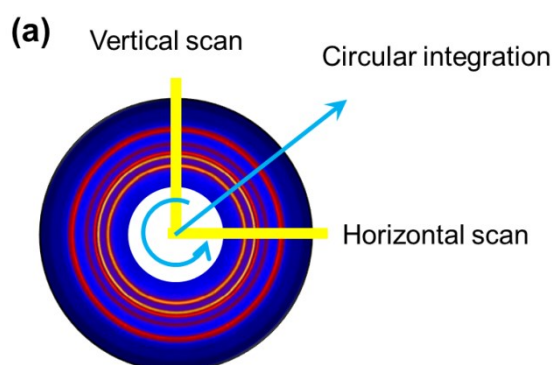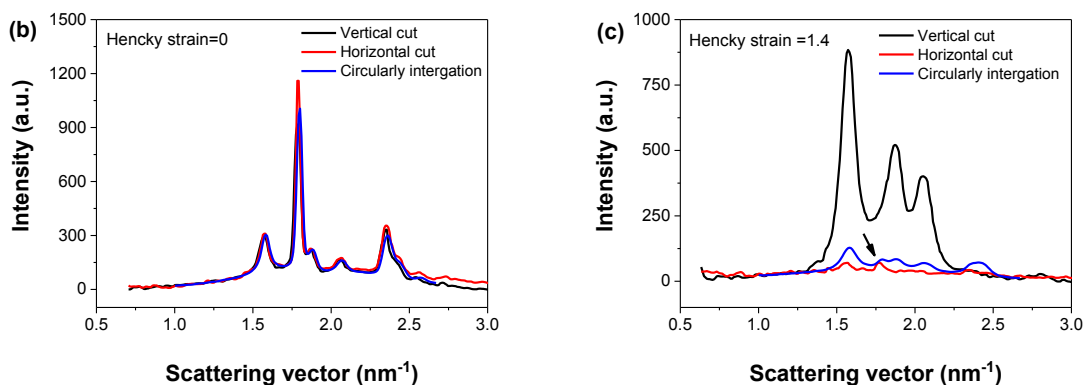
Figure 8-8 (a) The schematic diagram of getting 1D-WAXS curves from the 2D-WAXS pattern; 1D-WAXS curves before deformation **(b)** and with a strain of 1.4 **(c)**.

Generally, the evolution trend of the peak intensity on the 1D-WAXS curve during stretching is analogous for all samples. The 1D-WAXS curve of iPP/NJS03-290 during stretching is shown in **Figure 8-9a** as an example. As the strain is smaller than 0.1, the intensity of all peaks keeps invariant, suggesting that no crystal is broken during elastic deformation. A slight decrease of (300) peak intensity could be found in the strain range of 0.1~0.3. When the strain is beyond 0.3, a decrease of (110), (300), (040), and (111)/(-131)/(311) peak intensity shows up, indicating the deformation of both α-iPP and β-iPP. In the strain range of 0.6-1.2, the intensity of all peaks decreases drastically. As the strain is further increased, the intensity of all peaks stays nearly unchanged. The evolution of X_c is given in **Figure 8-9b**. It is obvious that Xc shows a steady decrease, as the strain is larger than 0.1. The slope of the curve is nearly constant in the whole deformation process. The decrease of X_c is caused by the breaking of both α-iPP and β-iPP crystals. The evolution of K_β is provided in **Figure 8-9c**. When the strain is smaller than 0.3, K_β keeps invariant for all samples implying that no β-α phase transition occurs before the yield point. As the strain is increased to 0.9, a moderate decrease of K_β can be found for iPP/NJS03-290, iPP/NJS03-300, and iPP/NJS03-310. In the strain range of 0.9~1.2, K_β decreases drastically for all samples. After that, K_β changes only slightly. At the end of stretching, K_β of iPP/NJS03-290, iPP/NJS03-300, and iPP/NJS03-310 is slightly higher than that of iPP/NJS03-260 and iPP/NJS03-270, and K_β of iPP/NJS03-280 is 0.
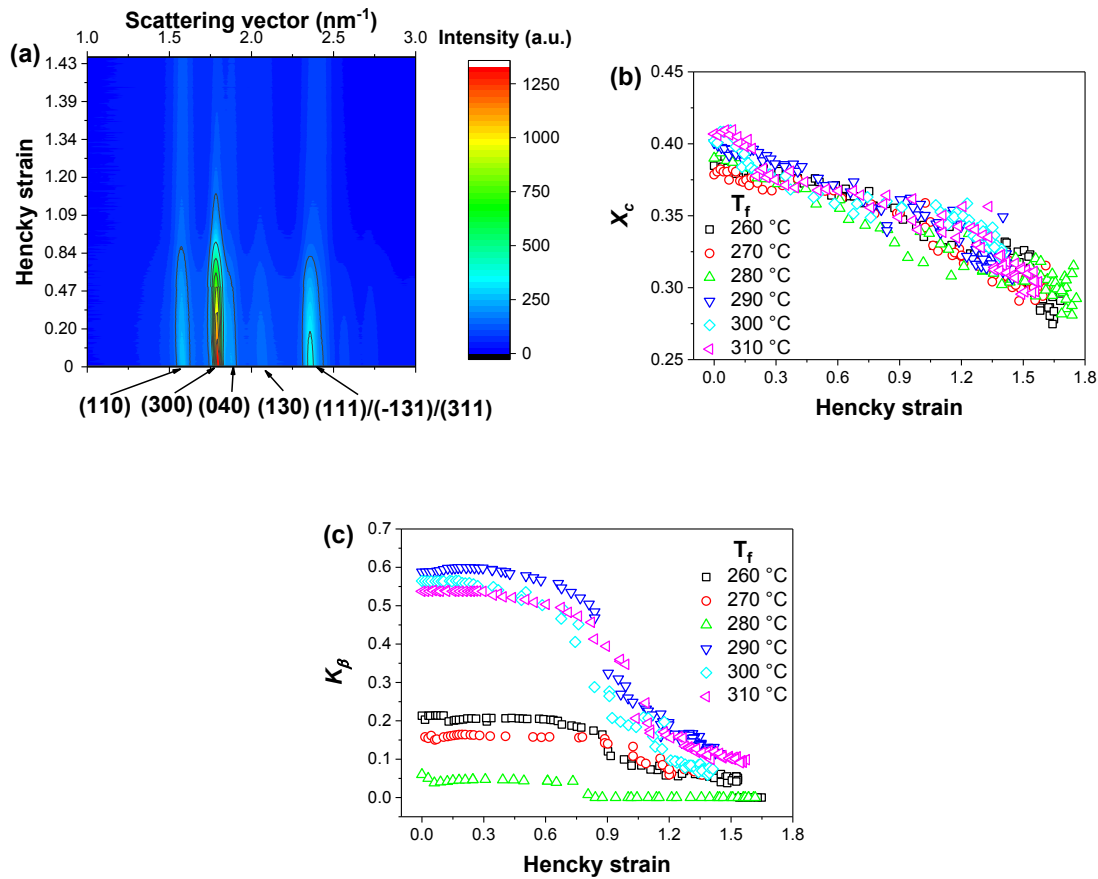
Figure 8-9 (a) 1D-WAXS curves of iPP/NJS03-290 obtained by circularly integration of the 2D-WAXS pattern; the evolution of X_c **(b)** and K_β **(c)** as a function of the strain of iPP/NJS composites with different T_f.

The decrease of K_β implies the deformation of β-iPP. In the literature, different values are reported for the onset strain where K_β starts to decrease. Li [274] found that K_β decreased gradually even at a low strain (50 %). Cai [290] revealed that in the temperature range from 60~80 °C, the critical strain is around 15~20 %. Bao [78] found that K_β decreased drastically when the strain is smaller than 100 %. Although different values have been reported, one consensus has been made, namely that K_β starts to decrease after the yielding point. As mentioned above, the transformation from unstable β-iPP to stable α-iPP can be achieved through two different processes. One is solid to solid martensitic-like transformation [276] and the other one is the local melting-recrystallization process [60]. In this study, the latter one is preferred since the drastic decrease of K_β is found at a strain larger than 0.6, which is far beyond the strain of 0.3 where the lamella melting happens (as has been proved in **Figure 8-9**).

114

Additionally, the intense void formation in the sample with higher K_β is recalled here. As proposed by Chu et. al. [74, 288], because that the density of β-iPP is lower than that of α-iPP, the β-α phase transition during deformation will lead to a volume contraction of the matrix. The volume contraction benefits the void formation greatly. However, it can be found in **Figure 8-9** that the β-α phase transition happens much later than the void formation. Consequently, the β-α phase transition cannot be the main reason for the intense cavitation in the composite with β-iPP high K_β.

8.5.2 The orientation of the crystal

In **Figure 8-7**, one can see that with the increase of strain, the scattering of the lattice plane changes from a homogeneous ring to arcs and finally to spots, indicating the orientation of the crystals. Consequently, the orientation of *c*-axis in the crystal of α-iPP (f_{Hc}^α) could be evaluated. f_{Hc}^α as a function of strain is given in **Figure 8-10a**.
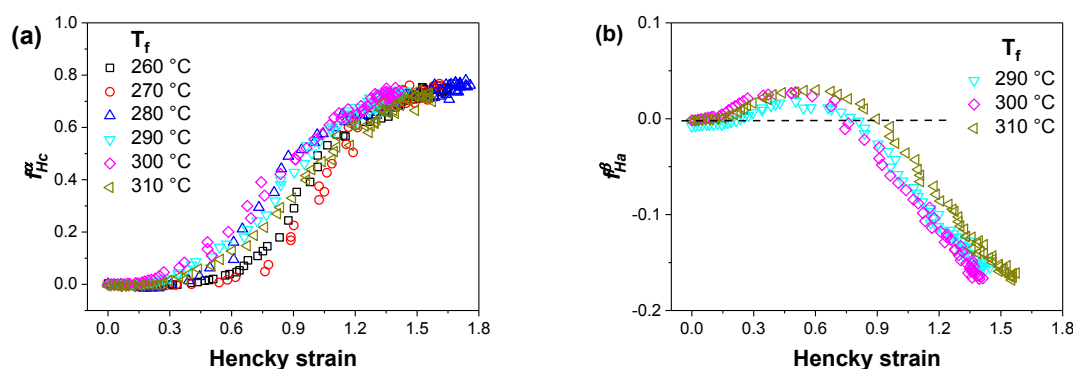
Figure 8-10 (a) The orientation of polymer chains in α-iPP (f_{Hc}^α); **(b)** the orientation of *a*-axis in β-iPP (f_{Ha}^β) evaluated by Herman's orientation factor of the iPP/NJS composite with different final heating temperatures (T_f) during stretching.

Before stretching, f_{Hc}^α is nearly 0 which suggests the random orientation of the crystal. Only a slight increase of f_{Hc}^α can be found when the strain is smaller than 0.45. This implies that although the initial lamellae are fragmented by intralamellar and interlamellar slip, no distinct orientation of the lamellae blocks could be found. In the strain range of 0.45~1.2, an obvious increase of f_{Hc}^α arises. The obvious increase of f_{Hc}^α is a result of melting-recrystallization. Via intralamellar and interlamellar slip, the initial lamellae are fragmented into blocks. The friction between the fragmented lamellae provides the energy for lamellae melting. The polymer chains in the crystal are pulled out after fragmentation and oriented mainly along the

stretching direction. In addition, the polymer chains in the amorphous phase are also stretched along the loading direction. Through the recrystallization process, the oriented polymer chains crystallize into crystals with their *c*-axis oriented along the stretching direction. When the strain is larger than 1.2, f_{Hc}^{α} continues to increase but the slope of the curve is decreased. In this range, the recrystallization process is nearly complete. The further orientation of the polymer chains in the crystal is realized by the rotation of the residual lamellae blocks and newly formed lamellae.

Because β-iPP belongs to a trigonal crystal system, Wilchinsky's method cannot be applied. So, the azimuthal intensity distribution of (300) lattice plane is employed to calculate the orientation of *a*-axis in the *β*-iPP crystal (f_{Ha}^{β}). Since the K_{β} of iPP/NJS-260, iPP/NJS-270, and iPP/NJS-280 is quite small at large strain. Therefore, the f_{Ha}^{β} of those samples is not given. The result in **Figure 8-10b** shows that at a strain smaller than 0.1, f_{Ha}^{β} is nearly 0, indicating that no *a*-axis orientation could be found during elastic deformation. As the strain is enlarged, f_{Ha}^{β} upturns a little bit, suggesting that the *a*-axis in β-iPP crystals tends to orient along the stretching direction. Generally, the tensile deformation will produce an oriented structure with the *c*-axis aligned preferentially along the stretching direction. So the *a*-axis orientation along the stretching direction in the strain of 0.1~0.6 is quite abnormal. The abnormal orientation of β-iPP crystal is related to its special lamellae deformation mode. With the help of rheo-optical, Fourier transformed infrared spectroscopy, Huy et. al found that in addition to intralamellar and interlamellar slip, lamellar twisting was also found in β-iPP during deformation [291]. The twisting of β-iPP lamellae at a small strain was verified by Lezak [278] with SEM. The twisting and related rotation of lamellae offers an additional route of crystal orientation. At a strain larger than 0.6, f_{Ha}^{β} starts to decrease, indicating that the *c*-axis in β-iPP crystals begins to orient along the loading direction. The critical strain where f_{Ha}^{β} starts to decrease is similar to the one where the drastic decrease of K_{β} can be found in **Figure 8-9**, suggesting that the orientation of the *c*-axis in β-iPP is related to the partial melting of β-iPP lamellae. The partial melting releases the constraint force for the rotation of the residual β-iPP lamellae, leading to the *c*-axis orientation along the stretching direction in β-iPP.

The twisting of β-iPP lamellae could accelerate the fragmentation of β-iPP lamellae. In the work by Lezak, it was observed that lamellae twisting is limited to the lamellae oriented along the loading direction initially, and becomes more widespread in the fragmented lamellae. Normally, the length of the voids is much larger than the long period of the lamellae. So voids

running through the fragmented lamellae were observed [78]. Through lamellae twisting the initial lamellae are fragmented into small blocks, which supports the void formation and growth. In addition, the twisting of lamellae happens at a strain of 0.1, which is the same strain at which the void is induced (see **Figure 8-6**). Consequently, it is proposed here that the twisting of β-iPP lamellae is probably responsible for the intense void formation in iPP/NJS composite with higher K_β.

8.6   Conclusion

Dotlike, needlelike, or treelike NJS are induced through self-assembly of NJS. The iPP/NJS composite with treelike NJS has the highest β-iPP relative crystallinity and longest long period. During uniaxial stretching, a higher β-iPP relative crystallinity could increase the number of voids. However, the length and width of the voids are similar regardless of the morphology of NJS. β-α phase transition proceeding by melting-recrystallization takes place later than void formation. No obvious orientation of polymer chains in the crystal can be found during intralamellar and interlamellar slip for both α-iPP and β-iPP. In addition, in the strain range of 0.1~0.6, the twisting of lamellae contributes to the abnormal orientation of polymer chains in the β-iPP crystal, where the *c*-axis in the crystal tends to orient perpendicular to the stretching direction. The twisting of β-iPP lamellae could accelerate the fragmentation of β-iPP lamellae. Since the growth of a void generally passes several adjacent lamellae, the twisting of β-iPP lamellae will support the void growth. Consequently, the twisting of lamellae is also proposed to be responsible for the intense void formation of the iPP/NJS composite with higher β-iPP relative crystallinity. At a strain larger than 0.6, the drastic orientation increase of polymer chains in the crystal is mainly caused by the rotation of the residual fragmented lamellae and the orientation of newly formed crystals.

9 Microstructural evolution of iPP during creep: an in-situ study by synchrotron SAXS[6]

The structure evolution of iPP during creep is investigated by in-situ synchrotron small angle X-ray scattering. During primary creep, strain grows nonlinearly to a value less than 15 %. The long period along loading direction ($L_p^{\parallel}$) increases with time, whereas the long period perpendicular to loading direction ($L_p^{\perp}$) decreases slightly. In secondary creep, strain increases linearly with time. Both $L_p^{\parallel}$ and $L_p^{\perp}$ exhibit the same tendency with strain. The increase of the long period is caused by lamellae thickening, which is a kind of cooperation motion of molecular chains with their neighbors onto the lamellae surface. Moreover, the increase rate of $L_p^{\parallel}$ is larger than that of $L_p^{\perp}$, indicating that the orientation of molecular chains along loading direction decreases the energy barrier for the cooperation motion. In tertiary creep, strain grows dramatically within a limited time. The lamellae are tilted and rotated, and then disaggregated. In addition, fibrillary structure is formed during lamellae breaking. The length of the fibrillary structure increases from 364 nm to 497 nm and its width stays at 102 nm as creep time increases.

9.1   Introduction

Unlike uniaxial drawing, compression and impact test, creep test serves as an effective method for the long-term life time assessment of polymer materials. Creep is generally defined as a time-dependent deformation of a material under constant loading for a prolonged period at a constant temperature. Mechanical background for the creep behavior of PP has been widely discussed in previous years. Generally, creep behavior could be well elaborated within the framework of linear viscoelasticity.[292] Under this circumstance, the master curve of creep compliance could be constructed by using time-temperature superposition concept based on the William-Landel-Ferry equation.[293, 294] One example is that by employing time-temperature superposition, Satapathy and his colleagues studied the short-term tensile creep behavior of PP/multi-walled carbon nanotubes composites. The results indicated that nanocomposites showed an increase in creep compliance with increasing temperature as a consequence of the temperature-activated motion of the polymer chains.[293] The prerequisite for linear viscoelasticity is that the creep compliance is assumed to be a function of time and temperature, which could not be fulfilled all the time, unfortunately. When the strain is beyond a certain limit, the creep compliance becomes a function of time, temperature and stress.[295] In that case, tensile creep at a constant stress and temperature should be viewed as a non-iso free-volume process. In the work by Kolařík,[295-298] a procedure was successfully proposed to transform the as-received creep data to a pseudo-iso free-volume state, which made it possible to construct a generalized creep compliance curve under any selected stress in the range of reversible deformations. The procedure was utilized to explain the influence of crystallinity or rubber content on the creep compliance of PPs, iPP, iPP blend consisting of 88 % of iPP and 12% of ethylene/propylene rubber (EPR), rubber-toughened iPP, etc.

As one kind of semi-crystalline polymer, many studies have demonstrated that the crystalline structure and morphology of iPP has a significant effect on its creep behavior. Sliding of tie chains and their detachment from lamellar blocks play a key role in the time-dependent response of iPP.[299, 300] The chain-segment mobility in amorphous phase influences the creep deformation of β-iPP.[301] The increased degree of crystallinity, the presence of subsidiary lamellae in the amorphous region, the integration of preexisting lamellar structure would enhance the creep resistance of iPP.[302, 303] Additionally, the creep resistance is sensitive not only to the crystallinity but also to the crystalline morphology of iPP, which has been demonstrated by Liao and her coworkers.[304] Well-developed spherulites, which have

integrated crystalline structure, showed poor creep resistance; bundle-like morphology, whose crystalline phase was imperfect, resulting in better creep resistance; needle-like morphology, in which the crystalline phase was disordered and displayed largest long spacing, resulting in best creep resistance.

Despite the fact that considerable attention have been devoted mentioned above, the microstructure evolution of iPP during creep is not yet well understood. In this study, the microstructural evolution of iPP during creep is characterized by in-situ synchrotron SAXS measurement. SAXS is employed because of its nondestructive feature and powerful detection ability for the microstructure with a size ranging from several nanometers to several hundred nanometers. In addition, modern synchrotron radiation sources enable us to get low-noise SAXS patterns with high time and spatial resolution, which benefits in situ investigation greatly. The results reveal that the microstructural development in different creep stage differs with each other distinctly. The evolution of long period and lamellae thickness in secondary creep, as well as the lamellae disaggregation, and fibrillary structure formation in tertiary creep are studied in detail.

9.2   The creep curve

The creep test was performed on the custom-made miniature tensile machine as shown in **Figure 3-3**. The creep temperature was set at 120 $^{\circ}$C. A typical creep curve is given in **Figure 9-1a**. It is obvious that the displacement (Δd, black triangle) and true strain (ε, blue square) increase with time. According to the change of Δd and ε, creep curve could be split into four intervals:[305]

(I)   Primary creep, in this stage, ε grows sharply to 15 % within sufficiently small time (no more than 80 s). The deformation obtained in the primary creep is fully recoverable after releasing the force. It can be attributed to the elastic deformation of the molecular chains in an amorphous phase inside the hard crystalline skeleton.[306]

(II)   Transition region, from 80 s to 280 s. In this stage, the dependence of Δd on time is convex, and strain rate ($\dot{\varepsilon}$) decreases with the increase of time.

(III)   Secondary creep, from 280 s to 1152 s. The creep process in this stage is a steady state. Δd increases linearly with time, and $\dot{\varepsilon}$ approaches to a constant value. The duration of the secondary creep is the longest period of the whole creep process. It is remarkably

longer than the primary creep and the tertiary creep. The evolution of strain during creep could be well described by the empirical function

$$\varepsilon(t, \sigma, T) = \varepsilon_e(\sigma, T) + \varepsilon_v(t, \sigma, T) + \varepsilon_p(t, \sigma, T)$$ **Equation (9-1)**

where $\varepsilon(t, \sigma, T)$ is the strain during tensile creep, t is creep time, σ is creep stress, and T is the temperature, $\varepsilon_e(\sigma, T)$ is the elastic component which is the reversible part, $\varepsilon_v(t, \sigma, T)$ is the time-dependent viscoelastic part which is also reversible and $\varepsilon_p(t, \sigma, T)$ is the irreversible plastic part.[296] Before plastic deformation produced by the creep, the strain can be described as

$$\varepsilon(t, \sigma, T) = \varepsilon_e(\sigma, T) + \varepsilon_v(t, \sigma, T)$$ **Equation (9-2)**

The secondary creep is a steady stage, where the strain rate is nearly constant,[304, 305] which should contribute to $\varepsilon_v(t, \sigma, T)$. Therefore, the investigation of the structural evolution during secondary creep will help to get a better understanding of the mechanism of creep, which enables making better predictions of the lifetime of the polymer materials in use.

(IV)   Tertiary creep, necking happens in this stage. ε grows rapidly within a short time, and the dependence of Δd on time first exhibits concave and then convex.

Loading stress (σ) has a great impact on the speed of creep deformation.[307] This can be understood by examining the data in **Figure 9-1b**. With a slight increase of σ, $\dot{\varepsilon}$ in secondary creep increases greatly and the creep failure lifetime decreases remarkably.[308, 309] The higher the σ applied, the faster the creep deformation proceeds. From the conventional view,[310] the dependence of $\dot{\varepsilon}$ on σ during secondary creep is approximated by the Eyring equation

$$\dot{\varepsilon} = \dot{\varepsilon}_0 exp[(\sigma V / kT)]$$ **Equation (9-3)**

where $\dot{\varepsilon}_0$ is a pre-factor, k the Boltzmann constant, T the temperature, and V the activation volume. The linearity of $\ln\dot{\varepsilon}$ vs. σ is checked by linear regression, and the correlation coefficient is 0.99. The activation volume calculated from the slope of the fitted line in **Figure 9-1c** is 2.12 nm^3, which agrees well with the values given by other researchers (in the range between 2-4 nm^3).[307, 310, 311] The critical strain (ε_c) occurs at the very end of the straight line portion of secondary creep decreases with the increase of σ. The decrease of ε_c indicates that the creep here should be treated as a non-linear viscoelasticity behavior. Otherwise ε_c

should keep constant regardless of σ.[312-316] Generally, the non-linearity of tensile creep is mainly brought about by the strain-induced increment of the free volume.[295, 317]
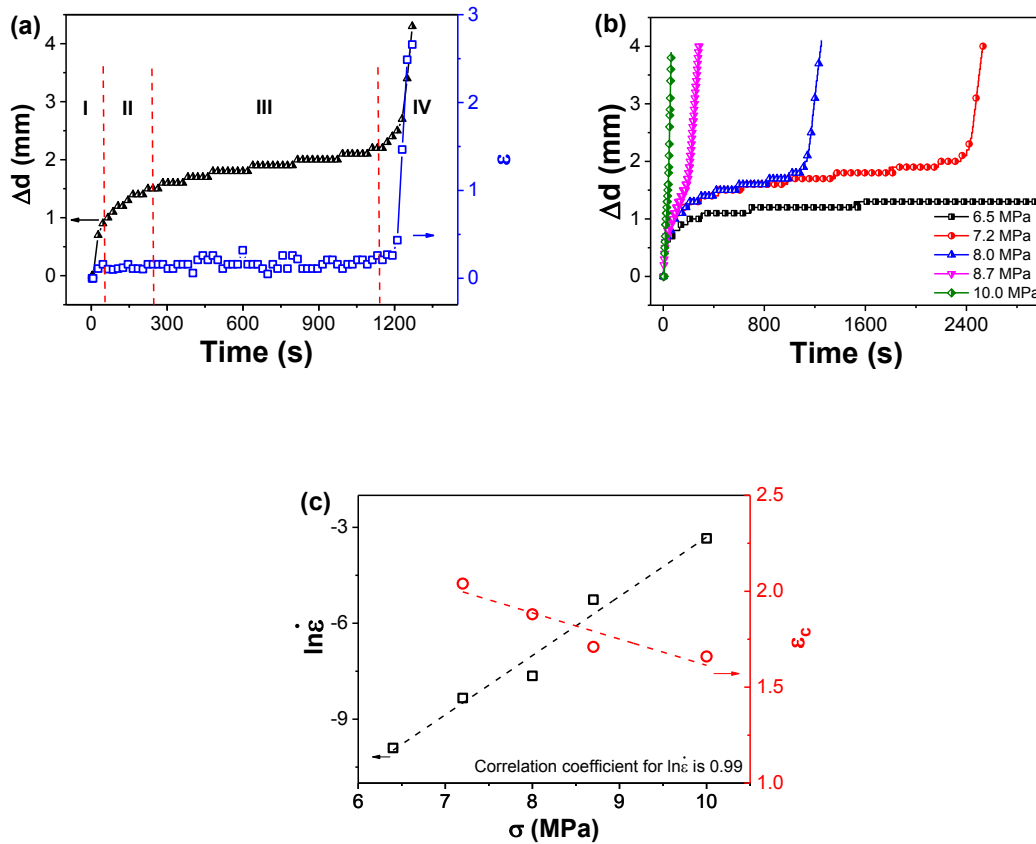
Figure 9-1 (a) Creep curve of iPP under constant stress (8 MPa) at 120 °C. The black triangle is displacement (Δd) and the blue square is true strain (ε); **(b)** Creep curves of iPP under various stresses (σ) at 120 °C; **(c)** plot of $\ln\dot{\varepsilon}$ and ε_c as a function of σ, the straight lines are obtained by linear regression.

9.3   In-situ SAXS results

In order to detect the microstructure evolution during creep, in-situ SAXS measurement was carried out on the specimen creep under 8 MPa at 120 °C. **Figure 9-2** shows a few characteristic SAXS patterns during creep in different abovementioned stages. The shape of scattering signal in 2D-SAXS patterns is associated with spatial ordering of the crystalline lamellae, which has been studied extensively.[318-321] As can be seen, the initial isotropic SAXS pattern results from randomly oriented lamellae before creep. During primary creep, the scattering intensity in the meridional direction enhances whereas the scattering intensity in the equatorial direction weakens slightly, indicating the slight orientation of lamellae. In

addition, dark arcs in the equatorial direction could be observed which are caused by the shift of the scattering in the meridional direction towards the center of the pattern, resulting from the change of lamellae stacking in the meridional and the equatorial direction. The change of lamellae stacking will be quantitatively discussed in the following part. In secondary creep, the SAXS pattern grows further to an anisotropic ellipse. The long axis of the ellipse is perpendicular to the loading direction. During tertiary creep, SAXS pattern changes from slight ellipse to distinct ellipse. This transition indicates that lamellae are tilted and rotated.[203] After that, the SAXS pattern transforms from a distinct ellipse into a "two-spot" pattern, meaning that lamellae are preferentially aligned along loading direction. What's more, a streak appears in the equator direction, which provides a hint that highly oriented fibrillary structure is formed in this region.
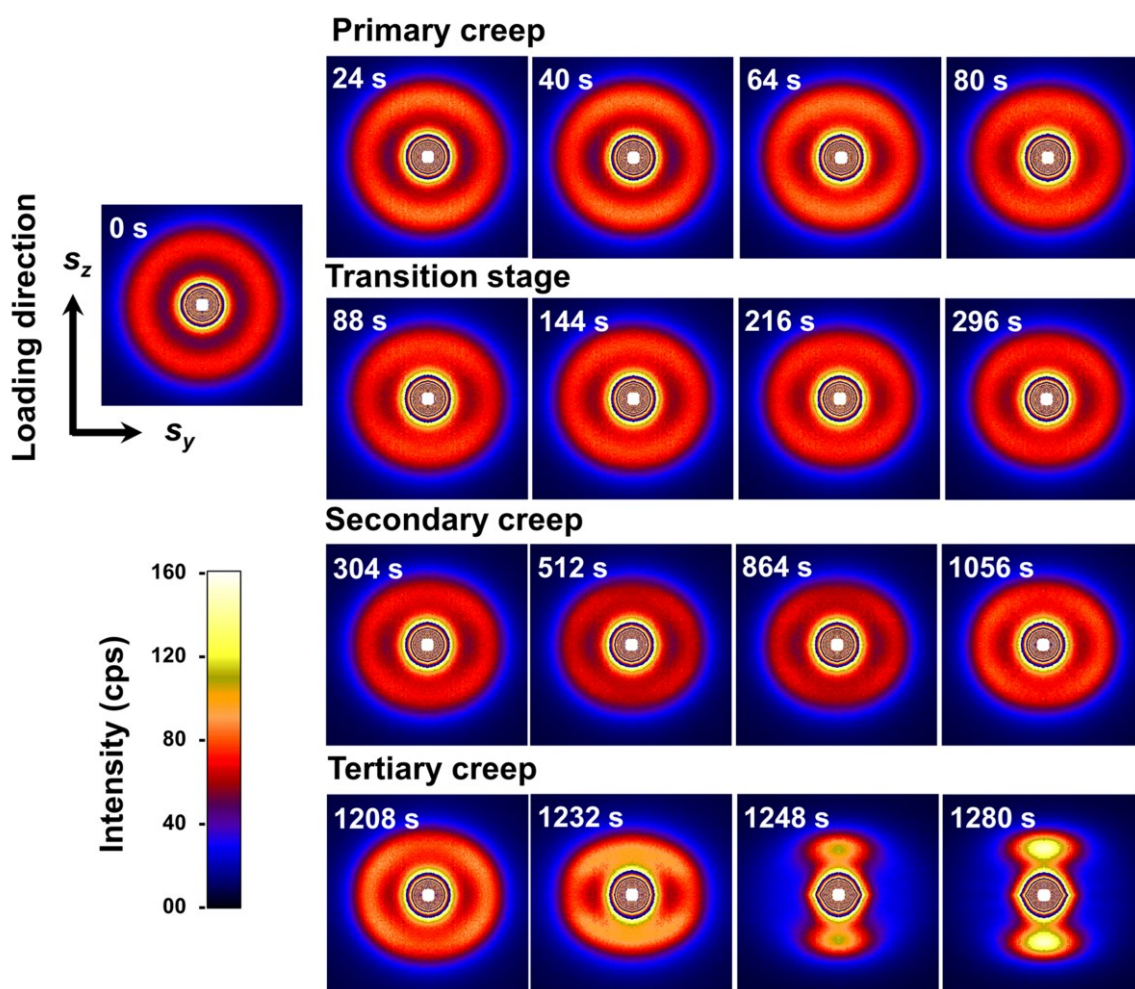
Figure 9-2 Representative 2D-SAXS patterns in different states of creep, the size of the pattern is $\pm 0.0525\,\text{nm}^{-1} \times \pm 0.0525\,\text{nm}^{-1}$. The scale refers to the number of counted

photons during the exposure time of 0.5 s. According to the much higher intensity in the center of the pattern each color change stands here for a repeated application of the scale.

9.3.1 Evolution of long period and domain thickness

It is widely accepted that in the spherulite of iPP lamellae grow radially along the radius, which can be illustrated in **Figure 9-3**. When the sample is subjected to a uniaxial force, the deformation behavior of the lamellae in region P and region A is different. In region A the normal direction of the lamellae is the same as with the loading direction. In region P the normal direction of the lamellae is perpendicular to the loading direction.
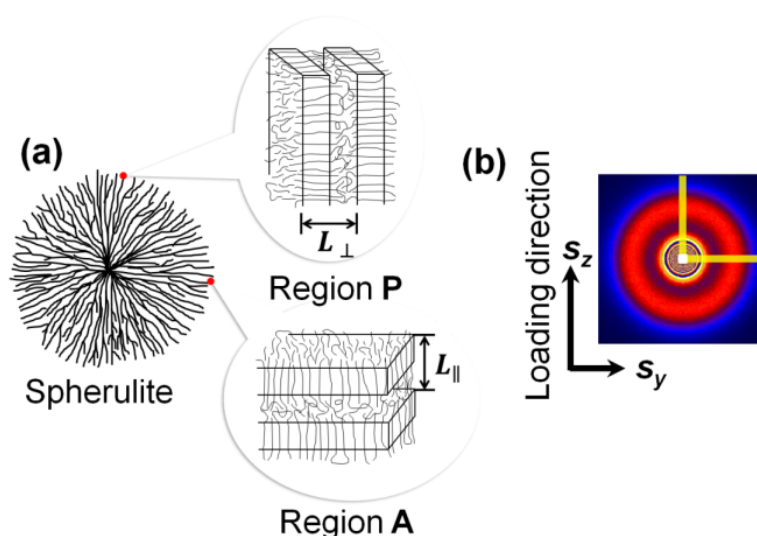
Figure 9-3 (a) Schematic diagram of iPP spherulite and (b) the scattering pattern for the spherulite, the size of the pattern is ± 0.0525 nm^{-1} $\times$ ± 0.0525 nm^{-1}. $L_p^{\parallel}$ can be obtained from the slice (the yellow strip) along s_z, and $L_p^{\perp}$ can be obtained from the slice along s_y. y and z stand for the equator and meridian directions in the scattering pattern, respectively.

In order to get a comprehensive evolution of crystalline structure during creep, the long period (L_p) in both regions are depicted in **Figure 9-4**. The one along the loading direction is labeled as $L_p^{\parallel}$ and the other one is labeled as $L_p^{\perp}$. It can be found that for both $L_p^{\parallel}$ and $L_p^{\perp}$ the whole curve could be divided into 4 stages, which coincides very well with the evolution of macroscopic Δd in **Figure 9-1a**.
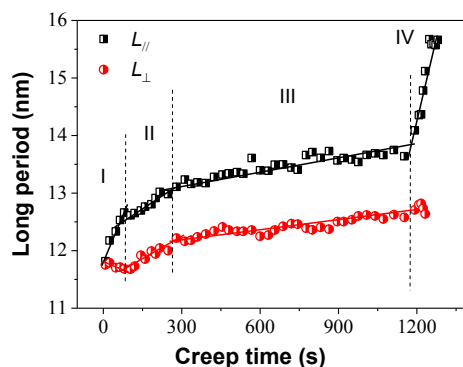
Figure 9-4 Evolution of long period along ($L_p^{\parallel}$) and perpendicular ($L_p^{\perp}$) to loading direction during creep.

In region I (primary creep), $L_p^{\parallel}$ increases linearly with creep time, whereas $L_p^{\perp}$ decrease slightly. As mentioned above, the deformation in region I is caused by the elastic deformation of the amorphous region which has a lower modulus compared to that of the crystalline region. The increase of $L_p^{\parallel}$ suggests that the molecular chains along loading direction are stretched.[321] As to the decrease of $L_p^{\perp}$, it means that the molecular chains perpendicular to loading direction are compressed. The compressing force comes from the squeeze of expanded lamellae along loading direction.[322] Region II is the transition stage. In region III (secondary creep), the evolution of $L_p^{\parallel}$ and $L_p^{\perp}$ show a similar trend. Both of them increase with creep time. The increase rate of $L_p^{\parallel}$ and $L_p^{\perp}$ can be obtained by linear fitting. The increase rate for $L_p^{\parallel}$ and $L_p^{\perp}$ are 6.34×10^{-4} nm·s^{-1} and 4.81×10^{-4} nm·s^{-1}, respectively. In the work by Li,[312] the elongation of micron-scale spherulites along the loading direction, accompanying with the increase of nano-scale lamellar long period were also observed when ε_t is smaller than 17 %. The long period along loading direction in the work of Li [312] increases from about 17.7 nm before drawing to 20.5 nm at the end of secondary creep, which is different from the results in this work where it changed from 11.8 nm before loading to 13.74 nm at the end of secondary creep. The difference may be caused mainly by differences in the sample preparation process. Nevertheless, the relative increase in long period is nearly the same: 15.8 % in the work of Li and 16.4 % in this work. In the following part, a more detailed study about the evolution of $L_p^{\parallel}$ and $L_p^{\perp}$ is given, especially for the increasing rate of $L_p^{\parallel}$ and $L_p^{\perp}$. In region IV (tertiary creep), $L_p^{\parallel}$ increases strongly while $L_p^{\perp}$ remains constant within the range of

uncertainty. After 1232 s, no $L_p^\perp$ can be detected, because the lamellae are strongly aligned in tensile direction and the lamellae perpendicular to loading direction are fragmented.

In order to have a better understanding of the structural evolution in secondary creep, one-dimensional correlation function ($K(z)$) is employed to gain the domain thickness of iPP, including crystalline region thickness (L_c) and amorphous region thickness (L_a). $K(z)$ is given in **Equation (3-13)**. It can be found in **Figure 9-5** that domain thickness of iPP increases with creep time, the increase rate for $L_p^\parallel$ and $L_p^\perp$ are 10.3×10^{-4} nm·s^{-1} and 7.52×10^{-4} nm·s^{-1}, for $L_c^\parallel$ and $L_c^\perp$ are 8.04×10^{-4} nm·s^{-1} and 6.28×10^{-4} nm·s^{-1}. The increase rate for $L_a^\parallel$ and $L_a^\perp$ are very small, only 2.29×10^{-4} nm·s^{-1} and 0.96×10^{-4} nm·s^{-1}, respectively. So, the increase of L in secondary creep could be attributed to the thickening of lamellae.
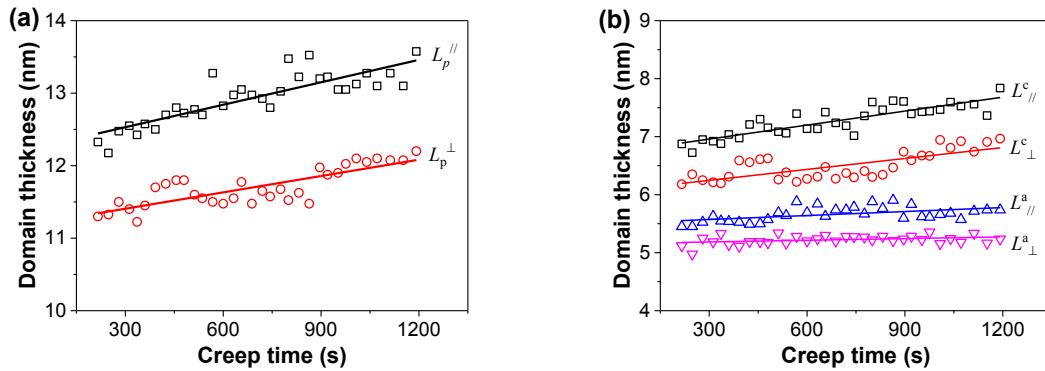
Figure 9-5 Evolution of long period along and perpendicular to loading direction during creep ($L_p^\parallel$ and $L_p^\perp$) **(a)** and evolution of thickness of crystalline and amorphous regions ($L_c^\parallel$, $L_c^\perp$, $L_a^\parallel$, and $L_a^\perp$) **(b)**.

For thin polymer crystals, the thermodynamic force capable of driving the thickening phenomena arises from the unequal free energies of the fold and lateral surfaces, the crystal moving in the direction of lowest free energy. By analogy with other irreversible processes, an appropriate phenomenological law for the rate of polymer crystal thickening can be expressed as [163]

$$\frac{dy}{dt} = \frac{2}{\tau}\left(\frac{1-y^{3/2}}{y}\right)$$

Equation (9-4)

$$y = l/l^*$$

Equation (9-5)

$$\frac{1}{\tau} = \frac{k\sigma_e}{l^{*2}}$$

Equation (9-6)

where l is the thickness of lamellae, l^* is the equilibrium thickness, t is time, τ is the relaxation time of chain segment, and k is the proportionality constant. Then the force dependence of the thickening rate should enter the theory through k, by invoking a molecular mechanism that involves the cooperative motion of a certain minimum number of molecular chains which have attained "liquid-like" mobility. For one molecular chain in the crystal, the free energy fluctuation needed to attain liquid-like mobility equal to the Gibbs free energy of melting, which in the simplest approximation is given by

$$\Delta G = \Delta H (T_m^0 - T)/T_m^0 = \Delta H \Delta T / T_m^0 \qquad \textbf{Equation (9-7)}$$

where ΔH is the heat of fusion per molecular chain and T_m^0 is the equilibrium melting point of the crystal. If ν is the minimum number of molecular chains required for this cooperative motion, then the probability that v molecular chains will simultaneously suffer a free energy fluctuation of ΔG is proportional to the product of the individual probabilities, or $\exp(-\nu \Delta G/RT)$, where R is the gas constant. Thus, k for this mechanism is given by [323]

$$k \propto k_0 exp[-\nu \Delta H \Delta T / RT T_m^0] \qquad \textbf{Equation (9-8)}$$

Generally, the structure of iPP could be well described by a skeleton of a crystalline phase with an amorphous phase between the crystallites.[36, 201, 306] In a recent work by Sotta[36] it is proved that the local tensile strain of lamellae is lower than the macroscopic one. The reduced local tensile strain must be compensated mainly by shear deformation in the amorphous phase causing an enhanced orientation of the chains within the amorphous regions. This enhances the probability for such cooperation and decreases the energy barrier, thus the rate for the increase of $L_p^{\|}$ is larger than that for $L_p^{\perp}$. This behavior is confirmed by the higher thickening rate along loading direction, shown in Figure 5.

9.3.2 Lamellae tilting and rotation

During tertiary creep, 2D-SAXS pattern changes from a slight ellipse into a distinct ellipse. For comparison, an isotropic 2D-SAXS pattern at the beginning of creep is also provided, see **Figure 9-6a** and **Figure 9-6b**. **Figure 9-6c** presents the long period as a function of azimuthal angle (φ) with respect to the loading direction. It can be found that before loading, the long period in all directions stays constant at 14 nm. For the elliptical pattern at 1208 s, the long period is greatest along loading direction and decreases gradually towards the direction perpendicular to the loading direction. During uniaxial drawing, the appearance of distinct

elliptical SAXS pattern is ascribed to intra-lamellae slip of those lamellae inclined to the loading direction. [209]
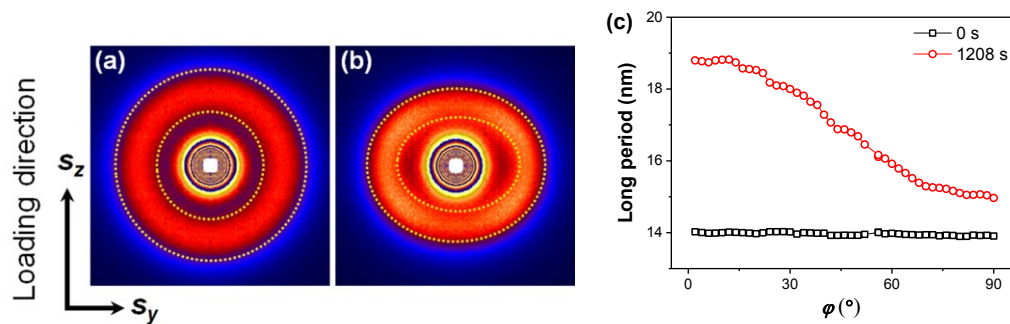
Figure 9-6 (a) Isotropic 2D-SAXS pattern at 0 s and **(b)** elliptical 2D-SAXS pattern at 1208 s in tertiary creep, the size of the pattern is ± 0.0525 nm$^{-1} \times \pm 0.0525$ nm^{-1}, color scale like in Figure 9-2; **(c)** long period as a function of azimuthal angle (φ) with respect to the loading direction.

Generally, the appearance of the elliptical pattern is related to lamellae tilting and rotation. The interpretation of the elliptical reflection is still an on-going topic up to now. In the very recent work by Murthy and his coworkers,[203, 320] models using an equilibrium distribution of molecular orientations and lamellar tilts are proposed which can predict elliptical reflections. Whereas, the models require some assumptions, these make the physical background of the fitting parameters unclear. So, a directly assignable structural basis for the parameters in their model is not possible yet. Therefore, the calculation of the lamellae tilting angle and rotating angle with respect to the loading direction remains unsolved in this work.

9.3.3 Lamellae orientation and fibrillary structure formation

As time further increases, the SAXS pattern transforms from ellipse to a "two-spot" pattern (see **Figure 9-7**), indicating that after lamella rotation and tilting, stress-induced crystalline block disaggregation happened, forcing the lamellae to orientate along loading direction. In addition, the "spot" exhibits a pronounced broadening in the equatorial direction. Such a broadening might be either due to misalignment of the lamellar structures with respect to the stretching direction or due to the limited lateral dimension of the lamellae making up the stacks.[324]
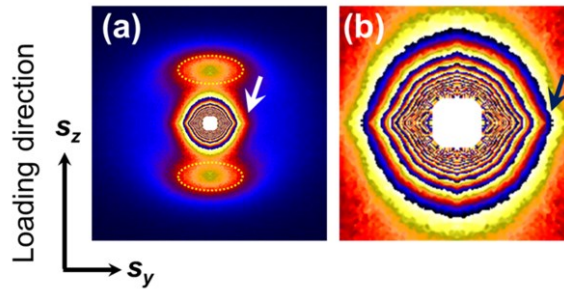
Figure 9-7 (a) "Two-spot" SAXS pattern with a streak signal (shown by the arrow) at 1248 s, the size of the pattern is $\pm 0.0525 \text{ nm}^{-1} \times \pm 0.0525 \text{ nm}^{-1}$; **(b)** is the enlargement of the center region of (a) with a size of $\pm 0.0262 \text{ nm}^{-1} \times \pm 0.0262 \text{ nm}^{-1}$, color scale like in Figure 2.

Herman's orientation function [94] could be used to calculate the degree of the lamellae orientation along loading direction. The lamellae orientation degree is 0.45 after yielding and it increases to 0.5 with time (see **Figure 9-8**).
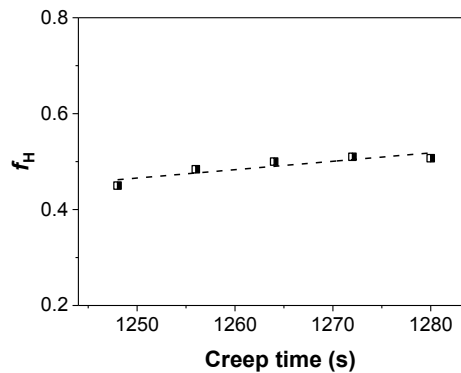
Figure 9-8 Herman's orientation degree of lamellae after yielding, corresponding to a creep time from 1248 s to 1280 s.

In addition to "two-spot" scattering signal, a streak (shown by the arrow) in equator direction could be found in **Figure 9-7**. The appearance of the streak indicates the formation of the fibrillary structure after yielding. Consuming that the fibrillary structure is oriented along the loading direction perfectly, the length of the fibrillary structure along ($L_f^{\parallel}$) and perpendicular to ($L_f^{\perp}$) loading direction can be evaluated by **Equation (2-14)**. The results are given in **Figure 9-9**.
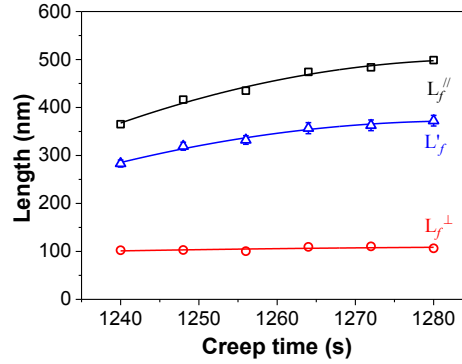
Figure 9-9 The length of the fibrillary structure along ($L_f^{\parallel}$) and perpendicular ($L_f^{\perp}$) to the loading direction under the assumption that the fibrillary structure is perfectly oriented, and the length (L_f') of the fibrillary structure after taking the misorientation into account as a function of creep time. The solid lines are the second order polynomial fitting for the experimental data for $L_f^{\parallel}$ and L_f' as well as a linear fit for $L_f^{\perp}$.

It can be found that $L_f^{\parallel}$ increases from 365 nm to 497 nm and $L_{f\perp}$ keeps at 102 nm. If misorientation of the fibrillary structure is taken into account, then the decrease of B_{obs} (s) with increasing s is a function of the analytical shape of the orientation distribution. The relation follows **Equation (2-15)**. L_f' as a function of creep time is also presented in **Figure 9-9**. One can see that L_f' shows a similar trend as $L_f^{\parallel}$ but it is slightly smaller than $L_f^{\parallel}$. L_f' is 283 nm once it is formed, and then it increases to 372 nm finally. It should be mentioned that there could be artificial errors due to the polydispersity of the fibrillary structure, which is not considered in the Ruland's method.[89] $L_f^{\parallel}$, $L_f^{\perp}$, and L_f' given in **Figure 10** are average value each of two measurements. In order to estimate the statistical certainty, $L_f^{\parallel}$, and L_f' are fitted by a second order polynomial

$$y = a_1 x^2 + a_2 x + a_3 \qquad\qquad \textbf{Equation (9-9)}$$

The fitted lines for these approximations are added in **Figure 9-9,** the coefficients of determination for both curves are $R^2 = 0.987$. $L_f^{\perp}$ is approximated by a straight line, the standard deviation is 4.1. Generally, the formation of the fibrillary structure could be triggered by lamellae breaking and reorganization during yielding.[312, 325] By comparing the length of the fibrillary structure (either $L_f^{\parallel}$ or L_f') with the long period of original lamellae (16 nm), it could be inferred that the formation of fibrillary structure needs the disaggregation of a group of lamellae connected by tie molecular chains.

9.4   Conclusions

The microstructure evolution during creep is investigated by in situ synchrotron SAXS. Results reveal that the microstructural evolution in a different creep stage differs from each other distinctly, especially in secondary and tertiary creep. During primary creep, strain grows nonlinearly to a value less than 15 % in a short time. In this stage, the long period along loading direction ($L_p^{\parallel}$) increases with time, whereas the long period perpendicular to loading direction ($L_p^{\perp}$) decreases slightly. The change of long period is caused by elastic deformation of molecular chains in the amorphous phase. In secondary creep, strain increases linearly with time. Both $L_p^{\parallel}$ and $L_p^{\perp}$ exhibit the same tendency with strain. The increase rate of $L_p^{\parallel} L_{\parallel}$ is larger than that of $L_p^{\perp}$, which benefits from a higher polymer chains orientation along loading direction. In tertiary creep, strain grows dramatically within a limited time, and the yielding of iPP happens in this stage. The reflections in 2D-SAXS pattern changes from light ellipse to a distinct ellipse firstly, and then grows into "two-spot" pattern. This significant transition indicates that the lamellae are tilted and rotated during the yielding process. After that, the lamellae are disaggregated and aligned mainly along the loading direction, leading to the yielding of the specimen. The lamellar orientation degree is about 0.45 after yielding, and it increases to 0.5 with creep time. In addition, fibrillary structure could be induced after yielding by lamellae breaking and subsequent reorganization. By Guinier' approximation the blank region in the small scattering angle region is extrapolated. Afterward, it is calculated that the length of the fibrillary structure increases from 364 nm to 497 nm as creep time increases; and its width keeps at 102 nm.

10   Microstructural evolution of iPP during stress relaxation[7]

The structural evolution of iPP during stress relaxation is investigated. The results show that the local deformation behavior of the long period is affine with the macroscopic stress relaxation. However, the evolution of the crystal orientation and the void size lag behind the macroscopic stress relaxation. The decrease of the long period is mainly caused by the relaxation of the strained polymer chains in the amorphous phase. The retardation of the evolution of the crystal orientation is probably caused by the phase transition from stable α-iPP to metastable mesomorphic-iPP. By phase transition, the highly oriented α-iPP is transferred to weakly oriented mesomorphic-iPP. Due to the fact that the void is confined by the network of the strained polymer chains where lamellae blocks serve as the physical anchoring points, the phase transition contributes greatly to the viscoplastic deformation of the network. Consequently, the evolution of the voids size shows a similar trend with that of the phase transition.

---

[7] The main part in this chapter will be submitted as "B. Chang, K. Schneider, G. Heinrich. Structural evolution of oriented isotactic-polypropylene during stress relaxation"

10.1 Introduction

In order to predict the mechanical response of semicrystalline polymers, numerous constitutive equations/models are derived in the past. For instance, the William-Landel-Ferry equation[293] is employed to rebuild the master curve of creep compliance. Popelar proposed a nonlinear viscoelastic model based on the viscoelasticity theory to develop the master curves for the relaxation modulus, maximum stress and the time-to-failure.[326] Khan and Zhang suggested a phenomenological viscoelasto-plastic constitutive model, presented by a series connection of a viscoelastic deformation module (represented by three elements standard solid spring dashpot model) and a viscoplastic deformation module represented by KHL (Khan, Huang and Liang) model, to describe the time dependent mechanical behavior of polytetrafluoroethylene qualitatively and quantitatively under uniaxial static and dynamic compression, creep and relaxation.[327] More recently, a viscoplasticity Theory Based on Overstress for Polymers (VBOP) was modified by Krempl et. al. to model the nonlinear behavior of PA66 and high density polyethylene (HDPE).[328]

One of the key topics during the establishment of the model is to correlate the microstructural evolution with the viscoelastic/viscoplastic response of semicrystalline polymers under mechanical load reasonably. Generally, the semicrystalline polymers are regarded as a two-phase continuum formed by a crystalline skeleton surrounded by the amorphous phase.[329] When the deformation temperature is higher than the glass transition temperature (T_g), the amorphous phase is in the rubbery state. The viscoplastic response of the crystalline phase includes fine and coarse slips of lamellae blocks. The viscoelastic response of the amorphous phase is associated with thermally activated rearrangement of strained polymer chains confined by lamellae blocks. The viscoplastic response of the amorphous phase is determined by the disentanglement of chains in the amorphous phase or detachment of chain folds and loops from surfaces of lamellae blocks.

In this chapter, the microstructural evolution during stress relaxation is monitored by in-situ synchrotron WAXS and SAXS. Before the stress relaxation, the homogeneous as compression molded specimens were stretched to produce oriented samples where the normal of the interior lamellae blocks are oriented along the stretching direction during stress relaxation. The evolution of the crystal orientation, the long period and also the size of the voids during stress relaxation are characterized. The aim of this work is to gain a deeper insight into the relationship between the microstructural evolution and viscoelastic-viscoplastic properties of semicrystalline polymers under mechanical load.

10.1.1 The structural evolution during stress relaxation at 60 ^{o}C

10.1.1.1 Phase transition and crystal orientation

The stress relaxation tests were performed on the custom-made tensile machine shown in **Figure 3-3**. The temperature was controlled by the heat gun. The stress during relaxation was recorded by the load cell. The stress-time curve during stress relaxation at 60 ^{o}C is shown in **Figure 10-1a**. With the increase of the relaxation time, the stress exhibits a nearly exponential decay, which can be described by

$$\sigma = \sigma_e + \sigma_0 \left[\exp(-\frac{t}{\eta_\sigma}) \right]$$ **Equation 10-1**

The former part (σ_e) is the elastic contribution part, and the rest part is the time-dependent stress part with η_σ is the characteristic relaxation time.

Synchrotron 2D-WAXS measurements were in-situ performed during the stress relaxation. Representative 2D-WAXS patterns during stress relaxation are provided in **Figure 10-1b**. On the initial 2D-WAXS pattern before relaxation, a few crystal planes can be found, which are (110), (040), (130), and (111)/(-131) from inner to the outer.[330] All crystal planes belong to α-iPP. The 2D-WAXS pattern shows a highly oriented fiber-symmetry due to the pre-stretching. In particular, the scattering of (110), (040), and (130) crystal planes is focused on the meridian. The scattering of (111)/(-131) crystal plane is focused at an angle off to the meridian. On the 2D-WAXS pattern after relaxation, the scattering intensity of the crystal planes is decreased obviously. In addition, a halo at scattering vector (s), $s = 2sin\theta/\lambda$, θ is the scattering angle and λ is the wavelength, of 1.6 nm^{-1} shows up indicating the formation of mesomorphic-iPP.[331, 332] The vertical cut (V-cut) and horizontal cut (H-cut) extracted from the 2D-WAXS patterns are reported in **Figure 10-1c** and **d**. On V-cut, the scattering intensity of the crystal plane decreases drastically as the relaxation time exceeds 40 s. With the further increases of relaxation time, the scattering intensity of the crystal planes continues to decrease. On H-cut, the intensity of the halo increases obviously as the relaxation time is larger than 40 s. What's more, the position of the halo shifts towards higher scattering vector (s) side. The results in **Figure 10-1c** and **d** indicate the transformation from α-iPP to the mesomorphic-iPP during relaxation.[183, 331] The formation of mesomorphic-iPP indicates that polymer chains are sliding out from the crystals.[204]
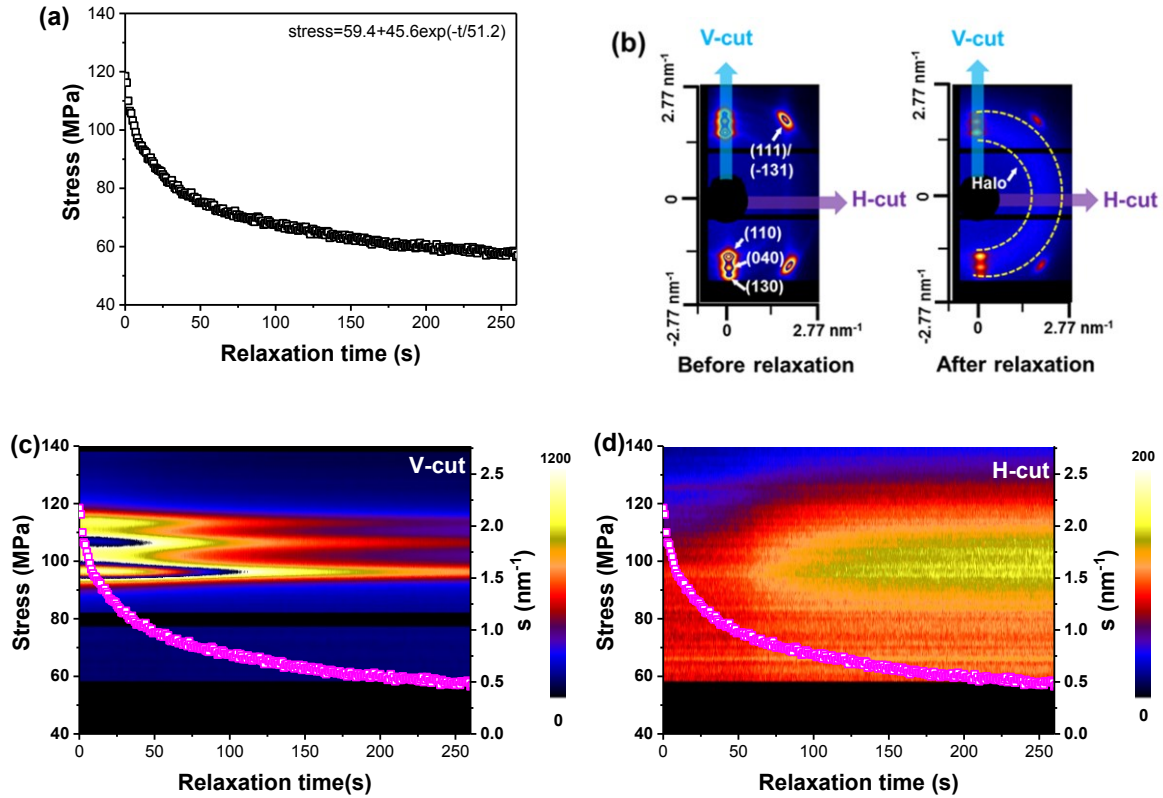
Figure 10-1 (a): Stress-relaxation curve at 60 $^{\circ}$C; **(b)**: representative 2D-WAXS pattern before relaxation and after relaxation, the stretching direction is horizontal; **(c)** and **(d)**: the vertical cut (V-cut) and horizontal cut (H-cut) extracted from the 2D-WAXS patterns collected during relaxation. s is scattering vector with $s = 2sin\theta/\lambda$, θ is the diffraction angle and λ is the wavelength of the X-ray.

The orientation of the crystal can be evaluated from the distribution of intensity of the crystal planes along the azimuthal angle. This is particularly evident for the changes in the azimuthal intensity distribution of (110) and (040) crystal planes, as shown in **Figure 10-2a** and **b**. In **Figure 10-2a**, the intensity around the meridian (azimuthal angle equals 90 $^{\circ}$) reduces obviously from 1350 a.u. before relaxation to 450 a.u. at the end of relaxation. In the meantime, the intensity around the equator (azimuthal angle equals 180 $^{\circ}$) increases from 85 a.u. (before relaxation) to 143 a.u. (after relaxation). The evolution of the distribution of intensity of (040) crystal plane (shown in **Figure 10-2b**) owns a similar trend with that of (110) crystal plane.
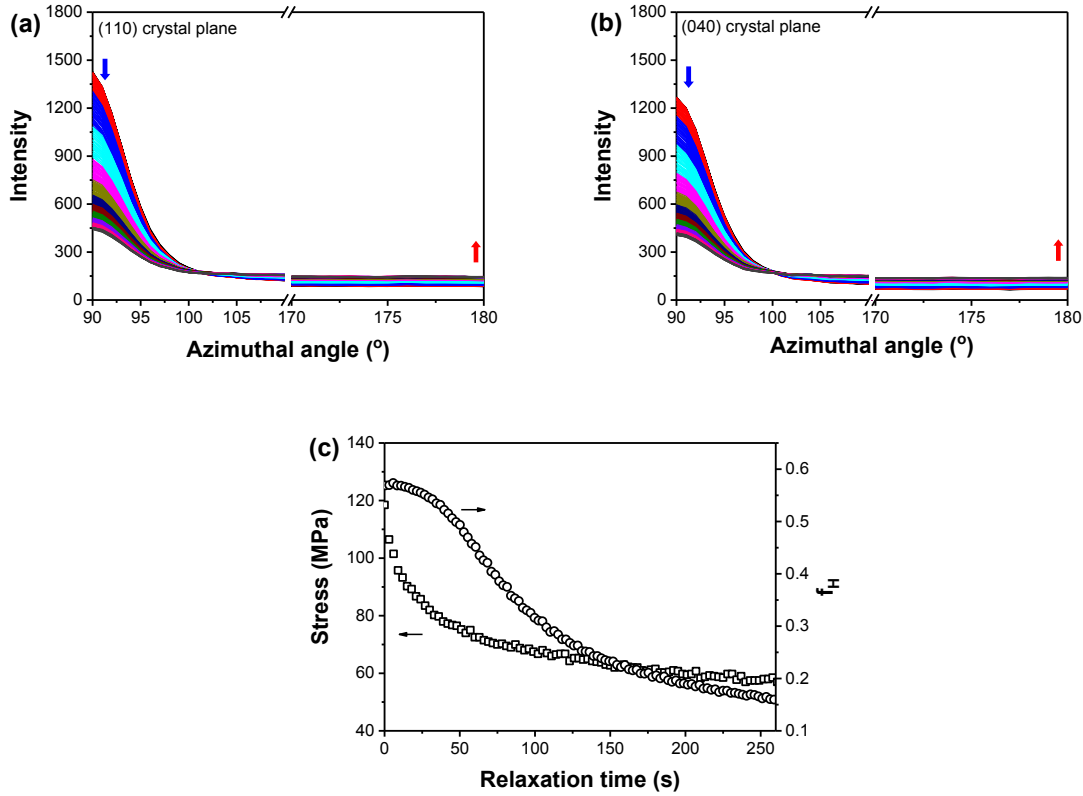
Figure 10-2 (a) and **(b)** Distribution of intensity along the azimuthal angle of (110) crystal plane and (040) crystal plane extracted from the WAXS patterns during relaxation at 60 °C; **(c)**: Herman's orientation factor (f_H) of the *c*-axis of the crystal as a function of the relaxation time.

The polarization intensity in the meridian of (110) and (040) crystal plane originates from the orientation of parallel chain axis along the loading direction. The Herman's orientation factor (f_H) is employed to describe the crystal orientation quantitatively.[333] For *α*-iPP, which belongs to monoclinic crystal system, the orientation of the polymer chains in the crystal can be estimated by combining the Wilchinsky method.[94] The evolution of f_H as a function of relaxation time is presented in **Figure 10-2c**. Different to the exponential decay of the macroscopic stress, f_H follows reverse S-shaped decrease. As the relaxation time is smaller than 40 s, f_H decreases slightly. However, in this region, the macroscopic stress suffers a steep decrease. As the relaxation time exceeds 40 s, a distinct reduction of f_H from 0.52 to 0.26 occurs but the macroscopic stress decreases only moderately. When the relaxation time is larger than 125 s, f_H and the macroscopic stress decrease slightly with relaxation time. The distinctly different relaxation modes of f_H and the macroscopic stress reveal the discrepancy between microscopic and macroscopic mechanical relaxation.

10.1.1.2 The cavitation behavior

The stress relaxation at 60 °C during 2D-SAXS measurement is shown in **Figure 10-3a**. Representative 2D-SAXS patterns during stress relaxation are provided in **Figure 10-3b**. On the 2D-SAXS pattern before relaxation, a streak can be found on the meridian. Normally, the appearance of a streak signal on the 2D-SAXS pattern indicates the formation of highly voids. In this case, the appearance of the streak signifies the formation of the voids. The streak is aligned vertically, considering that the stretching direction is horizontal, it can be inferred that the longitude of the voids is along the stretching direction. On the 2D-SAXS pattern after relaxation, the intensity of streak signal is reduced obviously, suggesting the change of the voids size. Additionally, no lamellae scattering during the whole relaxation process can be found. Two possible reasons are proposed to responsible for that: the first one is that the scattering from the voids is too strong, covering the scattering of the lamellae; the second one is that the density contrast between the amorphous phase and the crystal phase is too small, compared with that between the amorphous phase and the voids.
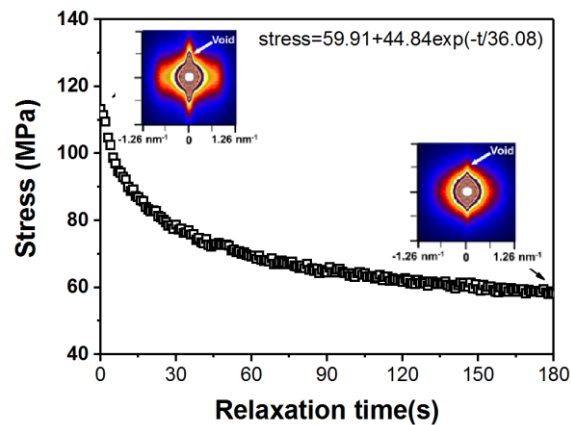
Figure 10-3 The stress-time curve during stress relaxation at 60 °C, and selective 2D-SAXS patterns during the relaxation process. The stretching direction is horizontal. The streak in the pattern indicates the existence of voids in the sample.

The size of the voids can be evaluated by the Ruland's streak method,[89] which has been introduced in the previous chapter.[245] The evolution of the voids size as a function of the relaxation time is presented in **Figure 10-4a**. As the relaxation time is smaller than 30 s, the voids length decreases slightly and the voids width remains nearly constant. When the relaxation time is larger than 30 s, a steep decrease of the voids length and a sharp increase of the voids width appear. In detail, the voids length is decreased from 215 nm to 182 nm as relaxation time is increased from 30 s to 80 s. As the relaxation time is further increased, the

138

voids length decreases continually to 158 nm and the voids width is increased slightly from 25 nm 37 nm. The results show that upon stress relaxation, voids are closed in the longitude direction and widened in the transverse direction. Assuming that the shape of the voids is a cylinder,[89] the volume of the voids is estimated and the result is given in **Figure 10-4b**. It is interesting to point out that the volume of the voids shows a similar evolution trend with the voids width. In the first 30 s, the volume of the voids stays nearly unchanged. As the relaxation time is larger than 30 s, an obvious increase of the volume of the voids can be seen. And the volume of the voids reaches a plateau when the relaxation time is larger than 80 s. The evolution of the scattering invariant is given in **Figure 10-4c**, which can be divided into two regions. Before 50 s, the scattering invariant is increased gradually to a maximum of 2.9×10^{7}, which can be ascribed to the widening of the voids. After that, the scattering invariant follows an exponential decrease. Considering that the voids volume is hardly changed as shown in **Figure 10-4b**, the reduction of the scattering invariant can be ascribed to the collapse of the voids.
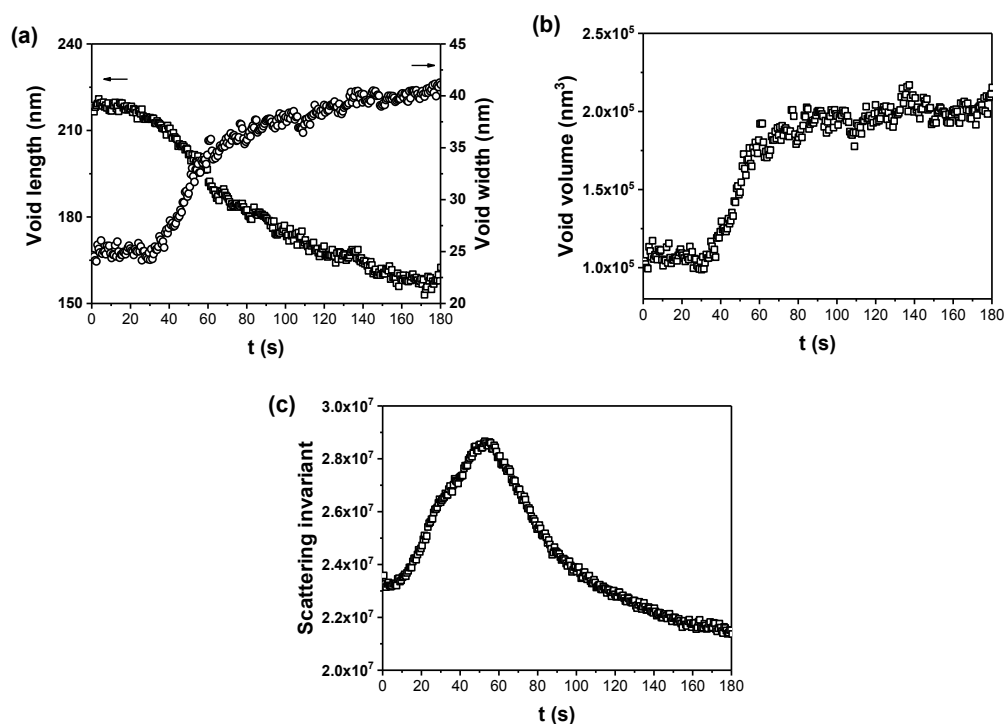
Figure 10-4 The evolution of the voids length and the voids width (a), the voids volume (b), and the scattering invariant (c) during the stress relaxation at 60 $^{\circ}$C.

10.1.2 The structural evolution during stress relaxation at 90 °C

10.1.2.1 Phase transition and crystal orientation

The stress relaxation behavior at 90 °C is similar to that at 60 °C. As expected, with the increase of relaxation time, the stress exhibits exponential decay. Representative 2D-WAXS patterns are shown in **Figure 10-5**. Generally, with increasing relaxation time the scattering intensity of the crystal planes is decreased and the scattering intensity of the halo is enhanced, suggesting that the α-iPP transforms into mesomorphic-iPP gradually.
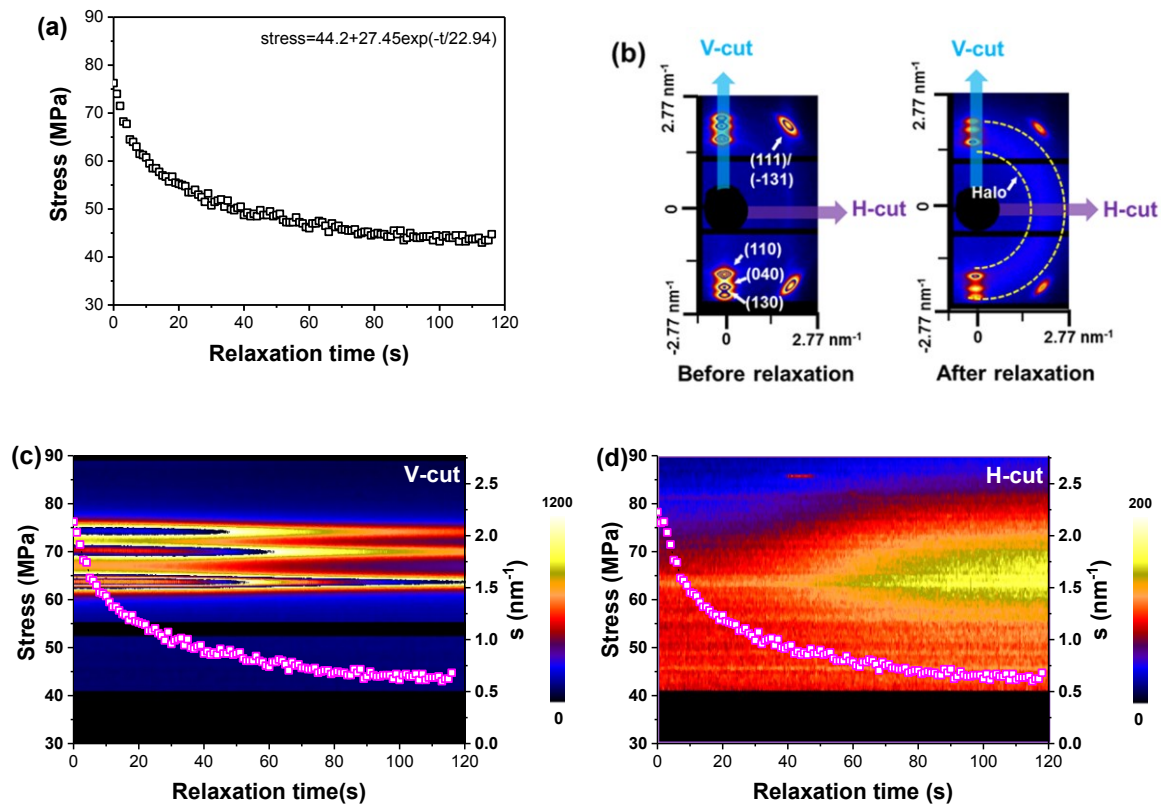
Figure 10-5 (a): Stress-time curve during relaxation at 90 °C; **(b)**: representative 2D-WAXS pattern before relaxation and after relaxation, the stretching direction is horizontal; **(c)** and **(d)**: the V-cut and H-cut extracted from the 2D-WAXS patterns collected during relaxation.

Moreover, the azimuthal intensity distribution of (110) and (040) crystal planes are shown in **Figure 10-6a** and **b**. The decrease at the azimuthal angle of 90 ° and increase at the azimuthal angle of 180 ° verify the transformation of α-iPP to mesomorphic-iPP. Additionally, the evolution of the polymer chains in the crystal owns the reverse S-shape which is similar to that at 60 °C.
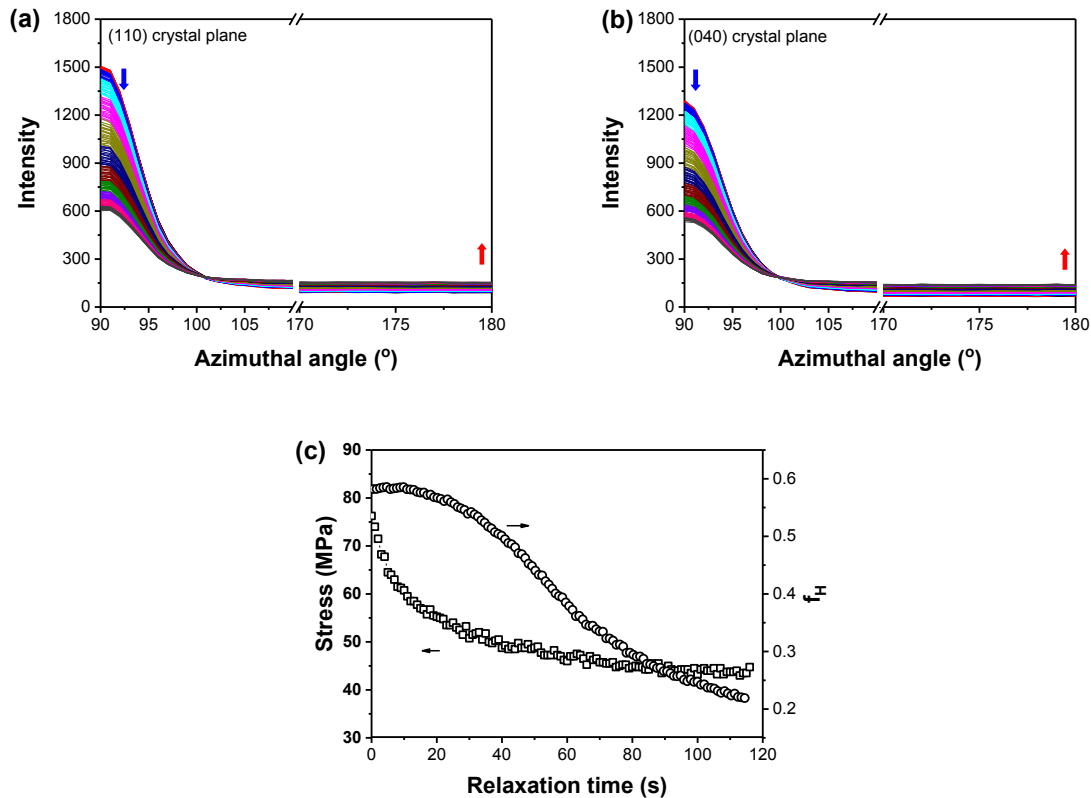
Figure 10-6 (a) and **(b)** Distribution of intensity along the azimuthal angle of (110) crystal plane and (040) crystal plane extracted from the 2D-WAXS patterns during relaxation at 90 °C; **(c)**: Herman's orientation factor (f_H) of the **c**-axis of the crystal as a function of the relaxation time.

10.1.2.2 The evolution of the long period

The stress relaxation at 90 °C during SAXS measurement is shown in **Figure 10-7a**. Representative 2D-SAXS patterns during stress relaxation are provided in **Figure 10-7b**. On the SAXS pattern before relaxation, a weak streak can be found on the meridian which is similar to that at 60 °C. Additionally, two scattering spot originated from the lamellae scattering can be found on the equator. On the pattern after relaxation, the intensity of streak signal is decreased. In the meantime, the intensity of the lamellae is also reduced.
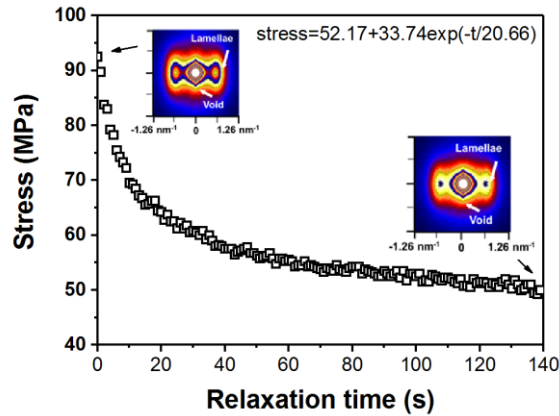
Figure 10-7 The stress-time curve during stress relaxation at 90 °C, and selective 2D-SAXS patterns during the relaxation process. The stretching direction is horizontal.

The appearance of equatorial "two spots" pattern on the SAXS patterns indicates the formation of the well-oriented fiber morphology, which is in agreement with the WAXS results of **Figure 10-5**. In the oriented morphology, the α-iPP lamellae are periodically stacked along the stretching direction, separated by amorphous regions. The long period (consisting of one amorphous phase and one crystalline phase) calculated from the position of the intensity maxima q_{max} on the equator is shown in **Figure 10-8**. The long period exhibits a regular exponential decay with relaxation time, indicating that the local relaxation of the lamellar stacks is affine with the macroscopic relaxation. Since the lamellar stacks contributing to the intensity on the equator are those characterized by layers oriented perpendicular to the stretching direction, the decrease of the long period indicates lamellar shrinkage, facilitated by the high mobility of the polymer chains in the amorphous phase.
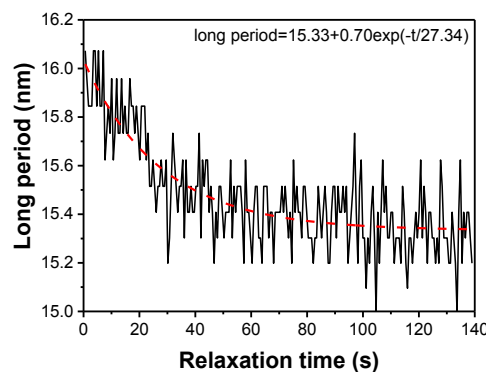
Figure 10-8 The evolution of the long period as a function of relaxation time during stress relaxation at 90 °C, the dashed red line is the fitted result of the raw data.

10.1.2.3 The cavitation behavior

The evolution of the voids size is presented in **Figure 10-9**. It can be found that in the first 80 s, both voids length and voids width stay nearly unchanged. As the relaxation time is increased from 80 s to 120 s, the voids length is decreased from 270.5 nm to 216.0 nm and the voids width is enlarged from 44.7 nm to 50.4 nm. The volume of the voids is nearly constant. The scattering invariant provided in **Figure 10-9c** shows that before 100 s, the scattering invariant is reduced only slightly. But as the relaxation time exceeds 100s, a steep decrease can be found on the curve, which should be caused by the collapse of the voids.
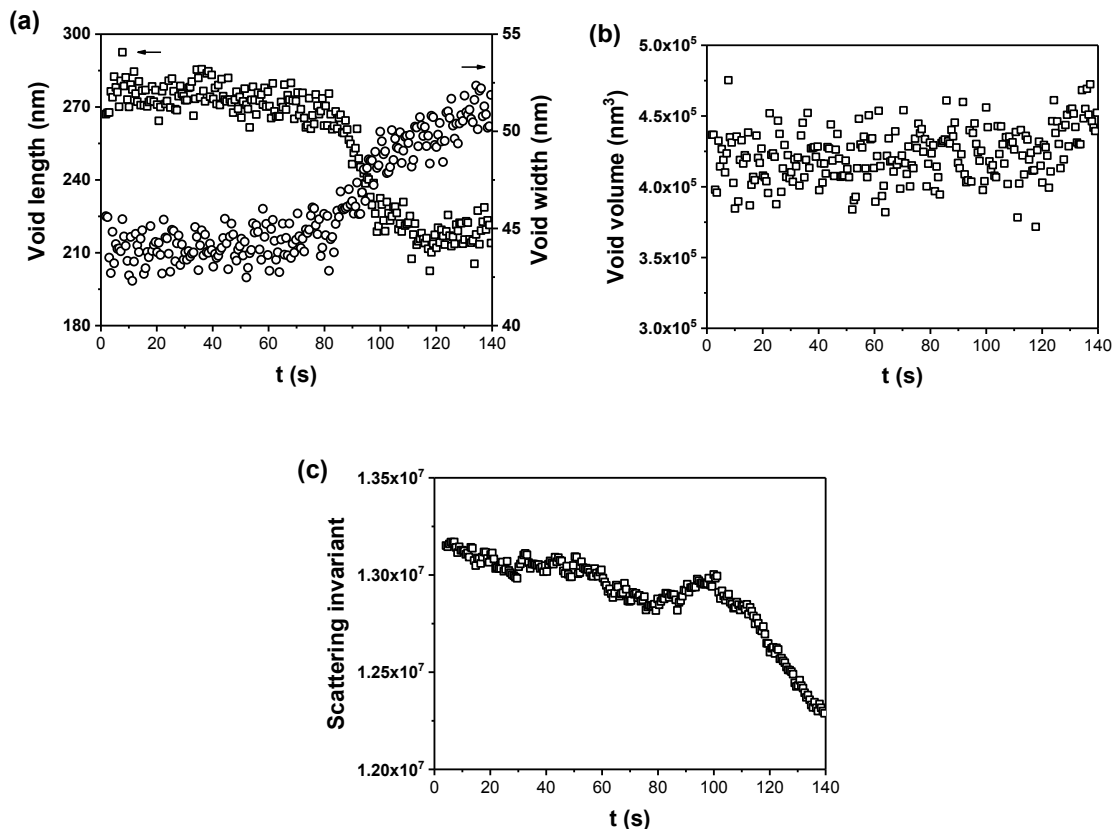
Figure 10-9 The evolution of the voids length and the voids width (a), the voids volume (b), and the scattering invariant (c) during the stress relaxation at 60 ^{o}C.

The results above reveal that the local relaxation behavior of the long period is affine with macroscopic stress relaxation. However, the evolution of the crystal orientation and the voids size lag behind the macroscopic stress relaxation. During stress relaxation, the semicrystalline polymer can be regarded as a two-phase continuum consisting of a crystalline skeleton and an amorphous phase treated as a transient network of chains.[334] Numerous attentions have been devoted to developing the constitutive models for semicrystalline polymers.[326, 328,

335] The relationship between microstructural evolution and the viscoelastic-viscoplastic property of the polymer was investigated. On the micro-level, the viscoplastic response of the crystalline phase was proposed to originate from the fine (homogeneous shear of crystal blocks) and coarse (heterogeneous inter-lamellar sliding) slip of lamellar blocks, the rotation and twist of individual lamellae and lamellar stacks, and micro-necking of lamellae.[329] The results in this study show that the phase transition from α-iPP to mesomorphic-iPP should also be taken into account for the viscoplastic deformation of the crystalline phase. The schematic drawing of the structural evolution during stress relaxation is provided in **Figure 10-10**.
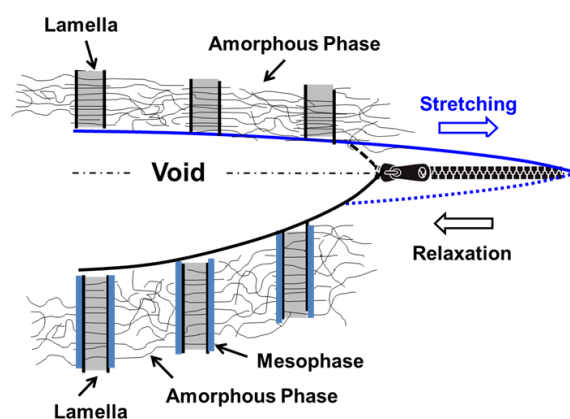
Figure 10-10 The schematic drawing of the structural evolution during stress relaxation.

The viscoelastic response of the amorphous phase is associated with thermally activated rearrangement of strained chains in the network, for instance the separation of active strands.[336] The affine deformation of the long period with macroscopic stress relaxation indicates that the decrease of the long period is mainly controlled by the relaxation of the strained polymer chains in the amorphous phase. The viscoplastic response of the amorphous phase is associated with disentanglement of polymer chains in the amorphous phase, chain slip through the crystals, or sliding of tie chains on the surfaces of lamellae. During stress relaxation, the disentanglement of polymer chains could be excluded since that the stress on the polymer chains is decreased with relaxation time. As has been proved in **Figure 10-2** and **Figure 10-6**, the stable α-iPP is transferred to metastable mesomorphic-iPP. The arrangement of polymer chains in mesomorphic-iPP is of a lower order than that in α-iPP,[24] which benefits the sliding of tie chains during relaxation. The size of the voids is much larger than the long period, it is reasonable to assume that the geometry of the voids is confined by the network of the strained polymer chains with lamellae blocks serving as the physical anchoring point. The viscoplastic response of the network correlates intimately with the phase transition

144

from α-iPP to mesomorphic-iPP. Therefore, the evolution of the voids size as a function of relaxation time exhibits a distinctive trend with the macroscopic stress relaxation.

10.2   Conclusion

The structural evolution of iPP during stress relaxation is investigated. The results show that the local deformation behavior of the long period is affine with macroscopic stress relaxation. However, the evolution of the crystal orientation and the voids size shows a distinctive trend with the macroscopic stress relaxation. The decrease of the long period is proposed to be mainly caused by the relaxation of the strained polymer chains in the amorphous phase. The distinct different evolution trend of the crystal orientation is caused by the phase transition from stable α-iPP to metastable mesomorphic-iPP. Since that the geometry of the voids is confined by the network of the strained polymer chains with lamellae blocks serving as the physical anchoring point. The viscoplastic response of the network correlates intimately with the phase transition from α-iPP to mesomorphic-iPP. Therefore, the evolution of the voids size as a function of relaxation time exhibits a distinctive trend with the macroscopic stress relaxation.

11   Conclusion and outlook

In this study, the structural evolution of iPP with well-defined microstructure under mechanical load is in-situ monitored by synchrotron X-ray scattering. The microstructure inside the sample is controlled either by annealing or adding nucleating agent. And three types of mechanical loads (uniaxial stretching, creep, and stress relaxation) are employed.

❖ During uniaxial stretching, we revealed how lamellae deformation occurs in the time scales of elastic deformation, intra-lamellar slip, and melting-recrystallization, separated by three critical strains which were only rarely found to be influenced by annealing. On the other hand, annealing significantly decreases the critical strain for voids formation and increases the voids number, but restricts the void size. In addition, depending on the annealing temperature, two types of voids are confirmed according to their direction with respect to the stretching direction. And lastly, the formation of voids influences neither the critical strains for lamellae deformation nor the final long period, the orientation of polymer chains or the crystal size.

❖ It is also revealed that during uniaxial stretching, a higher relative content of β-iPP (K_β) in the sample could increase the number of the voids. And the takes place after voids formation. According to the critical strains determining the appearance of the β-α phase transition and lamellae twisting of β-iPP, the lamellae twisting is proposed to be responsible for the intense voids formation of the composite with higher K_β.

❖ During creep, the evolution of the long period can be divided into four stages (primary creep, transition stage, secondary creep, and tertiary creep). This fits quite well with the macroscopic displacement and strain evolution. The increase of the long period during secondary creep is proposed to be caused by lamellae thickening, which is a kind of cooperative motion of molecular chains with their neighbors onto the lamellae surface. The increasing rate of $L_p^{\parallel}$ is larger than that of $L_p^{\perp}$, indicating that the orientation of molecular chains along loading direction decreases the energy barrier for the cooperative motion.

❖ During stress relaxation, the evolution of the long period is affine with the macroscopic stress relaxation. However, the change of the crystal orientation and the void size lag behind the macroscopic stress relaxation. The retardation of the change of the crystal orientation is probably caused by the phase transition from stable α-iPP to metastable mesomorphic-iPP. By phase transition, the highly oriented α-iPP is transferred to weakly oriented mesomorphic-iPP. Due to the fact that the void is confined by the network of the strained polymer chains where lamellae blocks serve as the physical anchoring points, the phase transition contributes greatly to the viscoplastic deformation of the network. Therefore, the evolution of the voids size shows a similar trend with that of the phase transition.

Via the results in this study, the critical strains for lamellae deformation and voids formation during uniaxial stretching are revealed; the relationship between lamellae deformation or β-α phase transition with voids formation is discussed; the lamellae thickening during secondary creep is discovered; and lastly, the α-mesophase transition and changing of voids size during stress relaxation are investigated.

The aim of this work is to get a further insight into the relationship between structure-mechanical properties of semicrystalline polymers. But, it is obviously far from enough considering the still on-going discussions about the existed topics and ever increasing new problems. In case that more works should be done in this field, a few interesting topics are listed below:

❖ The deformation of the crystal and amorphous phase of semicrystalline polymers in the elastic range (before the yield point).

❖ The dependence of phase transition on temperature during stress relaxation.

❖ The application of the self-assembly process of the nucleating agent in polymer processing (fiber spinning, injection molding etc.).

12   References

[1] E. Gérard, E. Bessy, C. Salvagnini, V. Rerat, M. Momtaz, G. Hénard, P. Marmey, T. Verpoort, J. Marchand-Brynaert, Polymer 52 (2011) 1223-1233.

[2] H. Ohtaki, F. Deplace, G.D. Vo, A.M. LaPointe, F. Shimizu, T. Sugano, E.J. Kramer, G.H. Fredrickson, G.W. Coates, Macromolecules 48 (2015) 7489-7494.

[3] Q. Wang, J.P. Undrell, Y. Gao, G. Cai, J.-C. Buffet, C.A. Wilkie, D. O'Hare, Macromolecules 46 (2013) 6145-6150.

[4] G. Natta, P. Pino, P. Corradini, F. Danusso, E. Mantica, G. Mazzanti, G. Moraglio, J. Am. Chem. Soc. 77 (1955) 1708-1710.

[5] Ceresana, http://www.ceresana.com/en/market-studies/plastics/polypropylene/ (2014).

[6] K. Busse, J. Kressler, R.-D. Maier, J. Scherble, Macromolecules 33 (2000) 8775-8780.

[7] R. Androsch, M.L. Di Lorenzo, C. Schick, B. Wunderlich, Polymer 51 (2010) 4639-4662.

[8] B. Lotz, J.C. Wittmann, A.J. Lovinger, Polymer 37 (1996) 4979-4992.

[9] J.M.G. Cowie, V. Arrighi, Polymers: chemistry and physics of modern materials, CRC press2007.

[10] S.-G. Yang, Z. Zhang, L.-Q. Zhang, D. Zhou, Y. Wang, J. Lei, L. Li, Z.-M. Li, Polymer Chemistry 6 (2015) 4588-4596.

[11] A.J. Lovinger, J.O. Chua, C.C. Gryte, J Polym. Polym. Phys. Ed. 15 (1977) 641-656.

[12] S. Kitade, K. Asuka, I. Akiba, Y. Sanada, K. Sakurai, H. Masunaga, Polymer 54 (2013) 246-257.

[13] J. Chen, K. Schneider, S. Gao, R. Vogel, G. Heinrich, Polymer 76 (2015) 182-190.

[14] M. Dong, Z. Guo, J. Yu, Z. Su, J. Polym. Sci. B: Polym. Phys. 46 (2008) 1725-1733.

[15] S.V. Meille, S. Bruckner, W. Porzio, Macromolecules 23 (1990) 4114-4121.

[16] I. Coccorullo, R. Pantani, G. Titomanlio, Polymer 44 (2003) 307-318.

[17] C. De Rosa, F. Auriemma, T. Circelli, R.M. Waymouth, Macromolecules 35 (2002) 3622-3629.

[18] S. Brückner, S.V. Meille, V. Petraccone, B. Pirozzi, Prog. Polym. Sci. 16 (1991) 361-404.

[19] R.A. Campbell, P.J. Phillips, J.S. Lin, Polymer 34 (1993) 4809-4816.

[20] D. Van der Meer, University of Twente (2003).

[21] P.B. McAllister, T.J. Carter, R.M. Hinde, J Polym. Polym. Phys. Ed. 16 (1978) 49-57.

[22] D.M. Gezovich, P.H. Geil, Polym. Eng. Sci. 8 (1968) 202-209.

[23] S. Yuan, Z. Li, J. Kang, Y.-l. Hong, A. Kamimura, A. Otsubo, T. Miyoshi, ACS Macro Letters 4 (2015) 143-146.

[24] P. Corradini, V. Petraccone, C. De Rosa, G. Guerra, Macromolecules 19 (1986) 2699-2703.

[25] F. Zuo, J.K. Keum, X. Chen, B.S. Hsiao, H. Chen, S.-Y. Lai, R. Wevers, J. Li, Polymer 48 (2007) 6867-6880.

[26] M.L. Di Lorenzo, M.C. Righetti, POLYMER CRYSTALLIZATION 1 (2018) e10023.

[27] H. Suzuki, J. Grebowicz, B. Wunderlich, British Polymer Journal 17 (1985) 1-3.

[28] F.J.P. Jr., H.D. Keith, J. Appl. Phys. 30 (1959) 1479-1484.

[29] B. Chang, K. Schneider, N. Patil, S. Roth, G. Heinrich, Polymer 142 (2018) 387-393.

[30] Y. Quan, H. Li, S. Yan, Ind. Eng. Chem. Res. 52 (2013) 4772-4778.

[31] J. Varga, J. Karger-Kocsis, Polymer 36 (1995) 4877-4881.

[32] B.S. Hsiao, L. Yang, R.H. Somani, C.A. Avila-Orta, L. Zhu, Phys. Rev. Lett. 94 (2005) 117802.

[33] H.X. Huang, J. Appl. Polym. Sci. 67 (1998) 2111-2118.

[34] A. Peterlin, J. Mater. Sci. 6 (1971) 490-508.

[35] B.A.G. Schrauwen, R.P.M. Janssen, L.E. Govaert, H.E.H. Meijer, Macromolecules 37 (2004) 6069-6078.

[36] C. Millot, R. Séguéla, O. Lame, L.A. Fillot, C. Rochas, P. Sotta, Macromolecules 50 (2017) 1541-1553.

[37] R. Seguela, J. Polym. Sci. B: Polym. Phys. 43 (2005) 1729-1748.

[38] R. Seguela, E-Polymers 7 (2007) 382-391.

[39] J.M. Peterson, J. Appl. Phys. 37 (1966) 4047-4050.

[40] L.G. Shadrake, F. Guiu, Philosophical Magazine 34 (1976) 565-581.

[41] R.J. Young, Mater Forum 11 (1988) 210-216.

[42] L. Lin, A.S. Argon, Macromolecules 27 (1994) 6903-6914.

[43] L. Lin, A.S. Argon, J. Mater. Sci. 29 (1994) 294-323.

[44] H. Wilhelm, A. Paris, E. Schafler, S. Bernstorff, J. Bonarski, T. Ungar, M.J. Zehetbauer, Materials Science and Engineering a-Structural Materials Properties Microstructure and Processing 387 (2004) 1018-1022.

[45] T. Kazmierczak, A. Galeski, A.S. Argon, Polymer 46 (2005) 8926-8936.

[46] B. Crist, Polymer Communications 30 (1989) 69-71.

[47] B. Crist, J.D. Tanzer, T.M. Finerman, J. Polym. Sci. B: Polym. Phys. 27 (1989) 875-878.

[48] O. Darras, R. Seguela, J. Polym. Sci. B: Polym. Phys. 31 (1993) 759-766.

[49] N.W.J. Brooks, M. Mukhtar, Polymer 41 (2000) 1475-1480.

[50] W.J. Okane, R.J. Young, J. Mater. Sci. Lett. 14 (1995) 433-435.

[51] R.J. Young, Philosophical Magazine 30 (1974) 85-94.

[52] M.A. Kennedy, A.J. Peacock, L. Mandelkern, Macromolecules 27 (1994) 5297-5310.

[53] G. Ayoub, F. Zaïri, C. Fréderix, J.M. Gloaguen, M. Naït-Abdelaziz, R. Seguela, J.M. Lefebvre, Int. J. Plasticity. 27 (2011) 492-511.

[54] Z. Bartczak, R.E. Cohen, A.S. Argon, Macromolecules 25 (1992) 4692-4704.

[55] A.S. Argon, A. Galeski, T. Kazmierczak, Polymer 46 (2005) 11798-11805.

[56] P.J. Flory, D.Y. Yoon, Nature 272 (1978) 226-229.

[57] R. Popli, L. Mandelkern, J. Polym. Sci. B: Polym. Phys. 25 (1987) 441-483.

[58] J.X. Li, W.L. Cheung, Polymer 39 (1998) 6935-6940.

[59] J.X. Li, W.L. Cheung, C.M. Chan, Polymer 40 (1999) 3641-3656.

[60] J.X. Li, W.L. Cheung, C.M. Chan, Polymer 40 (1999) 2089-2102.

[61] J.W. Maher, R.N. Haward, J.N. Hay, J Polym. Polym. Phys. Ed. 18 (1980) 2169-2179.

[62] G. Meinel, A. Peterlin, Journal of Polymer Science Part a-2-Polymer Physics 9 (1971) 67-&.

[63] P.J. Phillips, R.J. Philpot, Polymer Communications 27 (1986) 307-309.

[64] H.H. Chuah, J. Lin, R.S. Porter, Macromolecules 19 (1986) 2732-2736.

[65] A. Rozanski, A. Galeski, Macromolecules 44 (2011) 7273-7287.

[66] A. Pawlak, J. Appl. Polym. Sci. 125 (2012) 4177-4187.

[67] K. Schneider, S. Trabelsi, N.E. Zafeiropoulos, R. Davies, C. Riekel, M. Stamm, Macromol. Symp. 236 (2006) 241-248.

[68] A. Pawlak, A. Galeski, Polymer 51 (2010) 5771-5779.

[69] Y. Wang, Z. Jiang, L. Fu, Y. Lu, Y. Men, PLOS ONE 9 (2014) e97234.

[70] A. Peterlin, Plastic deformation of unoriented crystalline polymers under tensile load, 1972.

[71] R.P. Kambour, Journal of Polymer Science: Macromolecular Reviews 7 (1973) 1-154.

[72] A. Pawlak, Colloid Polym. Sci. 291 (2013) 773-787.

[73] M. Aboulfaraj, C. G'Sell, B. Ulrich, A. Dahoun, Polymer 36 (1995) 731-742.

[74] F. Chu, T. Yamaoka, H. Ide, Y. Kimura, Polymer 35 (1994) 3442-3448.

[75] B. Na, R. Lv, J. Appl. Polym. Sci. 105 (2007) 3274-3279.

[76] H. Bai, F. Luo, T. Zhou, H. Deng, K. Wang, Q. Fu, Polymer 52 (2011) 2351-2360.

[77] C. Thomas, R. Seguela, F. Detrez, V. Miri, C. Vanmansart, Polymer 50 (2009) 3714-3723.

[78] R.-Y. Bao, Z.-T. Ding, Z.-Y. Liu, W. Yang, B.-H. Xie, M.-B. Yang, Polymer 54 (2013) 1259-1268.

[79] A. Pawlak, A. Galeski, Macromolecules 41 (2008) 2839-2851.

[80] A. Rozanski, A. Galeski, M. Debowska, Macromolecules 44 (2011) 20-28.

[81] A. Rozanski, A. Galeski, Polimery-w. 57 (2012) 433-440.

[82] Wikipedia, 2017.

[83] N. Stribeck, X-ray scattering of soft matter, Springer Science & Business Media2007.

[84] H.B. Donald, E. Pascal, W. Edgar, Journal of Physics B: Atomic, Molecular and Optical Physics 38 (2005) S773.

[85] A. Buffet, A. Rothkirch, R. Dohrmann, V. Korstgens, M.M. Abul Kashem, J. Perlich, G. Herzog, M. Schwartzkopf, R. Gehrke, P. Muller-Buschbaum, S.V. Roth, J. Synchrotron. Radiat 19 (2012) 647-653.

[86] H. Xu, Z. Zhao, Nuclear Science and Techniques 19 (2008) 1-6.

[87] J. Als-Nielsen, D. McMorrow, Elements of Modern X-ray Physics, John Wiley & Sons, Inc.2011, pp. 1-28.

[88] B. Post, J Polym. B: Polym. Lett. 9 (1971) 635-636.

[89] A.F. Thünemann, W. Ruland, Macromolecules 33 (2000) 1848-1852.

[90] S.Z.D. Cheng, J.J. Janimak, A. Zhang, E.T. Hsieh, Polymer 32 (1991) 648-655.

[91] D.C. Bassett, R.H. Olley, Polymer 25 (1984) 935-943.

[92] K. Schneider, J. Polym. Sci. B: Polym. Phys. 48 (2010) 1574-1586.

[93] S.-G. Yang, Y.-H. Chen, B.-W. Deng, J. Lei, L. Li, Z.-M. Li, Macromolecules 50 (2017) 4807-4816.

[94] Z.W. Wilchinsky, J. Appl. Polym. Sci. 7 (1963) 923-933.

[95] B. Goderis, H. Reynaers, M.H.J. Koch, V.B.F. Mathot, J. Polym. Sci. B: Polym. Phys. 37 (1999) 1715-1738.

[96] M.E. Myers, A.M. Wims, T.S. Ellis, J. Barnes, Macromolecules 23 (1990) 2807-2814.

[97] C. Geng, G. Yang, H. Bai, Y. Li, Q. Fu, H. Deng, J. Supercrit. Fluid. 87 (2014) 83-92.

[98] A. Saffar, A. Ajji, P.J. Carreau, M.R. Kamal, Polymer 55 (2014) 3156-3167.

[99] R.J. Xu, X.D. Chen, Q. Cai, C.B. Chen, Y.F. Lin, C.H. Lei, L.B. Li, RSC Advances 5 (2015) 27722-27734.

[100] G. Strobl, M. Schneider, I. Voigt‐Martin, J Polym. Polym. Phys. Ed. 18 (1980) 1361-1381.

[101] G.R. Strobl, M. Schneider, J Polym. Polym. Phys. Ed. 18 (1980) 1343-1359.

[102] B. Wunderlich, Prog. Polym. Sci. 28 (2003) 383-450.

[103] B. Chang, K. Schneider, G. Heinrich, Macromol. Mater. Eng. 302 (2017) 1700152(1-9).

[104] L. Laiarinandrasana, O. Klinkova, F. Nguyen, H. Proudhon, T.F. Morgeneyer, W. Ludwig, Int. J. Plasticity. 83 (2016) 19-36.

[105] B. Crist, J.M. Schultz, Prog. Polym. Sci. 56 (2016) 1-63.

[106] A.G. Shtukenberg, Y.O. Punin, E. Gunn, B. Kahr, Chem. Rev. 112 (2012) 1805-1838.

[107] D.C. Bassett, J Macromol. Sci. B 42 (2003) 227-256.

[108] J.H. Magill, J. Mater. Sci. 36 (2001) 3143-3164.

[109] F.L. Binsbergen, B.G.M. de Lange, Polymer 9 (1968) 23-40.

[110] H.D. Keith, F.J.P. Jr., J. Appl. Phys. 34 (1963) 2409-2421.

[111] D.C. Bassett, A.S. Vaughan, Polymer 26 (1985) 717-725.

[112] Y. Jiang, D.-D. Yan, X. Gao, C.C. Han, X.-G. Jin, L. Li, Y. Wang, C.-M. Chan, Macromolecules 36 (2003) 3652-3655.

[113] C.-M. Chan, L. Li, in: H.-H. Kausch (Ed.), Intrinsic Molecular Mobility and Toughness of Polymers II, Springer Berlin Heidelberg, Berlin, Heidelberg, 2005, pp. 1-41.

[114] H.M. White, D.C. Bassett, Polymer 38 (1997) 5515-5520.

[115] D.R. Norton, A. Keller, Polymer 26 (1985) 704-716.

[116] N.E. Zafeiropoulos, R.J. Davies, S.V. Roth, M. Burghammer, K. Schneider, C. Riekel, M. Stamm, Macromol. Rapid. Comm. 26 (2005) 1547-1551.

[117] G. Santoro, S. Yu, C. Krywka, S.V. Roth, G. Ellis, physica status solidi (RRL) – Rapid Research Letters 8 (2014) 724-727.

[118] Y. Shinohara, K. Yamazoe, T. Sakurai, S. Kimata, T. Maruyama, Y. Amemiya, Macromolecules 45 (2012) 1398-1407.

[119] K.G. Gatos, C. Minogianni, C. Galiotis, Macromolecules 40 (2007) 786-789.

[120] J. Varga, J. Macromol. Sci. Phys. B41 (2002) 1121-1171.

[121] C.-M. Wu, M. Chen, J. Karger-Kocsis, Polymer 40 (1999) 4195-4203.

[122] J. Varga, G.W. Ehrenstein, Polymer 37 (1996) 5959-5963.

[123] F. Khoury, J. Res. Natl. Bur. Stand. A 70 (1966) 29-61.

[124] Y. Cong, Z. Hong, W. Zhou, W. Chen, F. Su, H. Li, X. Li, K. Yang, X. Yu, Z. Qi, L. Li, Macromolecules 45 (2012) 8674-8680.

[125] R. Kolb, C. Wutz, N. Stribeck, G. von Krosigk, C. Riekel, Polymer 42 (2001) 5257-5266.

[126] Z. Peng-Wei, G. Edward, J. Mater. Sci. 43 (2008) 6459-67.

[127] K. Yamaji, M. Haisa, Jpn. J. Appl. Phys. 15 (1976) 225.

[128] R.H. Boyd, Polymer 26 (1985) 323-347.

[129] R.H. Boyd, Polymer 26 (1985) 1123-1133.

[130] B.E. Read, Polymer 30 (1989) 1439-1445.

[131] M. Pluta, M. Kryszewski, Acta Polym. 38 (1987) 42-52.

[132] P. Tiemblo, J.M. Gómez-Elvira, S.G. Beltrán, L. Matisova-Rychla, J. Rychly, Macromolecules 35 (2002) 5922-5926.

[133] C. Jourdan, J.Y. Cavaille, J. Perez, J. Polym. Sci. B: Polym. Phys. 27 (1989) 2361-2384.

[134] I. Quijada-Garrido, J.M. Barrales-Rienda, J.M. Pereña, G. Frutos, J. Polym. Sci. B: Polym. Phys. 35 (1997) 1473-1482.

[135] M. Hoyos, P. Tiemblo, J.M. Gómez-Elvira, Polymer 48 (2007) 183-194.

[136] E. Suljovrujic, S. Trifunovic, D. Milicevic, Polym. Degrad. Stabil. 95 (2010) 164-171.

[137] N.G. McCrum, Polymer 25 (1984) 299-308.

[138] H.W. Starkweather, P. Avakian, R.R. Matheson, J.J. Fontanella, M.C. Wintersgill, Macromolecules 25 (1992) 6871-6875.

[139] Y. Wada, Y. Hotta, R. Suzuki, J Polym. Sc.i Polym. Sym. 23 (1968) 583-595.

[140] R.F. Boyer, J Macromol. Sci. B 8 (1973) 503-537.

[141] G.M. Bartenev, R.M. Aliguliev, Polymer Science U.S.S.R. 26 (1984) 1383-1394.

[142] D. Milicevic, M. Micic, E. Suljovrujic, Polym. Bull. 71 (2014) 2317-2334.

[143] M. Jarrigeon, B. Chabert, D. Chatain, C. Lacabanne, G. Nemoz, J Macromol. Sci. B 17 (1980) 1-24.

[144] W.G. Hu, K. Schmidt-Rohr, Acta Polym. 50 (1999) 271-285.

[145] K. Schmidt-Rohr, H.W. Spiess, Macromolecules 24 (1991) 5288-5293.

[146] M. Hoyos, P. Tiemblo, J.M. Gómez-Elvira, Eur. Polym. J. 45 (2009) 1322-1327.

[147] I.S. Kolesov, R. Androsch, H.-J. Radusch, Macromolecules 38 (2005) 445-453.

[148] M.L. Di Lorenzo, M.C. Righetti, Polymer 49 (2008) 1323-1331.

[149] J. Menczel, B. Wunderlich, Journal of Polymer Science: Polymer Letters Edition 19 (1981) 261-264.

[150] J. Grebowicz, S.F. Lau, B. Wunderlich, J. Polym. Sci. Polym. Sym. 71 (1984) 19-37.

[151] C. Schick, A. Wurm, A. Mohamed, Thermochim. Acta 392–393 (2002) 303-313.

[152] Q. Zia, D. Mileva, R. Androsch, Macromolecules 41 (2008) 8095-8102.

[153] M. Varma-Nair, P. Agarwal, Abstracts of Papers of the American Chemical Society 218 (1999) U652-U652.

[154] M.K. Agarwal, J.M. Schultz, Polym. Eng. Sci. 21 (1981) 776-781.

[155] C. Hedesiu, D.E. Demco, R. Kleppinger, G.V. Poel, W. Gijsbers, B. Blümich, K. Remerie, V.M. Litvinov, Macromolecules 40 (2007) 3977-3989.

[156] B. Lotz, J. Wittmann, A. Lovinger, Polymer 37 (1996) 4979-4992.

[157] Q. Zia, R. Androsch, H.-J. Radusch, S. Piccarolo, Polymer 47 (2006) 8163-8172.

[158] T. Konishi, K. Nishida, T. Kanaya, Macromolecules 39 (2006) 8035-8040.

[159] A. Martorana, S. Piccarolo, D. Sapoundjieva, Macromol. Chem. Phys. 200 (1999) 531-540.

[160] G. Strobl, Rev. Mod. Phys. 81 (2009) 1287-1300.

[161] M.L. Di Lorenzo, R. Androsch, I. Stolte, Polymer 55 (2014) 6132-6139.

[162] M.L. Di Lorenzo, M.C. Righetti, Eur. Polym. J. 49 (2013) 510-517.

[163] I.C. Sanchez, J.P. Colson, R.K. Eby, J. Appl. Phys. 44 (1973) 4332-4339.

[164] Q. Zhang, Z. Mo, S. Liu, H. Zhang, Macromolecules 33 (2000) 5999-6005.

[165] H. Bai, H. Deng, Q. Zhang, K. Wang, Q. Fu, Z. Zhang, Y. Men, Polym. Int. 61 (2012) 252-258.

[166] B.B. Sauer, W.G. Kampert, E. Neal Blanchard, S.A. Threefoot, B.S. Hsiao, Polymer 41 (2000) 1099-1108.

[167] Y.-T. Shieh, Y.-S. Lin, Y.-K. Twu, H.-B. Tsai, R.-H. Lin, J. Appl. Polym. Sci. 116 (2010) 1334-1341.

[168] Y. Lee, R.S. Porter, J.S. Lin, Macromolecules 22 (1989) 1756-1760.

[169] C. Qi, X. Ruijie, W. Shuqiu, C. Changbin, M. Haibin, L. Caihong, L. Liangbin, Z. Li, Polym. Int. 64 (2015) 446-452.

[170] H.-Y. Wu, J.-W. Chen, X.-C. Du, J.-H. Yang, T. Huang, N. Zhang, Y. Wang, Polym. Test. 32 (2013) 123-132.

[171] A. Esposito, N. Delpouve, V. Causin, A. Dhotel, L. Delbreilh, E. Dargent, Macromolecules 49 (2016) 4850-4861.

[172] Z. Cai, X. Liu, Q. Zhou, Y. Wang, C. Zhu, X. Xiao, D. Fang, H. Bao, Polymer 117 (2017) 249-258.

[173] P.I. Vincent, Polymer 1 (1960) 7-19.

[174] K.-H. Nitta, H. Nomura, Polymer 55 (2014) 6614-6622.

[175] A. Peterlin, Colloid Polym. Sci. 253 (1975) 809-823.

[176] Y. Higuchi, M. Kubo, Macromolecules 50 (2017) 3690-3702.

[177] N. Selles, P. Cloetens, H. Proudhon, T.F. Morgeneyer, O. Klinkova, N. Saintier, L. Laiarinandrasana, Macromolecules 50 (2017) 4372-4383.

[178] Z. Jiang, R. Chen, Y. Lu, B. Whiteside, P. Coates, Z. Wu, Y. Men, J. Phys. Chem. B 121 (2017) 6673-6684.

[179] C.R. López-Barrón, Y. Zeng, J.J. Schaefer, A.P.R. Eberle, T.P. Lodge, F.S. Bates, Macromolecules (2017).

[180] B. Xiong, O. Lame, J.-M. Chenal, C. Rochas, R. Seguela, G. Vigier, Polymer 55 (2014) 1223-1227.

[181] Y. Wang, Z. Jiang, Z. Wu, Y. Men, Macromolecules 46 (2013) 518-522.

[182] Y. Lu, Y. Wang, R. Chen, J. Zhao, Z. Jiang, Y. Men, Macromolecules 48 (2015) 5799-5806.

[183] F. Auriemma, C. De Rosa, R. Di Girolamo, A. Malafronte, M. Scoti, G.R. Mitchell, S. Esposito, Macromolecules 50 (2017) 2856-2870.

[184] A. Rozanski, A. Galeski, Macromolecules 48 (2015) 5310-5322.

[185] X. Chen, F. Lv, F. Su, Y. Ji, L. Meng, C. Wan, Y. Lin, X. Li, L. Li, Polymer 118 (2017) 12-21.

[186] Y. Wang, Y. Lu, Z. Jiang, Y. Men, Macromolecules 47 (2014) 6401-6407.

[187] Q. Fu, B. Heck, G. Strobl, Y. Thomann, Macromolecules 34 (2001) 2502-2511.

[188] A. Pawlak, A. Galeski, Macromolecules 38 (2005) 9688-9697.

[189] F. Addiego, S. Patlazhan, K. Wang, S. André, S. Bernstorff, D. Ruch, Polym. Int. 64 (2015) 1513-1521.

[190] R. Chen, Y. Lu, J. Zhao, Z. Jiang, Y. Men, J. Polym. Sci. B: Polym. Phys. 54 (2016) 2007-2014.

[191] A. Pawlak, A. Galeski, A. Rozanski, Prog. Polym. Sci. 39 (2014) 921-958.

[192] J.L. Way, J.R. Atkinson, J. Mater. Sci. 6 (1971) 102-109.

[193] M.F. Butler, A.M. Donald, A.J. Ryan, Polymer 39 (1998) 39-52.

[194] A. Boger, B. Heise, C. Troll, O. Marti, B. Rieger, Eur. Polym. J. 43 (2007) 3573-3586.

[195] A. Pawlak, Polymer 48 (2007) 1397-1409.

[196] F. Addiego, A. Dahoun, C. G'Sell, J.-M. Hiver, O. Godard, Polym. Eng. Sci. 49 (2009) 1198-1205.

[197] K.H. Nitta, M. Takayanagi, J. Mater. Sci. 38 (2003) 4889-4894.

[198] S. Humbert, O. Lame, J.M. Chenal, C. Rochas, G. Vigier, Macromolecules 43 (2010) 7212-7221.

[199] D.J. Hughes, A. Mahendrasingam, W.B. Oatway, E.L. Heeley, C. Martin, W. Fuller, Polymer 38 (1997) 6427-6430.

[200] F. Auriemma, C. De Rosa, R. Di Girolamo, A. Malafronte, M. Scoti, G.R. Mitchell, S. Esposito, in: G.R. Mitchell, A. Tojeira (Eds.), Controlling the Morphology of Polymers: Multiple Scales of Structure and Processing, Springer International Publishing, Cham, 2016, pp. 287-327.

[201] R. Hiss, S. Hobeika, C. Lynn, G. Strobl, Macromolecules 32 (1999) 4390-4403.

[202] J.C. Viana, Polymer 46 (2005) 11773-11785.

[203] D. Grubb, N.S. Murthy, O. Francescangeli, J. Polym. Sci. B: Polym. Phys. 54 (2016) 308-318.

[204] S. Ran, X. Zong, D. Fang, B.S. Hsiao, B. Chu, R.A. Phillips, Macromolecules 34 (2001) 2569-2578.

[205] B. Chang, K. Schneider, R. Vogel, G. Heinrich, Macromol. Mater. Eng. 302 (2017) 1700291(1-12).

[206] A. Pawlak, A. Rozanski, A. Galeski, Mech. Mater. 67 (2013) 104-118.

[207] Y. Lu, R. Chen, J. Zhao, Z. Jiang, Y. Men, The Journal of Physical Chemistry B (2017) 6969-6978.

[208] Z. Jiang, Y. Tang, J. Rieger, H.-F. Enderle, D. Lilge, S.V. Roth, R. Gehrke, W. Heckmann, Y. Men, Macromolecules 43 (2010) 4727-4732.

[209] Z. Jiang, Y. Tang, J. Rieger, H.-F. Enderle, D. Lilge, S.V. Roth, R. Gehrke, Z. Wu, Z. Li, Y. Men, Polymer 50 (2009) 4101-4111.

[210] Y. Lu, Y. Wang, R. Chen, Y. Men, J. Polym. Sci. B: Polym. Phys. 55 (2017) 957-963.

[211] G. Strobl, Rev. Mod. Phys. 81 (2009) 1287-1300.

[212] Y. Lin, X. Li, L. Meng, X. Chen, F. Lv, Q. Zhang, R. Zhang, L. Li, Macromolecules 51 (2018) 2690-2705.

[213] R. Bao, Z. Ding, G. Zhong, W. Yang, B. Xie, M. Yang, Colloid Polym. Sci. 290 (2012) 261-274.

[214] A. Guinier, X-ray diffraction in crystals, imperfect crystals, and amorphous bodies, Courier Corporation1994.

[215] D. Lyu, R. Chen, Y. Lu, Y. Men, Ind. Eng. Chem. Res. (2018).

[216] Z.G. Liu, W.H. Wong, T.F. Guo, Int. J. Plasticity. 84 (2016) 183-202.

[217] T. Ge, C. Tzoumanekas, S.D. Anogiannakis, R.S. Hoy, M.O. Robbins, Macromolecules 50 (2017) 459-471.

[218] A. Krajenta, A. Rozanski, J. Polym. Sci. B: Polym. Phys. 54 (2016) 1853-1868.

[219] A. Rozanski, R. Idczak, Eur. Polym. J. 69 (2015) 186-200.

[220] H. Janeschitz-Kriegl, E. Ratajski, Colloid Polym. Sci. 288 (2010) 1525-1537.

[221] S. Kimata, T. Sakurai, Y. Nozue, T. Kasahara, N. Yamaguchi, T. Karino, M. Shibayama, J.A. Kornfield, Science 316 (2007) 1014-1017.

[222] G. Kumaraswamy, R.K. Verma, J.A. Kornfield, F. Yeh, B.S. Hsiao, Macromolecules 37 (2004) 9005-9017.

[223] R.H. Somani, I. Sics, B.S. Hsiao, J. Polym. Sci. B: Polym. Phys. 44 (2006) 3553-3570.

[224] H. Janeschitz-Kriegl, Colloid Polym. Sci. 281 (2003) 1157-1171.

[225] G. Lamberti, Chem. Soc. Rev. 43 (2014) 2240-2252.

[226] A.J. Pennings, A.M. Kiel, Kolloid-Zeitschrift und Zeitschrift für Polymere 205 (1965) 160-162.

[227] P.J. Flory, The Journal of Chemical Physics 15 (1947) 397-408.

[228] G. Galgali, C. Ramesh, A. Lele, Macromolecules 34 (2001) 852-858.

[229] P.G.D. Gennes, The Journal of Chemical Physics 60 (1974) 5030-5042.

[230] T. Yan, B. Zhao, Y. Cong, Y. Fang, S. Cheng, L. Li, G. Pan, Z. Wang, X. Li, F. Bian, Macromolecules 43 (2010) 602-605.

[231] Z. Wang, Z. Ma, L. Li, Macromolecules 49 (2016) 1505-1517.

[232] K. Cui, Z. Ma, N. Tian, F. Su, D. Liu, L. Li, Chem. Rev. 118 (2018) 1840-1886.

[233] M.C. García-Gutiérrez, J.J. Hernández, A. Nogales, P. Panine, D.R. Rueda, T.A. Ezquerra, Macromolecules 41 (2008) 844-851.

[234] N. Patil, L. Balzano, G. Portale, S. Rastogi, Carbon 48 (2010) 4116-4128.

[235] A.W. Phillips, A. Bhatia, P.-w. Zhu, G. Edward, Macromolecules 44 (2011) 3517-3528.

[236] A. Nogales, G.R. Mitchell, A.S. Vaughan, Macromolecules 36 (2003) 4898-4906.

[237] M. D'Haese, P. Van Puyvelde, F. Langouche, Macromolecules 43 (2010) 2933-2941.

[238] P.-W. Zhu, A. Phillips, G. Edward, L. Nichols, Phys. Rev. E 80 (2009) 051801.

[239] A. Cacciuto, S. Auer, D. Frenkel, Nature 428 (2004) 404-406.

[240] J.-Z. Xu, T. Chen, C.-L. Yang, Z.-M. Li, Y.-M. Mao, B.-Q. Zeng, B.S. Hsiao, Macromolecules 43 (2010) 5000-5008.

[241] A. Rozanski, B. Monasse, E. Szkudlarek, A. Pawlak, E. Piorkowska, A. Galeski, J.M. Haudin, Eur. Polym. J. 45 (2009) 88-101.

[242] N. Patil, L. Balzano, G. Portale, S. Rastogi, Macromolecules 43 (2010) 6749-6759.

[243] D. Byelov, P. Panine, K. Remerie, E. Biemond, G.C. Alfonso, W.H. de Jeu, Polymer 49 (2008) 3076-3083.

[244] J. Fan, Q. Zhang, D. Hu, Q. Ren, J. Feng, Phys. Chem. Chem. Phys. 18 (2016) 8926-8937.

[245] B. Chang, K. Schneider, R. Vogel, G. Heinrich, Polymer 138 (2018) 329-342.

[246] R. Han, M. Nie, Q. Wang, S. Yan, Ind. Eng. Chem. Res. 56 (2017) 2764-2772.

[247] J. Varga, A. Menyhárd, Macromolecules 40 (2007) 2422-2431.

[248] D. Hu, G. Wang, J. Feng, X. Lu, Polymer 93 (2016) 123-131.

[249] N. Mohmeyer, H.-W. Schmidt, P.M. Kristiansen, V. Altstädt, Macromolecules 39 (2006) 5760-5767.

154

[250] D. Kluge, J.C. Singer, J.W. Neubauer, F. Abraham, H.-W. Schmidt, A. Fery, Small 8 (2012) 2563-2570.

[251] P. Pötschke, M. Abdel-Goad, I. Alig, S. Dudkin, D. Lellinger, Polymer 45 (2004) 8863-8870.

[252] A.L. Yarin, M.D. Graham, J. Rheol. 42 (1998) 1491-1504.

[253] J. Sun, Y. Song, Q. Zheng, H. Tan, J. Yu, H. Li, J. Polym. Sci. B: Polym. Phys. 45 (2007) 2594-2602.

[254] S. Merabia, P. Sotta, D.R. Long, Macromolecules 41 (2008) 8252-8266.

[255] J. Wang, J. Yang, L. Deng, H. Fang, Y. Zhang, Z. Wang, ACS Applied Materials & Interfaces 7 (2015) 1364-1375.

[256] J. Ren, R. Krishnamoorti, Macromolecules 36 (2003) 4443-4451.

[257] A. Einstein, Ann. Phys-berlin. 324 (1906) 371-381.

[258] S. Jain, J.G.P. Goossens, G.W.M. Peters, M. van Duin, P.J. Lemstra, Soft Matter 4 (2008) 1848-1854.

[259] J.W. Housmans, G.W.M. Peters, H.E.H. Meijer, J. Therm. Anal. Calorim 98 (2009) 693-705.

[260] F. Langouche, Macromolecules 39 (2006) 2568-2573.

[261] J.-W. Housmans, R.J.A. Steenbakkers, P.C. Roozemond, G.W.M. Peters, H.E.H. Meijer, Macromolecules 42 (2009) 5728-5740.

[262] M. Avrami, The Journal of Chemical Physics 7 (1939) 1103-1112.

[263] N.V. Pogodina, H.H. Winter, S. Srinivas, J. Polym. Sci. B: Polym. Phys. 37 (1999) 3512-3519.

[264] Y. Zhong, H. Fang, Y. Zhang, Z. Wang, J. Yang, Z. Wang, ACS Sustainable Chemistry & Engineering (2013).

[265] G. Mago, F.T. Fisher, D.M. Kalyon, Macromolecules 41 (2008) 8103-8113.

[266] J. Bian, S.-R. Ye, L.-X. Feng, J. Polym. Sci. B: Polym. Phys. 41 (2003) 2135-2144.

[267] M. Naffakh, C. Marco, M.A. Gómez-Fatou, The Journal of Physical Chemistry B 115 (2011) 2248-2255.

[268] Y.-H. Chen, G.-J. Zhong, J. Lei, Z.-M. Li, B.S. Hsiao, Macromolecules 44 (2011) 8080-8092.

[269] J.K. Keum, C. Burger, B.S. Hsiao, R. Somani, L. Yang, B. Chu, R. Kolb, H. Chen, C.-T. Lue, in: N. Stribeck, B. Smarsly (Eds.), Scattering Methods and the Properties of Polymer Materials, Springer Berlin Heidelberg, Berlin, Heidelberg, 2005, pp. 114-126.

[270] Z.-G. Wang, B.S. Hsiao, E.B. Sirota, P. Agarwal, S. Srinivas, Macromolecules 33 (2000) 978-989.

[271] Y.-H. Chen, D.-F. Fang, J. Lei, L.-B. Li, B.S. Hsiao, Z.-M. Li, The Journal of Physical Chemistry B 119 (2015) 5716-5727.

[272] H. Huo, S. Jiang, L. An, J. Feng, Macromolecules 37 (2004) 2478-2483.

[273] C. Riekel, J. Karger-Kocsis, Polymer 40 (1999) 541-545.

[274] X. Li, H. Wu, T. Huang, Y. Shi, Y. Wang, F. Xiang, Z. Zhou, Colloid Polym. Sci. 288 (2010) 1539-1549.

[275] C. Zhang, G. Liu, Y. Song, Y. Zhao, D. Wang, Polymer 55 (2014) 6915-6923.

[276] X. Li, H. Wu, Y. Wang, H. Bai, L. Liu, T. Huang, Materials Science and Engineering: A 527 (2010) 531-538.

[277] Y. Men, G. Strobl, Macromolecules 36 (2003) 1889-1898.

[278] E. Lezak, Z. Bartczak, J. Polym. Sci. B: Polym. Phys. 46 (2008) 92-108.

[279] J. Karger-kocsis, J. Varga, J. Appl. Polym. Sci. 62 (1996) 291-300.

[280] J. Karger-Kocsis, P.P. Shang, J. Therm. Anal. Calorim 51 (1998) 237-244.

[281] S. Shi, W. Liu, M. Nie, Q. Wang, RSC Advances 6 (2016) 98104-98108.

[282] M. Dong, Z.-X. Guo, J. Yu, Z.-Q. Su, J. Polym. Sci. B: Polym. Phys. 47 (2009) 314-325.

[283] H. Bai, Y. Wang, Z. Zhang, L. Han, Y. Li, L. Liu, Z. Zhou, Y. Men, Macromolecules 42 (2009) 6647-6655.

[284] A. Menyhárd, J. Varga, Eur. Polym. J. 42 (2006) 3257-3268.

[285] Y. Men, J. Rieger, J. Homeyer, Macromolecules 37 (2004) 9481-9488.

[286] T.S. Motsoeneng, A.J. van Reenen, A.S. Luyt, Polym. Int. 64 (2015) 222-228.

[287] S. Henning, R. Adhikari, G.H. Michler, F.J.B. Calleja, J. Karger-Kocsis, Macromol. Symp. 214 (2004) 157-172.

[288] F. Chu, T. Yamaoka, Y. Kimura, Polymer 36 (1995) 2523-2530.

[289] Y. Chen, S. Yang, H. Yang, G. Zhong, D. Fang, B.S. Hsiao, Z. Li, Polymer 84 (2016) 254-266.

[290] Z.W. Cai, Y. Zhang, J.Q. Li, F.F. Xue, Y.R. Shang, X.H. He, J.C. Feng, Z.H. Wu, S.C. Jiang, Polymer 53 (2012) 1593-1601.

[291] T.A. Huy, R. Adhikari, T. Lüpke, S. Henning, G.H. Michler, J. Polym. Sci. B: Polym. Phys. 42 (2004) 4478-4488.

[292] K.S. Fancey, J. Mater. Sci. 40 (2005) 4827-4831.

[293] M. Ganß, B.K. Satapathy, M. Thunga, R. Weidisch, P. Pötschke, A. Janke, Macromol. Rapid. Comm. 28 (2007) 1624-1633.

[294] A. Greco, C. Musardo, A. Maffezzoli, Compos. Sci. Technol. 67 (2007) 1148-1158.

[295] J. Kolařík, A. Pegoretti, Polymer 47 (2006) 346-356.

[296] J. Kolařík, J. Polym. Sci. B: Polym. Phys. 41 (2003) 736-748.

[297] J. Kolařík, A. Pegoretti, L. Fambri, A. Penati, J. Appl. Polym. Sci. 88 (2003) 641-651.

[298] J. Kolařík, A. Pegoretti, L. Fambri, A. Penati, Macromol. Mater. Eng. 288 (2003) 629-641.

[299] K.-H. Nitta, M. Takayanagi, J. Polym. Sci. B: Polym. Phys. 37 (1999) 357-368.

[300] K.-H. Nitta, M. Takayanagi, J. Polym. Sci. B: Polym. Phys. 38 (2000) 1037-1044.

[301] X.-w. Wang, J. Dai, J.-w. Chen, J. Duan, J.-h. Yang, J.-h. Zhang, Y. Wang, Ind. Eng. Chem. Res. 54 (2015) 4976-4987.

[302] A.D. Drozdov, J.D. Christiansen, Polym. Eng. Sci. 43 (2003) 946-959.

[303] A.D. Drozdov, J.d. Christiansen, Comp. Mater. Sci. 27 (2003) 403-422.

[304] C. Jia, X. Liao, J. Zhu, Z. An, Q. Zhang, Q. Yang, G. Li, RSC Advances 6 (2016) 30986-30997.

[305] A.D. Drozdov, Eng. Fract. Mech. 77 (2010) 2277-2293.

[306] Y. Men, J. Rieger, G. Strobl, Phys. Rev. Lett. 91 (2003) 095502.

[307] M. Deng, J. Zhou, J. Appl. Polym. Sci. 90 (2003) 3882-3888.

[308] J. Yang, Z. Zhang, K. Friedrich, A.K. Schlarb, Macromol. Rapid. Comm. 28 (2007) 955-961.

[309] O.U. Colak, Int. J. Plasticity. 21 (2005) 145-160.

[310] P.K. Mallick, Y. Zhou, J. Mater. Sci. 38 (2003) 3183-3190.

[311] Y.C. Zhang, J. Huang, H.Y. Wu, Y. Qiu, Mater. Sci. Forum., Trans Tech Publ, 2009, pp. 316-322.

[312] C. Jia, Q. Zhang, X. Liao, J. Zhu, L. Wu, K. Ni, Q. Yang, Z. An, G. Li, Polymer 67 (2015) 92-100.

[313] R.D. Sudduth, J. Mater. Sci. 38 (2003) 1123-1134.

[314] Y. Rao, R.J. Farris, Int. J. Fatigue. 30 (2008) 793-799.

[315] X. Liu, Y. Huang, C. Deng, X. Wang, W. Tong, Y. Liu, J. Huang, Q. Yang, X. Liao, G. Li, Polymer Engineering & Science 49 (2009) 1375-1382.

[316] A.D. Drozdov, A.L. Høg Lejre, J.d. Christiansen, Compos. Sci. Technol. 69 (2009) 2596-2603.

[317] S. Goyanes, W. Salgueiro, A. Somoza, J.A. Ramos, I. Mondragon, Polymer 45 (2004) 6691-6697.

[318] H. Koerner, J.J. Kelley, R.A. Vaia, Macromolecules 41 (2008) 4709-4716.

[319] N.S. Murthy, K. Zero, D.T. Grubb, Polymer 38 (1997) 1021-1028.

[320] N.S. Murthy, D.T. Grubb, K. Zero, Macromolecules. 33 (2000) 1012-1021.

[321] N.S. Murthy, D.T. Grubb, J. Polym. Sci. B: Polym. Phys. 44 (2006) 1277-1286.

[322] T. Kida, T. Oku, Y. Hiejima, K.-h. Nitta, Polymer 58 (2015) 88-95.

[323] L.D.L.D. Landau, E.M.E.M. Lifshitz, Statistical physics, 2d rev. and enl. ed ed., Pergamon Press1969.

[324] Y. Tang, Z. Jiang, Y. Men, L. An, H.-F. Enderle, D. Lilge, S.V. Roth, R. Gehrke, J. Rieger, Polymer 48 (2007) 5125-5132.

[325] Y. Tian, C. Zhu, J. Gong, S. Yang, J. Ma, J. Xu, Polymer 55 (2014) 4299-4306.

[326] C.F. Popelar, C.H. Popelar, V.H. Kenner, Polym. Eng. Sci. 30 (1990) 577-586.

[327] A. Khan, H. Zhang, Int. J. Plasticity. 17 (2001) 1167-1188.

[328] F. Khan, E. Krempl, Journal of Engineering Materials and Technology 128 (2005) 64-72.

[329] K. Hong, A. Rastogi, G. Strobl, Macromolecules 37 (2004) 10165-10173.

[330] R. Krache, R. Benavente, J.M. López-Majada, J.M. Pereña, M.L. Cerrada, E. Pérez, Macromolecules 40 (2007) 6871-6878.

[331] F. Auriemma, C. De Rosa, R. Di Girolamo, A. Malafronte, M. Scoti, G.R. Mitchell, S. Esposito, Polymers 10 (2018) 162.

[332] Q. Zia, H.-J. Radusch, R. Androsch, Polym. Bull. 63 (2009) 755-771.

[333] C.R. Desper, R.S. Stein, J. Appl. Phys. 37 (1966) 3990-4002.

[334] A.D. Drozdov, J. deC. Christiansen, Comp. Mater. Sci. 39 (2007) 729-751.

[335] B.J. Lee, D.M. Parks, S. Ahzi, J. Mech. Phys. Solids. 41 (1993) 1651-1687.

[336] F. Tanaka, S.F. Edwards, Macromolecules 25 (1992) 1516-1523.

13 Appendix

13.1 List of symbols and abbreviations

PP	polypropylene
iPP	isotactic-polypropylene
aPP	atactic-polypropylene
sPP	syndiotactic-polypropylene
cPP	propylene/ethylene copolymer
PE	polyethylene
HDPE	high density polyethylene
PA	polyamide
PA6	polyamide 6
PCL	poly(ε-caprolactone)
PI	polyimide
P1B	poly(1-butene)
E_2	scattered wave
E_1	incident wave
r_0	electron radius
r	position of the electron
q	scattering vector
s	scattering vector
θ	scattering angle
λ	wavelength
$d\sigma/d\Omega$	differential scattering cross-section
Φ_0	strength of the incident beam
I_m	measured scattering intensity
$\Delta\Omega$	solid angle
R	distance between the object and the detector
WAXS	wide-angle X-ray scattering
MAXS	middle angle X-ray scattering
SAXS	small angle X-ray scattering
2D	2-dimensional
1D	1-dimensional

$\boldsymbol{R_n}$	vector sets in the lattice
d_{hkl}	lattice spacing
τ_{hkl}	crystal size
$\Delta\rho$	electron density difference
$\mathcal{F}(\boldsymbol{s})$	form factor
V_p	volume fraction of particles
R_g	radius of gyration
Q	scattering invariant
B_{obs}	integral breadth
$\langle L \rangle$	average length of the elongated structure
B_p	instrumental broadening
B_g	true integral breadth of the orientation distribution
M_{w}	weight-average molecular weight
M_{n}	number-average molecular weight
NJS	N,N'-dicyclohexyl-2,6-naphthalene dicarboxamide
NA	nucleating agent
CF	carbon fiber
T_{a}	annealing temperature
T_f	final heating temperature
DSC	differential scanning calorimetry
TMDSC	temperature-modulated differential scanning calorimetry
DMA	dynamic mechanical analysis
SEM	scanning electron microscopy
POM	polarized optical microscopy
$X_{c\text{-DSC}}$	crystallinity calculated from DSC
ΔH_m	fusion enthalpy
ΔH_m^*	equilibrium melting enthalpy
SAOS	small amplitude oscillatory shear
γ	strain amplitude
ω	angular frequency
$\dot{\gamma}$	shear rate
G'	storage modulus
GPC	Gel Permeation Chromatography

DESY	Deutsches Elektronen Synchrotron
SSRL	Standford Synchrotron Radiation Laboratory
ESRF	European Synchrotron Radiation Facility
SSRF	Shanghai Synchrotron Radiation Facility
ε_H	Hencky strain
L_0	initial length
ΔL	displacement of the painted grid pattern
σ	stress
F	force
A_0	initial cross section area
DIC	digital image correlation
X_c	crystallinity calculated by WAXS measurement
K_β	relative content of β-iPP
f_H	Herman's orientation factor
f_{Ha}	Herman's orientation factor of a-axis
f_{Hb}	Herman's orientation factor of b-axis
f_{Hc}	Herman's orientation factor of c-axis
φ	azimuthal angle
L_p	long period
$L_p^{\parallel}$	long period along the loading direction
$L_p^{\perp}$	long period perpendicular to the loading direction
L_c	thickness of the crystalline phase
$L_c^{\parallel}$	thickness of the crystalline phase along the loading direction
$L_c^{\perp}$	thickness of the crystalline phase perpendicular to the loading direction
L_a	thickness of the amorphous phase
$L_a^{\parallel}$	thickness of the amorphous phase along the loading direction
$L_a^{\perp}$	thickness of the amorphous phase perpendicular to the loading direction
L_{im}	thickness of the intermediate phase
$K(z)$	1D correlation function
$S^{\parallel}$	void size along the stretching direction
$S^{\perp}$	void size perpendicular to the stretching direction
V_m	volume ratio of the matrix

V_v	volume ratio of the void
ρ_m	electron density of the matrix
ρ_v	electron density of the void
$R_{D/M}$	ratio between "daughter" lamellae and "mother" lamellae
E_α	activation energy
$FWHM$	full width at half maximum
G_s	surface free energy
ΔH	heat of fusion per mole of molecular chains
T_m^0	equilibrium melting point
v	the number of molecular chains
σ_b	surface free energy of the basal plane
σ_l	surface free energy of the lateral surface
$T_{\alpha c}$	peak temperature of α_c-relaxation
k_B	Boltzmann's constant
ε_y	yield strain
ε_h	onset strain of the strain hardening
ΔG_a	Gibbs free energy for dislocation nucleation
b_v	magnitude of the Burgers vector
σ	stress
σ_y	yield stress
σ_{cav}	critical stress for cavitation
σ_{sh}	critical stress for crystallographic slip
ΔH_{cm}	heat of transition from mesomorphic phase to crystalline phase
Δz	stem length increment per structural unit
σ_{ac_n}	surface free energy of the native crystal layer
σ_{cm}	the surface free energy of the mesomorphic layer
T_{mc}^∞	transition temperature between the mesomorphic phase and crystalline phase
SIC	shear induced crystallization
DBS	dibenzylidene sorbitol
SB	sodium benzoate
HPN	isotropic bicycle [2.2.1] heptane-2,3-dicarboxylic acid
WBG-II	rare earth β-iPP nucleating agent

DCTH	N,N′-dicyclohexylterephthalamide
FTIR	Fourier transform infrared spectroscopy
η	steady-state shear viscosity
η^*	dynamic complex viscosity
Δd	displacement
ε	true strain
$\dot{\varepsilon}$	strain rate
$L_f^{\parallel}$	length of the fibrillary structure along the loading direction
$L_f^{\perp}$	length of the fibrillary structure perpdendicular to the loading direction
R	gas constant
VBOP	Viscoplasticity Theory Based on Overstress for Polymers
T_g	glass transition temperature
σ_e	elastic dtress during stress relaxation
η_σ	characteristic relaxation lifetime

13.2 List of figures and tables

163

13.3 List of publications

Journal articles

1. **Chang** B., Schneider K., Xiang F., Vogel R., Roth S., Heinrich G. Critical Strains for Lamellae Deformation and Cavitation during Uniaxial Stretching of Annealed Isotactic Polypropylene. **Macromolecules** 2018, Doi: 10.1021/acs.macromol.8b00642

2. **Chang** B., Schneider K., Patil N., Roth S., Heinrich G.. Microstructure characterization in a single isotactic polypropylene spherulite by synchrotron microfocus wide angle X-ray scattering. **Polymer** 2018, Doi: 10.1016/j.polymer.2018.03.061

3. **Chang B.**, Schneider K., Vogel R., Heinrich G.. Influence of nucleating agent self-assembly on structural evolution of isotactic polypropylene during uniaxial stretching. **Polymer** 2018, Doi: 10.1016/j.polymer.2018.01.081

4. **Chang B.**, Schneider K., Heinrich G.. Microstructural Evolution of Isotactic-Polypropylene during Creep: An In Situ Study by Synchrotron Small-Angle X-Ray Scattering. **Macromol. Mater. Eng.** 2017, Doi: 10.1002/mame.201700152 (**selected as front cover**)

5. **Chang B.**, Schneider K., Vogel R., et al. Influence of Annealing on Mechanical α_c-Relaxation of Isotactic Polypropylene: A Study from the Intermediate Phase Perspective. **Macromol. Mater. Eng.** 2017, Doi: 10.1002/mame.201700291

6. **Chang B.**, Schneider K., Heinrich G., et. al. Competition effect of shear-induced nuclei and multiwalled carbon Nanotubes (MWCNT) on β-isotactic polypropylene (iPP) formation in preshear injection-molded iPP/MWCNT nanocomposites, **Polym. Composite.** 2017, Doi: 10.1002/pc.24650

7. **Chang B.**, Wang B., Zheng G., et al. Tailoring microstructure and mechanical properties of injection molded isotactic–polypropylene via high temperature preshear. **Polym. Eng. Sci.** 2015, Doi: 10.1002/pen.24078

Book chapter

1. **Chang B**., Schneider K., Kuehnert I., Heinrich G., Cavitation behavior of semi-crystalline polymers during uniaxial stretching studied by synchrotron small-angle X-Ray scattering, **Small Angle Scattering and Diffraction**, http://dx.doi.org/10.5772/intechopen.74224, IntechOpen

Poster

1. Cavitation and lamellae fragmentation-reconstruction of isotactic polypropylene during uniaxial drawing: the influence of annealing, Europe Africa Conference 2017 of the Polymer Processing Society (PPS-33), June 26-29, Dresden, 2017

2. Structural evolution of isotactic-polypropylene during creep under sub-yield stress: lamellae thickening, tilting and fragmentation, 32nd International Conference of the Polymer Processing Society (PPS-32), July 25-29, Lyon, 2016

Unpublished articles

1. Accelerating shear-induced crystallization and enhancing crystal orientation of isotactic-polypropylene via N,N'-dicyclohexyl-2,6-naphthalene dicarboxamide self-assembly, under revision.

I would like thank all my colleagues in the Department of Mechanical and Structure for the pleasant working atmosphere, and the interesting outdoor activities during each spring and autumn. My special thanks goes to Mrs. Kristina Eichhorn for her kind help during my early period here, and Mrs. Gudrun Schwarz for the support and help various administrative works related to IPF.

I would like to express my thanks to my Chinese friends in Dresden. We spent together many times for the barbecue, hot-pot, card playing during weekends and special Chinese festivals.

Moreover, I wish to express my special thanks to my parents for their love, encouragement and mental support throughout this work and my life.

Finally and but not the least, I gratefully acknowledge China Scholarship Council for the financial support of my living and study in Germany.

June 2018, Dresden

15   Eidesstattliche Erklärung

Hiermit versichere ich, dass ich die vorliegende Arbeit ohne unzulässige Hilfe Dritter und ohne Benutzung anderer als der angegebenen Hilfsmittel angefertigt habe; die aus fremden Quellen direkt oder indirekt übernommenen Gedanken sind als solche kenntlich gemacht.

Weitere Personen waren an der geistigen Herstellung der vorliegenden Arbeit nicht beteiligt. Insbesondere habe ich nicht die Hilfe eines kommerziellen Promotionsberaters in Anspruch genommen. Dritte haben von mir keine geldwerten Leistungen für Arbeiten erhalten, die in Zusammenhang mit dem Inhalt der vorgelegten Dissertation stehen.

Die Arbeit wurde bisher weder im Inland noch im Ausland in gleicher oder ähnlicher Form einer anderen Prüfungsbehörde vorgelegt und ist auch noch nicht veröffentlicht worden.

Die Promotionsordnung wird anerkannt.